INFORMATION TO USERS

This material was produced from a microfilm copy of the original document. While the most advanced technological means to photograph and reproduce this document have been used, the quality is heavily dependent upon the quality of the original submitted.

The following explanation of techniques is provided to help you understand markings or patterns which may appear on this reproduction.

1. The sign or "target" for pages apparently lacking from the document photographed is "Missing Page(s)". If it was possible to obtain the missing page(s) or section, they are spliced into the film along with adjacent pages. This may have necessitated cutting thru an image and duplicating adjacent pages to insure you complete continuity.

2. When an image on the film is obliterated with a large round black mark, it is an indication that the photographer suspected that the copy may have moved during exposure and thus cause a blurred image. You will find a good image of the page in the adjacent frame.

3. When a map, drawing or chart, etc., was part of the material being photographed the photographer followed a definite method in "sectioning" the material. It is customary to begin photoing at the upper left hand corner of a large sheet and to continue photoing from left to right in equal sections with a small overlap. If necessary, sectioning is continued again — beginning below the first row and continuing on until complete.

4. The majority of users indicate that the textual content is of greatest value, however, a somewhat higher quality reproduction could be made from "photographs" if essential to the understanding of the dissertation. Silver prints of "photographs" may be ordered at additional charge by writing the Order Department, giving the catalog number, title, author and specific pages you wish reproduced.

5. PLEASE NOTE: Some pages may have indistinct print. Filmed as received.

Xerox University Microfilms
300 North Zeeb Road
Ann Arbor, Michigan 48106

73-26,872

MILLER, Robert Bruce, 1947-
CONVERSION ELECTRON LINE SHAPE ANALYSIS AND APPLICATIONS TO MOSSBAUER SPECTROSCOPY.

The Ohio State University, Ph.D., 1973
Engineering, nuclear

University Microfilms, A XEROX Company, Ann Arbor, Michigan

© Copyright by

Robert Bruce Miller

1973

THIS DISSERTATION HAS BEEN MICROFILMED EXACTLY AS RECEIVED.

CONVERSION ELECTRON LINE SHAPE ANALYSIS AND APPLICATIONS TO MOSSBAUER SPECTROSCOPY

DISSERTATION

Presented in Partial Fulfillment of the Requirements
for the Degree Doctor of Philosophy in the
Graduate School of The Ohio State
University

By

Robert Bruce Miller, B.Sc., M.Sc.

* * * * * *

The Ohio State University
1973

Approved by

Reading Committee:

Robert F. Redmond

Shoichiro Nakamura

Richard B. Nicholson

Advisor

Department of

Nuclear Engineering

ACKNOWLEDGMENTS

The author wishes to thank Dr. Robert A. Krakowski (now at Los Alamos Scientific Laboratory) for invaluable assistance in formulating the problem of spatially resolved Mossbauer spectroscopy. Special thanks are also extended to Dr. J.P.S. Pringle of the Chalk River Laboratories for generously providing the Xe^{125} conversion electron spectra at a critical period in the research. The author is also grateful to Dr. R. F. Redmond, Dr. R. B. Nicholson, and especially Dr. S. Nakamura for reviewing the initial drafts and making many helpful suggestions.

The author also wishes to thank the U. S. Atomic Energy Commission for the award of a Special Fellowship, the U. S. Air Force for delaying entrance to active duty, and the O. S. U. Instructional and Research Computer Center for helpful programming assistance.

Finally, the author wishes to acknowledge the typing of the initial draft by his sister, Mrs. Debby Dowty, the final draft by Mrs. Linda Thorne and Mrs. Carolyn Quinn, the encouragement of his parents, Mr. and Mrs. Robert W. Miller, and the help, patience, and encouragement of his wife, Cindy, without which this research would not have been possible.

VITA

October 14, 1947.	Born - Piqua, Ohio
1969 - 1972	Atomic Energy Commission Special Fellow, The Ohio State University, Columbus, Ohio
1970	B.Sc., The Ohio State University, Columbus, Ohio
1972	M.Sc., The Ohio State University, Columbus, Ohio
1972	Teaching Assistant, Department of Mechanical Engineering, The Ohio State University, Columbus Ohio

PUBLICATIONS

"An Analysis of Backscatter Mossbauer Spectra Obtained with Internal Conversion Electrons." Nuclear Instruments and Methods 100. pp. 93-105, 1972.

FIELDS OF STUDY

Major Field: Nuclear Engineering

Studies in Radiation Interaction and Radiation Damage. Professors Robert A. Krakowski and David A. Mosher.

Studies in Nuclear Reactor Theory. Professors Robert F. Redmond and Shoichiro Nakamura.

TABLE OF CONTENTS

		PAGE
ACKNOWLEDGMENTS		ii
VITA		iii
LIST OF TABLES		vii
LIST OF FIGURES		viii
LIST OF PLATES		xi
CHAPTER		
1.0	INTRODUCTION	1
	Problem and Objectives	1
	Related Work by Others	2
	Organization of Dissertation	10
2.0	ANALYTICAL MODEL	12
	The Source Distribution of Conversion Electrons	12
	The Electron Transport Kernel	19
3.0	CALCULATION OF THE ELECTRON TRANSPORT KERNEL, W(E,z)	23
	Analytical Models - The Age Diffusion Theory	23
	Results and Discussion of the Age Diffusion Theory	28
	Determination of the Transport Kernel W(E,z) from Experimental Data	36
	Results of the DACES1 Computer Code	57
	Response Function Computation by Analog Simulation	63
	Calculation of W(E,z) Using ELTRAS	81

TABLE OF CONTENTS

CHAPTER		PAGE
4.0	DETERMINATION OF THE DEPTH DISTRIBUTION OF CONVERSION ELECTRON SOURCES FROM CONVERSION ELECTRON ENERGY SPECTRA	91
	Numerical Inversion with DACES2	92
	Conclusion Regarding DACES2	126
5.0	APPLICATION OF THE ELTRAS AND DACES2 CODES TO THE CASE OF CO57 IN AN IRON SPECIMEN	129
	The Electron Transport Kernel W(E,z) for Metallic Iron	130
	The Determination of Depth Distributions from Fe^{57} Conversion Electron Spectra	138
6.0	DISCUSSION OF RESULTS AND APPLICATIONS	147
	Discussion	147
	Applications of Spatially Resolved Mossbauer Spectroscopy	161
7.0	CONCLUSIONS AND RECOMMENDATIONS	165
	Conclusions	165
	Recommendations	166
APPENDICES		
A	THEORY OF ELECTRON COLLISIONS AND TRANSPORT . . .	173
B	THE COMPUTER CODE ELTRAS	197
C	FREDHOLM INTEGRAL EQUATIONS OF THE FIRST KIND . .	218
D	THE UNFOLD ALGORITHM FOR DACES1 AND DACES2	228

TABLE OF CONTENTS

PAGE

APPENDICES

E ANALYTICAL INVERSION OF THE FERMI AGE DIFFUSION KERNEL 246

BIBLIOGRAPHY 250

LIST OF TABLES

TABLE		PAGE
3-1	Radiative and Radiationless Transitions Associated with De-excitation of Fe^{57} from the 14.4 KeV Excited State	33
3-2	Xe^{125} Depth Distributions Corresponding to the Associated Xe^{125} Conversion Electron Spectra	38
3-3	Initial Estimate Kernel Expansion Functions	53
3-4	Summary of Unfold Results from DACES1 E_k = 21.781 KeV	55
3-5	Spline Function Coefficients from DACES1 for the Empirical Pringle Kernel (Xe^{125} in Ta_2O_5)	59
3-6	Spline Function Coefficients from DACES2 for the ELTRAS Kernel	87
4-1	Summary of Results of Unfolding with DACES2 z_o = 100 A	111
5-1	Spline Function Coefficients for the Kernel of Co^{57} in Metallic Iron	139

LIST OF FIGURES

FIGURE		PAGE
2-1	Schematic of Backscattering Geometry	13
3-1	Probability that an Electron of Energy E_k Originated at (z,dz) for 2% Energy Resolution According to the Fermi Age Diffusion Theory	31
3-2	Normalized K55 Conversion Electron Spectra of J. P. S. Pringle	41
3-3	Normalized K188 Conversion Electron Spectra of J. P. S. Pringle	42
3-4	Ratio of Area under K55 Line to Area under K188 Line vs Mean Depth of Distribution	43
3-5	Xe^{125} in Ta_2O_5 Kernel vs Depth for Various Energies	58
3-6	Flow Outline of the ELTRAS Code	66
3-7	Conversion Electron Spectrum of an Infinitely Thin Layer of Xe^{125} Deposited on the Surface of a Ta_2O_5 Sample	74
3-8	Energy Loss Spectrum (P_{ij}) from ELTRAS	75
3-9	Source-Weighted Spectrum from ELTRAS	76
3-10	Computed and Experimental Conversion Electron Spectra for $S(z) = \delta(z - 300\ A)$. E_o = 21.786 KeV Used as Emission Energy	78
3-11	Computed and Experimental Conversion Electron Spectra for $S(z) = \delta(z - 300\ A)$. E_o = 21.790 KeV	80
3-12	ELTRAS Final Spectra for Various Depths. E_o = 21.790 KeV	82

LIST OF FIGURES

FIGURE		PAGE
3-13	ELTRAS Emission Energy Required for Agreement with Experiment as a Function of Depth	83
3-14	Ratio of Total Weight Emerging above Cut-Off to the Total Emerging Weight as a Function of Depth	85
3-15	Comparison of the Empirical Kernel and the ELTRAS Kernel for Various Energies	89
4-1	DACES2 Solution with No Auxiliary Information	98
4-2	DACES2 Solutions with Prior Estimation	100
4-3	DACES2 Solutions with Smoothing	103
4-4	DACES2 Solutions with Smoothing and Prior Estimation	104
4-5	Solution Obtained Through Iterative Use of DACES2	106
4-6	Solution Obtained Through Iterative Use of DACES2	107
4-7	Solution Obtained Through Iterative Use of DACES2	108
4-8	DACES2 Solution with Inequality Constraints	110
4-9	DACES2 Solutions for the Gaussian Distribution with Mean Depth of 200 A	114
4-10	DACES2 Solutions for a Mean Depth of 300 A	115
4-11	DACES2 Solutions for a Mean Depth of 400 A	116
4-12	Iterative DACES2 Solutions for Xe^{125} in Ta_2O_5 for Various Depths	118
4-13	DACES2 Solutions for a Mean Depth of 100 A $\alpha = 0.0125$	120

LIST OF FIGURES

FIGURE		PAGE
4-14	DACES2 Solutions for a Mean Depth of 200 A α = 0.0125	121
4-15	DACES2 Solutions for a Mean Depth of 300 A α = 0.0125	122
4-16	DACES2 Solutions for a Mean Depth of 400 A α = 0.0125	123
4-17	Iterative DACES2 Solutions for a Mean Depth of 400 A	125
5-1	ELTRAS Final Spectra for Various Depths in Fe Metal. E_o = 7.3 KeV	136
5-2	ELTRAS Kernel for Co^{57} (E_o = 7.3 KeV) in Metallic Iron	141
5-3	DACES2 Solutions for Co^{57} in Metallic Iron at Various Depths	144
5-4	DACES2 Solutions for a Mean Depth of 300 A	145
6-1	Mossbauer Spectrum as a Function of Depth	162
7-1	Diagram of Experimental Apparatus	169
B-1	Generalized Flow Diagram for Electron Transport Calculation	199
B-2	Flow Diagram of Prejudiced Source Subroutine	202
B-3	Flow Diagram of Mean Free Path and Transmission Routine	205
B-4	Flow Diagram of Collision Routine	211

LIST OF PLATES

PLATE		PAGE
I.	Xe^{125} Distribution in the Ta_2O_5 after (a) Ion Implantation, (b) Anodization, and (c) Stripping	39
II.	Evaluation of Best Solution Parameters for W(E,z) at E = 21.781 KeV. (a) no smoothing, prior estimation, equality or inequality constraints; (b) eight inequality constraints; (c) prior estimates, PMUL = 0.4; (d) smoothing, SMUL = 0.4; (e) smoothing, SMUL = 1.0; (f) prior estimates, PMUL = 0.6, and smoothing, SMUL = 1.0	50
III.	Comparison of the Fermi Age Diffusion Theory with the Results of DACES1; (a) E = 21.806 KeV; (b) E = 21.790 KeV; (c) E = 21.757 KeV; (d) E = 21.724 KeV . . .	61

1.0 INTRODUCTION

1.1 Problem and Objectives

When exposed to chemically active environments, numerous metals and alloys form a protective film which controls the chemical reaction rate. Because of the immediate technological importance, the general topic of surface chemistry has received the widespread attention of both experimental and theoretical researchers, and several monographs and review papers have been written which treat the subject from various viewpoints. The bulk of the previous research, however, has been concerned primarily with the steady-state reaction rate, and relatively little is known about the transient films which form during the initial, non-steady stages. This area is particularly important because the spatial distribution, amount, composition, and structure of the initial phases often determine the subsequent reaction rate and the approach to steady-state, and sometimes even influence the nature of the steady-state scale.

These remarks are especially true in relation to the development of transient surface oxides during the high temperature oxidation of commercially important metals and alloys, where a lack of basic data prevents even semi-quantitative interpretation (1). Further knowledge of the spatial distribution and size of phases in the oxide scale, consideration of diffusional parameters both

parallel to and perpendicular to the alloy-oxide interface, and details of internal oxidation and plastic deformation are required before a more quantitative analysis is possible. Particular quantities of interest include pre-parabolic oxidation rate constants, alloy interdiffusion coefficients, oxygen solubilities and diffusivities in metals and alloys, and transport properties in doped alloy oxides.

The primary goals of this research are to develop and analyze a method capable of providing information concerning the above-mentioned quantities. The nondestructive method proposed here utilizes the techniques of both Mossbauer spectroscopy and beta spectroscopy to obtain spatial information concerning the various chemical phases on the surface of a specimen. The method is descriptively referred to as spatially resolved Mossbauer spectroscopy.

1.2 Related Work by Others

In view of the importance of the sub-microscopic aspects of surface chemistry, many new techniques which had previously been used only in the study of atomic, nuclear, and solid state phenomena have recently been applied to problems in surface analysis. Such techniques, including low energy electron diffraction (LEED), electron spin resonance (ESR), electron impact spectroscopy, Auger spectroscopy, positron decay, etc., are rather uncertain when used alone, but extremely valuable when used together with more conventional techniques, and have markedly improved our ability to

understand, predict, and enhance the performance of metals and alloys in hostile environments.

Mossbauer spectroscopy (2) represents one of the newest, most potentially promising techniques now available to the surface scientist, because the position, shape, and intensity of Mossbauer resonances are intimately related to the chemical environment in which the resonant nucleus is embedded. The Mossbauer effect is the recoil-free emission and resonant re-absorption of low energy γ-rays (up to about 150 KeV). This phenomenon, which can only occur when both emitting and absorbing nuclei are firmly bound in solids, is due to the fact that the recoil momentum of the transitions may be transferred to the crystal lattice as a whole. In this event the mass of the recoiling unit is very large, and essentially zero energy is transferred to the crystal lattice. Under ideal conditions, the width of the resonance is just the combined width of the nuclear levels involved (typically 10^{-8} eV), and is frequently small in comparison with hyperfine interaction energies resulting from interactions with the atomic environment. Thus, by studying these resulting line shifts and splittings, detailed information about the local environment of the nuclei may be obtained. It is primarily the influence of the environment on the γ-ray transitions which makes the Mossbauer effect a significant tool for chemical analysis.

The Mossbauer effect has been observed in over thirty isotopes (3), but only a few possess appropriate nuclear properties

for it to be seen easily. Of these, Fe^{57} and Sn^{119} are the most significant. While the Mossbauer effect has been widely applied to materials science involving iron and tin, relatively little attention has been given to its potential for surface studies. In the classical mode of Mossbauer investigation (transmission), the Mossbauer source is axially aligned with the sample, in the form of a thin foil or powder, and the detector. The emitted γ-rays pass through the sample containing the absorber nuclei to the detector and counting system. To sweep through the energies at which resonant absorption occurs, the Doppler effect is employed. A controlled relative motion is introduced between source and absorber so that the γ-ray energy becomes $E \pm \frac{v}{c} E$, where E is the transitional energy, v is the Doppler velocity and c is the velocity of light. At resonance, a decrease in count-rate is noted. Usually the absorber is the specimen, a single line source is used, and the spectrum is obtained directly. With this geometry not only may the signal intensity be limited by the low values of resonant half-lengths associated with the thin surface films, but resonance phenomena occurring in the substrate material may interfere or mask resonance processes occurring in the surface film. To circumvent these objections, Mossbauer scattering experiments which detect either the scattered photon, the X-ray associated with nuclear de-excitation via internal conversion, or the internal conversion electron itself, have been proposed. The description of a typical Mossbauer scattering

experiment has been given by Spijkerman (4).

Mossbauer scattering studies of surface chemistry utilizing detection of the conversion electron appear very attractive for two reasons: (i) since electrons of a particular energy have a well-defined range, information carried by conversion electrons originates from a minimum depth into the film, and (ii) since the conversion electrons are initially monoenergetic, a relationship must exist between the conversion electron energy spectrum and the depth distribution of Mossbauer nuclei within the resonator. Therefore, it seems plausible that the microscopic chemical information carried by the conversion electrons via Mossbauer spectrum parameters can be related to regions in the film which are quite small and which are semi-controllable via beta spectrometry; i.e., depth information concerning the chemical phases can be determined by energy analyzing the conversion electrons. Such a measurement, when applied to problems of surface chemistry, would be able to provide information about not only the chemical features of the various reaction phases, but also about their spatial distribution as well. Such results in conjunction with results obtained from more standard analyses would be expected to have a tremendous impact in understanding the previously outlined complex chemical processes that occur when metals and alloys are subjected to corrosive environments.

The feasibility of such a measurement has been crudely examined in a preliminary study by Bonchev et al. (5). This group recorded

Mossbauer spectra for a tin surface treated over bromine vapors by detecting conversion electrons of various energies. The means of energy selection was provided by a magnetic beta spectrometer. Changes in the Mossbauer spectra for various electron energies were interpreted with the help of a Bethe-Bloch expression deduced for low energy electrons, which related the electron energy loss to the total electron path length (6). While the possibilities of this technique for surface analysis are qualitatively evident from this study, the experimental technique can be criticized on a number of points. First and foremost, the interpretation of layer thickness from the Bethe-Bloch theory is inadequate. The layer depth determined in this manner assumes that all conversion electrons are emitted in the direction of the outward surface normal, lose energy continuously, and do not suffer scattering collisions. In fact, conversion electrons are emitted approximately isotropically, lose energy in discrete amounts, and do suffer scattering collisions. These deficiencies are also reflected in Bonchev's Mossbauer spectra. At momentum settings which should correspond to different chemical phases according to the Bethe-Bloch formulation, Mossbauer spectrum characteristics of all phases are apparent. To obtain quantitative results some method of unfolding the Mossbauer spectra (i.e., inferring the spatial distribution of emitted electrons) is evidently necessary. The second objection concerns the resolution of the beta spectrometer used by Bonchev. Even for very thick samples

emitting conversion electrons of approximately the same energy, the widths of conversion electron line spectra reported elsewhere in the literature are considerably less than those reported by Bonchev. With 5% momentum resolution, the conversion line is approximately symmetric and displays no energy loss structure that is so characteristic of results obtained with higher resolution instruments.

With a beta spectrometer exhibiting better resolution characteristics and an efficient method for unfolding Mossbauer spectra, the technique of Bonchev et al. could undoubtedly be used to obtain quantitative results. Another method based upon the same principles but somewhat more general in scope, however, is advocated here.

From studies of the range distribution versus incident energy of atoms embedded in solids by ion beam accelerators, several techniques for locating the position of subsurface foreign atoms have been previously developed. These include both chemical methods (etching (7) and electropeeling (8)) and nuclear spectroscopic methods (proton scattering (9) and monoenergetic α-particle emission (10)). The chemical methods are destructive in nature and are necessarily limited to those few materials having the appropriate chemical properties. The proton scattering method is restricted to foreign atoms much heavier than those of the host lattice, while the spectroscopic technique is limited to high-Z tracer species unstable to α-decay.

Finally, Graham et al. (11) have developed a conversion electron spectroscopic technique applicable to a variety of medium- and high-Z

tracer species. This method requires that the conversion electron line shape dependence on emitter atom depth be calibrated by successively subliming weighed amounts of a suitable absorber over the source. While this method in its present form is limited in that it does not provide quantitative information on the tracer atom depth distribution, this objection could be remedied by the development of an unfolding capability. This method also suggests an alternative to Bonchev's technique, which is described below.

A preliminary Mossbauer scan of the specimen under study would most probably reveal a complex, super-imposed pattern of individual Mossbauer spectra due to each of the chemical phases present in the sample. This complex spectrum could be analyzed into its components by any one of a number of computer routines written for this purpose (12, 13). Once the peaks are identified with their corresponding chemical phases, by adjusting the source velocity to provide a Doppler shifted photon which lies in resonance with a particular peak in the absorber, a beta spectrometer could measure the conversion electron energy spectrum of that particular chemical phase. Since conversion electron energy spectra observed at the surface are known to vary with conversion electron source depths, it should be possible to measure the depth distribution of any particular chemical phase by efficiently unfolding conversion electron energy spectra. To summarize, if it is desired to measure the depth distribution of a particular chemical phase, that phase is first selected by adjusting

the velocity of the Mossbauer source. The conversion electron current, due solely to the selected layer, is then energy analyzed, and the spectrum unfolded to obtain the depth distribution of the layer.

As an example, consider the oxidation of metallic iron to its possible oxides, FeO, α-Fe_2O_3, and Fe_3O_4. Metallic iron, α-Fe_2O_3 and Fe_3O_4 are all magnetically ordered materials and the dominant Mossbauer spectrum feature is due to Zeeman splitting of the nuclear levels. The respective iron nuclei in the metal and α-Fe_2O_3 all have equivalent sites; the Zeeman pattern in each instance is therefore characteristic of a unique internal magnetic field and consists of six lines corresponding to the allowed γ-ray transitions. In Fe_3O_4, the iron atoms occupy lattice positions with either tetrahedral or octahedral oxygen co-ordination, and the Mossbauer spectrum is a superposition of two six-line patterns. The relative shift of the spectra causes coincidence of the two right-most lines in each set.

FeO is paramagnetic at room temperature. In previous Mossbauer work on FeO, a partially resolved doublet pattern has been found in most instances. This is generally understood in terms of a quadrupole interaction associated with the non-stoichiometry of this oxide. Strictly, the phase should be represented by Fe_xO, where x is typically 0.92 (14).

The Mossbauer spectrum of an oxidizing thin film of metallic iron would thus be a complex pattern of the superimposed Mossbauer

spectra of the various phases. By Doppler shifting the source line to lie in resonance with a particular peak in the composite spectrum corresponding to an absorption line characteristic of a particular chemical phase, only the nuclei under the selected chemical environment become the source of conversion electrons. By energy analyzing the conversion electron spectrum, the depth distribution of the particular chemical phase is determined.

The fundamental equation which must be solved is a Fredholm integral equation of the first kind that relates the conversion electron spectrum, N(E), to the depth distribution of the conversion electron source, S(z), (the selected chemical phase) by means of an electron transport kernel, W(E,z). This equation is written as

$$N(E) = \int W(E,z)\ S(z)\ dz \qquad (1\text{-}1)$$

1.3 Organization of Dissertation

The general theoretical framework of the problem of spatially resolved Mossbauer spectroscopy is established in Chapter 2. Since the shape of the transport kernel largely determines the ease with which source distributions can be unfolded from conversion electron spectra, much effort is devoted to characterizing this response function. Chapter 3 presents computations of the response function obtained according to three methods: (i) a Fermi age diffusion theory, (ii) unfolding from experimental data (computer code DACES1), and (iii) a Monte Carlo simulation (computer code ELTRAS). The

results of these computations are discussed and compared, and the age diffusion theory is shown to be inadequate because of the continuous energy loss assumption.

To assess the feasibility of unfolding source distributions from conversion electron spectra, the unfold code DACES2 is developed and used to unfold unknown Xe^{125} (E_o = 21.79 KeV) source distributions in Ta_2O_5 from conversion electron spectra generated by the DACES1 kernel (Chapter 4), and Fe^{57} (E_o = 7.3 KeV) source distribution in metallic iron from conversion electron spectra generated by the ELTRAS kernel (Chapter 5).

Chapter 6 presents a discussion of the results and suggests possible applications, while Chapter 7 presents conclusions and recommendations. Much background material on electron transport and integral unfolding, in addition to many calculational details, is presented in the appendices.

Although the analyses are presented here with the primary goal of studying the feasibility of spatially resolved Mossbauer spectroscopy, the results should be of immediate interest to surface scientists performing radioactive tracer studies with conversion electron emitters. Also, the results are expected to be of general interest in the fields of beta spectroscopy, electron microscopy, and electron microprobe analysis where measurements are often obscured by the basis of the proposed measurement, electron scattering and energy loss.

2.0 ANALYTICAL MODEL

2.1 Introduction

In Chapter 1 it was indicated that the spectrum of conversion electrons emerging from a specimen in a Mossbauer experiment is dependent upon the source distribution of conversion electrons and an electron transport kernel. In this chapter both the source distribution and the transport kernel are examined in detail. In particular, the relationship between the conversion electron source distribution and the number density of Mossbauer-active nuclei is derived taking into account the attenuation of incident Mossbauer photons. In addition, the electron transport kernel is explicitly described in terms of the natural lineshape of conversion electrons after ejection from the inner atomic shell, the electron energy losses suffered while traversing the material, and the finite resolution of the beta spectrometer.

2.2 The Source Distribution of Conversion Electrons

Only the general aspects of nuclear resonance absorption necessary to introduce notation will be considered here. Detailed reviews of the Mossbauer effect are available in the literature. (3, 4, 15, 16)

The geometry used in the analysis is depicted in Figure 2-1. The resonator is represented by a semi-infinite slab which contains a depth-dependent number density of Mossbauer-active nuclei, $n_m(z)$.

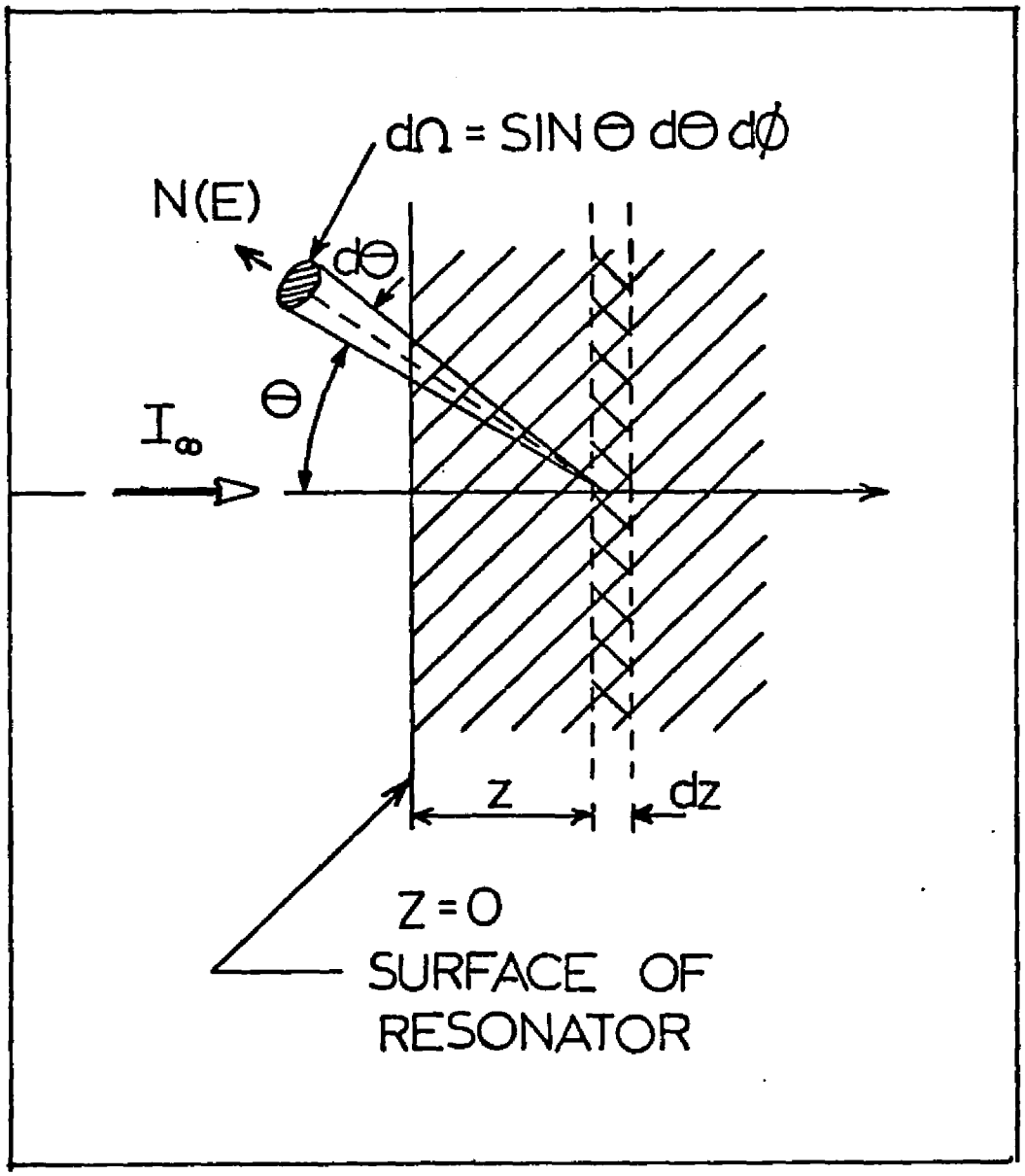

Figure 2-1. Schematic of Backscattering Geometry

Recoilless photons of intensity I_∞ photons/cm^2 - sec impinge onto the $z = 0$ surface of the resonator. The energy distribution of the incident photons is given by

$$I(E)dE = I_\infty L(E)dE \tag{2-1}$$

where $L(E)$ is the normal Lorentzian distribution written as

$$L(E)dE = \frac{\left(\frac{\pi}{2}\ \Gamma_S\right)^{-1}\ dE}{1 + \left[(E - E_{RS})/\tfrac{1}{2}\ \Gamma_S\right]^2} \tag{2-2}$$

E_{RS} denotes the peak of the emission spectrum and Γ_S the width. Defining the dimensionless quantity x as

$$x = \frac{E - E_{RS}}{\frac{1}{2}\ \Gamma_S} \tag{2-3}$$

Equation (2-2) can be written in a more convenient, dimensionless form as

$$L(x) = \frac{1}{\pi}\ \frac{dx}{1 + x^2} \tag{2-4}$$

If the source of recoilless photons is in motion relative to the resonator with a velocity v, the photons will be Doppler shifted. Defining $y = \frac{2E_{RS}}{\Gamma_S}\ \frac{v}{c}$, the incident photon energy distribution

becomes

$$I(x)dx = I_{\infty} L(x + y)dx \tag{2-5}$$

where

$$L(x + y) = \frac{1}{\pi} \cdot \frac{1}{1 + (x + y)^2} \tag{2-6}$$

A photon will interact with the resonator atoms primarily through two important mechanisms: (1) conventional interactions (photoelectric and Compton effects), and (2) nuclear resonance absorption (Mossbauer effect). Conventional gamma ray/electronic interactions can be represented by a linear absorption coefficient, μ_E . That is $\mu_E = N_e\sigma_{pe} + N_e\sigma_c$ where N_e is the atomic electron density, and σ_{pe} and σ_c are the cross sections for the photoelectric and Compton interactions. The microscopic cross-section for nuclear resonance absorption is given by the Breit-Wigner formula, $\sigma(E) = \dfrac{\sigma_o}{1 + \left(\dfrac{E - E_{RA}}{\frac{1}{2}\Gamma_A}\right)^2}$. The peak of the resonance occurs at E_{RA}, while the resonance width is denoted by Γ_A . The maximum absorption cross-section is given by

$$\sigma_o = \frac{2\pi\lambda\!\!\!^{-2}}{1 + \alpha} \cdot \frac{2I^* + 1}{2I + 1} \tag{2-7}$$

where I^* is the spin of the excited state, I is the spin of the ground state, and $2\pi\lambda\!\!\!^{-}$ is the wavelength of the incident photon.

Although the source has been assumed to be unsplit (no hyperfine interactions), this assumption is not generally valid for the resonator. Hence, if $(E_{RA})_j$ represents the resonance energy of the j^{th} hyperfine resonance level, the absorption cross section due to the j^{th} resonance becomes

$$(\sigma(E))_j = \frac{\beta_j \sigma_o}{1 + (\gamma_j x + \delta_j)^2} \tag{2-8}$$

where

$$\gamma_j = \Gamma_S / \Gamma_{A_j} \tag{2-9}$$

$$\delta_j = \left[E_{RS} - E_{RA_j}\right] / \Gamma_{A_j} \tag{2-10}$$

γ_j is the ratio of the photon emission width to the width of the j^{th} hyperfine resonance, while δ_j is the dimensionless difference between the peak of the emission spectrum and the j^{th} resonance. β_j represents a normalized statistical weight which is associated with the j^{th} level. A linear absorption coefficient, μ_{R_j}, associated with resonance absorption can be defined as

$$\mu_{R_j} = n_m(z)\, f\, \sigma_o \beta_j$$

where f is the fraction of the recoil-free Mossbauer nuclei in the resonator, and $n_m(z)$ represents the density of resonantly absorbing nuclei.

Hence, the probability, $P(z)$, that a resonant photon with reduced energy $x = \frac{2(E - E_{RS})}{\Gamma_S}$ experiences no interaction after traversing a distance z into the resonator is given by

$$P(z) = \exp - \left[\sum_j \frac{\mu_{R_j} z}{1 + \left[\gamma_j x + \delta_j\right]^2} + \mu_E z \right] \qquad (2\text{-}11)$$

If the separation of the j and $j \pm 1$ resonance is much greater than the resonance width Γ_{A_j}, each resonance level may be treated separately. (The interaction when the resonance levels are close to each other has been investigated by Bykov and Pham (17).) Furthermore, if the velocity v of the source is adjusted so that the source energy becomes exactly the same as the j^{th} resonance energy, then δ_j becomes zero and Equation (2-11) is reduced to

$$P(z) = \exp - \left[\frac{\mu_R z}{1 + (\gamma x)^2} + \mu_E z \right] \qquad (2\text{-}12)$$

where the subscript j is ignored. (It will be ignored also in subsequent discussion.)

The rate of nuclear resonance absorption in the thickness z to $z + dz$ is given by $\frac{I_\infty L(x + y)\ P(z)\mu_R dz}{1 + (\gamma x)^2}$. When multiplied by $\alpha/(1 + \alpha)$, where α is the conversion coefficient, quantity gives the rate of conversion electron emission from the thickness dz at z. If $W(\eta)d\eta$ represents the angular density distribution of emitted

conversion electrons, where $\eta = \cos\theta$ (refer to Figure 2-1), the depth dependent source strength of conversion electrons is given by

$$S(x,y,z,\eta) = S(x,y,z)\ W(\eta)$$

which becomes, assuming an isotropic angular distribution,

$$S(x,y,z) = I_\infty \left(\frac{\alpha}{1+\alpha}\right) \frac{L(x+y)}{1+x^2} \cdot \mu_R \cdot \exp\left[-\frac{\mu_R z}{1+(\gamma x)^2} - \mu_E z\right] \qquad (2\text{-}13)$$

Assuming for computational convenience that $\gamma = 1$, the total source distribution of conversion electrons as a function of depth into the resonator is given by integrating Equation (2-13) over all reduced energies, x:

$$S(z) = I_\infty \left(\frac{\alpha}{1+\alpha}\right) \mu_R e^{-\mu_E z} \int_{-\infty}^{\infty} \frac{dx}{(1+x^2)^2} \exp\left[-\frac{\mu_R z}{1+x^2}\right]$$

Using the identity (18)

$$\frac{1}{\pi}\int_{-\infty}^{\infty} \frac{e^{-c/(1+x^2)}}{(1+x^2)^2}\,dx = \tfrac{1}{2}e^{-c/2}\left[I_o\left(\frac{c}{2}\right) + I_1\left(\frac{c}{2}\right)\right] \qquad (2\text{-}14)$$

where I_o and I_1 are the modified Bessel functions of zeroth and first orders, Equation (2-13) becomes

$$S(z) = I_\infty \left(\frac{\alpha}{1+\alpha}\right)\mu_R \cdot \exp\left[-\frac{\mu_R z}{2} - \mu_E z\right] \cdot \frac{\pi}{2} \cdot \left[I_o\left(\frac{\mu_R z}{2}\right) + I_1\left(\frac{\mu_R z}{2}\right)\right] \qquad (2\text{-}15)$$

Thus, in general the conversion electron source distribution depends on the distribution of Mossbauer nuclei (through μ_R) in a rather complicated fashion.

2.3 The Electron Transport Kernel

The transport kernel $W(E,z)$ of Equation (1-1) must relate the conversion electron spectrum, as measured by the beta spectrometer, to the source depth distribution. Thus, computations of the kernel must take into account not only the natural line shape of conversion electrons upon atomic ejection, and electron energy losses suffered while traversing the material, but also the beta spectrometer resolution (or "window") function.

The natural line shape of conversion electrons is determined by the natural line shape of X-rays which follow the corresponding conversion. This depends, in turn, upon the atomic level widths associated with the transition. The shape of an X-ray emission line (and, hence, the internal conversion line) can be calculated in terms of a classical model by treating the radiating atom as a damped harmonic oscillator and using Fourier analysis (19). For the energy distribution of internal conversion electrons ejected from the atomic energy level C, the result is a Lorentzian line shape

$$J_c(E)dE = \frac{2}{\pi\Gamma_c} \cdot \frac{dE}{(E_c - E_x - E)^2 + (\Gamma_c/2)^2} \qquad (2\text{-}16)$$

where Γ_c , E_c , and E_x are the natural atomic level width, the binding energy of the C-shell electron, and the X-ray energy, respectively.

The primary mode of energy loss for KeV-energy electrons is the excitation of volume plasmons. A detailed discussion of electron interactions in solid materials for the energy region of interest is provided in Appendix A. Although the basic energy loss mechanisms are thought to be understood, unfortunately no entirely satisfactory electron transport model presently exists. For the purposes of this section, however, it is sufficient to characterize the electron transport by a kernel, $W(E' \longrightarrow E,z)$, which represents the probability that an electron born at depth z with energy E' will emerge from the surface with energy E into the acceptance angle of the spectrometer. Since conversion electrons are born with the Lorentzian distribution of Equation (2-16), the energy spectrum of conversion electrons, emitted at a depth z, is given by the integral

$$\int_E^\infty dE' \; J_c(E') \; W(E' \longrightarrow E,z)$$

The lower limit on the integration over E' is established by assuming that it is impossible for an electron to gain energy during a scattering collision (upscattering). This statement is strictly incorrect in that it is possible for primary electrons to gain energy during scattering events. The energy gain is very small, however ($\sim$.01eV). (20)

The broadening effects due to the finite resolving power of the spectrum analyzing instrument have long been recognized in determining natural level widths by analyzing conversion electron energy distributions from very thin sources (which minimize electron transport and energy loss effects). In these instances, since the instrumental window curve is probably Gaussian, (21) and the electron line shape to be measured is Lorentzian, the width of the observed line shape is neither the sum (Lorentzian) nor the root of the sum of the squares (Gaussian) of the widths of the two distributions. Assuming that the instrumental window is represented by the function $\chi(E,E')$, the integration over E'

$$W(E,z) = \int_0^\infty dE' \; \chi(E,E') \int_{E'}^\infty dE'' \; J_c(E'') \; W(E'' \longrightarrow E',z) \qquad (2\text{-}17)$$

yields the conversion electron spectrum due to a conversion electron source placed at a depth z, as measured by the beta spectrometer. This quantity is identified as the transport kernel $W(E,z)$. Thus, the conversion electron spectrum due to Mossbauer-active nuclei distributed in depth is explicitly written as

$$N(E) = \int_0^\infty dz \; S(z) \int_0^\infty dE' \quad (E,E') \int_{E'}^\infty dE'' \; J_c(E'') \; W(E'' \longrightarrow E',z) \qquad (2\text{-}18)$$

where $S(z)$ is given by Equation (2-15).

The adequacy with which equation (2-18) describes the experimentally obtained spectrum is solely dependent on the adequacy of the electron slowing-down kernel $W(E,z)$. If the kernel is known either

from theory or calibration experiments, the spatial distribution, S(z), can in principle be determined from the conversion electron energy spectrum by inverting, or unfolding, the depth integral. The quantity of specific interest is not the conversion electron source, S(z), however, but the spatial distribution of Mossbauer nuclei, $n_m(z)$. Hence, the solution of a transcendental equation is required in general to obtain $n_m(z)$.

3.0 CALCULATION OF THE ELECTRON TRANSPORT KERNEL, W(E,Z)

3.1 Introduction

In section 2.3 the construction of the kernel W(E,z) was explicitly exhibited. Since the unfolding of the depth integral depends critically upon the shape of W(E,z), it is necessary to develop accurate methods of characterizing the kernel before the question of unfolding feasibility can be examined. In this chapter, therefore, the nature of the transport kernel is thoroughly examined both theoretically (using analytical and numerical techniques) and experimentally (analyzing appropriate pre-existing experimental conversion electron spectra).

3.2 Analytical Models - The Fermi Age Diffusion Theory

Due to the general importance of electron transport, a number of analytical methods have been proposed for a wide variety of applications. These various models are not discussed here in detail, but are reviewed in Appendix A.

For any specific situation of interest, the electron energy, range, the boundary conditions imposed by the experimental configuration, and the importance of statistical fluctuations of energy losses and deflections should serve to indicate the most appropriate electron transport approach. For example, in the case of the

"thin foil-beam penetration" experiment, any one of the several multiple scattering theories will usually provide adequate results (22); on the other hand, computations of expected electron and electron bremsstrahling dose rates to astronauts protected by multi-layered shields can only be performed at the present time by complex Monte Carlo codes.

In the particular case at hand the initial energy of conversion electrons is typically much less than 1 MeV (for example, Fe^{57} and Sn^{119} emit conversion electrons of 7.3 KeV and 19.6 KeV, respectively), and bremsstrahlung reactions may be neglected without error in any transport calculation. The requirement that the energy distribution of the electron current be correlated with depth of origin necessitates a transport theory that differentiates between path length and position, thereby eliminating all simple multiple scattering theories from consideration. Furthermore, the moments method of Spencer (23) is not applicable because of the required finite boundary conditions. Therefore, the simplest applicable electron transport approach is the age diffusion treatment of Bethe, Rose, and Smith (24).

Applications of the age diffusion theory have been given by Meister (25), Weymouth (26), Roesch (27), and Archard (28). Meister examined the electron current from a plane isotropic source of 0.312 MeV electrons, sandwiched between various thicknesses of gold, indium, and aluminum foils. Interpreting the electron current

normalized to unit source strength as a transmission coefficient, Meister found good agreement between experiment and the age diffusion theory for gold and indium. Discrepancies in the results for aluminum were attributed to the low atomic number of that material. As with the other studies, however, the energy spectrum of the transmitted electron current was not measured, although Roesch has indicated that the age diffusion approach should not be valid for energies near the source energy.

For the present situation, the initial energy of the electrons is much smaller than initial energies employed in the previous studies. Furthermore, since conversion electrons are emitted relatively isotropically, the approximation that they immediately enter a diffusion process on emission should be more nearly correct, and good results should be obtained in experiments similar to those of Meister. On the other hand, if the age diffusion theory does not yield the correct energy spectrum, either the age diffusion approach must be modified, or else one of the more detailed numerical transport calculations (finite difference approximation, ANISN, or Monte Carlo) must be employed.

Since rather complete derivations of the age diffusion theory are available in the literature (24, 29), only the pertinent results of the calculation will be presented here. Assuming that only small angle scatterings are important, and under the diffusion approximation, the homogeneous Boltzmann equation reduces to an equation analogous to that obtained from neutron Fermi age theory (30).

$$\frac{\partial F}{\partial \tau} = \nabla^2 F \qquad (3\text{-}1)$$

$F(\vec{r}, \tau)$ is the total electron density, and the electron age τ and transport mean free path λ are given by

$$\tau(s) = \frac{1}{6} \int_0^S \lambda(s)ds = \frac{1}{6} \int_E^{E_o} 2(E) \frac{ds}{dE} dE \qquad (3\text{-}2)$$

$$\frac{1}{\lambda} = n\pi \int \sin\theta \ \sigma(\theta,v) \ (1 - \cos\theta)d\theta \qquad (3\text{-}3)$$

n is the number of scattering centers per unit volume, and σ is the microscopic cross section for electrons moving at velocity v scattering into an angle θ. The pathlength variable s is related to time through $ds = vdt$, and also to electron energy through the Bethe stopping power formula (31), $|dE/ds|$, through the expression

$$s = \int_E^{E_o} \frac{dE}{|dE / ds|} \qquad (3\text{-}4)$$

where E_o is the initial electron energy. The use of the stopping power formula yields a unique relationship between the total pathlength and the residual energy of the electron. Such a relationship is ambiguous, however, since electrons lose energy discretely and are sometimes subject to high energy losses. As a consequence of these statistical fluctuations, an energy spectrum is possible after any particular value of the pathlength.

Specific solutions to Equation (3-1) depend on the boundary and initial conditions imposed by the physical situation and are well known in the areas of heat transfer (32), diffusion of material (33), and neutron diffusion (34). In particular, the electron current due to a distributed, monoenergetic ($\tau = 0$) source which leaves a unit area at $z = 0$ per unit time with age τ has been shown to be (29)

$$N^*(\tau) = \int S(z)dz \left| (4\pi\tau^3)^{-\frac{1}{2}}(ze^{-z^2/4\tau} + (z+2d)e^{-(z+2d)^2/4\tau}) \right| \qquad (3\text{-}5)$$

where $d = \lambda/3$ is the extrapolation length.

Defining the quantity $W(\tau,z)$ by the expression

$$W(\tau,z) = (4\pi\tau^3)^{-\frac{1}{2}} \left| ze^{-z^2/4\tau} + (z+2d)e^{-(z+2d)^2/4\tau} \right| \qquad (3\text{-}6)$$

$W(\tau,z)$ is seen to represent the probability that an electron emitted from a monoenergetic electron source placed at depth z will contribute to the current emerging from the surface with age τ. $W(\tau,z)$ thus corresponds to the kernel $W(E' \longrightarrow E,z)$ once a connection between $E' \longrightarrow E$ and τ is established. Such a relationship has been derived in an approximate fashion and is given as (29)

$$\tau(\epsilon,\epsilon') = \frac{\epsilon'^4 - \epsilon^4}{24B_1B_2Z^3(4\pi a_o n)^2} \qquad (3\text{-}7)$$

where the reduced energy $\epsilon = \frac{E}{E_R}$, E_R is the Rydberg energy, and

a_o is the Bohr radius. B_1 and B_2 are weakly varying functions of energy given by

$$B_1 \simeq \log (2\epsilon/Z) \tag{3-8}$$

$$B_2 \simeq \log (367 \beta Z^{-1/3}) \tag{3-9}$$

n refers to the atom density of charge Z, and $\beta = \frac{v}{c}$.

Having established Equations (3-6) and (3-7) it is now possible to explicitly compute the kernel $W(E' \longrightarrow E,z)$ using the Fermi age diffusion theory. The final kernel $W(E,z)$ is then computed directly from Equation (2-17) using the $W(E' \longrightarrow E,z)$ given above.

3.3 Results and Discussion of the Fermi Age Diffusion Theory

In the technique of Bonchev et al., the Bethe-Bloch stopping power formula was used to provide a correlation between electron energy and source depth. In this section a similar correlation is sought in terms of the Fermi age diffusion theory. A number of assumptions are made for computational convenience: (1) the semi-infinite resonator is assumed to be uniformly dense, i.e., Mossbauer resonant atoms are uniformly distributed throughout the resonator, (2) both the energy distribution of the incident recoilless photons and the resonance flourescence cross section are assumed to be Dirac delta functions, (3) conventional gamma ray/electronic interactions are assumed to be negligible, (4) the energy distribution of the internal conversion electrons is also assumed to be a delta function, and (5) the beta spectrometer is assumed to have no dispersion.

With assumptions (1), (2), and (3), the spatial distribution of conversion electron sources, Equation (2-15), reduces to

$$S(z) = S_o \mu_R e^{-\mu_R z} \tag{3-10}$$

Assumptions (4) and (5) imply that in the Fermi age diffusion model the conversion electron line shape is given directly by Equation (3-5). When the source distribution is given by Equation (3-10), this becomes

$$N(\tau) = \frac{S_o \mu_R}{\sqrt{4\pi\tau^3}} \int_o^\infty e^{-\mu_R z} \left[z e^{-z^2/4\tau} + (z+2d) e^{-(z+2d)^2/4\tau} \right] dz \tag{3-11}$$

Assuming that the extrapolation length, d, is negligible, Equation (3-11) becomes

$$N(\tau) = \frac{S_o \mu_R}{\sqrt{\pi \tau}} \left| 1 - \sqrt{\pi}\ \mu_R \sqrt{\tau}\ e^{\mu_R^2 \tau}\ \operatorname{erfc}(\mu_R \sqrt{\tau}) \right| \tag{3-12}$$

$N(\tau)$ is the number of electrons with age τ which leave a unit area at $z = 0$ per unit time.

Of primary interest in relating the surface current of conversion electrons with kinetic energy in the range (E, E + dE) to a given depth of origination (z, z + dz) is the probability, $P(z, \tau)dz$, that an electron of age τ was created by a resonance event in (z, z + dz). $P(z, \tau)dz$ is given by the ratio $\frac{N(z, \tau)dz}{N(\tau)}$. Since $N(z, \tau)$ is given by the integrand of Equation (3-11),

$P(z, \tau)$ becomes

$$P(z, \tau) = \frac{(z/\tau)\ \exp(-z^2/4\tau - \mu_R z)}{1 - \sqrt{\pi}\ \mu_R \sqrt{\tau}\ \exp(\mu_R{}^2\tau)\ \operatorname{erfc}(\mu_R \sqrt{\tau})} \qquad (3\text{-}13)$$

where the extrapolation distance is neglected and $P(z, \tau)$ is normalized as $\int_0^\infty P(z, \tau)dz = 1$. $P(z, \tau)$ has been converted to $P(z, E)$ by $P(z, E) = P(z, \tau) \left|\frac{d\tau}{dE}\right|$. $P(z, E)$ is illustrated as a function of depth for various energies in Figure 3-1 for the case of Fe^{57} uniformly distributed in metallic iron.

It is readily apparent that spatial resolution rapidly degrades with increasing energy loss due to the randomizing effect of collisions. In addition, $P(z, E)$ exhibits an overlapping behavior. For an energy of ~ 4 KeV, $P(z, E)$ is a maximum for $z \sim 600$A; however, a 7.0 KeV electron is much more likely to be emitted from a depth of 600A, than is a 4.0 KeV electron. Other factors which are expected to interfere with the measurement of conversion electron energy spectra include the radiative and non-radiative transitions which accompany the de-excitation of Fe^{57}. It has been assumed that the excited Fe^{57} nucleus de-exites primarily via the emission of a 7.3 KeV electron. The total internal conversion coefficient, α, is defined as $\alpha = N_e/N_\gamma$ where N_e and N_γ are respectively the number of conversion electrons and photons emitted from a sample per unit of time. The total internal conversion coefficient is the sum of individual coefficients which describe separately conversion processes for each atomic subshell; i.e., $\alpha = \alpha_K + \alpha_L + \alpha_M + \ldots$,

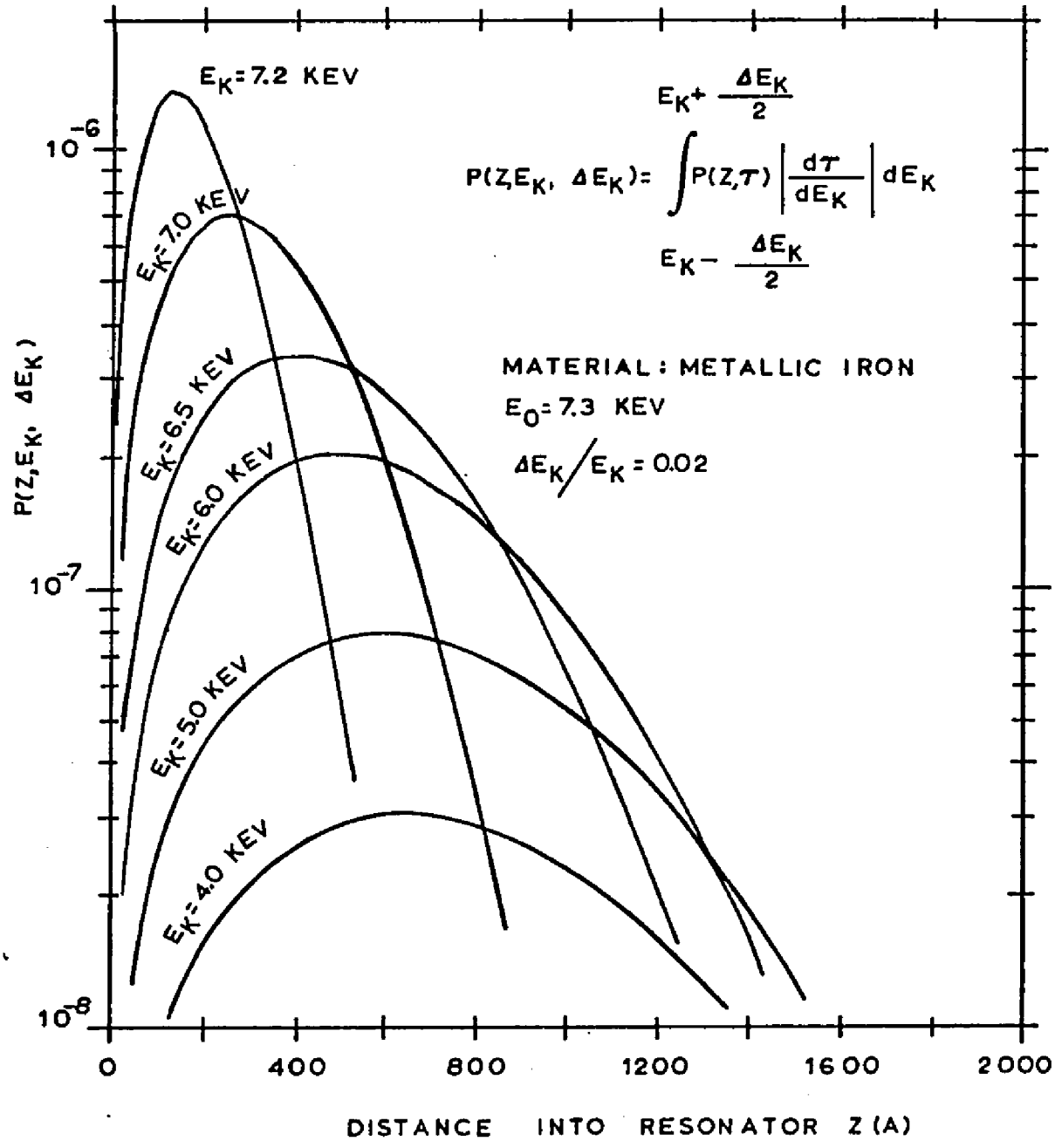

Figure 3-1. Probability that an electron of Energy E_k Originated at (z,dz) for 2% Energy Resolution according to the Fermi Age Diffusion Theory.

where α_i is the internal conversion coefficient for the i^{th} electron shell. The kinetic energy of a conversion electron emitted from the i^{th} shell is $E_i = E_{RA} - B_i$, where B_i is the binding energy of the i^{th} shell. Following ejection of the internal conversion electron, the energy B_i, represented by a vacancy in the i^{th} shell, is emitted as characteristic X-rays and Auger electrons. The probability of X-ray emission is given by the flourescent yield, $(FY)_i$. For example, a K shell vacancy is filled by a transition of an L electron to the K shell and the emission of either a K X-ray with energy $B_K - B_L$ (equal to 6.3 KeV for iron) or an L shell Auger electron with energy $(B_K - 2B_L)$. The flourescence yield, $(FY)_k$ describes the competition between K_α X-ray emission and Auger electron yield. Vacancies produced in the L shell are then filled with electrons from higher shells, and additional characteristic X-rays and Auger electrons are emitted. These processes continue until the total transition energy, E_{RA}, is released.

With knowledge of the B_i (35), α_i (36), and $(FY)_i$ (37), a complete enumeration is possible. Such a compilation is presented in Table 3-1 for the case of Fe^{57}. These data indicate the probability of occurrence of a given radiation on the basis of a single nuclear de-excitation of Fe^{57}. The importance of the 5.4 KeV Auger electron with respect to the K shell conversion electron is noted. For every K shell conversion electron observed, an accompanying L shell Auger electron will be observed with a probability of 0.71. Preliminary experimental results obtained using a thin

TABLE 3-1

Radiative and Radiationless Transitions Associated with De-excitation of Fe^{57} from the 14.4 KeV Excited State

Kind of Radiation	Energy (KeV)	Probability of Occurrence
resonant gamma ray	$E_{RS} = 14.4$	$1/(1+\alpha) = 0.09$
M shell conversion electron	$E_{RS} - B_M = 14.3$	$\alpha_M/(1+\alpha) = 0.01$
L shell conversion electron	$E_{RS} - B_L = 13.6$	$\alpha_L/(1+\alpha) = 0.09$
K shell conversion electron	$E_{RS} - B_K = 7.3$	$\alpha_K/(1+\alpha) = 0.81$
K_α X-ray	$B_K - B_L = 6.3$	$\left[\alpha_K/(1+\alpha)\right](FY)_K = 0.24$
L shell Auger electron	$B_K - 2B_L = 5.4$	$\left[\alpha_K/(1+\alpha)\right](1 - (FY)_K) = 0.57$
other X-rays and electrons	$< B_L = 0.85$	$\alpha/(1+\alpha) = 0.91$

"pancake" proportional detector (38) by Mr. Jacques Lingenfelter with the collaboration of this author have indicated that conversion electron spectral analysis with this type of detector is impossible because of these spectral complexities. To avoid this difficulty, a high resolution beta spectrometer must be employed.

This analysis, although not expected to be exact, does serve to further illustrate the inadequacy of the technique of Bonchev et al. The current due to electrons that have suffered many energy loss collisions will not only be of extremely small intensity, but will also carry very little spatial information. In view of these limitations, together with spectral complexities associated with the low energy end of the electron energy spectrum, it does not appear to be feasible to obtain meaningful spatial information via the analysis of "broad" internal conversion spectra. (The term "broad" is used to designate spectra calculated over the broad energy range $(\frac{E_o}{2}, E_o)$.) In fact, this author has been unable to find any published experimental data relating the spatial distribution of conversion electron emitters to variations in the sort of "broad" conversion electron spectra just discussed. While this does not preclude the possibility of such an effect, the validity of any particular theoretical model could not be easily verified.

On the other hand, the variation of "narrow" conversion line spectra with emission depth is well documented (39). (The term "narrow" is used to designate spectra whose lower range limit is typically less than 500 eV below E_o.) Since this energy range of

interest lies very close to the electron emission energy, it is necessary to re-examine the validity of the age diffusion theory before it is applied to this energy range.

In devising the age diffusion approach, one of the basic tenets was the assumption of the continuous slowing-down theory of Bethe which led to a transport equation involving the pathlength variable, s, rather than the energy variable. The connection between the pathlength variable, s, age, τ, and energy, E, was then made by employing the Bethe-Bloch stopping power formula. In this formulation, the scattering centers were represented by free electrons. The relativistic quantum mechanical cross section for the problem of free electron scattering has been calculated by Moller. Valence forces were factored into this interaction model by specifying a minimum scattering angle below which the scattering was ineffective in transferring energy.

Over the past decade the energy loss mechanism in the Bethe stopping power model has come under attack from workers investigating energy loss interactions of kilovolt electron beams in thin films. Energy losses have been observed to occur in multiples or combinations of discrete amounts, not in agreement with known atomic energy level structures. Subsequent theoretical investigations (40) of electron plasma excitation modes in solids have provided a basis for the interpretation of these experimental results, and the plasmon loss mechanism has been incorporated into the stopping power formulation (41). Regardless of which stopping power formula is used,

however, the validity of the continuous slowing-down model in discribing "narrow" conversion spectra is questionable because of the discrete nature of electron energy losses.

In addition, the electron scattering cross section is strongly peaked in the forward direction, and the validity of the diffusion approximation must be questioned. Finally, the transport mean free path for electrons is typically 10^2 - 10^3 A , and the diffusion approximation cannot be expected to be valid for source depths in this region. Because of the questionable validity of the age diffusion theory it is necessary to provide an experimental comparison. To provide a basis for assessing the applicability of the age diffusion treatment, experimental Xe^{125} conversion electron spectra and associated source distributions generously supplies by J. P. S. Pringle (42) have been used to determine the response function $W(E,z)$. These computations are described in the following section.

3.4 Determination of the Transport Kernel $W(E,z)$ from Experimental Data

In this section the computer code DACES1 (Data Analysis of Conversion Electron Spectra, No. 1) is developed to provide a method of determining the transport kernel $W(E,z)$ from experimentally obtained conversion electron spectra and their associated source distributions. The kernel computed in this fashion is then compared with results of the age diffusion theory.

In connection with atomic transport number measurements, Pringle has recently measured conversion electron energy spectra from Xe^{125} implanted in anodized tantalum by an ion beam accelerator. Using a stripping technique (43) he was able to very accurately measure the Xe^{125} depth distribution. For ion beam energies of 5 KeV, the stripping experiments have shown the depth distribution of Xe^{125} to be given approximately by a Gaussian function with a most probable depth of penetration of 30 A and a standard deviation of 20 A. After subsequent anodization the Xe^{125} is still distributed according to a Gaussian function, although both the mean depth and the standard deviation increase as the anodization proceeds. At the end of the anodization various layers of Ta_2O_5 were stripped from the surface of the sample. Conversion electron spectra were recorded at various stages in the anodization and stripping processes, as given in Table 3-2 (all values in Angstrom units). The quantity t_i indicates the initial depth of the anodized layer in which the Xe^{125} was implanted (see Plate Ia). After the implantation, the samples were subsequently anodized (Plate Ib) until the oxide layer reached a depth indicated by the quantity t_f. Thus, the incremental anodization depth is given by $(inc) = (t_f - t_i)$. As a result of oxygen and tantalum migration during the anodization, the Xe^{125} distribution is also seen to vary. The specimen labelled αXVII in Table 3-2 was subsequently stripped of various amounts of oxide (Plate Ic). The stripping process removed material (Ta_2O_5) only from the surface, leaving the lower-lying Xe^{125} distribution unaltered.

TABLE 3-2

Xe^{125} Depth Distribution Corresponding to the Associated Xe^{125} Conversion Electron Spectra
(t_i = initial anodization depth, t_f = final anodization depth, inc = $t_f - t_i$)

SPECIMEN NO.	ANODIZATION			Xe^{125}	
	t_f	t_i	inc	MEAN DEPTH	STD. DEV.
αXVI(a)					
αXVIII(a)	----	----	----	30 ± 2	20 ± 1
αXVI(b)	1328	881	447	144 ± 3	26 ± 1
αXIV	1766	881	885	256 ± 3	32 ± 1
αXVIII(b)	2216	881	1335	371 ± 4	36 ± 1
αXVII (a)	2647	879	1768	481 ± 5	40 ± 1
(b)	2561			395 ± 4	40 ± 1
(c)	2471			305 ± 3	40 ± 1
(d)	2373			207 ± 3	40 ± 1
(e)	2273			107 ± 3	40 ± 1

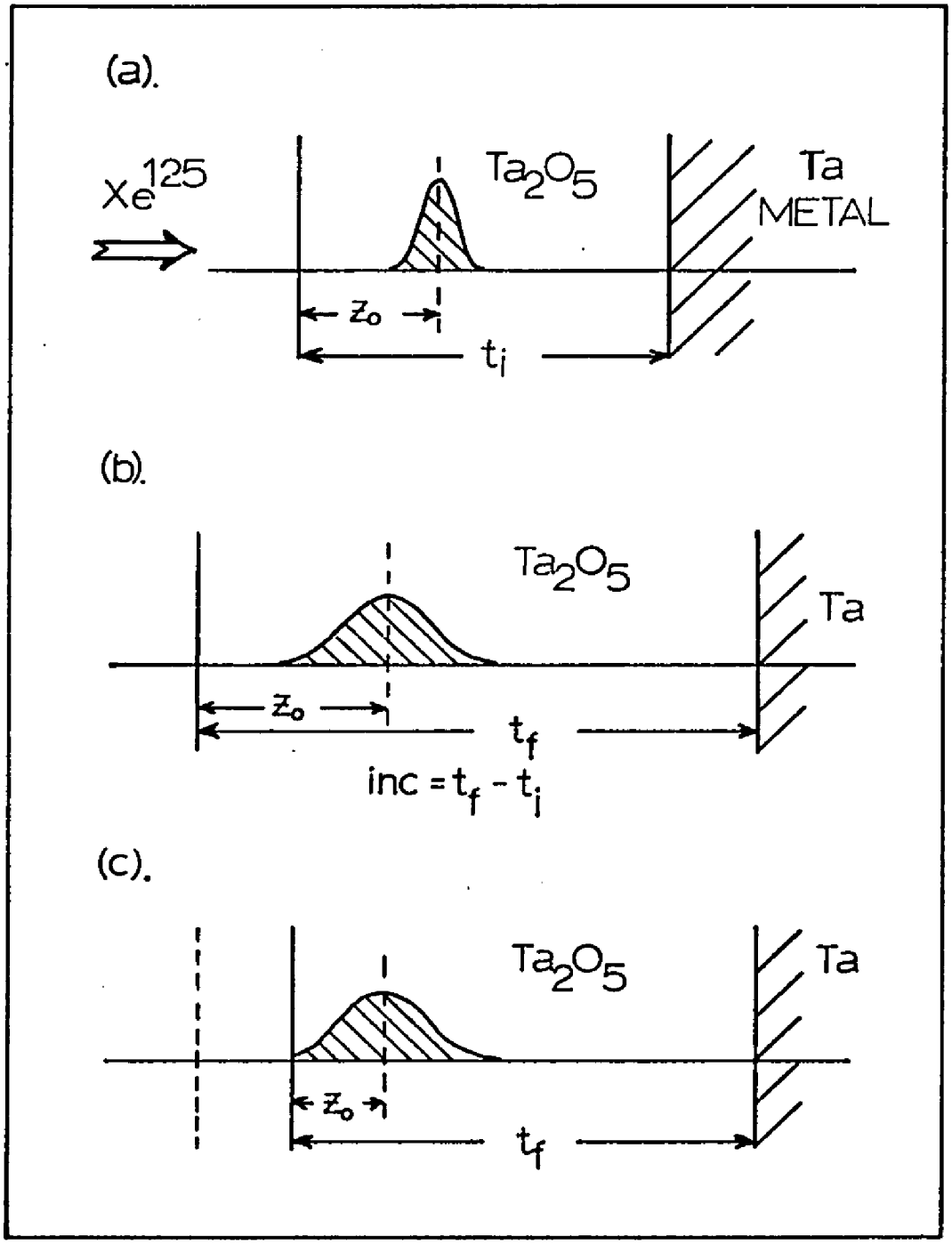

Plate I. X_e^{125} Distribution in Ta_2O_5 after (a) Ion Implantation, (b) Anodization, and (c) Stripping.

Xe^{125} emits two intense conversion lines at 21.79 KeV and 155.2 KeV, which arise from K shell conversion of the 54.96 KeV and 188.4 KeV nuclear transitions, respectively. These lines are designated K55 and K188, and are plotted in Figures 3-2 and 3-3, respectively, for selected source distributions listed in Table 3-2. While depth effects are small for the K188 line, for the K55 line the shift of the spectrum peak to lower energies and the line broadening with increasing mean depth are readily apparent.

Since the absolute value of the Xe^{125} source strength is an unknown quantity in the data of Pringle, the following normalization procedure was adopted. As previously noted, variations of the K188 line shape with increasing source depth have been found to be small compated to variations in the K55 line shape. The area of the K188 line has previously been used by Pringle as a measure of the source strength. A more obvious normalization factor, however, would be the area under the K55 line. For source distributions fairly close to the surface, the ratio of the area under the K55 line to the area under the K188 line should be approximately constant. This ratio has been evaluated and is plotted in Figure 3-4 as a function of the mean depth of the source distribution. For greater mean depths, the ratio A55/A188 decreases because more of the K55 electrons have slowed down to energies below the lower range limit of the beta spectrometer. Extrapolation to zero mean depth yields a value of (A55/A188) = 3.5 . The area of the K55 line is then

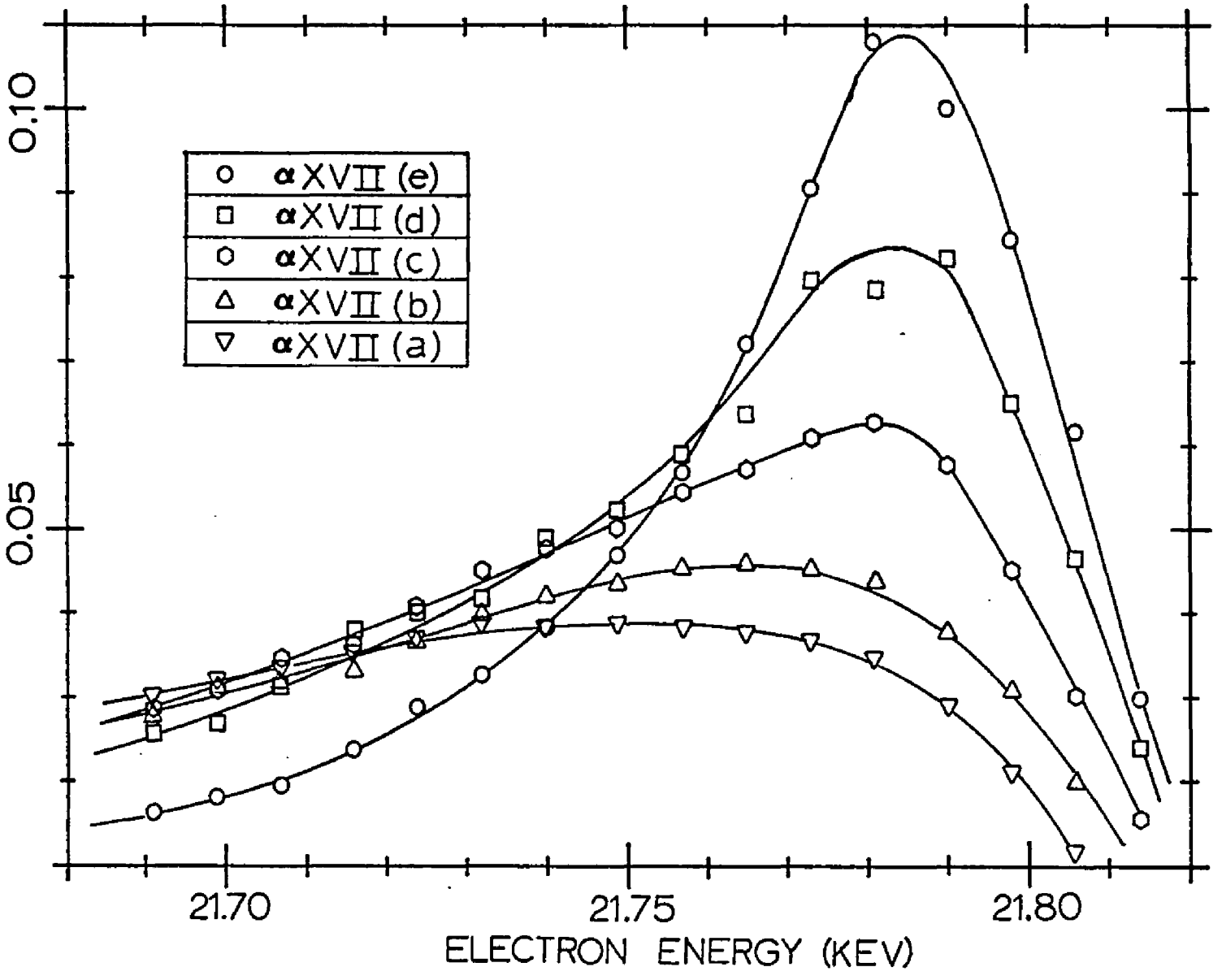

Figure 3-2. Normalized K55 Conversion Electron Spectra of J.P.S. Pringle.

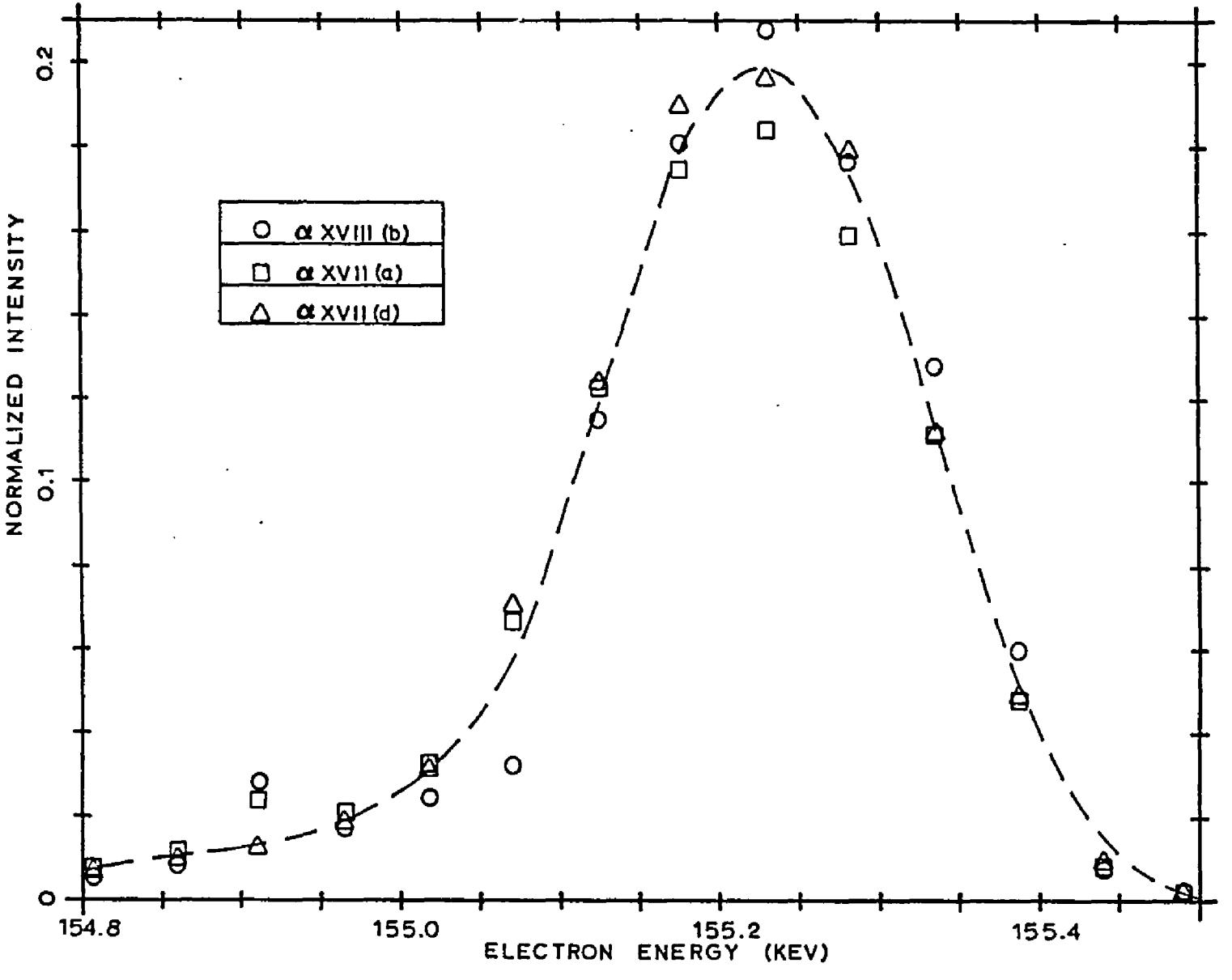

Figure 3-3. Normalized K188 Conversion Electron Spectra of J.P.S. Pringle.

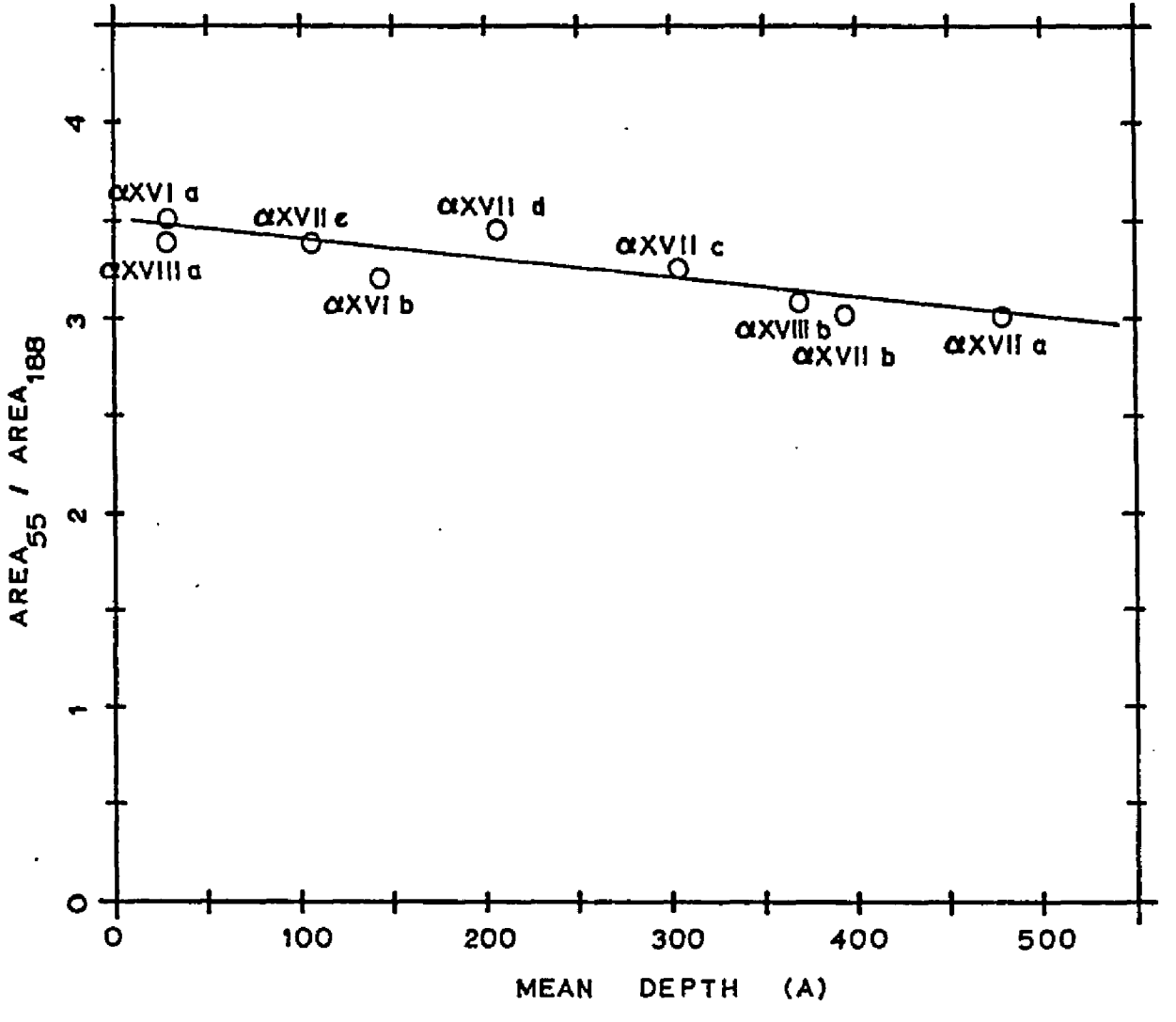

Figure 3-4. Ratio of Area under K55 Line to Area under K188 Line vs Mean Depth of Distribution.

approximately given by (3.5)A188, and this value was used as the normalizing factor in Figure 3-2.

These Xe^{125} source distributions and associated conversion electron spectra can be used to numerically construct the response function $W(E,z)$. According to Equation (1-1), at every energy E_k the following relation must hold for the i^{th} source distribution

$$N_i(E_k) = \int_0^\infty W(E_k,z)\ S_i(z) \qquad (3\text{-}14)$$

Equation (3-14) is known as a Fredholm integral equation of the first kind (refer to Appendix C).

The computer code DACES1, which is based upon the recently given UNFOLD code of Biggs and Amos (44), has been developed and used to solve Equation (3-14) for the kernel $W(E_k,z)$. The details of the UNFOLD algorithm are contained in Appendix D and Reference (45).

Since solutions of Fredholm integral equations of the first kind are inherently unstable DACES1 relies on making optimum use of all available information to obtain an acceptable solution. In particular, provisions are made to incorporate smoothing criteria, prior data estimates, equality constraints, inequality constraints, available error estimates, and any other miscellaneous information that may exist about the solution. The nature of the solution estimate obtained is that it is the estimate that minimizes a least squares functional subject to any equality and/or inequality constraints, a typical quadratic programming problem which is solved

in DACES1 by the Theil-Van de Panne procedure (46). The solution results are also checked for consistency with the auxiliary error information to insure feasibility of the solution estimate.

The successful solution of the DACES1 unfolding problem depends greatly upon the shape of the $S_i(z)$, the availability and accuracy of data and auxiliary information, and the efficiency with which the auxiliary information is used. Since the source distributions for this problem are relatively narrow Gaussian distribution functions, the existence of acceptable solution estimates is virtually guaranteed, and the primary task is to optimize the use of the auxiliary information. In the following the data of Pringle and the physics of the problem are analyzed to determine values for the various parameters which are incorporated into DACES1.

Since the kernel represents, in effect, the electron spectrum due to a source placed at a depth z, the DACES1 solution estimate of $W(E,z)$ is required to be non-negative. Further, since the medium in which the conversion electron sources are embedded is approximately homogeneous, $W(E,z)$ is expected to be continuous and non-oscillatory with continuous first and second derivatives. Finally, at energies above the peak energy position, $W(E,z)$ is expected to be a monotonically decreasing function of depth, because the greater the pathlength an electron must travel to reach the surface, the greater the possibility for an energy loss collision. At lower energies, however, $W(E,z)$ may actually increase with depth due to higher energy electrons suffering energy loss collisions which bring them

into the energy range of interest before they emerge from the surface.

The input data sets, $N_i(E_k)$, ($k = 1\cdots,NE$) for DACES1 are formed from the data values reported by Pringle (see Figure 3-2) at energy E_k, for each source distribution (denoted by subscript i, $i = 1,\cdots,NS$).

For the purpose of estimating the error in the conversion electron data there are two primary sources: (i) statistical fluctuations in the measurements recorded by the spectrometer, and (ii) variations in the mean depths and standard deviations of the source distributions, $S_i(z)$, as evidenced in Table 3-2. Since the measurement data are available in numerical form, the statistical errors of i above are relatively easy to enumerate, and were found to be generally of the order of $\lesssim 10\%$.

Errors due to ii above are somewhat more difficult to evaluate. Returning to Equation (3-14) it is evident that data errors due to variations in the source distribution will be influenced by the shape of the kernel function, $W(E_k,z)$. To properly estimate the magnitude of these errors would require an approximate evaluation of the kernel for each data set energy E_k. Rather than proceeding in this manner the following simple procedure was adopted. When the conversion spectra data points for the higher energies ($E \gtrsim 21.781$ KeV) were plotted on semilogrithmic paper versus the mean depths of the corresponding Xe^{125} depth distributions, a smooth curve drawn through the data points appeared roughly linear, thereby suggesting exponential depth dependence. Accordingly, the

kernel was approximated by

$$W(E_k,z) \simeq a(E_k)\ e^{-b(E_k)z} \tag{3-15}$$

After graphically evaluating the constants a and b for E_k = 21.781 KeV, the kernel representation of Equation (3-15) was used to estimate data errors due to variation in the mean depth of the source distributions. The results of these computations indicate that such errors are generally of the order of $\lesssim$5%.

Although they are extremely approximate, the results of these error analyses would seem to indicate that relative errors in the data should seldom exceed 10%. This value was consequently used to specify the data error parameter ERU of Equation (D-4); i.e., $ERU_i(E_k) = 0.1N_i(E_k)$.

After the spectral data and the error estimates have been specified, DACES1 proceeds by assuming the solution can be parameterized as

$$W(E_k,z) = \sum_j C_j(E_k)D_j(z) \tag{3-16}$$

where the $D_j(z)$ are a set of linearly independent functions and the C_j are the elements of the solution vector now to be determined.

The expansion functions, $D_j(z)$, of Equation (3-16) can be any set of linearly independent functions, Legendre polynomials, for example. For many problems, however, cubic splines have been used successfully (47), and they have been used in the present problem. The functional form of the cubic spline is given by

$$CS = \sum_{j=1}^{4} C_j z^{j-1} + \sum_{j=5}^{NJ+4} C_j (z - J_{j-4})_+^3 \qquad (3\text{-}17)$$

NJ indicates the number of spline joints, the J_{j-4} are the joint values, and the + symbol indicates multiplication by the unit Heaviside function $h(z - J_{j-4})$. With this fitting function choice the D_j expansion functions are given as

$$D_1(z) = 1 \qquad D_5(z) = (z - J_1)\ 3_h(z - J_1)$$
$$D_2(z) = z \qquad D_6(z) = (z - J_2)\ 3_h(z - J_2)$$
$$D_3(z) = z^2 \qquad D_7(z) = (z - J_3)\ 3_h(z - J_3)$$
$$D_4(z) = z^3 \qquad D_8(z) = (z - J_4)\ 3_h(z - J_4)$$

Since eight source distributions were used (NS = 8), the maximum number of spline function coefficients that can be determined is also eight. Thus, NJ of Equation (3-17) was set equal to four. The choice of the spline joint positions is not altogether arbitrary; the joints should be more densely spaced in regions in which $W(E,z)$ is expected to be more rapidly varying. Since it was expected that the most rapid variation with depth would occur near the surface, the four spline joints were placed at depths of 50, 100, 175, and 350 A, respectively.

3.4.1 Evaluation of Best Solution Estimate Parameters Using DACES1

Having selected an appropriate fitting function, and having organized the data into suitable form and estimated the magnitude of data errors, the means of incorporating the available auxiliary

information into DACES1 to yield the best solution estimate were next investigated. Plate II exhibits some of the results of $W(E,z)$ with E_o = 21.781 KeV, determined by DACES1 with different sets of auxiliary data, which will be described more in detail in this section.

The data points in these figures enclosed by circles on the solution estimate graphs represent the actual conversion electron spectra data, $N_i(E_k)$. Equation (3-14) can be viewed in the following manner: the data $N_i(E_k)$ represent samplings of the kernel $W(E_k,z)$ obtained with Gaussian response (sampling) functions, $S_i(z)$. As the standard deviation σ_i of each source distribution becomes small, $S_i(z)$ approaches a delta function, $\delta(z - z_{oi})$, and $N_i(E_k)$ approaches $W(E_k,z_{oi})$. To verify this interpretation the data were recorded on the graphs at depths corresponding to the mean depths of the various source distributions.

To investigate the inherent instability of the problem, the unfold term alone (Z_u of Equation (D-4)) was employed first to obtain a result without aid of equality or inequality constraints. The integral of Equation (D-4) was evaluated by dividing the integration interval (0-650 A) into 32 subintervals specified by explicitly reading into computer storage the appropriate subinterval boundaries. The integrations in each subinterval were carried out to an accuracy of 10^{-5} by using four-point Gaussian quadrature and subdividing each subinterval until the specified accuracy was obtained. An example of the simple least squares calculation is shown in Plate IIa.

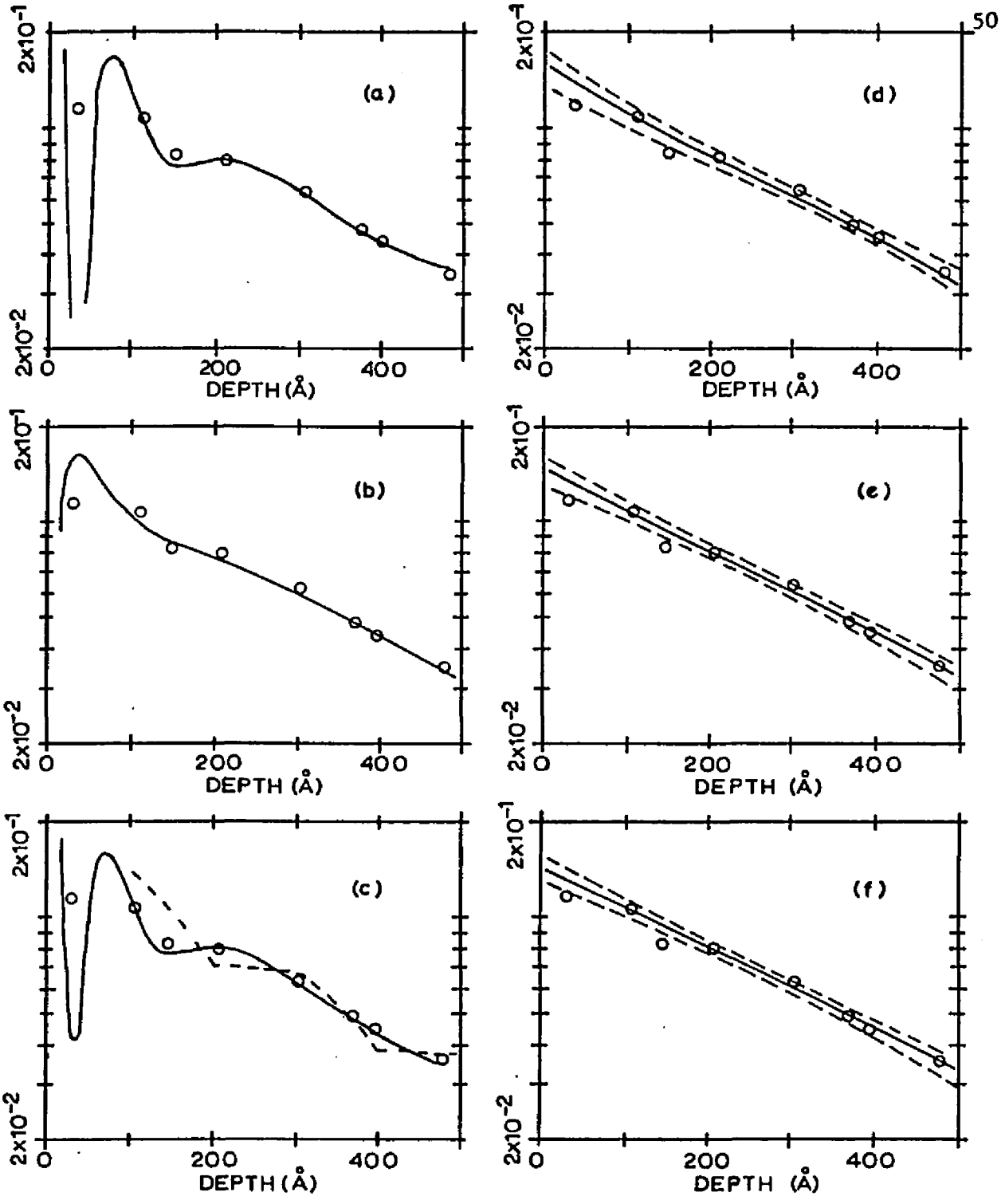

Plate II. Evaluation of Best Solution Parameters for W(E,z) at E=21.781 KeV. (a) no smoothing, prior estimation, equality or inequality constraints; (b) eight inequality constraints; (c) prior estimates, PMUL=0.4; (d) smoothing, SMUL=0.4; (e) smoothing, SMUL=1.0; (f) prior estimates, PMUL=0.6, and smoothing, SMUL=1.0.

The oscillatory behavior of this solution estimate, especially apparent at small depths, makes this result unacceptable.

In Plate IIb eight inequality constraints have been imposed in an attempt to subdue oscillations. Using the auxiliary information and the prior estimate data as guidelines, the following inequality constraints were constructed:

$$W(E_k,z) \geq 0 \qquad z = 0,\ 0.5,\ 1.0,\ 6.5$$

$$W'(E_k,z) \leq 0 \qquad z = 1.75,\ 3.5$$

$$W''(E_k,z) \geq 0 \qquad z = 1.75,\ 3.5$$

In the context of UNFOLD (see Equation (D-9)) these constraints, with all V_i set equal to zero, are written as:

$$L_1\ D_j(z) = -D_j\ (0.0)$$

$$L_2\ D_j(z) = -D_j\ (0.5)$$

$$L_3\ D_j(z) = -D_j\ (1.0)$$

$$L_4\ D_j(z) = -D_j\ (6.5)$$

$$L_5\ D_j(z) = D_j'(1.75)$$

$$L_6\ D_j(z) = D_j'(3.5)$$

$$L_7\ D_j(z) = -D_j''(1.75)$$

$$L_8\ D_j(z) = -D_j''(3.5)$$

With the addition of the eight inequality constraints much of the oscillatory behavior has been eliminated; for small z this solution estimate decreases unnaturally, however, and consequently does not satisfy the auxiliary information.

For the next trial, the inequality constraints were removed and the prior estimate functional, Z_p was added to the unfold functional. The initial estimate of the kernel was obtained by approximating the kernel as a linear expansion of arbitrary functions $u_j(z)$ spanning an identical range of depths as spanned by the $S_i(z)$, i.e.,

$$W(E_k,z) = \sum_j W_{kj}\, u_j\,(z) \tag{3-18}$$

With this expansion Equation (3-14) becomes

$$N_i(E_k) = \sum_j W_{kj} \int_o^\infty u_j(z)\; S_i(z)\; dz \tag{3-19}$$

or, written in matrix notation, $\vec{N} = \left[S\right]\vec{W}$. The initial estimate is then given by Equation (3-18), where the W_{kj} are computed from $\vec{W} = \left[S\right]^{-1}\vec{N}$.

Employing this formulation, $W(E,z)$ was evaluated as a function of z for several energies, E_k, between 21.750 KeV and 21.810 KeV for five data sets αXVII (a), (b), (c), (d), (e). The expansion functions were chosen to be five triangular functions whose depth dependence is indicated in Table 3-3.

TABLE 3-3

Initial Estimate Kernel Expansion Functions
(a_j, b_j, and c_j in Angstrom units)

Triangle Functions

$$u_j = \begin{cases} .1z + \beta_j & a_j \le z \le b_j \\ -.01z + \gamma_j & b_j \le z \le c_j \end{cases}$$

j	β_j	γ_j	a_j	b_j	c_j
1	0	2	0	100	200
2	-1	3	100	200	300
3	-2	4	200	300	400
4	-3	5	300	400	500
5	-4	6	400	500	600

Assuming the prior estimates generated in this fashion were accurate to 25%, i.e., $ERP_i = .25P_i$, the DACES1 code was cycled on PMUL values from 0.4 to 2.0. (Since the parameter PMUL multiplies the prior estimate function, increasing the value of PMUL corresponds to giving increased weight to the prior estimate functional.)

The DACES1 result with PMUL = 0.4 is plotted in Plate IIc. The prior estimate data is indicated by the dashed line. The prior estimate data do not extend below z = 100 A, and the violent

oscillations have returned, especially below this limit. In fact there is very little visible improvement over the result obtained using the simple unfold functional only.

In the next three examples the prior estimate data were removed and the smoothing functional, Z_s, was added to control oscillations. In Equation (D-6), m was set equal to 2, and the function Y(z) was set equal to zero. These choices prevent the 2^{nd} derivative of the solution estimate from becoming too large. Also, ERS(z) now becomes an estimate of the maximum value of $W''(E_k,z)$. From Equation (3-15) ERS(z) was estimated to be equal to a constant, 0.015, and the program was cycled on values of SMUL ranging from 0.4 to 2.0. Estimates obtained from these computations are plotted in Plate IId, e, and f. For values of SMUL equal to or greater than one, the objectionable oscillations have been eliminated. Also included on these graphs are dashed lines indicating the error bands obtained from UNFOLD. Error bands for the previous estimates were deleted because they were off scale.

For the final examples all the a priori information discussed above was incorporated into UNFOLD to obtain a best solution estimate for the problem. A results summary for all calculations performed in the analysis of this problem are included in Table 3-4. The statistical parameters PROB MEAN and PROB CHISQ serve to ensure that the residual errors of the computations are consistent with the specified error information. Values for these parameters are obtained in the following manner. For each data set the mean and

TABLE 3-4

Summary of UNFOLD Results
E_k = 21.781 KeV

RUN NO.	SMUL	PMUL	INEQU. CONST.	PROB. MEAN	PROB. CHI SQ.	Plate II
1	0	0	0	0.83	1.00	a
2	0	0	8	0.95	1.00	b
3	0	0.4	0	0.49	0.99	c
4	0	0.7	0	0.90	1.00	
5	0	1.0	0	0.79	1.00	
6	0	1.5	0	0.53	0.97	
7	0	2.0	0	0.54	0.91	
8	0	4.0	0	0.38	0.65	
9	0.4	0	0	0.94	0.99	d
10	0.7	0	0	0.92	0.97	
11	1.0	0	0	0.90	0.95	e
12	1.5	0	0	0.88	0.92	
13	2.0	0	0	0.87	0.89	
14	4.0	0	0	0.82	0.73	
15	0.6	0.6	0	0.98	0.97	
16	1.0	0.6	0	0.99	0.95	f
17	2.0	0.6	0	0.93	0.90	
18	0.6	1.0	0	0.84	0.96	
19	1.0	1.0	0	0.88	0.94	
20	2.0	1.0	0	0.96	0.90	
21	0.6	2.0	0	0.49	0.87	
22	1.0	2.0	0	0.54	0.87	
23	2.0	2.0	0	0.66	0.88	

standard deviation of the differences between the residual errors and the estimated errors are calculated. The parameter CHISQ is the sum of the squares of these differences. The parameter PROB MEAN is the probability that the mean of the differences times the square root of the number of source distributions used (eight) could exceed the observed value when sampled from a unit normal distribution. The parameter PROB CHISQ is the probability that CHISQ exceeds the observed value when it is sampled from a chi-squared distribution with eight degrees of freedom.

In the calculations performed with all a priori information the imposed inequality constraints were not found to be constraining. That is, the addition of both the smoothing and prior estimate functionals to the unfold term produced a solution estimate which automatically satisfied the inequality constraints. By comparing Runs 10, 11, and 13 with 15, 16, and 17, it was observed that while the solution estimates did not change perceptibly when the prior estimate functional was added to the smoothing functional, a definite improvement was noted in the statistical parameters. Based solely upon the statistical parameters, the best solution estimates appear to be those obtained in run numbers (15) and (16). The estimate obtained with SMUL = 0.6 was not completely free of oscillations, however, and the solution obtained with SMUL = 1.0 and PMUL = 0.6 was consequently designated the best estimate. This result, together with the error band and measurement data, is exhibited in Plate IIf.

3.5 DACES1 Results

Using the experience gained in the previous examples similar calculations were performed for energies ranging from E_k = 21.814 KeV to E_k = 21.600 KeV although not in as great detail as that for E_k = 21.781 KeV. The best solution estimates for each of these calculations have been incorporated onto Figure 3-5 to illustrate depth dependence as a function of energy. The kernel shape is seen to be consistent with the physical notions expressed earlier in this section.

The major purpose of these kernel unfolding calculations was to obtain an accurate analytical expression for the kernel function, W(E,z), which could be compared with further theoretical treatments. This representation is now complete with the evaluation of the coefficients, C_j, of the cubic splines obtained from the best solution estimates. These coefficients are presented in Table 3-5.

3.5.1 Comparison of the Fermi Age Diffusion Theory with the DACES1 Results

A comparison of the age diffusion theory with the DACES1 results is presented in Plate III. The strong peaking behavior exhibited by the age diffusion theory is not reflected in the unfolded experimental results. Although the centroid of the emission spectrum for Xe^{125} is approximately E = 21.786 KeV, the magnitude of W(E,z) from the age diffusion theory is largest for an energy of 21.733 KeV, peaking at a depth of approximately 150 A, whereas the experimental result is largest for E = 21.790 KeV and

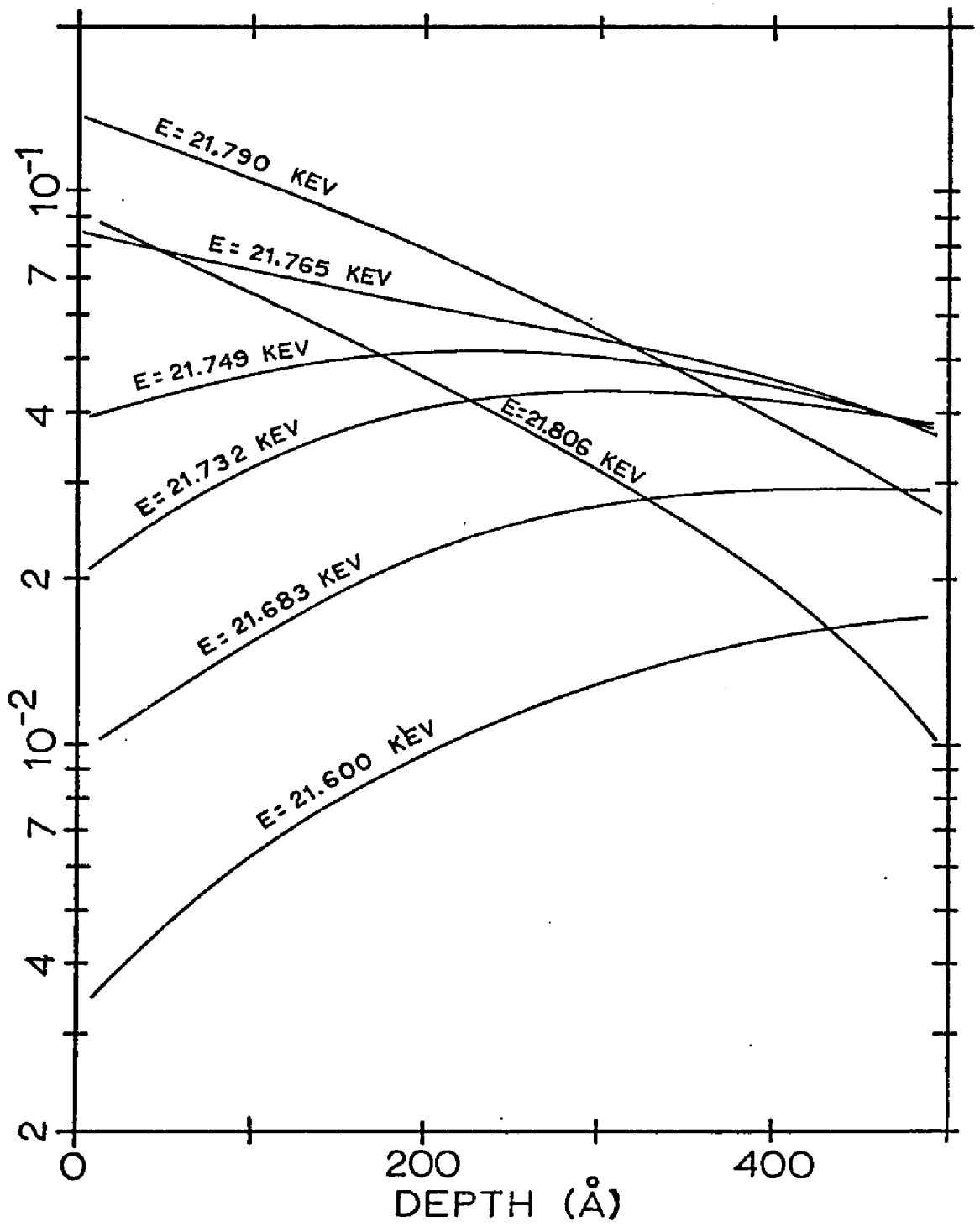

Figure 3-5. Xe^{125} in Ta_2O_5 Kernel vs Depth for Various Energies.

TABLE 3-5

Spline Function Coefficients from DACES1
for Empirical Kernel (Xe^{125} in Ta_2O_5). Spline Joints Placed
at 50 A, 100 A, 175 A, and 350 A, Respectively

Energy	C_1	C_2	C_3	C_4
21.806	.92164 E-1	-.26826 E-1	-.41018 E-4	.45586 E-3
21.798	.11556 E00	-.29529 E-1	.38860 E-4	.20275 E-3
21.790	.13658 E00	-.31807 E-1	.44519 E-4	.21442 E-3
21.781	.14242 E00	-.36056 E-1	.40014 E-4	.23859 E-3
21.773	.11401 E00	-.22134 E-1	.10601 E-3	.18420 E-4
21.765	.84891 E-1	-.12838 E-1	.34658 E-4	.25936 E-4
21.757	.54063 E-1	.22950 E-2	.16247 E-3	-.39670 E-3
21.749	.38922 E-1	.84816 E-2	.74447 E-4	-.29155 E-3
21.740	.24980 E-1	.12678 E-1	.22480 E-3	-.58305 E-3
21.732	.20163 E-1	.12263 E-1	.14272 E-3	-.48415 E-3
21.724	.16273 E-1	.11610 E-1	.26478 E-3	-.59278 E-3
21.716	.19393 E-1	.36832 E-2	.99282 E-4	.22983 E-4
21.707	.13255 E-1	.58634 E-2	.40438 E-4	.15091 E-3
21.699	.13584 E-1	.38745 E-2	.28586 E-4	.13844 E-3
21.691	.11246 E-1	.39771 E-2	.84216 E-4	.26043 E-4
21.683	.95341 E-2	.52555 E-2	-.12059 E-3	.52416 E-3
21.642	.72286 E-2	.17494 E-2	.73837 E-6	.11293 E-3
21.600	.32652 E-2	.29671 E-2	-.50156 E-4	.14379 E-3

TABLE 3-5
(Cont.)

Energy	C_5	C_6	C_7	C_8
21.806	.23081 E-2	-.38592 E-2	.97348 E-3	-.17830 E-3
21.798	.26411 E-2	-.39739 E-2	.11387 E-2	-.29178 E-3
21.790	.27368 E-2	-.49214 E-2	.26267 E-2	-.11574 E-2
21.781	.30872 E-2	-.37725 E-2	-.56504 E-4	-.30477 E-3
21.773	.29185 E-2	-.50377 E-2	.24429 E-2	-.53818 E-3
21.765	.11579 E-2	-.13130 E-2	-.37385 E-3	.69037 E-3
21.757	.10853 E-2	-.25669 E-2	.24246 E-2	-.40456 E-3
21.749	-.53279 E-3	-.25472 E-3	.16584 E-2	-.41369 E-3
21.740	.11573 E-2	-.36450 E-2	.43137 E-2	-.11793 E-2
21.732	-.14429 E-3	-.33251 E-3	.14131 E-2	-.19985 E-3
21.724	.22061 E-2	-.52194 E-2	.48552 E-2	-.12316 E-2
21.716	.26683 E-2	-.54776 E-2	.28719 E-2	.18566 E-3
21.707	.19518 E-2	-.48572 E-2	.30326 E-2	-.51823 E-4
21.699	.16812 E-2	-.36482 E-2	.17681 E-2	.29017 E-3
21.691	.22971 E-2	-.47520 E-2	.25751 E-2	.44314 E-4
21.683	.41126 E-3	-.26982 E-2	.19076 E-2	.34247 E-4
21.642	.84376 E-3	-.16505 E-2	.62338 E-3	.12767 E-3
21.600	-.29719 E-3	.33097 E-3	-.36957 E-3	.29972 E-3

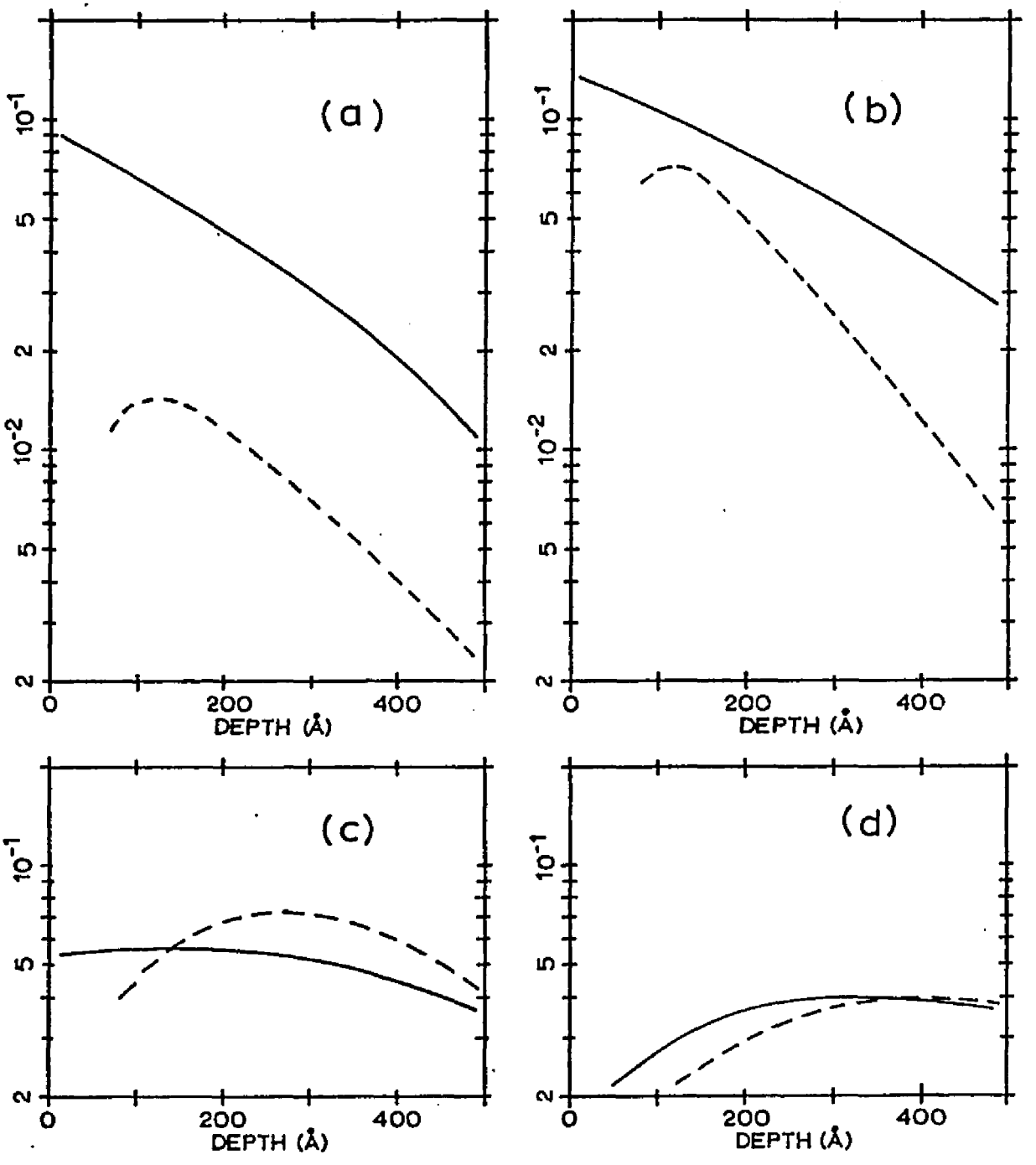

Plate III. Comparison of the Fermi Age Diffusion Theory (----) with the Results of DACES1 (——): (a) E=21.806 KeV; (b) E=21.790 KeV; (c) E=21.757 KeV; (d) E=21.724 KeV.

monotonically decreases as a function of depth. This behavior of the age diffusion theory is analogous to the shift in α-particle spectra and is due to the continuous energy loss assumption. In fact, the experimental result is a monotonically decreasing function of depth for energies as low as 21.765 KeV. Although the Fermi age diffusion theory has been previously shown to give good results in certain instances, it must be concluded that this theory is not adequate for predicting conversion electron line spectra because the basic assumption of continuous slowing down is not valid under these circumstances. A further remark is that the Fermi age diffusion theory indicates a certain correlation between the mean depth of origin and energy at emergence, a correlation which is not evident in the experimental results. In the former case, an unfolding capability is a convenience, but in the latter, it is a necessity for calculating source distributions.

Having concluded that the Fermi age diffusion calculation is not valid for this problem, a more sophisticated theoretical calculation exhibiting better experimental agreement was sought. A common feature of all electron transport calculations based upon the Boltzmann transport equation, is the immediate assumption of continuous slowing down made for computational convenience. While a formulation of the Boltzmann transport equation in terms of energy is no doubt possible, an analog simulation of the electron transport process was devised to explicitly account for discrete energy loss collisions. A description of this Monte Carlo code ELTRAS (Electron

Transport Simulator) with results and discussion is presented in the next section.

3.6 Response Function Computation by Analog Simulation

In the Monte Carlo method statistical estimates for quantities of interest are found by following an analog of the physical problem. The occurrences of physical phenomena, such as scattering and absorption events in the life history of a particle, are specified by a set of deterministic rules and probabilities. If these rules and probabilities are correct, the analog simulation must correctly represent the physical process, provided that a sufficient number of trials have been performed to yield statistically meaningful results.

Several Monte Carlo codes have been previously devised for simulating electron transport, including the codes of Perkins (48), McGarrigle and Mar (49), Burger (50), Lilley and Yucker (51), and Hill et al. (52). These were developed, however, to calculate the penetration of energetic electrons through thick complex-geometry shields, a typical problem being the radiation dose rate received by an astronaut during a space flight. Because of the enormous number of collisions that occur as an electron traverses a fraction of its range, a complete simulation of this type of problem would be prohibitive in terms of required computer time. To circumvent this objection these codes minimize the detailed simulation by utilizing analytic and empirical results to describe segments of the transport problem. The calculation then proceeds through the simulation

segment by segment. These Monte Carlo codes are consequently not suitable for the present problem of interest in which a detailed collision by collision simulation is desired.

3.6.1 Outline of the ELTRAS Routine

For a given source distribution, $S(z)$, natural conversion electron line shape, $J_c(E')$, and spectrometer window function, $\chi(E,E')$, the experimentally observed line shape, $N(E)$, could be determined completely by Monte Carlo techniques. For example, the origin depth z and initial energy E' could be chosen by random numbers, r, properly distributed on $0 \leq r \leq 1$, if the functions $S(z)$ and $J_c(E')$ were identified as probability density functions.

However, the objective of the ELTRAS code is to compute the kernel $W(E,z)$. Thus, the source depth distribution is of no importance. Moreover, since the energy range of interest is extremely small, all electrons can be introduced with an energy $E' = E_o$, where E_o is the mean energy of the natural conversion electron line shape, and the energy dependent cross sections involved in the computation can be evaluated at the energy E_o. Consequently, the only analog aspects of ELTRAS involve calculation of the energy spectrum for electrons born at a depth z with energy E_o. In the terminology of Chapter 2, the result of this calculation is the quantity, $W(E' \longrightarrow E,z)$, identified as the probability that an electron born at depth z with energy $E' = E_o$ will emerge from the surface with energy E into the acceptance angle of the spectrometer. $(W(E' \longrightarrow E,z)$ thus depends only on the initial depth z,

and the energy difference $\Delta E = (E'-E)$.) The kernel $W(E,z)$ is then calculated from Equation (2-17).

The ELTRAS routine is consequently divided into three major sections as described in Figure 3-6. The first section is composed of the basic Monte Carlo simulation. The result of this computation is the probability $P_{ij}(z)$ that an electron emitted with energy E_o at depth z from an assumed isotropic angular distribution emerges from the surface with an energy E and direction cosine w such that $\Delta E_{i-1} \leq \Delta E = E_o - E \leq \Delta E_i$ and $w_{j-1} \leq w \leq w_j$, where the parameters ΔE_{i-1}, ΔE_i, w_{j-1}, and w_j denote the boundaries of a two-dimensional energy loss, direction cosine tally box. Using the acceptance angle of the spectrometer to limit the range of acceptable direction cosines, the second calculation performed by ELTRAS computes the source-weighted conversion electron spectrum assuming the natural conversion electron line shape, $J_c(E)$. The final calculation of ELTRAS folds the source-weighted spectrum with the spectrometer window (resolution) function to yield the observed conversion electron line shape due to the hypothetical depth distribution $S(z') = \delta(z'-z)$.

A detailed description of ELTRAS is presented in Appendix B. In the remainder of this section the ELTRAS code is applied to the problem of computing the transport kernel $W(E,z)$ due to Xe^{125} embedded in Ta_2O_5. The results of these computations are then compared with the experimental results of Pringle.

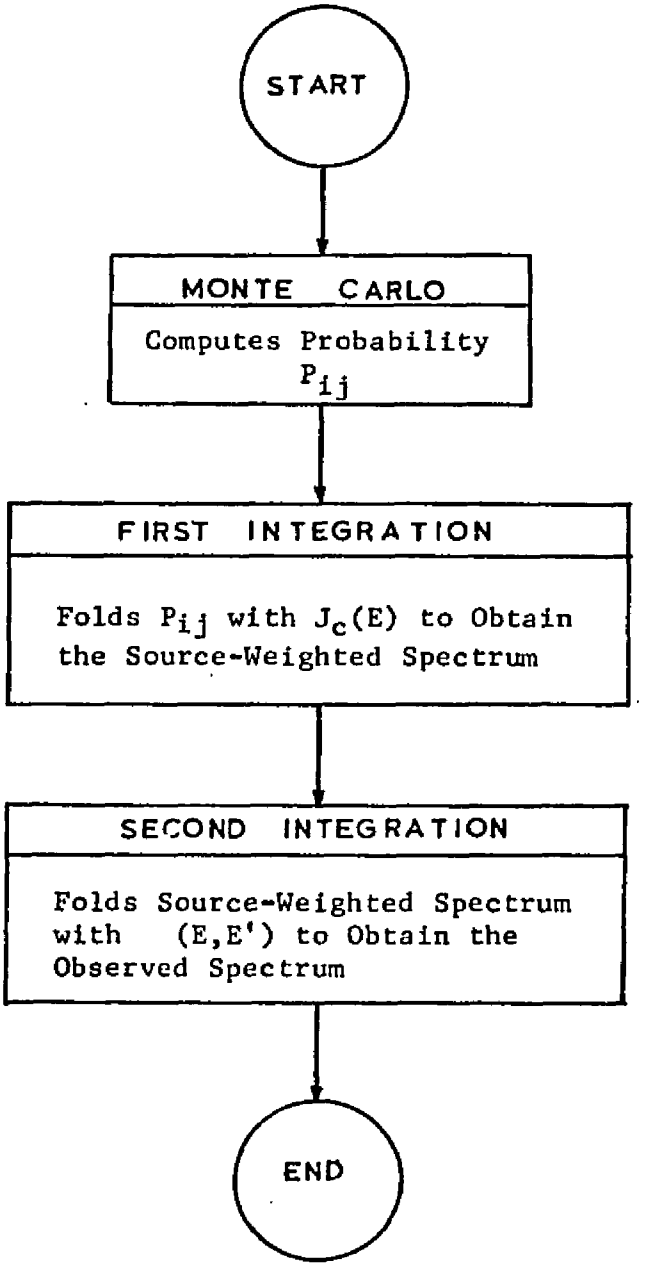

Figure 3-6. Flow Outline of the ELTRAS Code.

ELTRAS has been designed to include the effects of both elastic and inelastic collisions. The macroscopic elastic scattering cross section for the compound Ta_2O_5 must be calculated according to $\Sigma_e = N_{Ta}\,\sigma_{e_{Ta}} + N_O\,\sigma_{e_O}$, where N_{Ta} and N_O are the number densities of tantalum and oxygen, and $\sigma_{e_{Ta}}$ and σ_{e_O} are the total elastic nuclear scattering cross sections for tantalum and oxygen. However, because of dependence on the square of the atomic numbers, the contribution due to oxygen atoms ($Z = 8$) is negligible compared to the contribution due to tantalum atoms ($Z = 73$). Using a value of $8.03\ gm/cm^3$ for the density of Ta_2O_5, the macroscopic elastic cross section for 21.79 KeV Xe^{125} conversion electrons is evaluated as $1.6 \times 10^5\ cm^{-1}$.

The inelastic collision cross section is not determined as easily as the elastic cross section because of the difficulty in distinguishing between the two most important loss mechanisms, the plasmon interaction and single electron-electron collisions. Tantalum is the third element of the third transition series and has an outer electronic configuration of $5d^36s^2$. Assuming all of these electrons are "free," the theoretical plasmon energy loss $\hbar\omega_p$ (where $\omega_p^2 = \frac{4\pi ne^2}{m}$ is the plasma frequency) is approximately 19.5 eV, which compares favorably with the experimental value of 19.6 eV.

Unfortunately, no experimental electron loss spectra or optical absorption spectra are available for Ta_2O_5. The most comprehensive characteristic electron energy losses in compounds

have been performed by Best (53), including the loss spectra of vanadium oxide (V_2O_3). Since vanadium has an outer electron configuration similar to tantalum ($3d^34s^2$), agreement of the loss energy for vanadium oxide is expected to be indicative of the agreement for tantalum oxide. Using the total number of valence electrons per atom (54), i.e., five for vanadium and six for oxygen, the theoretical plasma loss energy is 25.4 eV which agrees well with the experimental value of 24.4 eV. In fact, the results of Best indicate that for all oxides with bonding of a predominantly covalent nature, there is a relatively intense broad loss peak which is due to plasma oscillations. Consequently, the most important electron energy loss interaction in Ta_2O_5 is expected to be the plasmon interaction. Because of the basic lack of data concerning the optical absorption spectra and the electron energy loss spectra, however, the inelastic contribution due to electron-electron induced interband transitions cannot be neglected. Since the differential stopping power of a solid for a given incident electron energy is independent of the mechanism of energy loss (55), an increase in the probability of one type of loss reduces the probability of energy loss by other causes.

Assuming that all the valence electrons of Ta_2O_5 may be considered as free, the theoretical plasma loss energy, $\hbar\omega_p$, is 24.4 eV. Both the cutoff scattering angle θ_c, and the parameter α of the plasma dispersion relation depend upon the Fermi level energy in Ta_2O_5, which may be estimated according to (56)

$$E_F = (3.64 \times 10^{-19}) n^{2/3} \qquad (3\text{-}20)$$

where n is the number of valence electrons per cubic meter. For Ta_2O_5, the Fermi energy is approximately 20.9 eV, of the order of $\hbar\omega_p$. Consequently the parameter $\alpha = \frac{3}{5}\frac{E_F}{\hbar\omega_p}$ is approximately 0.6, $\theta_c = \frac{\hbar\omega_p}{2E_F}$ is about 0.5. Since $\theta_E = \frac{\hbar\omega_p}{2E} \simeq .0005$, the assumption that $\theta_E \ll \theta_c$ is, indeed, valid. The total plasmon cross section for 21.79 KeV electrons in Ta_2O_5 is approximately 7.3×10^5 cm^{-1}. Because loss spectra are not available for Ta_2O_5, an exact value for the width, Γ, of the loss peak, is not available. Since the loss peak is expected to be relatively broad, however, an arbitrary value of $\Gamma = 20$ eV has been assumed. The lack of basic data also prevents an accurate estimation of the inelastic cross section due to interband transitions, and also the loss energies due to these interactions. Based upon the experimental work of Best, the effect of the interband transitions is expected to be small, however, contributing primarily to the loss spectrum at higher loss energies.

The cross sections and various other parameters described above are used in the Monte Carlo simulation portion of ELTRAS which computes the probabilities P_{ij}. The second calculation performed by ELTRAS, the folding of the P_{ij} with the natural conversion electron line shape, $J_c(E)$, requires an estimation of the spectrometer acceptance angle. Since the Chalk River Beta Spectrometer is iron-free, the field form and, hence, the electron trajectories are calculable. Such computations have been performed by Lee-Whiting

using the optic circle as the reference basis (57). The electron trajectories leave the source at angles defined by the parameters $H = \sqrt{2} \tan \phi_r$ and $T = \sqrt{2} \tan \phi_z$ where ϕ_r and ϕ_z are the radial and axial departure angles in radians measured with respect to the tangent to the optic circle at the source position. The radial and axial distances between the trajectory and the optic circle at any value of the parameter $4 = \theta / \sqrt{2}$ (θ in radians) are expressed by the dimensionless parameters $\eta(\psi) = \left(\frac{r - r_o}{r_o}\right)$ and $\tau(\psi) = \left(\frac{z - z_o}{z_o}\right)$. In a perfect double-focusing instrument the orbits leaving a point source on the optic circle at $\eta(0) = \tau(0) = 0$ should come to focus on the optic circle at the point $\eta(\pi) = \tau(\pi) = 0$, i.e., at the angle $\theta = \pi \sqrt{2}$ radians where $\psi = \pi$. Non-zero values of $\eta(\pi)$ or $\tau(\pi)$ are the radial and axial aberrations respectively. Theoretical expressions for $\eta(\pi)$ and $\tau(\pi)$, valid for small departure angles, H and T, are given by (58)

$$\eta(\pi) = -\eta(0) - \tfrac{1}{2}\tau^2(0) + \ldots \qquad (3\text{-}21)$$
$$-0.00063\ H - 2/3\ H^2 - 0.0065\ HT^2 + 0.0023\ H^3 + .00093\ T^4$$
$$+0.173\ H^2T^2 + 0.296\ H^4 + 16.16\ HT^4 - 5.29\ T^6 + \ldots$$

$$\tau(\pi) = -\tau(0) + \ldots \qquad (3\text{-}22)$$
$$+ .00063\ T - 0.1288\ T^3 - 0.0065\ H^2T + .00372\ HT^3$$
$$- .107\ H^3T - 3.214\ T^5 + \ldots$$

Since the instrumental dispersion factor is four, i.e., the images of electron groups having momenta p and $p + dp$ have a radial separation of $4(\frac{\Delta p}{p}) \times r_o$, the aberration $\eta(\pi) = -4 \times 10^4$ is that which gives an apparent shift in momentum of $\Delta p/p = 0.01\%$. For the conversion electron spectra reported by Pringle, a momentum resolution setting of 0.05% was used, corresponding to aberrations of $\eta(\pi) = \tau(\pi) = -2 \times 10^{-3}$. Solving Equations (3-21) and (3-22) for the parameters H and T yields approximately 0.055 and 0.2, respectively, which corresponds to a rectangular aperture "area" of 0.044. For a corresponding circular aperture of equivalent "area," the radius r_m is 0.12. With the definition of the maximum acceptance angle ϕ_m given as

$$r_m = \sqrt{2} \tan \phi_m \simeq \sqrt{2}\, \phi_m \qquad (3\text{-}23)$$

a momentum resolution of 0.05% corresponds to an equivalent maximum acceptance angle of 0.085 rad, while the limiting direction cosine is found to be $w_\ell \simeq -0.9964$. Thus, all electrons emerging from the sample with angles less than 0.085 rad measured with respect to the surface normal of the sample will be collected by the spectrometer. With the evaluation of w_ℓ, the probability, $P_i(z)$, that an electron emitted with energy E_o at depth z emerges from the surface within the spectrometer acceptance angle with energy E such that $\Delta E_{i-1} \leq \Delta E = E_o - E \leq \Delta E_i$ can be defined in terms of the previously computed P_{ij} as

$$P_i(z) = \sum_{j=1}^{J} P_{ij}(z) \qquad (3\text{-}24)$$

The summation limit J is defined by $w_J \leq w_\ell$.

Assuming that the natural conversion electron line shape is a Lorentzian, the ELTRAS source-weighted spectrum may be evaluated analytically, as indicated in Appendix B. For Xe^{125} the width of the natural conversion electron line shape has been experimentally evaluated as approximately 13 eV, with the peak occurring at approximately 21.786 KeV.

To perform the final folding integration of ELTRAS, an estimation of the width of the spectrometer window function is required. Using Equation (8-17) Ewan and Graham (59) have found that $n = 1.2$ is a satisfactory value for the Chalk River Spectrometer at momentum resolution settings of 0.05 to 0.12%.

For the experimental arrangement used by Pringle, including a proportional counter detector having a defining aperture 3mm wide, at a momentum resolution setting of 0.05% the expected line width for monoenergetic conversion electrons was ~0.08% in momentum. For non-relativistic energies, the electron kinetic energy E is related to momentum p according to $E = p^2/2m$, where m is the rest mass of the electron. Thus, $\frac{\Delta E}{E} = 2\left(\frac{\Delta p}{p}\right)$, and 0.08% momentum resolution corresponds to 0.16% energy resolution. For 21.8 KeV electrons, the expected instrumental line width is evaluated as ~35 eV. This value was checked according to the following procedure: the experimentally determined kernel $W(E,z)$ was evaluated at the surface ($z = 0$). The conversion spectrum obtained in this manner represents the spectrum due to an infinitely

thin layer of Xe^{125} deposited on the surface of the Ta_2O_5 sample. For such a geometry, spectrum effects due to electron energy loss collisions are minimized, and the width of the conversion line depends only upon the natural line width and the width of the instrumental window function. This spectrum is shown in Figure 3-7. The observed width is approximately 45 eV. For $\Gamma_L \simeq 45$ eV, $\Gamma_e \simeq 13$ eV, and $n = 1.2$, the spectrometer line width, Γ_{sp}, as evaluated from Equation (B-17), is ~36 eV, which is in good agreement with the expected value of 35 eV.

Before proceeding immediately to a calculation of the transport kernel $W(E,z)$, several preliminary trials were performed to insure the correct operation of each ELTRAS computation. Example results of the Monte Carlo simulation and the first folding integration are exhibited in Figures 3-8 and 3-9. During these preliminary calculations it was noted that statistical fluctuations in the loss spectra could be much reduced by employing a forced collision routine for particles directed toward the surface and by using a prejudiced source routine. Since electrons emitted toward the surface are more likely to emerge from the sample, better accuracy is achieved by directing more particles of correspondingly smaller weight into the importance cone. The solid angle of the importance cone must be large enough, however, to prevent particles of relatively large weight from scattering into the importance cone.

In the source-weighted spectrum of Figure 3-9, three distinct peaks are readily apparent: (1) the zero-loss peak at 21.786 KeV

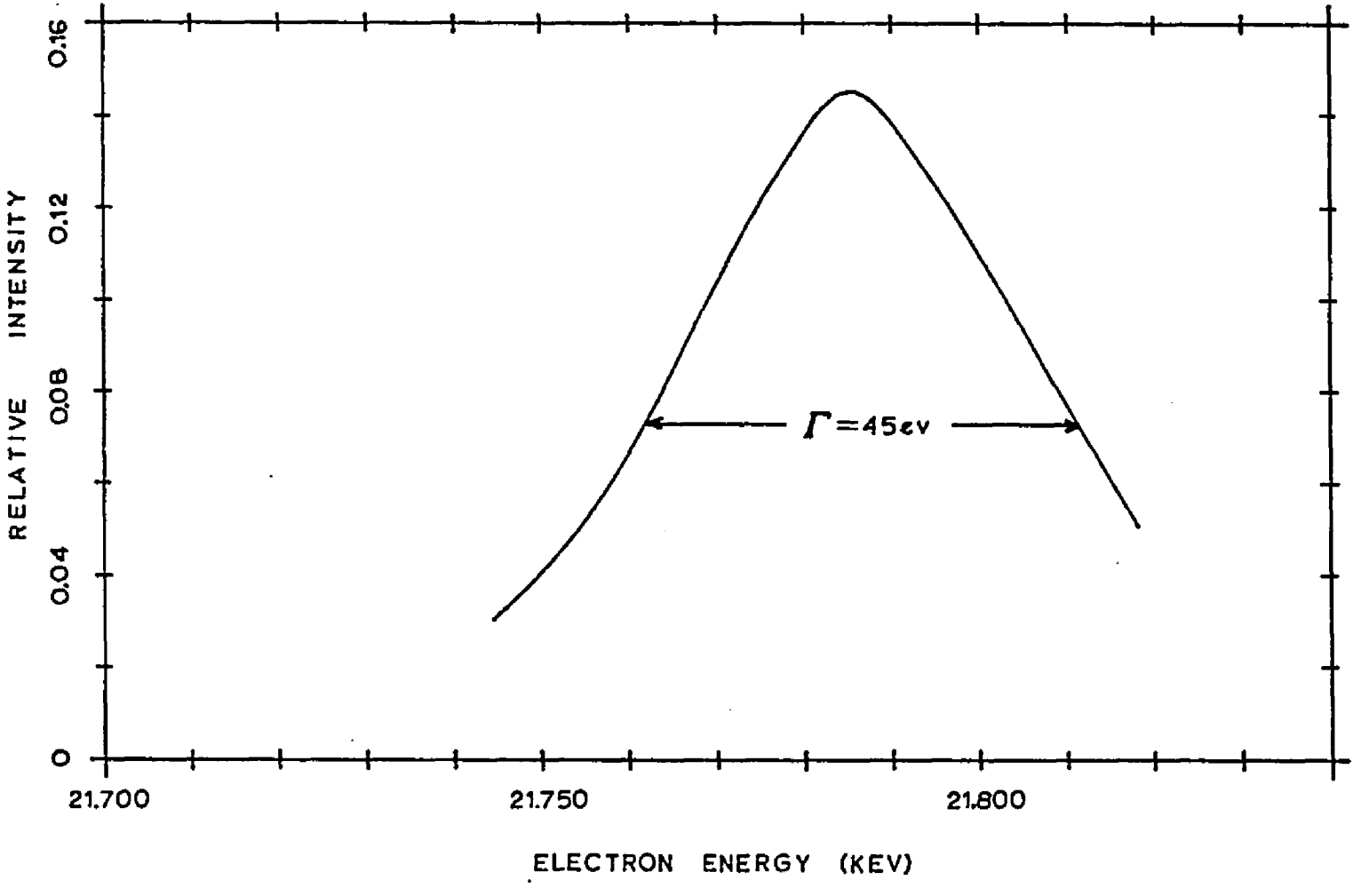

Figure 3-7. Conversion Electron Spectrum of an Infinitely Thin Layer of Xe^{125} Deposited on the Surface of a Ta_2O_5 Sample.

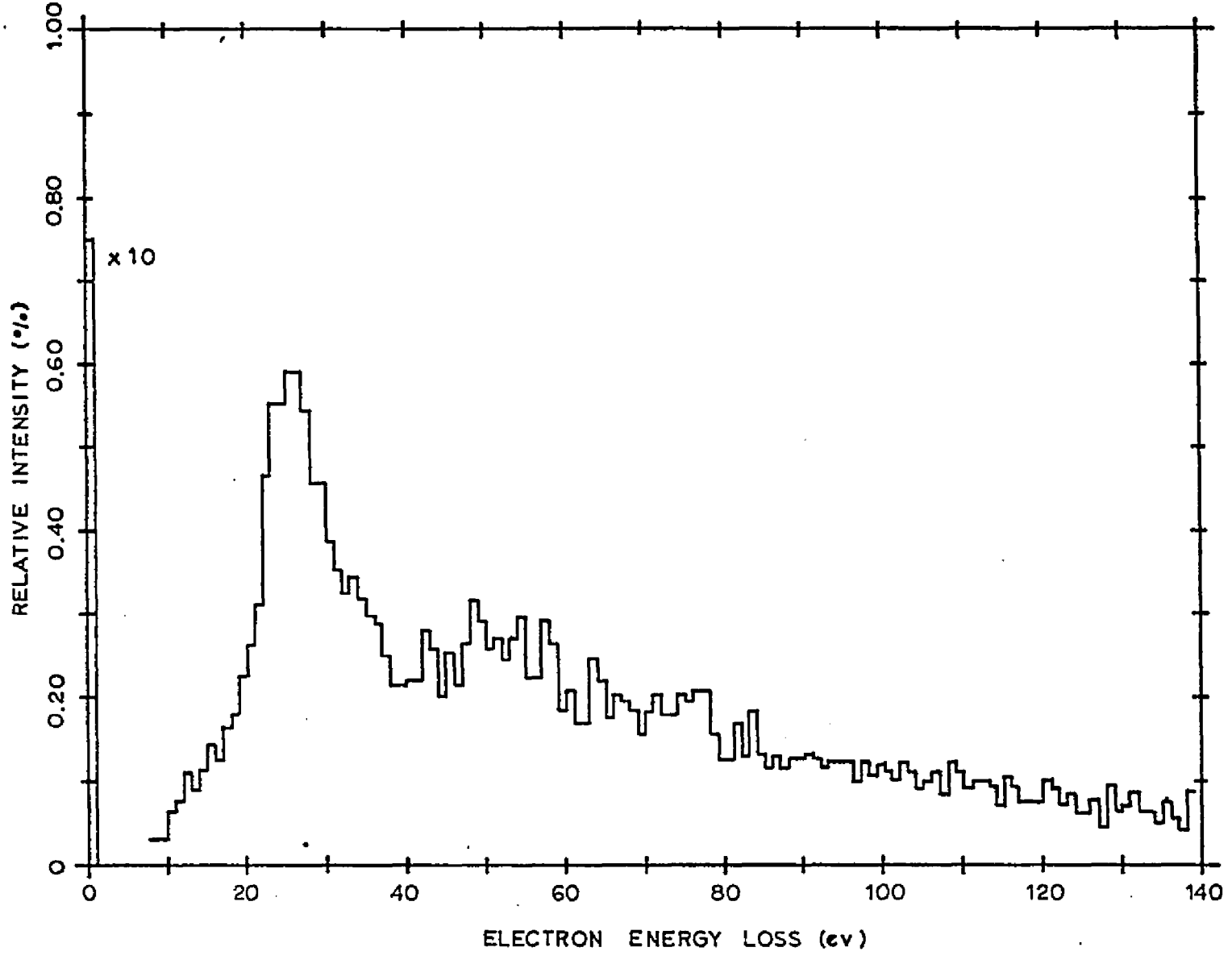

Figure 3-8. Energy Loss Spectrum (P_{ij}) from ELTRAS.

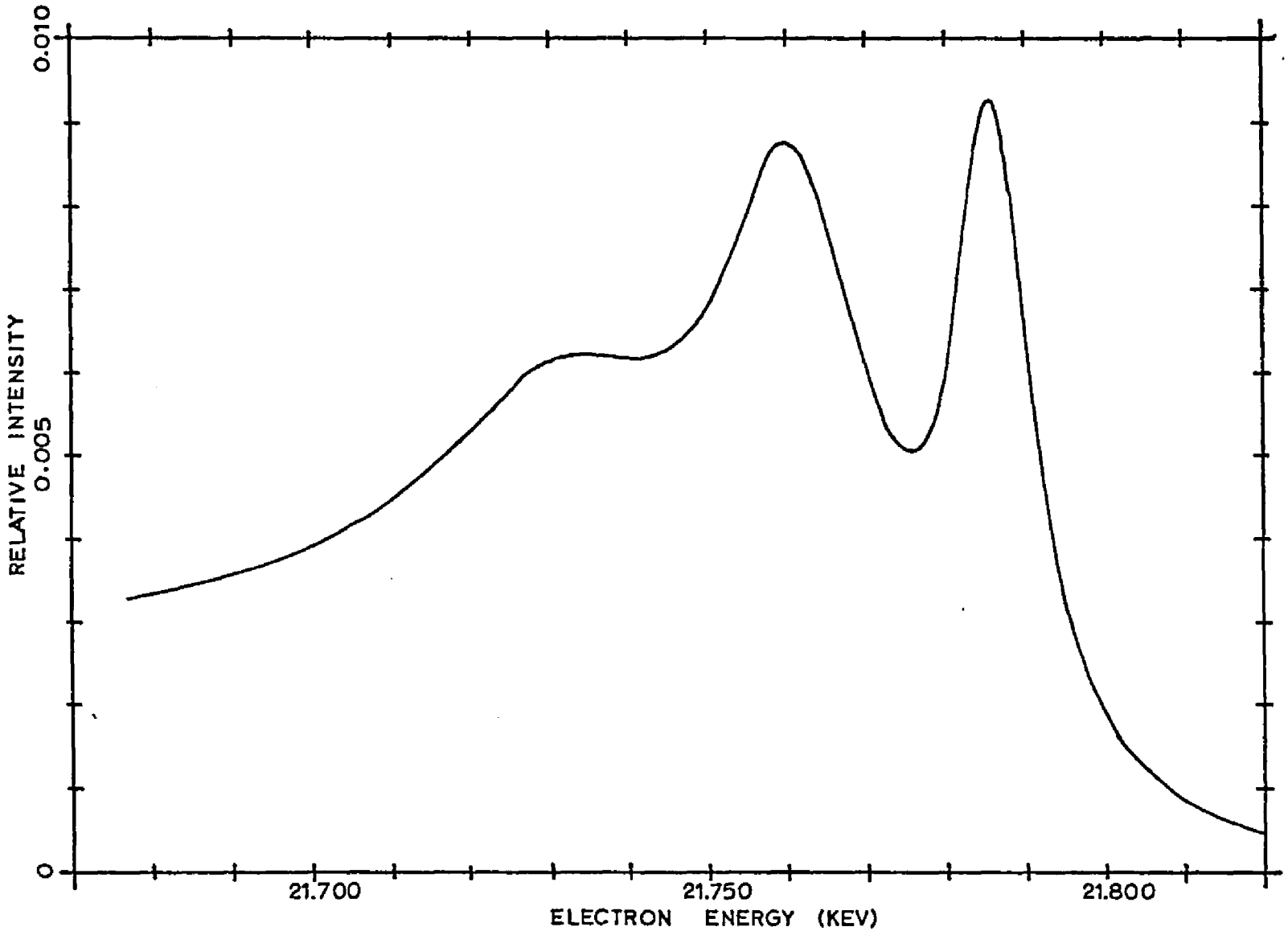

Figure 3-9. Source-Weighted Spectrum from ELTRAS.

displaying the natural line width (~ 13 eV), (2) a relatively narrow single-loss peak at 21.760 KeV, and (3) a broad double-loss peak at 21.734 KeV. Higher multiple loss peaks are very much broader and form a low energy continuum.

When the source-weighted spectrum was folded with the spectrometer window function the observed conversion electron spectrum displayed in Figure 3-10 was obtained. Shown for comparison is the spectrum due to a hypothetical depth distribution $S(z) = \delta(z - 300\ A)$ as calculated from the experimental kernel. Because the width of the instrumental window is approximately three times as great as the natural conversion electron line width, the peaks of the source-weighted spectrum are much broadened due to the resolution of the spectrometer. In addition, the intensity of the zero-loss peak of the Monte Carlo spectrum is too low while the intensity of the single-loss peak is too large. It was concluded that the plasmon interaction cross section was probably too large. Since the spectrum is of the correct magnitude, however, the total inelastic cross section was assumed to be correct. Consequently, the effects of interband collisions and ionization losses must be considered by computing the inelastic scattering cross section according to $\sigma_i = \sigma_p + \sigma_{e-e}$, where $\sigma_p = \gamma\sigma_i$ and $\sigma_{e-e} = (1 - \gamma)\sigma_i$. While interband collisions may result in energy losses of the same order as plasma losses, energy losses due to ionizing interactions are generally much larger. An accurate account of energy losses due to a single electron-electron collisions would require detailed

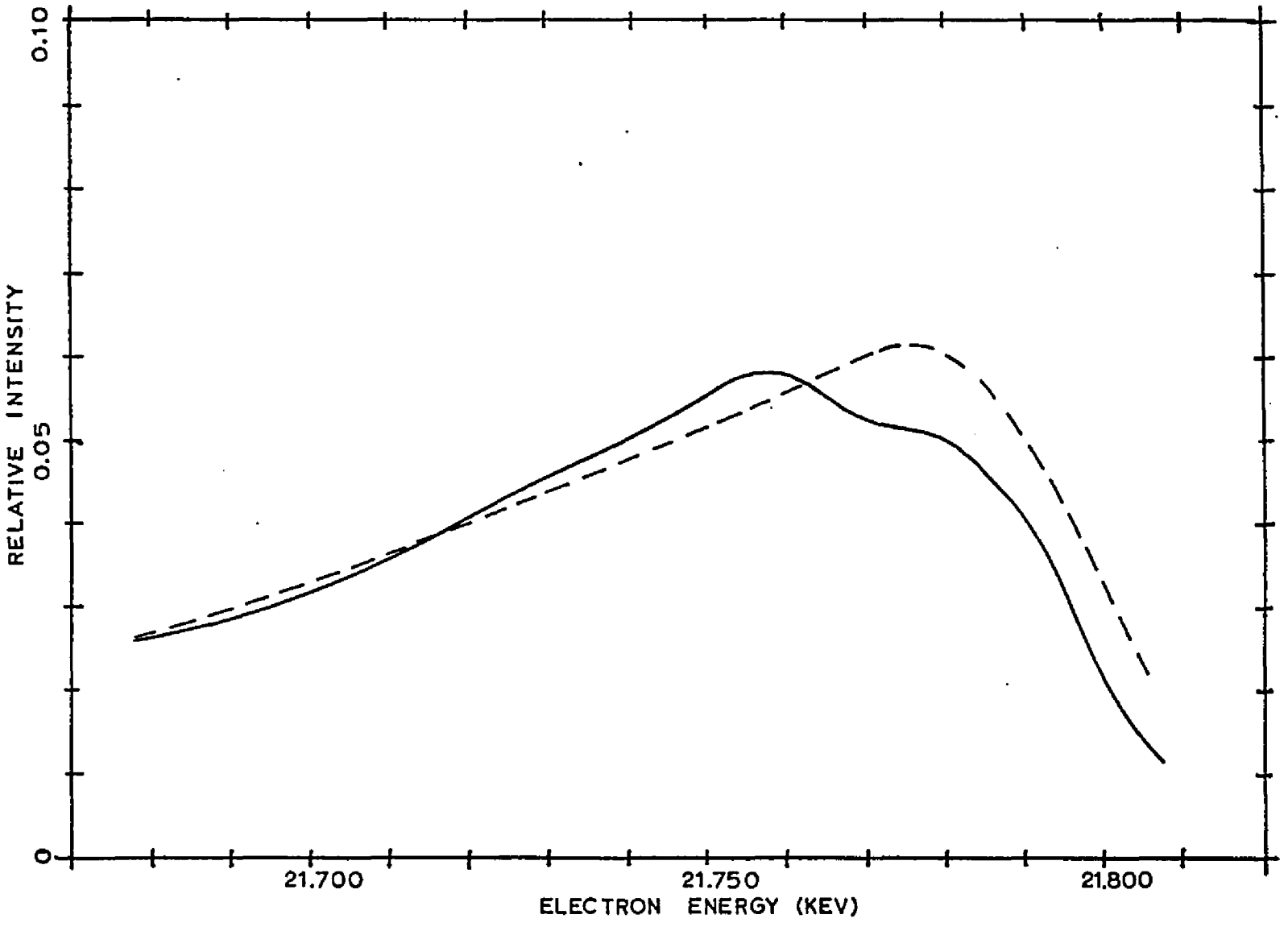

Figure 3-10. Computed (——) and Empirical (---) Conversion Electron Spectra for $S(z) = \delta(z-300\ A)$. E_o = 21.786 KeV used as Emission Energy.

knowledge of the transition probabilities between the various electron bands and ionization levels. Since such detailed information does not exist for Ta_2O_5, the following approximate procedure was adopted. It was postulated that all single electron-electron collisions would result in energy losses greater than the maximum energy loss cut-off. The single electron collision cross section becomes, in effect, an electron capture cross section. With this approximation, several trial spectrum calculations were performed as the value of γ was varied over the range $0.5 \leq \gamma \leq 1$, corresponding to an equal probability of capture or plasmon interaction, to negligible capture probability. As a result of this procedure $\gamma \simeq 0.8$ was determined to give the best agreement with the spectrum as calculated from the experimental Pringle kernel.

An additional interesting feature of the graph in Figure 3-10 is that the theoretical spectrum appears to be shifted to lower energies by approximately 4 eV; i.e., for better agreement the mean energy of the Lorentzian energy distribution should have been 21.790 KeV rather than 21.786 KeV. This shifting behavior, which persisted as the value of γ was varied, was originally thought to be due to the averaging of the zero-and single-loss peaks by the spectrometer window function. Later results have cast doubt on this interpretation, however. For a mean source energy of 21.790 KeV and $\gamma = 0.8$, the observed spectrum as calculated by the ELTRAS code for a depth of 300 A is presented in Figure 3-11.

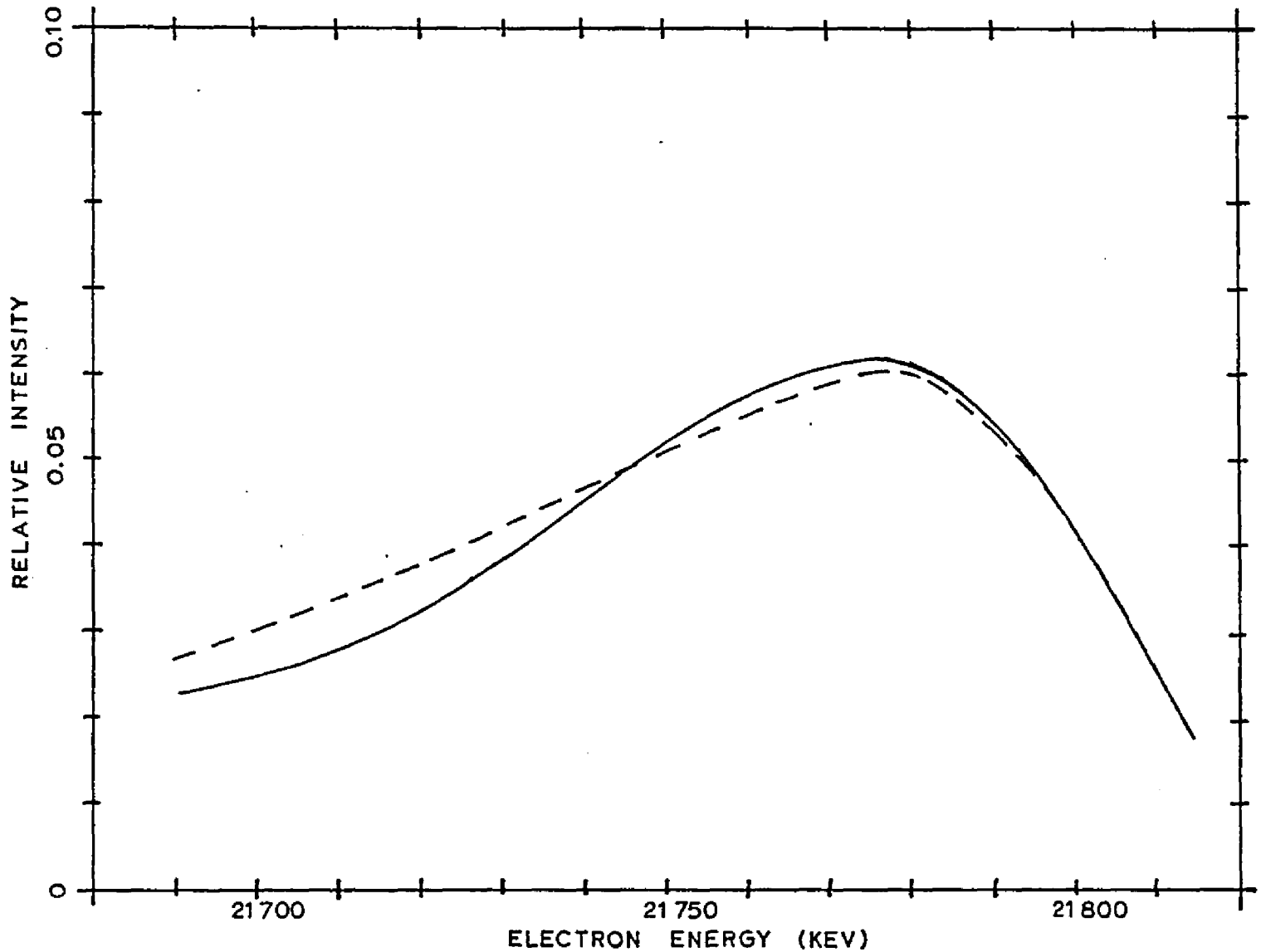

Figure 3-11. Computed (——) and Experimental (---) Conversion Electron Spectra for S(z) = (z-300 A). E_o = 21.790 KeV.

3.7 Calculation of W(E,z) Using ELTRAS

Following the preliminary check-out computations the ELTRAS code was used to simulate conversion electron spectra from ten Xe^{125} source distributions $S_i(z) = \delta(z - z_i)$. The z_i were placed at 50 A intervals ranging from 50 A to 500 A. Both the forced collision and prejudiced source routines were employed. The value of the inelastic collision parameter γ was held at 0.8. The total number of particles processed for each trial was 40,000. The observed spectra are shown in Figure 3-12. Also presented for comparison (as dashed lines) are the corresponding spectra computed according to the empirical Pringle kernel. For large source depths the theoretical and experimental spectra agree quite well. For depths near the surface, however, the peaks of the experimental spectra fall below the peaks of the theoretical spectra; for better agreement the mean source energy used in ELTRAS should be decreased. The source energies required for agreement are plotted in Figure 3-13 as a function of depth. The origin of this shifting behavior, which appears at a depth of approximately 200 A, is not completely understood. A possible explanation is that the binding energy of the K shell of the Xe^{125} atom varies according to depth, i.e., a surface effect may exist. In fact, for the more well-resolved spectrum of the 7.3 KeV Fe^{57} conversion electron, a shift to higher mean energy (by 3 eV) for increasing depth has been observed (60). In this case, the shift was attributed to surface oxidation, however.

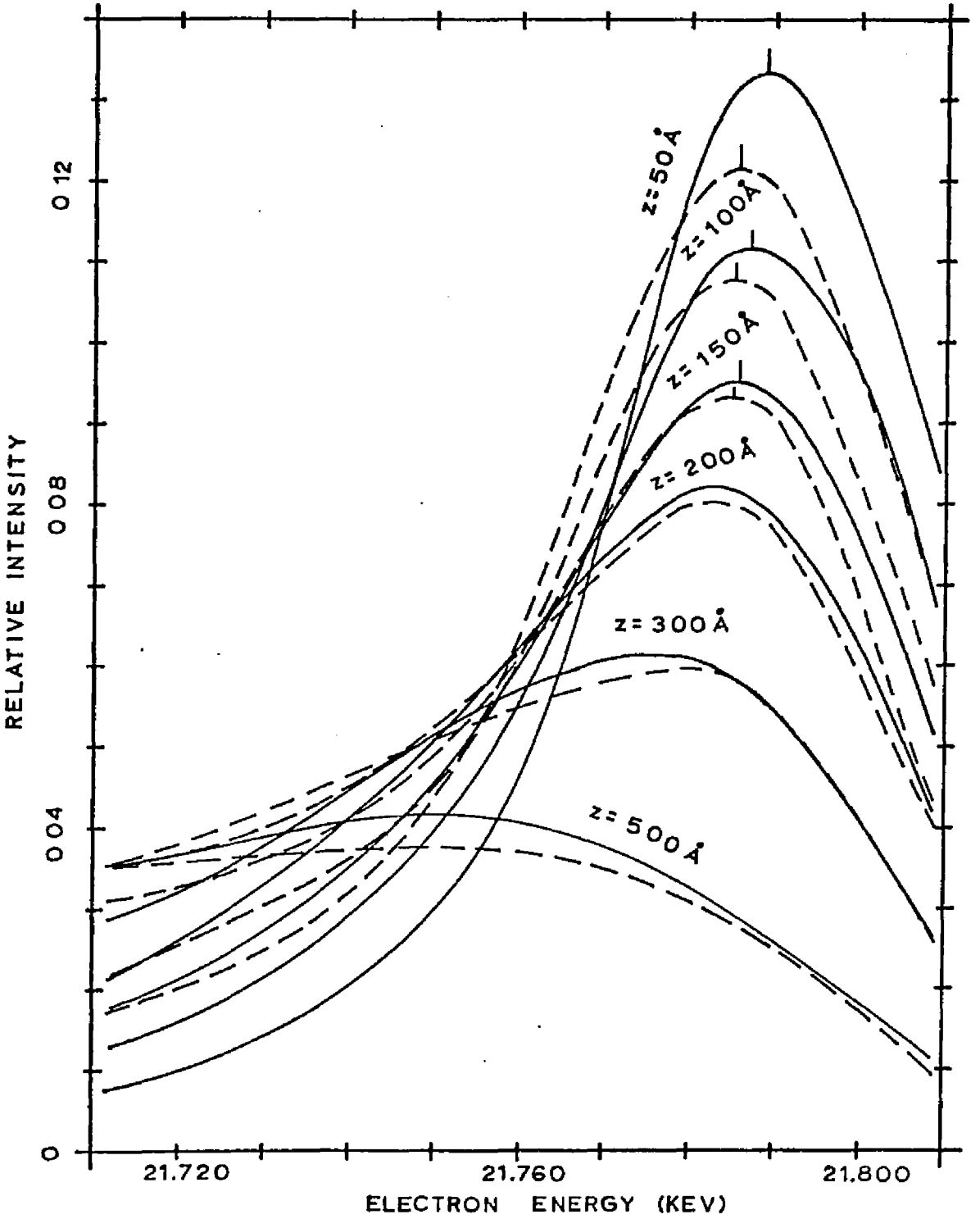

Figure 3-12. ELTRAS Final Spectra for Various Depths. E_o = 21.790 KeV.

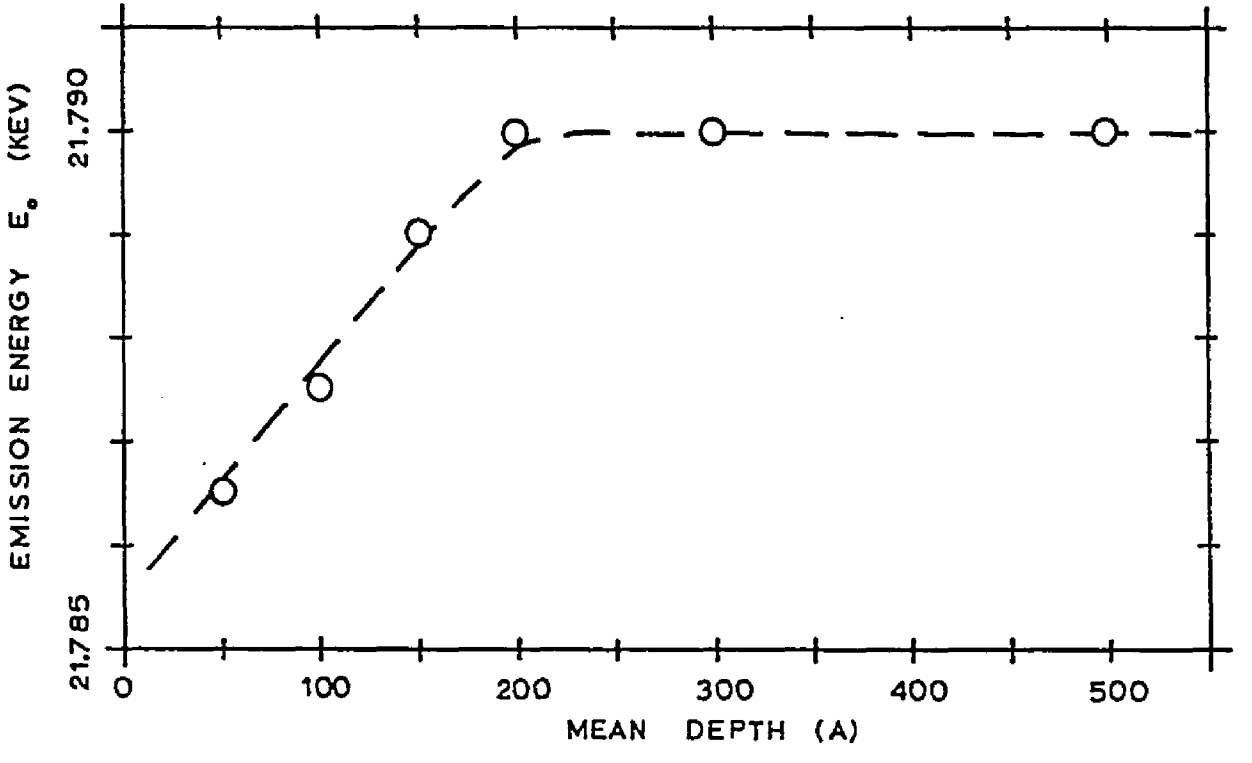

Figure 3-13. ELTRAS Emission Energy Required for Agreement with Experiment as a Function of Depth.

Separate Monte Carlo trials were performed for each depth to determine the approximate total weights of particles of all energy losses and with energy losses above the cut-off of 250 eV emerging from the sample into the spectrometer acceptance angle. The total number of particles introduced in each case was 10000. The ratio of the weight emerging above the cut-off energy loss to the total emerging weight is displayed in Figure 3-14 as a function of depth. Shown for comparison are the data points obtained from Figure 3-4 for the experimental results. With the normalizing ratio determined in this fashion, it is not necessary to follow the life history of each particle until it either emerges from the surface or terminates in a capture collision or reaches the depth cut-off. Rather, the history of a particle can be terminated at the energy loss cut-off, even if it has not emerged from the surface. The spectrum normalizing factor (the total area of the conversion electron spectrum) for a particular depth is found by summing the total weight emerging from the surface into the spectrometer acceptance angle with energy losses less than the cut-off, and then dividing this weight by the ratio shown in Figure 3-14. The spectra displayed in Figure 3-12 were normalized in this fashion.

After shifting the mean source energies so that the Monte Carlo computed spectra closely coincided with the spectra calculated from the Pringle kernel, the theoretical kernal was constructed from the ELTRAS spectra in the following manner. Data points for each depth, z_i , were evaluated at various energies E_k , thus

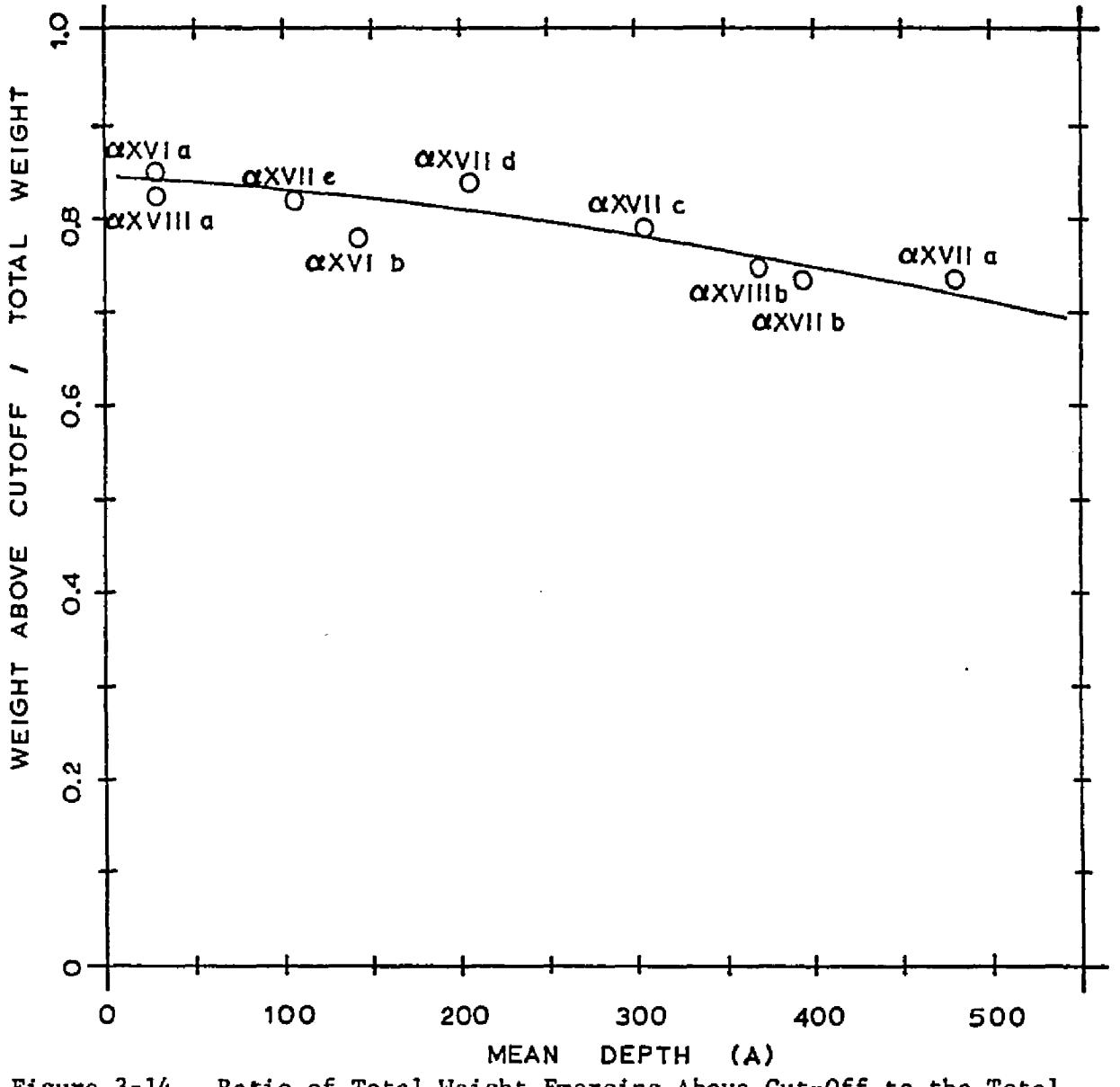

Figure 3-14. Ratio of Total Weight Emerging Above Cut-Off to the Total Emerging Weight as a Function of Depth.

forming a set of vectors $\vec{W_k} = \left| W_{ki} \right|$ $= \left[W(E_k,z_1),\ W(E_k,z_2),\ldots,\ W(E_k,z_{10}) \right]$. The energies E_k were chosen to correspond to the energies used in determining the experimental Pringle kernel. In addition, it was assumed that $W(E_k,z)$ could be expanded according to

$$W(E_k,z) = \sum_{j=1}^{8} C_j(E_k)\ D_j(z) \tag{3-25}$$

where the $D_j(z)$ are the same set of cubic splines used to evaluate the Pringle kernel. The C_j were determined as the expansion coefficients which minimized the functional Z_k given by

$$Z_k = \sum_{i=1}^{10} \frac{1}{ERP_i}^2 \left\{ \sum_{j=1}^{8} C_j(E_k)\ D_j(z_i) - W_{ki} \right\}^2 + SMUL \int_A^B \frac{dz}{ERS^2} \left\{ \sum_{j=1}^{8} C_j(E_k)\ \frac{\partial^2 D_j(z)}{\partial z^2} \right\}^2 \tag{3-26}$$

where ERP_i is an estimate of the accuracy of the data points W_{ki}, and ERS is an estimate of the magnitude of the second derivative of $W(E_k,z)$. The first term of Equation (3-26) thus corresponds to a least squares functional, while the second term represents a smoothing functional. For values of the parameters $ERP_i = 0.05\ W_{ki}$, ERS = 2.4 and SMUL = 2.0, the spline function coefficients were determined at each energy E_k, and they are listed in Table 3-6. The graphs of the kernel computed from these coefficients are presented in Figure 3-15. Shown for comparison are dashed lines representing the experimental Pringle kernel. In general, the agreement

TABLE 3-6

Spline Function Coefficients from DACES2 for ELTRAS Kernel. Spline Joints Placed at 50 A, 100 A, 175 A, and 350 A, Respectively

Energy	C_1	C_2	C_3	C_4
21.806	.11760 E00	-.46381 E-1	.71980 E-3	-.15350 E-2
21.798	.11798 E00	-.25824 E-1	-.23469 E-4	.50202 E-4
21.790	.14369 E00	-.34563 E-1	.85652 E-4	-.18280 E-3
21.781	.14657 E00	-.36586 E-1	.23235 E-3	-.49554 E-3
21.773	.12371 E00	-.28275 E-1	.32857 E-3	-.69935 E-3
21.765	.83057 E-1	-.93885 E-2	.10064 E-3	-.21456 E-3
21.757	.51896 E-1	.14317 E-2	.14372 E-3	-.30713 E-3
21.749	.28200 E-1	.13067 E-1	.84873 E-5	-.18183 E-4
21.740	.17299 E-1	.14285 E-1	.20631 E-3	-.43893 E-3
21.732	.10874 E-1	.13927 E-1	.48458 E-3	-.10335 E-2
21.724	.73513 E-2	.11595 E-1	.84584 E-4	-.18035 E-3
21.716	.46058 E-2	.10480 E-1	.21276 E-3	-.45369 E-3
21.707	.26020 E-2	.10050 E-1	.64080 E-3	-.13669 E-2

TABLE 3-6
(Cont.)

Energy	C_5	C_6	C_7	C_8
21.806	.14660 E-1	-.19209 E-1	.56657 E-2	.13784 E-3
21.798	-.67091 E-3	.18738 E-2	-.90293 E-3	-.87343 E-3
21.790	.18385 E-2	-.12471 E-2	-.26373 E-3	-.61259 E-3
21.781	.51656 E-2	-.61284 E-2	.13619 E-2	-.21807 E-3
21.773	.66120 E-2	-.89099 E-2	.29474 E-2	-.13369 E-4
21.765	.17759 E-2	-.27005 E-2	.11208 E-2	.13083 E-3
21.757	.32959 E-2	-.67056 E-2	.42760 E-2	-.29773 E-3
21.749	-.15250 E-2	.64690 E-3	.14218 E-2	-.26167 E-3
21.740	-.73514 E-3	.54044 E-3	.99980 E-3	-.21316 E-4
21.732	.61852 E-3	-.14426 E-3	.83064 E-3	.69764 E-4
21.724	-.23139 E-3	-.23902 E-3	.83836 E-3	.22718 E-4
21.716	.35366 E-3	-.18241 E-3	.24935 E-3	.26728 E-3
21.707	.17284 E-2	-.87535 E-4	-.52068 E-3	.52732 E-3

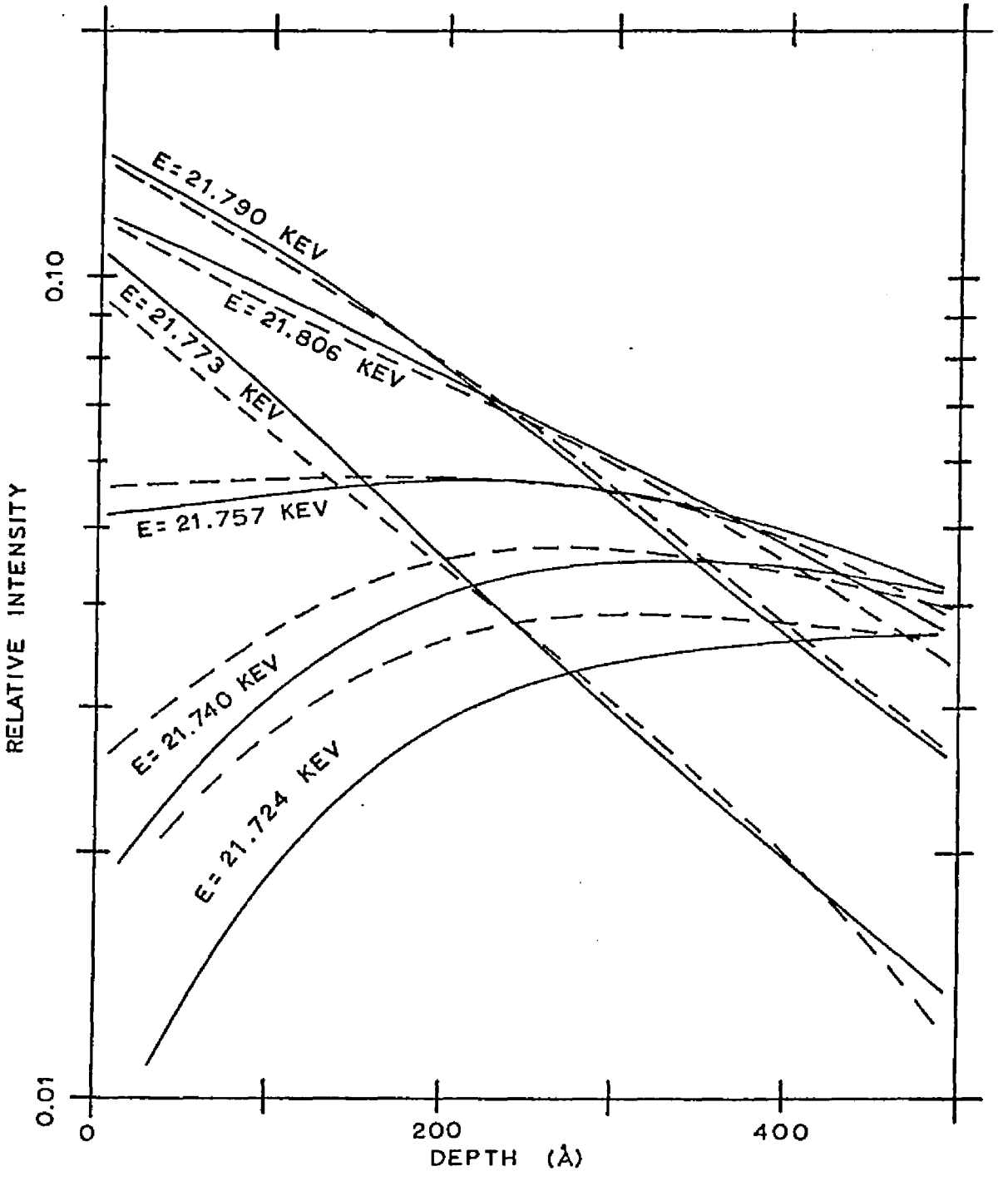

Figure 3-15. Comparison of the Empirical Kernel (---) and the ELTRAS Kernel (——) for Various Energies.

is quite good. The only major difficulty is that at lower energies the theoretical kernel is too small. This discrepancy is believed to be due to an interband transition(s) or an ionization process with a corresponding energy loss in the range of 50 - 100 eV. Otherwise, the general features of both the experimental and theoretical Monte Carlo kernel correspond in almost every way, and it is concluded that the major assumptions on which the ELTRAS code was constructed are undoubtedly valid.

4.0 DETERMINATION OF THE DEPTH DISTRIBUTION OF CONVERSION ELECTRON SOURCES FROM CONVERSION ELECTRON ENERGY SPECTRA

4.1 Introduction

The purpose of this chapter is to assess the feasibility of obtaining the depth distribution, S(z), of conversion electron sources by solving the Fredholm integral equation of the first kind given by

$$N(E) = \int W(E,z)\ S(z)dz \qquad (4\text{-}1)$$

In the above equation, S(z), constitutes the unknown function, while the transport kernel, W(E,z), and the conversion electron spectrum, N(E), are considered to be known functions. As seen from the previous chapter, W(E,z) is a rather "flat" function, particularly for low energies and large depths, and the integration of Equation 4-1 tends to average out fine structure in S(z). As a result, the unfolding problem can be expected to be very difficult. (For a general discussion of the theory of integral unfolding refer to Appendix C.)

In general two distinct approaches are available for unfolding Equation (4-1). The first recasts N(E) and W(E,z) into appropriate parametric representations, and a Laplace transform is found which expresses the solution for S(z). The second method replaces

the integral equation with an appropriate set of simultaneous linear equations which can be solved, for example, by the Gaussian elimination method.

As an example of the first technique, the correctness of the Fermi age diffusion kernel was assumed, and a parametric, Laplace transform method was developed based upon the explicit functional dependence of the age diffusion kernel. In view of the questionable validity of the age diffusion approach for the electron transport problem of interest in this study, the details of this calculation are not presented here. Since an age diffusion kernel is known to be a valid approximation in problems of heat conduction and diffusion of material, however, the details of the inversion may be of interest to readers familiar with these areas, and they have been included in Appendix E.

In the remainder of this chapter, the kernel obtained from the experimental conversion electron spectra of Pringle is assumed to be correct and the feasibility of inverting Equation (4-1) is examined using the computer code DACES2 (Data Analysis of Conversion Electron Spectra No. 2).

4.2 Numerical Inversion with DACES2

In Section 3.3 the electron transport kernel $W(E,z)$ was constructed as a function of depth for various energies of emergence using the computer program DACES1. As a result of that analysis, $W(E,z)$ was represented by a four-joint cubic spline function whose

coefficients are listed in Table 3-5. In this section the possibility of obtaining the Xe^{125} distribution in Ta_2O_5 from conversion electron spectra and a known kernel is examined. In Section 3.3 the kernel was the unknown while the source distributions, $S_i(z)$, were known as the result of quantitative stripping measurements. In this section, however, the situation is reversed: $S(z)$ now represents the unknown while the response function is given by the kernel $W(E,z)$ in the spline function representation.

To simulate experimentally obtained results, conversion electron spectra, for the unfolding experiments to be described later in this chapter, were generated according to $\hat{N}(E_k) = \int_o^\infty W(E_k,z)\ S(z)\ dz$ where $W(E_k,z) = \sum_{j=1}^{8} C_j(E_k)\ D_j(z)$, and $S(z)$ is the known source distribution. Making the substitution yields

$$\hat{N}(E_k) = \sum_{j=1}^{8} C_j(E_k) \int_o^\infty D_j(z)\ S(z)\ dz \qquad (4\text{-}2)$$

The integrals in the above equation were performed in the following manner. The range of the integration was first divided into a number of intervals, and the integration over each interval was performed using four-point Gaussian quadrature. Each interval was then divided in half, and the integration over the two subintervals was compared with the original integration. If the results did not agree to within an accuracy of 10^{-4}, the intervals were further subdivided until the desired accuracy was achieved. Since the kernel $W(E,z)$ is a decreasing function for large z, and since the source distributions were anticipated to lie relatively close to the surface,

an upper integration limit of 650 A was specified.

The source distributions chosen for use in these numerical experiments were assumed to be Gaussian functions for two primary reasons. First, by using narrow distributions, the difficulty of unfolding can be examined as the centroid and the width of the distribution is varied. In addition, since the source distributions of Pringle were Gaussians, by using Gaussian distributions in this work it was anticipated that results immediately applicable to Pringle's spectra could be obtained. Accordingly, electron spectra were generated for ten Gaussian source distributions, $S_i(z)$, $i = 1,\ldots,10$, with centroids placed at 50 A intervals from 50 A to 500 A. The standard deviation for all distributions was chosen to be 50 A.

After the conversion spectra $\hat{N}_i(E_k)$ (the subscript i denotes the spectrum due to the i^{th} source distribution) had been generated using the assumed source distributions in the integration and summation of Equation (4-2), the spectra were altered by introducing errors according to

$$N(E_k) = \hat{N}(E_k) \left| 1 + \frac{\alpha}{\sqrt{\hat{N}_k}} ERR_k \right| \qquad (4\text{-}3)$$

where α is a constant and ERR_k is a random number generated in the range (-1, 1). The specific form of Equation (4-3) was chosen because it represents spectra for which errors in the data points are dominated by statistical fluctuations. As a result of the manner in which the experimental conversion electron spectra were

normalized the maximum value attained by $\hat{N}(E_k)$ is approximately 0.1, and the minimum value seldom falls below 0.01. Thus, for values of the parameter α corresponding to 0.0032 and 0.0125, the percent error in the altered spectra can range from 1% to 3.2% and from 4% to 12.5%, respectively. Increasing the amount of data error was expected to increase the difficulty of unfolding the source distributions. The conversion electron spectra generated in this fashion constituted the input information for this application of the DACES2 code.

Since the DACES2 program is also based upon the UNFOLD algorithm, the basic features of the code are identical to those of the DACES1 code, i.e., a quadratic functional is minimized subject to equality and inequality constraints. The primary difference between the two codes is the solution objective. Using known source distributions and conversion electron spectra DACES1 solves for the kernel; using the DACES1 kernel and conversion electron spectra DACES2 solves for the source distributions. By employing narrow (Gaussian) source distributions it is relatively easy to obtain an accurate representation of the smooth kernel function from DACES1. Because of the "smoothness" of the kernel, however, the determination of source distributions using DACES2 was expected to be much more difficult.

For these trials, the functional form of the "unknowns" has already been established. In actual practice, however, such complete information would obviously not be available, and the physical

nature of the process that produced the source distribution must be examined. For example, the Xe^{125} source distributions of Pringle were produced by bombarding an amorphous Ta_2O_5 specimen with singly ionized Xe^{125}. Knowing the range and straggling data (61), a fairly accurate estimate of the Xe^{125} distribution can be made. This auxiliary information could then be incorporated in DACES2 in a number of ways such as prior estimate data, smoothing estimates, and placement of spline function joints, for example. At the start of an unfolding investigation, however, the correct course is to assume a minimum amount of auxiliary information. Consequently, the only auxiliary information assumed concerning the "unknown" distribution was that the source distributions were non-negative and single-peaked.

Error estimates for the input data were generated according to

$$\mathrm{ERU}\ (E_k) = \alpha\ \sqrt{N(E_k)} \tag{4-4}$$

in agreement with Equation (4-3). In DACES1 the kernel, W(E,z), was expanded in a set of linearly independent cubic splines. In DACES2, however, the source distribution must be expanded as

$$S(z) = \sum_j C_j\ D_j(z) \tag{4-5}$$

where the $D_j(z)$ represent a set of linearly independent functions. The cubic splines were again used for the $D_j(z)$. The number of spline joints was limited to five to restrict the number of degrees

of freedom, and the placement of the joints varied according to the estimated depth of the source distribution. The objective of DACES2 is to obtain the spline function coefficients, C_j, that yield a best solution estimate, with any available auxiliary information.

4.3 Evaluation of Best Solution Estimate Parameters Using DACES2

The first spectrum to be examined was the spectrum corresponding to the source distribution of 100 A mean depth with $\alpha = 0.0032$. Since this distribution lies relatively near the surface where the kernel is more rapidly varying, it was expected that this spectrum would be more easily unfolded than spectra due to lower-lying sources. For all results obtained with this source distribution the spline joints were placed at 40, 70, 100, 130, and 160 A, respectively. While this choice of spline joints presupposes additional knowledge about the "unknown," this assumption will be justified later.

To investigate the inherent instability of the problem, the first trial of DACES2 did not employ any prior estimates, smoothing, miscellaneous information, or equality or inequality constraints. The result is exhibited as (a) in Figure 4-1, with the known function shown as the dashed line for comparison. The DACES2 result is clearly incorrect, and the need for auxiliary information is apparent.

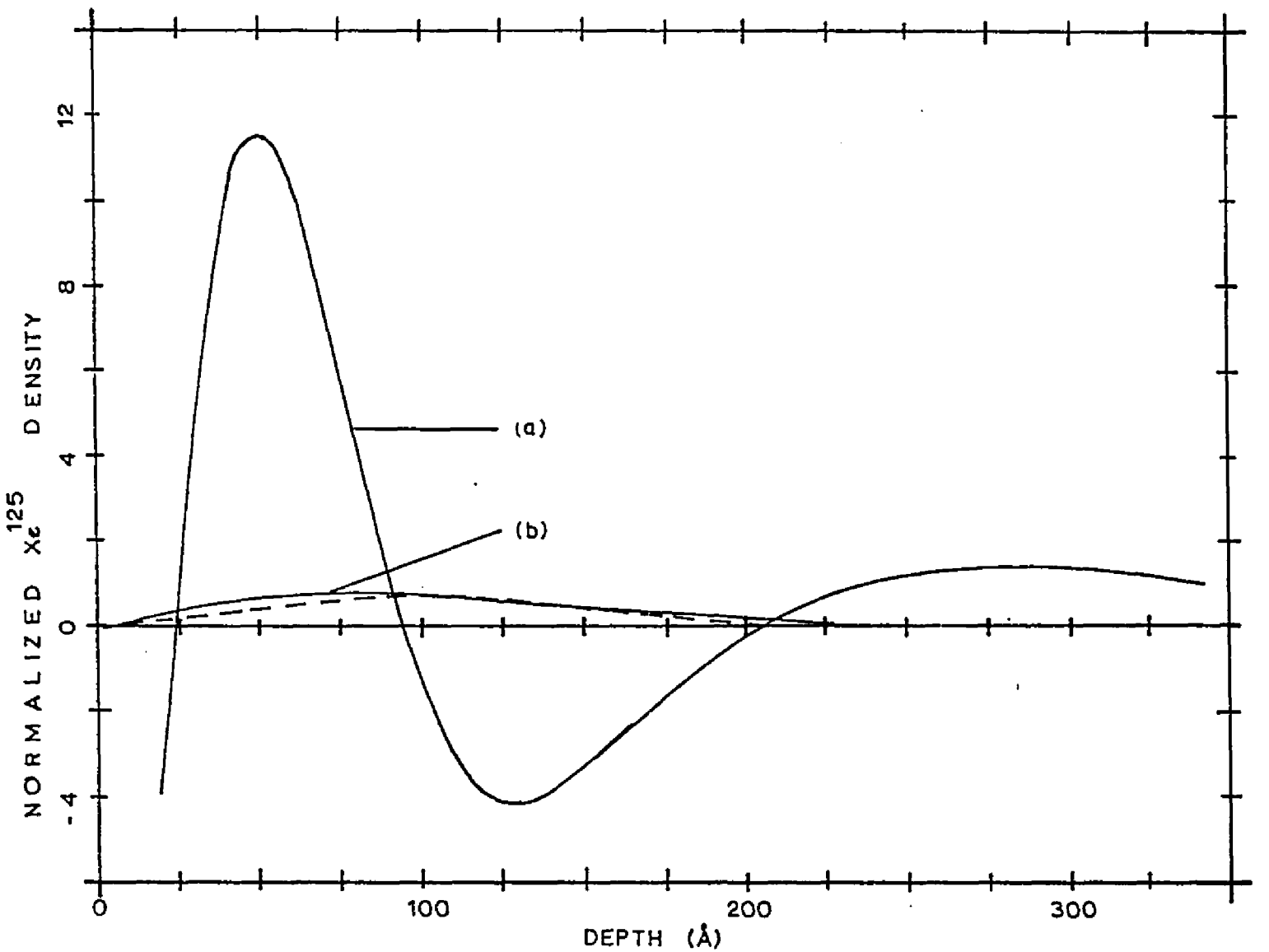

Figure 4-1. DACES2 Solution with no Auxiliary Information. (a) Altered Spectrum, (b) Unaltered Spectrum.

To evaluate the effect of the statistical errors in the conversion electron spectrum, the unaltered conversion electron spectrum, $N(E_k)$, was next unfolded, again without additional information. As seen in (b) of Figure 4-1, the violent oscillatory behavior is much reduced, and the result strongly resembles the true source distribution. Since the difference between curves (a) and (b) is solely due to the simulated errors, the major difficulty in solving the unfolding problem arises from "experimental" errors in the conversion spectra, rather than errors generated in the numerical computations.

Returning to the altered spectrum, $N(E_k)$, the next three runs, exhibited in Figure 4-2, indicate the effect of using prior estimate data in obtaining a solution estimate. The prior estimate data were obtained by the least-squares fit of a symmetric triangular function given by

$$\hat{S} = \begin{cases} 0 & 0 \le z \le z_0 \\ b(z - z_0) & z_0 \le z \le z_1 \\ b(-z_0 + 2z_1 - z) & z_1 \le z \le (2z_1 - z_0) \\ 0 & z \ge (2z_1 - z_0) \end{cases} \tag{4-6}$$

The peak of the distribution occurs at $z = z_0$, while $z_1 - z_0$ denotes the half width and b denotes the slope in absolute value. These least-squares parameters were determined by minimizing the functional F given by

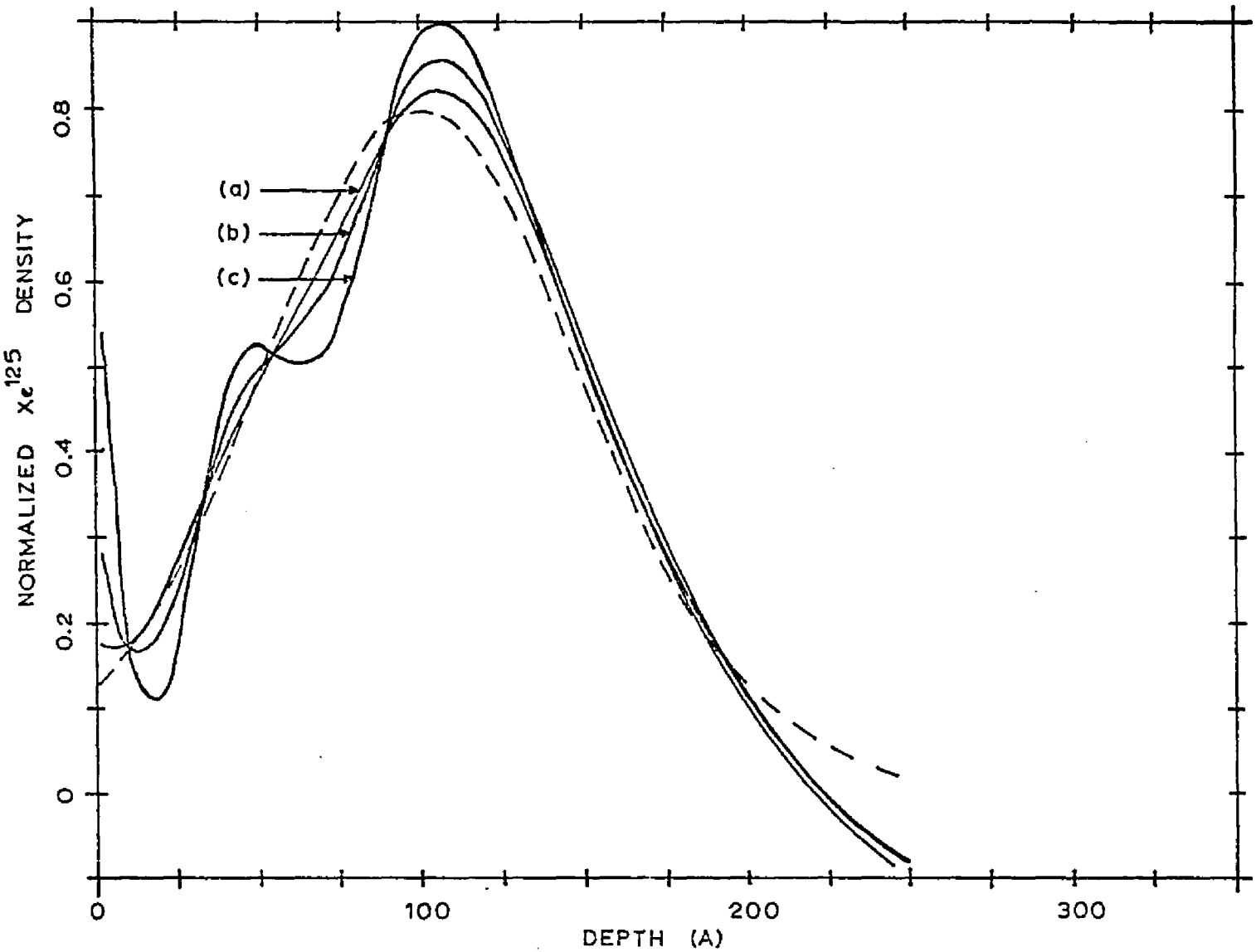

Figure 4-2. DACES2 Solutions with Prior Estimation. (a) PMUL = 2.0; (b) PMUL = 1.0; (c) PMUL = 0.6.

$$F = \sum_{i=1}^{NU} \left(\frac{f_i - N(E_i)}{ERU_i * N(E_i)} \right)^2 \qquad (4\text{-}7)$$

where $N(E_i)$ denotes the conversion electron data, ERU_i the estimated error, and f_i is computed from the rough estimate $\hat{S}$ according to

$$f_i = \int_o^\infty W(E_i,z)\ \hat{S}(z)\ dz \qquad (4\text{-}8)$$

The values of b, z_o, and z, obtained in this fashion were

$$b = 0.0074\ A^{-1}$$

$$z_o = 12.592\ A$$

$$z_1 = 102.649\ A$$

Using these parameter values in Equation (4-6), prior estimate data were computed for abscissa values ranging from 10 A to 210 A at 20 A intervals. The prior estimates were assumed to be accurate within 10% ($ERP_i = 0.1 * P_i$), and the DACES2 routine was cycled on values of the parameter PMUL ranging from 0.6 to 2.0. As PMUL increases, the prior estimate term is given increasing weight with respect to the unfold functional, and this effect is clearly demonstrated in Figure 4-2. As PMUL increases, oscillations decrease in the depth range of 0 A to 100 A. In addition, the peak of the source distribution occurs at approximately 103 A, which agrees well with the value of the prior estimate parameter z_1 .

The next few trials were performed without prior estimates, but including a smoothing term to control oscillations by minimizing

the second derivative of the solution estimate. This was done because, firstly, it is very likely that prior estimate data would not always be available; secondly, the calculation of the prior estimates by the least-square method was generally found to be very unstable. Estimating the maximum value of the second derivative to be 1.0, (ERS = 1.0) the DACES2 routine was cycled on values of the parameter SMUL ranging from 0.6 to 2.0. As SMUL increases, the inportance of the smoothing term also increases. The results of these trials, shown in Figure 4-3, indicate that the best value of SMUL is 1.0, while 0.6 and 2.0 correspond to under- and over-smoothing. Of great importance is that the peak of the distribution occurs in the correct location. As a consequence of this somewhat unexpected result, the spline joints could have been appropriately positioned after only one preliminary run, thereby minimizing the need for assuming additional auxiliary information.

The next nine runs were performed using both the prior estimate data and smoothing. The values of PMUL and SMUL ranged from 0.6 to 2.0. Sample results from these computations are exhibited in Figure 4-4 with PMUL = 0.6 and SMUL = 2.0, and with PMUL = 2.0 and SMUL = 0.6. These results are typical of the remaining runs. In general, increased emphasis of the prior estimate data tends to increase lower-lying oscillatory behavior.

Next, the iterative use of DACES2 code was studied. The source distributions with PMUL = 0.6, SMUL = 1.0, and SMUL = 1.0, were used as initial estimates of the source distribution and

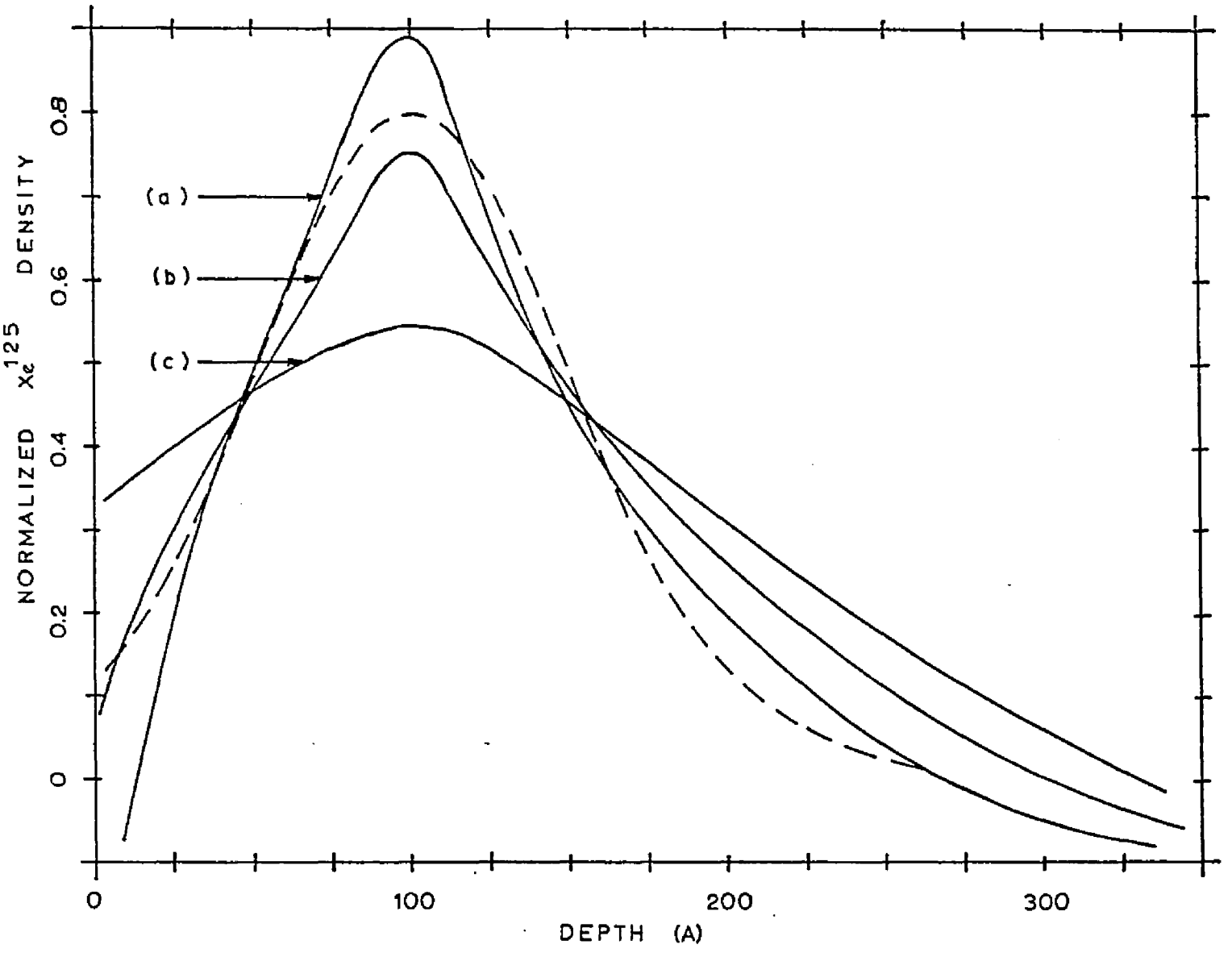

Figure 4-3. DACES2 Solutions with Smoothing. (a) SMUL = 0.6; (b) SMUL = 1.0; (c) SMUL = 2.0.

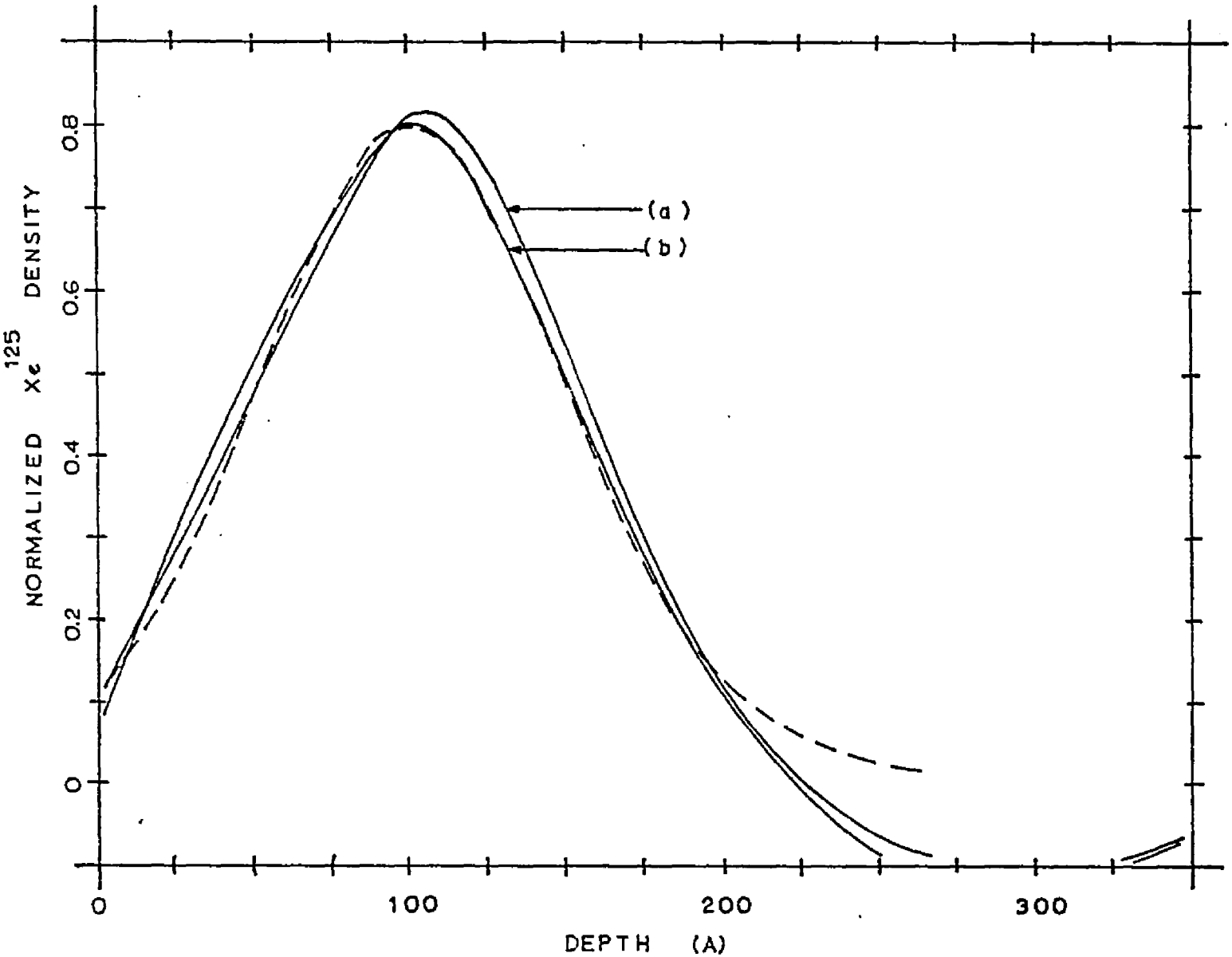

Figure 4-4. DACES2 Solutions with Smoothing and Prior Estimation. (a) SMUL = 0.6, PMUL = 2.0; (b) SMUL = 2.0, PMUL = 0.6.

incorporated through the prior estimate functional of DACES2. In addition, one bit of miscellaneous information was added in the second iteration. Since the conversion electron spectra of Pringle were normalized the source distributions correspond to normalized Gaussian functions. Consequently, the integral of the unknown source distributions over the range of 0 A to 650 A should approach unity. This information was coded into DACES2 by specifying the integration of the source distribution as

$$\int S(z) = \sum_j C_j \int D_j (z)\, dz \simeq 1.0$$

The integration value was assumed to be accurate to 10%, and the error parameter ERM was set equal to 0.1.

The best results for these unfolding computations were obtained for small values of PMUL and large values of SMUL and are presented in Figures 4-5, 4-6, and 4-7. Conformance to the expected Gaussian behavior is especially good in the 0-200 A depth region.

Without exception, all of the previously shown unfolding results have indicated negative values and/or oscillations at large depths. In an effort to reduce these unwanted effects, four inequality constraints were imposed upon the solution estimate in addition to prior estimate data provided from run no, smoothing cycled on SMUL values of 0.6 to 2.0, and the miscellaneous information term. In particular, the physical impossibility of negative sources was imposed at depths of 0 A, 300 A, 400 A and 500 A. In the context of DACES2 these constraints were written as

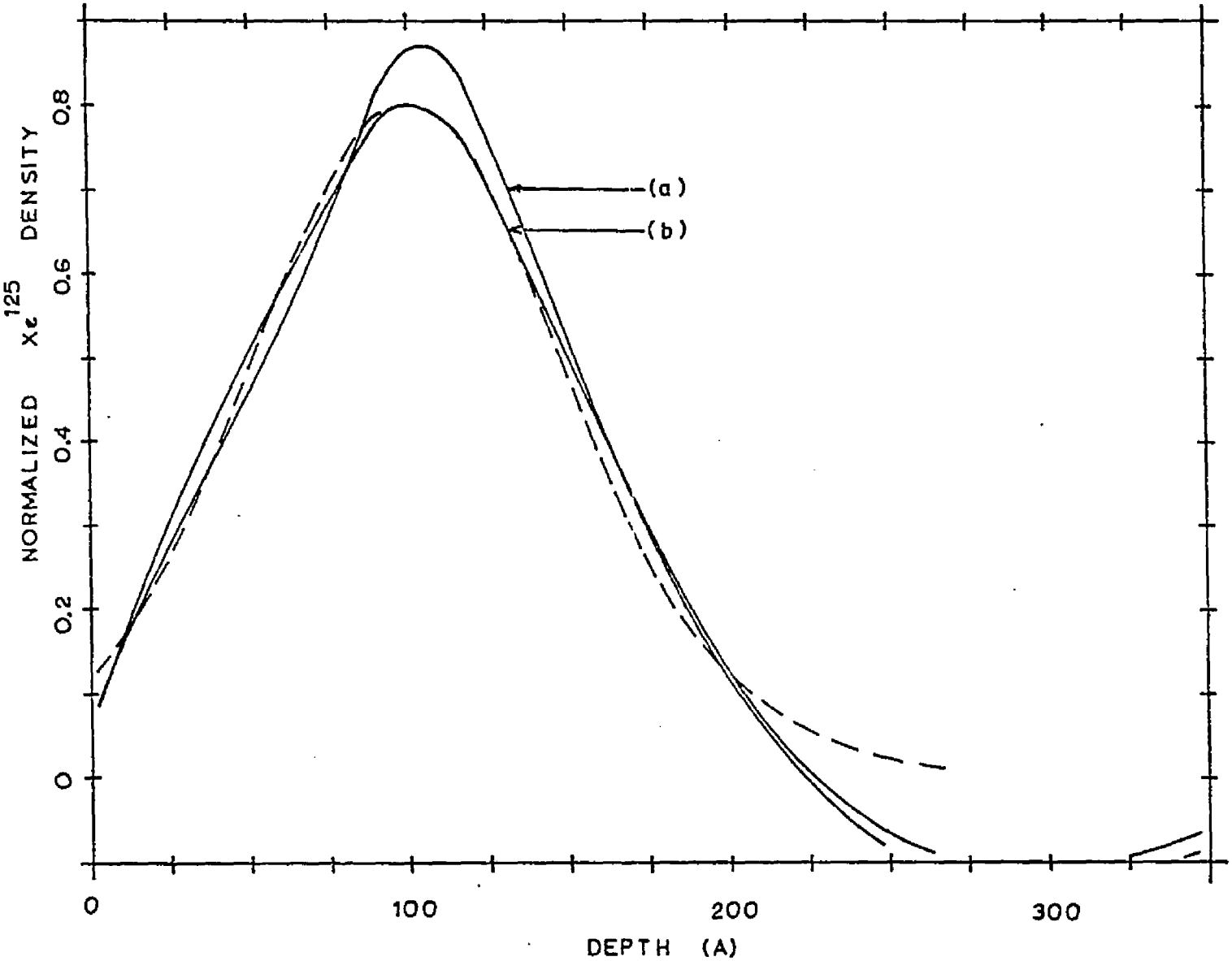

Figure 4-5. Solutions Obtained through Iterative Use of DACES2. SMUL=1.0, PMUL=0.6 Used as the Prior Solution Estimate. (a) PMUL=0.6, SMUL=0.6; (b) PMUL=0.6, SMUL=2.0.

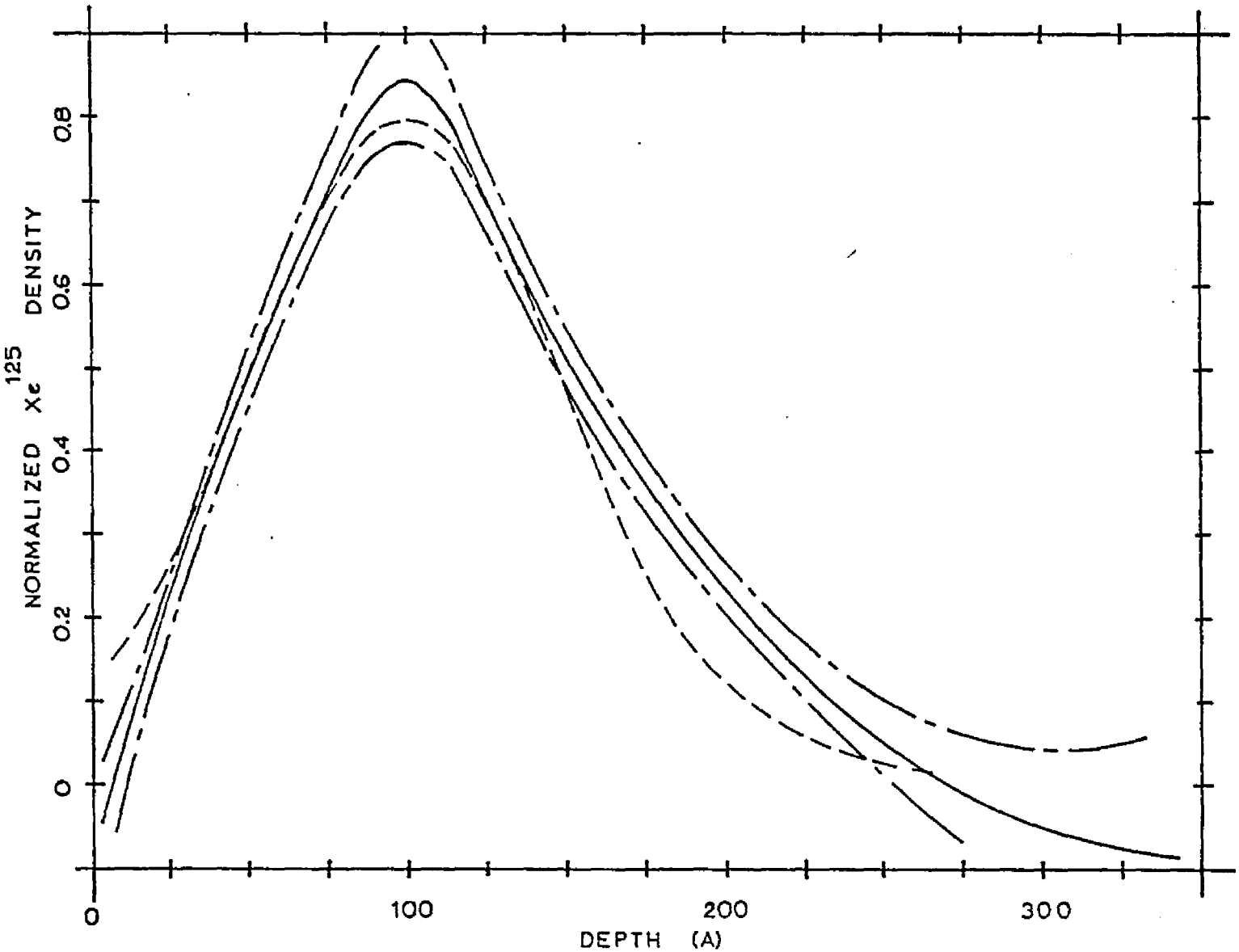

Figure 4-6. Solution Obtained through Iterative Use of DACES2 with PMUL = 1.0, SMUL = 0.6. The Prior Estimate was SMUL = 0.6.

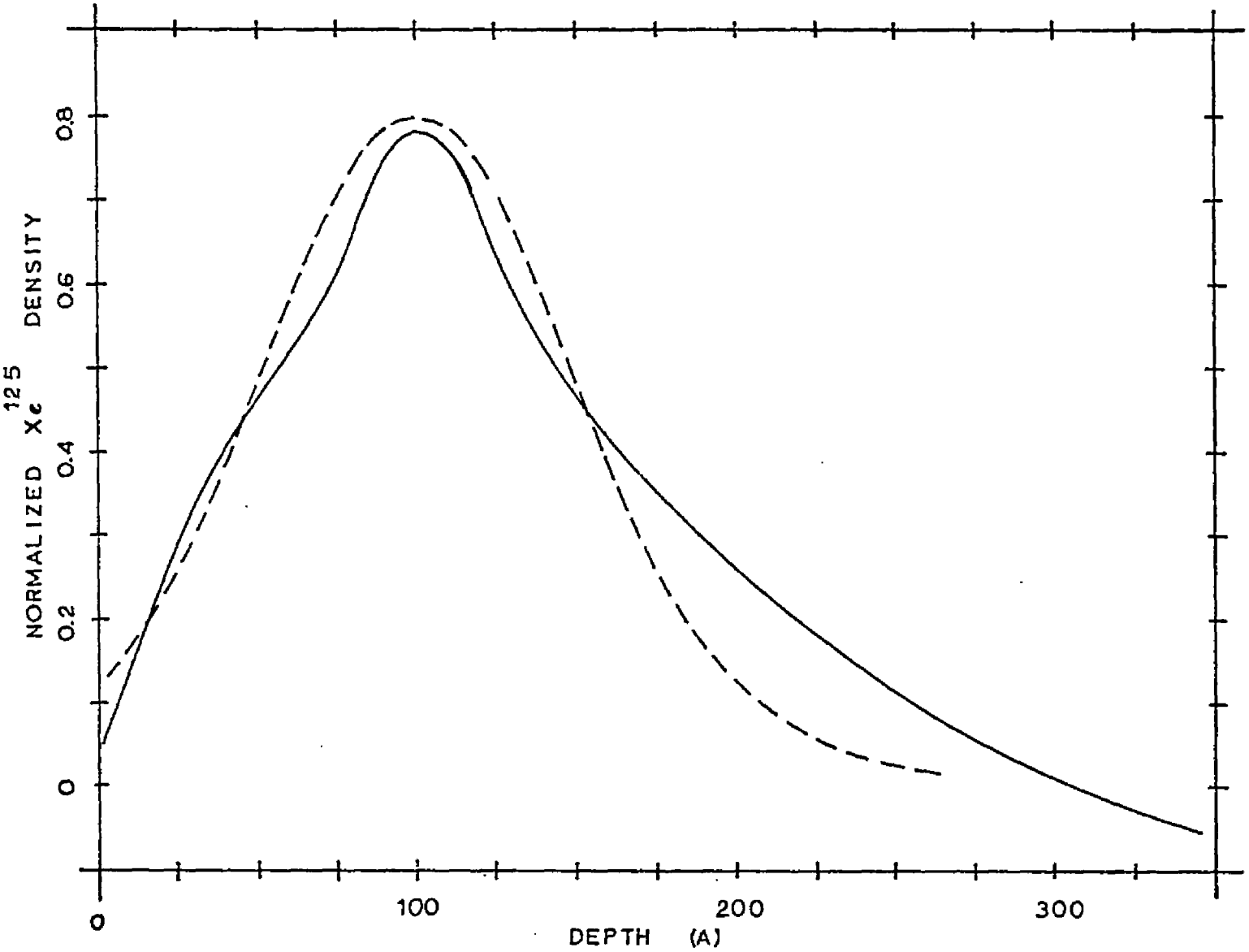

Figure 4-7. Solution Obtained through Iterative Use of DACES2 with PMUL=1.0, SMUL=0.6. The Prior Estimate was SMUL=1.0.

$$L_1\ (D_j(z)) = -D_j(0.0)$$
$$L_2\ (D_j(z)) = -D_j(3.0)$$
$$L_3\ (D_j(z)) = -D_j(4.0)$$
$$L_4\ (D_j(z)) = -D_j(5.0)$$

The result of the trial with SMUL = 2.0 is shown in Figure 4-8. While the oscillations and negativity have been suppressed, the solution estimate is obviously not a symmetric Gaussian distribution with a mean depth of 100 A, indicating that the auxiliary information was not used to maximum benefit. An additional result of this trial was that the second inequality constraint was not found to be limiting, i.e., the second constraint could have been deleted without affecting the unfolding result.

All the results of unfolding performed with the generated conversion electron spectrum corresponding to the normalized Gaussian distribution with 100 A mean depth are summarized in Table 4-1. It is somewhat difficult to judge which combination of auxiliary information yielded the "best" unfolding result. For many instances the trial using only smoothing with SMUL = 1.0 (run no. 7) would probably suffice. The inclusion of prior estimate data generated from a least-squares triangular function yielded results which closely agreed with the known Gaussian distribution over the range 0 A to 200 A. At larger depths, however, these trials were marked by ambiguous oscillations. While these oscillations could undoubtedly be reduced by the inclusion of equality

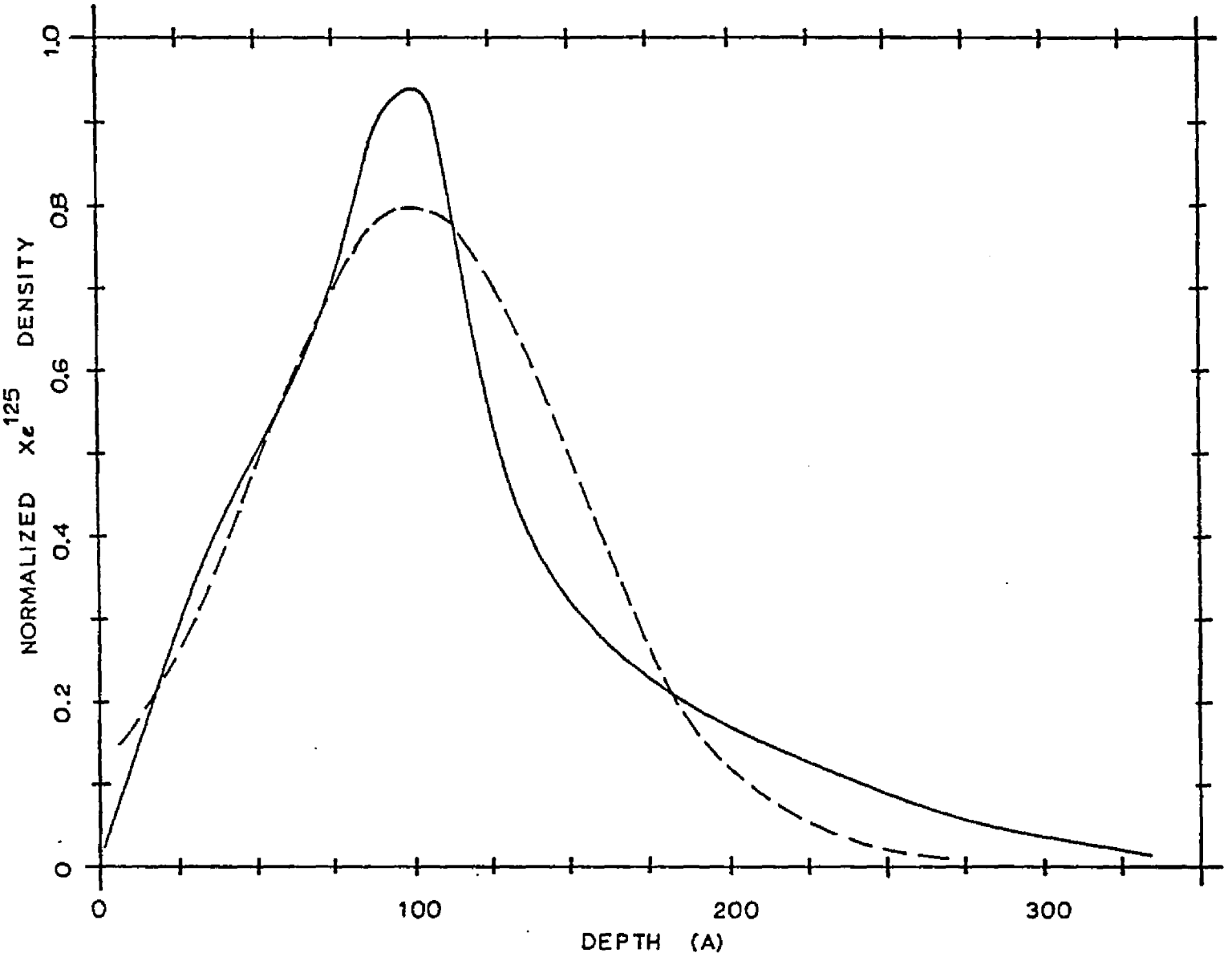

Figure 4-8. DACES2 Solution with Inequality Constraints. Four Inequality Constraints were Used to Supress Negativity and Oscillation at Large Depths with PMUL=1.0, SMUL=1.0.

TABLE 4-1

Results of Unfolding with DACES2
z_o = 100 A

RUN NO.	SMUL	PMUL	INEQU. CONST.	PROB. MEAN	PROB. CHI SQ.	FIGURE
1	0	0	0	0.0	0.0	4-1a
2	0	0	0	0.97	1.00	4-1b
3	0	0.6	0	0.46	0.0	4-2c
4	0	1.0	0	0.39	0.02	4-2b
5	0	2.0	0	0.62	0.0	4-2a
6	0.6	0	0	0.69	0.46	4-3a
7	1.0	0	0	0.78	0.34	4-3b
8	2.0	0	0	0.94	0.25	4-3c
9	0.6	0.6	0	0.87	0.49	
10	1.0	0.6	0	0.89	0.35	
11	2.0	0.6	0	0.48	0.03	4-4b
12	0.6	1.0	0	0.94	0.41	
13	1.0	1.0	0	0.96	0.24	
14	2.0	1.0	0	0.41	0.01	
15	0.6	2.0	0	0.70	0.08	4-4a
16	1.0	2.0	0	0.97	0.04	
17	2.0	2.0	0	0.58	0.00	
18	0.6	0.6	0	0.52	0.69	4-5a
19	1.0	0.6	0	0.03	0.00	
20	2.0	0.6	0	0.54	0.25	4-5b
21	0.6	1.0	0	0.18	0.38	4-6
22	1.0	1.0	0	0.06	0.00	
23	2.0	1.0	0	0.01	0.00	

TABLE 4-1
(Cont.)

RUN NO.	SMUL	PMUL	INEQU. CONST.	PROB. MEAN	PROB. CHI SQ.	FIGURE
24	0.6	2.0	0	0.00	0.00	
25	1.0	2.0	0	0.00	0.00	
26	2.0	2.0	0	0.00	0.00	
27	0.6	1.0	0	0.59	0.90	4-7
28	1.0	1.0	0	0.73	0.88	
29	2.0	1.0	0	0.64	0.73	
30	0.6	2.0	4	0.00	0.00	
31	1.0	2.0	4	0.00	0.00	4-8
32	2.0	2.0	4	0.00	0.00	

or inequality constraints, or by increasing the importance of smoothing at the greater depths, for experimental spectra the use of prior estimate data generated in this fashion is subject to criticism. The most predictable results were obtained by iterating the DACES2 program. (run nos. 18-29). The best results of the iteration trials are graphed in Figures 4-5 and 4-6, for which run no. 6 was used as an initial estimate of the source distribution. Cycling on small values of PMUL and large values of SMUL yielded reasonable solutions, and for source distributions expected to lie fairly close to the surface, (< 200 A) this is the suggested solution technique.

4.4 Evaluation of Best Solution Estimate Parameters for Lower-Lying Source Distributions

As the depth of the unknown source distribution becomes greater the difficulty of unfolding is expected to increase because of the flatness of the kernel. To examine this possibility the generated conversion electron spectra corresponding to Gaussians with mean depths of 200, 300 and 400 A were next unfolded. Selected results of runs with the error parameter SMUL ranging from 0.05 to 0.4 are exhibited in Figures 4-9, 4-10 and 4-11 for the three generated spectra. Of special note is the small value of SMUL required to "over-smooth" the solution estimates, in contrast to the results obtained with the 100 A source distribution. For less smoothing, however, the solution estimates exhibit oscillations.

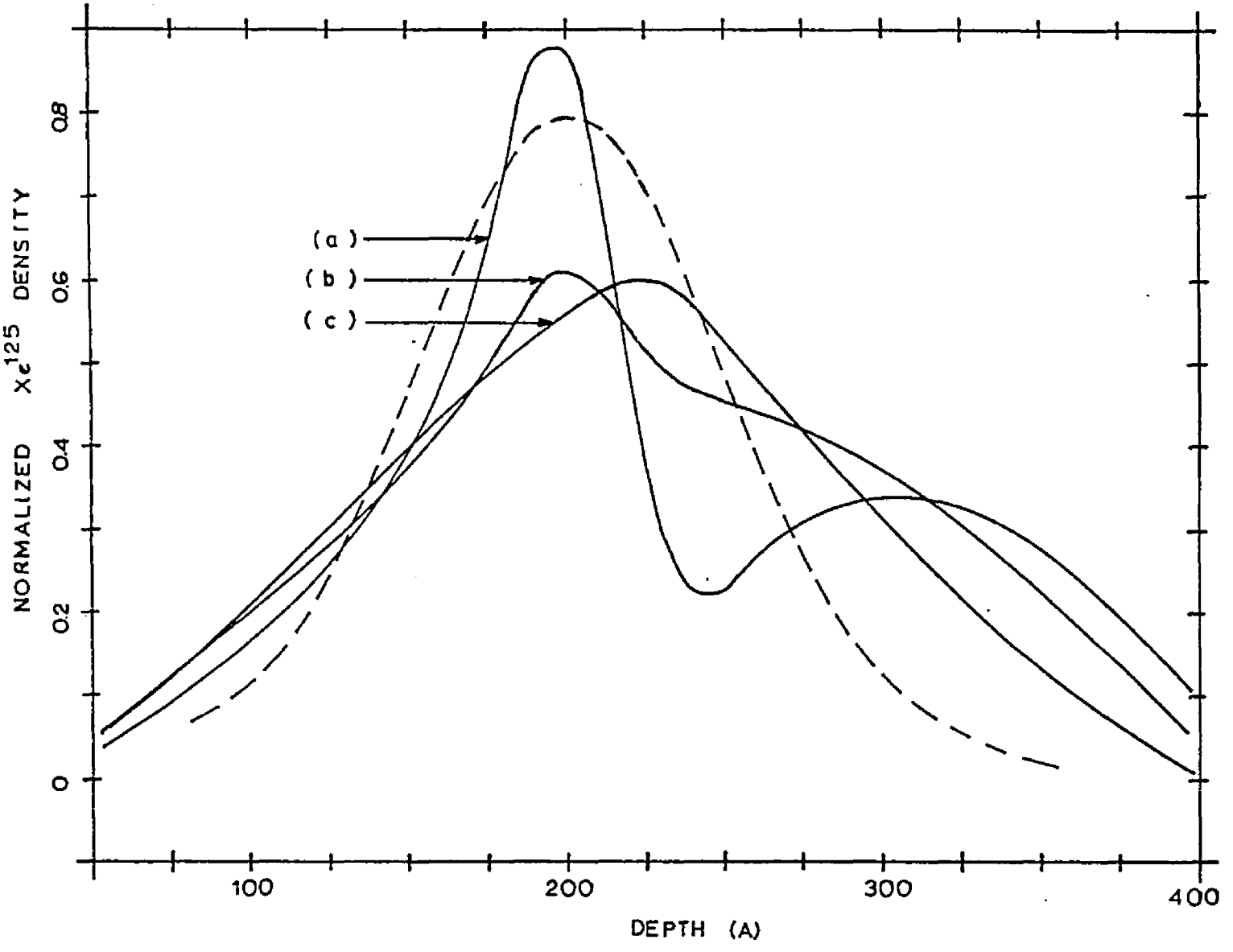

Figure 4-9. DACES2 Solutions for the Gaussian Distribution with Mean Depth of 200 A. (a) SMUL=.05; (b) SMUL=0.1; (c) SMUL=0.4.

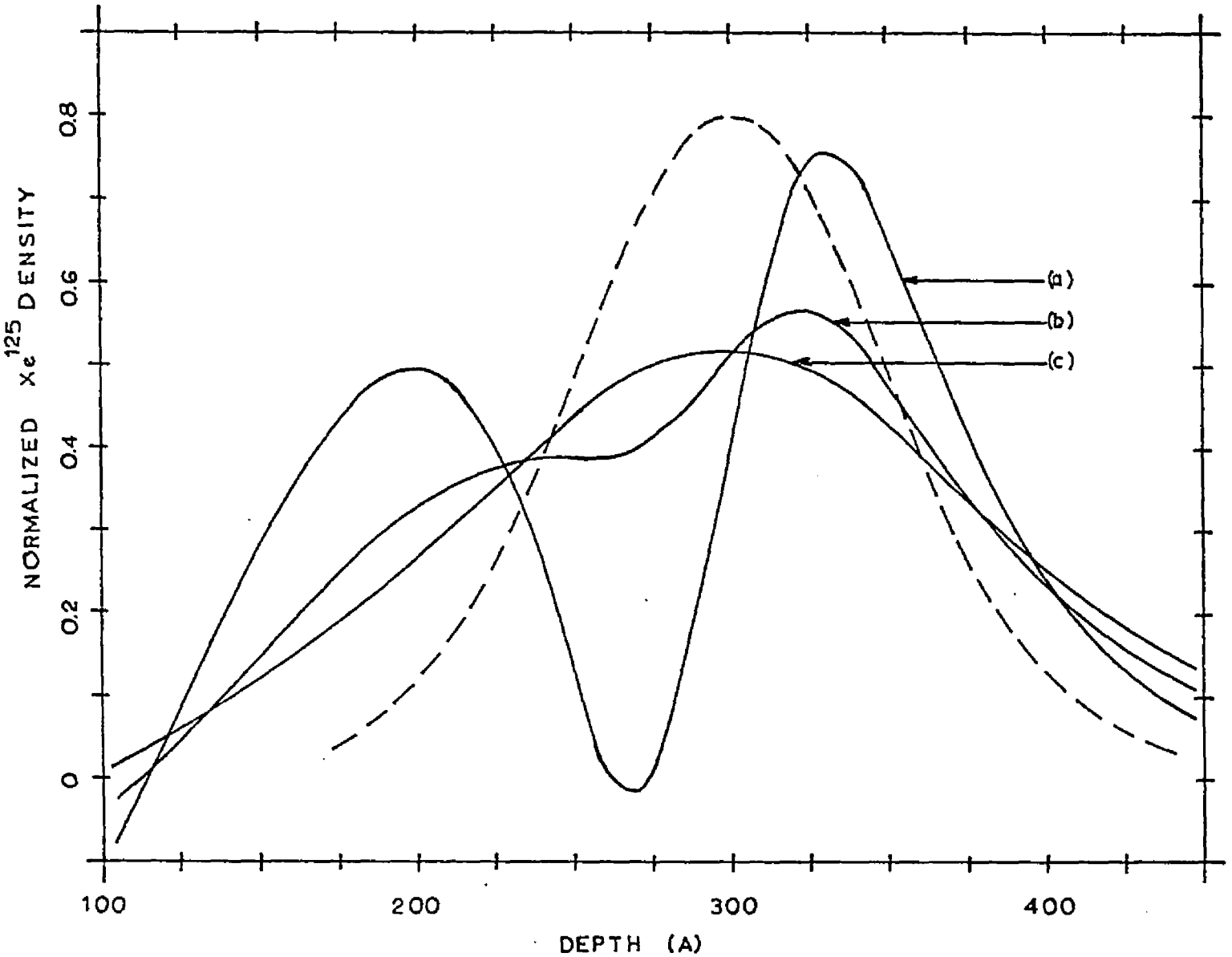

Figure 4-10. DACES2 Solutions for Mean Depth of 300 A. (a) SMUL=.05; (b) SMUL=0.1; (c) SMUL=0.4.

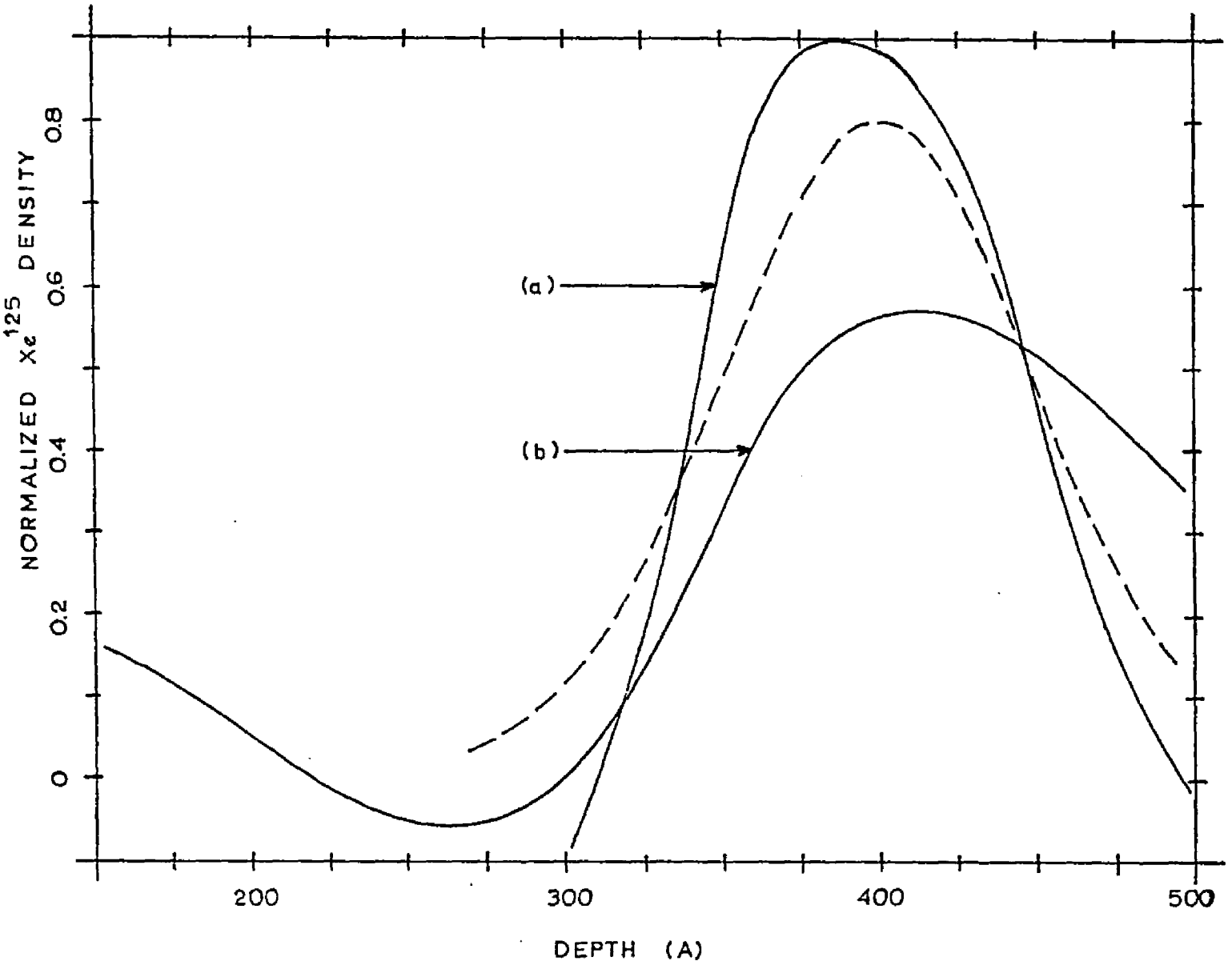

Figure 4-11. DACES2 Solutions for Mean Depth of 400 A. (a) SMUL=0.1; (b) SMUL=0.4.

As the kernel becomes flatter, the unfolding problem becomes more ill-posed, and the statistical errors in the generated data increase the difficulty of obtaining accurate source distribution estimates.

To overcome these difficulties additional auxiliary information must be incorporated into the DACES2 routine. For example, in the case of the 200 A distribution, the assumption of a symmetric unknown was incorporated directly by reflecting the left side of the SMUL = .4 estimate (graph (a) of Figure 4-9) about an imaginary axis at z = 200 A, and using the result as prior estimate data. An example of the improved estimates obtained in this fashion is shown in Figure 4-12 with values of the parameters PMUL and SMUL set equal to 1.0 and 0.4 respectively.

For the 300 A distribution a somewhat improved answer was obtained by using the SMUL = 0.4 result as prior estimate data for a subsequent trial. The improvement given by even the small value of PMUL = 0.05 is evident by comparing Figure 4-12 with graph (a) of Figure 4-10, since the parameter SMUL was equal to 0.05 for both trials.

In the case of the 400 A distribution improved estimates were obtained by imposing additional information in the form of non-negativity and smoothness of the expected result. In particular, the SMUL = 0.1 solution estimate was used as an initial source distribution estimate for the depth range of 320 A to 480 A; for the depths of 100 A, 200 A and 250 A and 550 A, however, the

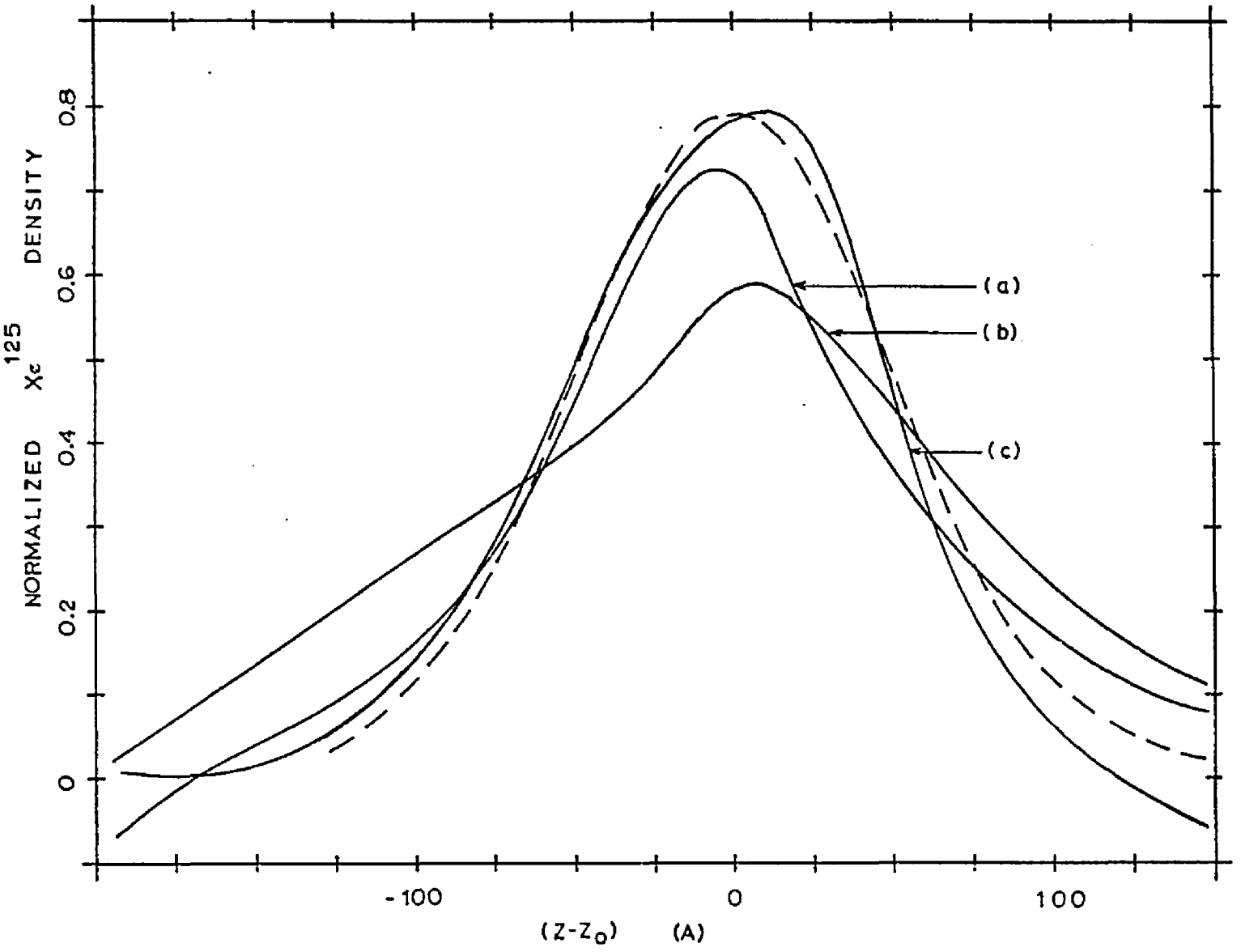

Figure 4-12. Iterative DACES2 Solutions for Xe^{125} in Ta_2O_5 for Various Depths. (a) z_o=200 A, PMUL=1.0, SMUL=0.4; (b) z_o=300 A, PMUL=.05, SMUL=.05; (c) z_o=400 A, PMUL=0.6, SMUL=2.0.

initial estimate was specified as zero. An example result of these computations is shown in Figure 4-12 for SMUL = 1.0 and PMUL = 0.6. The additional auxiliary information has noticeably improved the solution estimate for this source distribution.

For the unfolding calculations carried out thus far, the simulated statistical errors in the conversion electron spectra were generated according to a value of the error parameter α (see Equation (4-3)) equal to 0.0032. As the value of α increases, the magnitude of the simulated error in the conversion spectrum also increases, and the difficulty of unfolding would be expected to increase. To evaluate the effect of the error, α was increased from 0.0032 to 0.0125 in the subsequent unfolding trials corresponding to source distributions with mean depths of 100 A, 200 A, 300 A and 400 A. Representative results for the smoothing-only trials are presented in Figures 4-13, 4-14, 4-15 and 4-16 for values of the smoothing parameter SMUL ranging from 0.05 to 0.5. As expected the increased error in the spectra considerably worsened the results of the unfolding calculation. Moreover, the results progressively worsened as the depth of the source distribution increased, until virtually no information was available from the computations as shown in Figure 4-16. In unfolding the 400 A distribution with smoothing alone, for small values of SMUL the results displayed particularly violent oscillations. For larger values of SMUL the oscillations were damped, but only at the expense of all spatial resolution. Unfolding of the 400 A distribution was

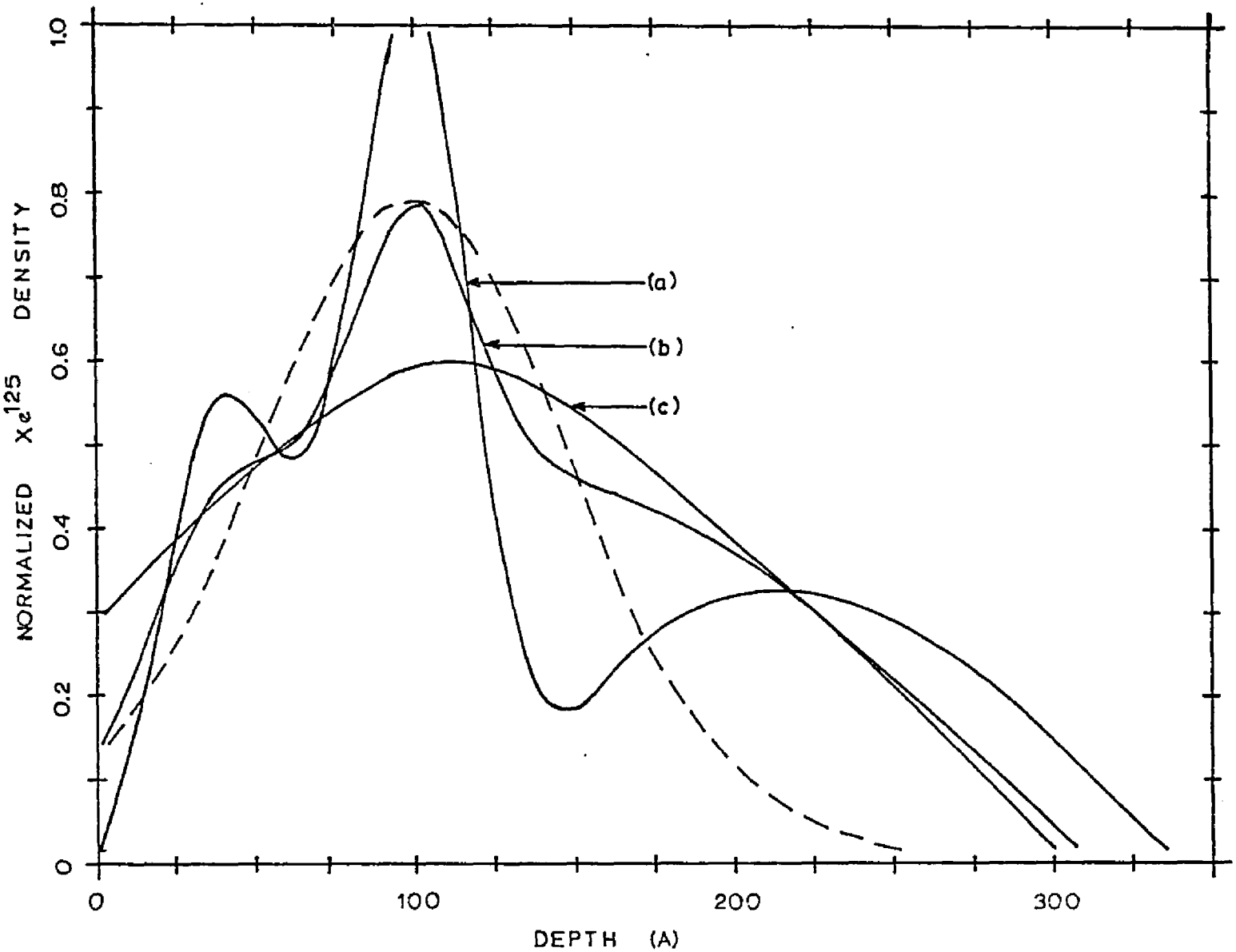

Figure 4-13. DACES2 Solutions for a Mean Depth of 100A. α=0.0125. (a)SMUL=0.1; (b)SMUL=0.2; (c)SMUL=0.5.

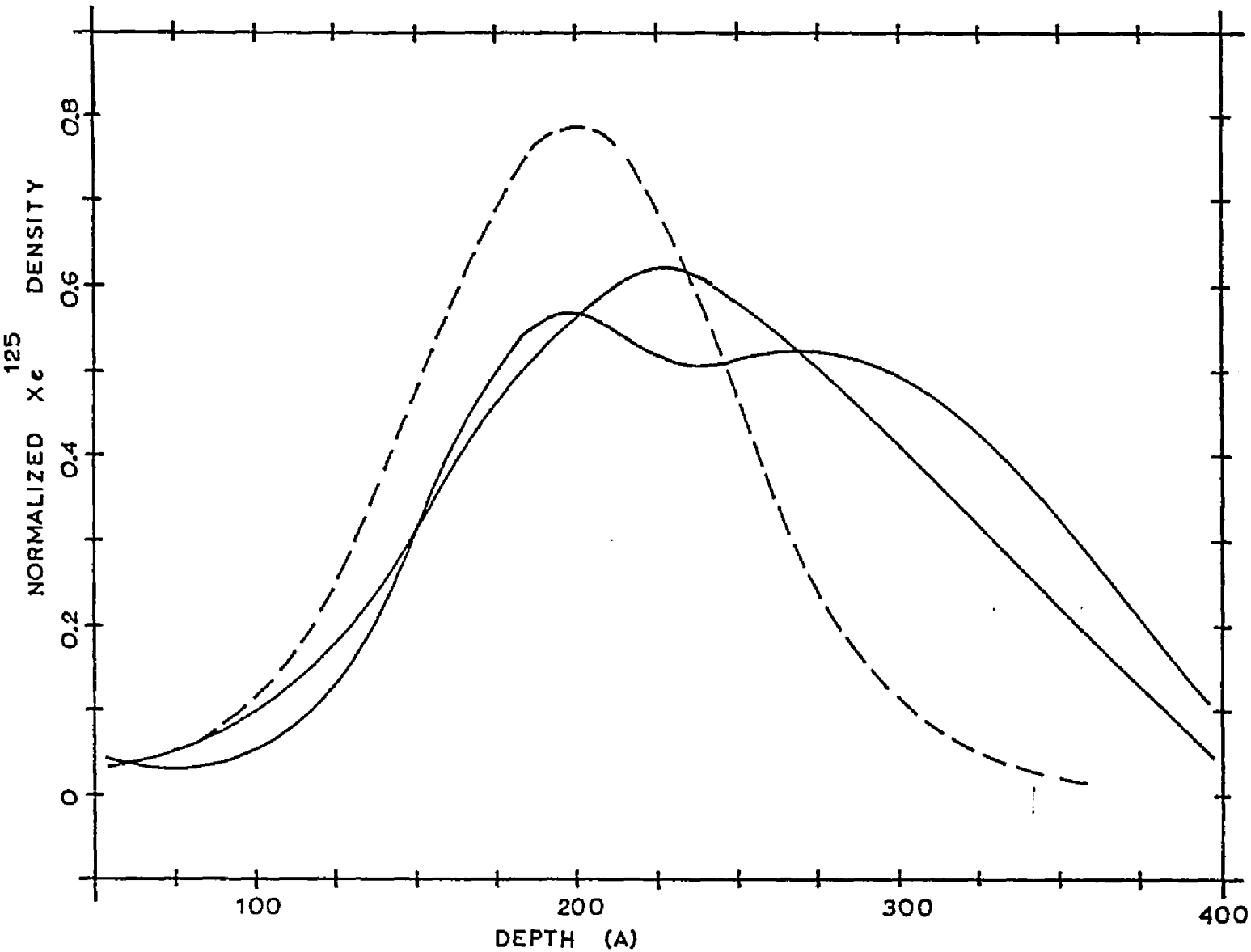

Figure 4-14. DACES2 Solutions for a Mean Depth of 200 A. α=0.0125.
(a) SMUL=0.05; (b) SMUL=0.10.

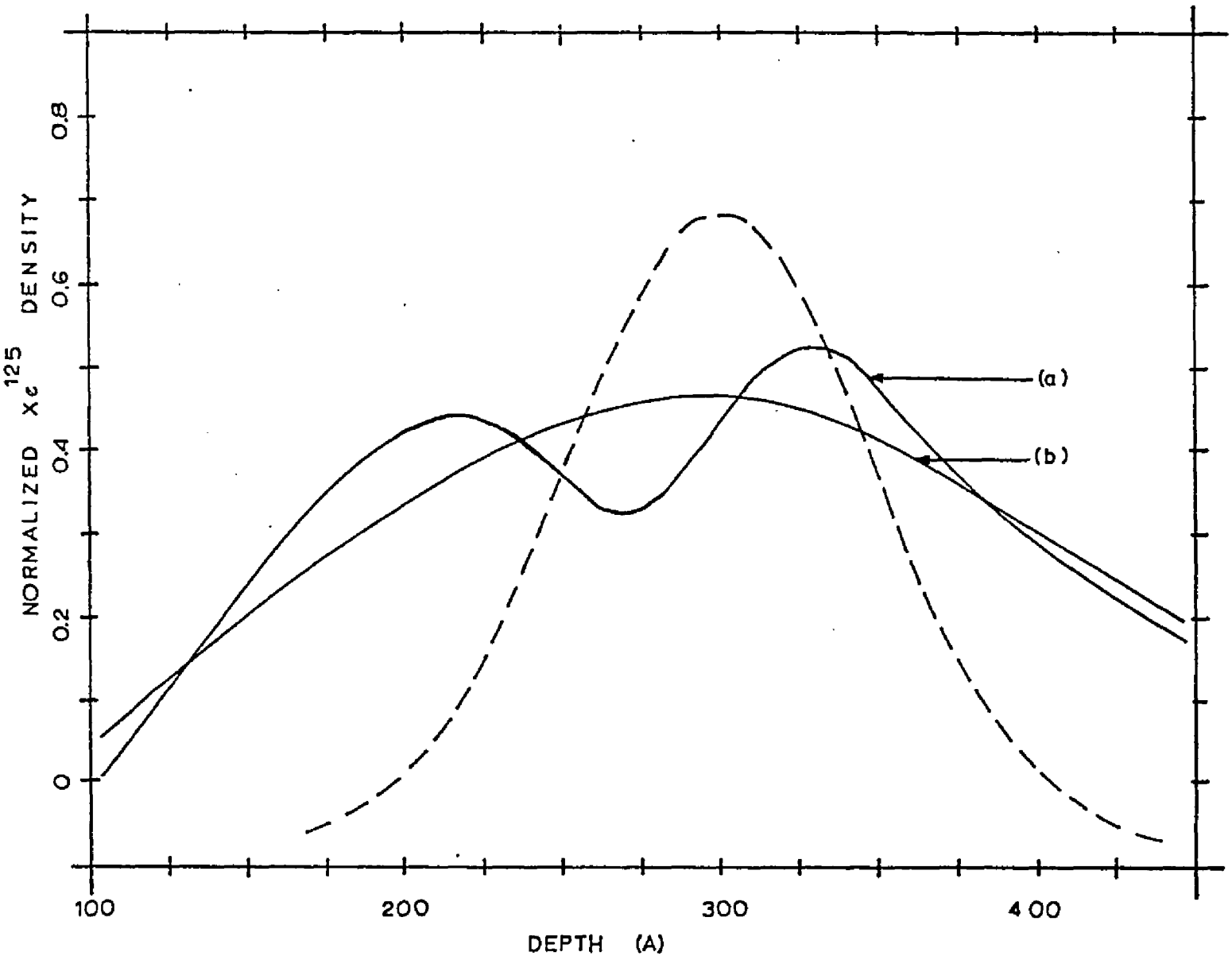

Figure 4-15. DACES2 Solutions for a Mean Depth of 300A. =0.0125. (a) SMUL=0.05; (b) SMUL=0.5.

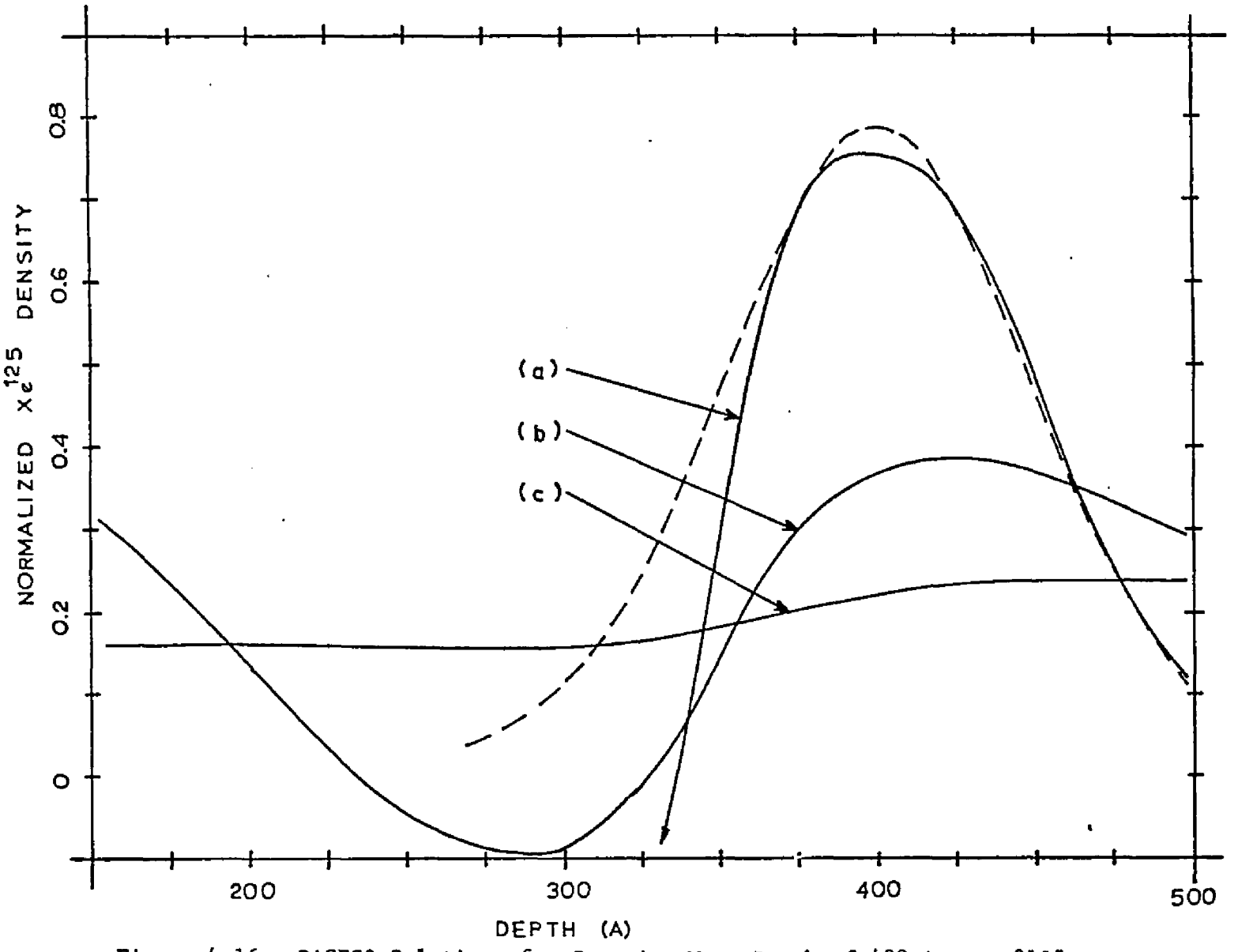

Figure 4-16. DACES2 Solutions for Gaussian Mean Depth of 400 A. =.0125.
(a) SMUL=0.1; (b) SMUL=0.2; (c) SMUL=0.5.

consequently designated a worst case, and further unfolding calculations were performed using various combinations of auxiliary information to obtain more reasonable results.

For the first set of trials auxiliary information was incorporated in the form of equality and inequality constraints. An examination of the generated conversion electron data indicated an obvious shift of the main spectrum peak to lower energies which suggested that the solution estimate should be a low-lying distribution. Consequently, it was assumed that S(0 A) = S(100 A) = 0.0. In addition, the slope of the distribution was assumed to vanish at the surface. This information was incorporated into DACES2 as equality constraints given by

$$D_j(z) = 0 \qquad z = 0.0,\ 1.0$$

$$D_j'(z) = 0 \qquad z = 0.0$$

The physical requirement that the solution estimate must be positive was specified in the form of inequality constraints as $D_j(z) \geq 0$ for z = 2.0, 3.0, 5.5. With these constraints the DACES2 routine was then cycled on small values of SMUL. The SMUL = 0.05 result is shown as curve (a) in Figure 4-17. Only one inequality constraint turned out to be limiting (non-negativity at 550 A). The violent oscillatory behavior was reduced with a marked increase in resolution. However, the result seemed to be oversmoothed, and became negative in the 500 A region. To eliminate these undersirable features the next trial employed equality constraints given by

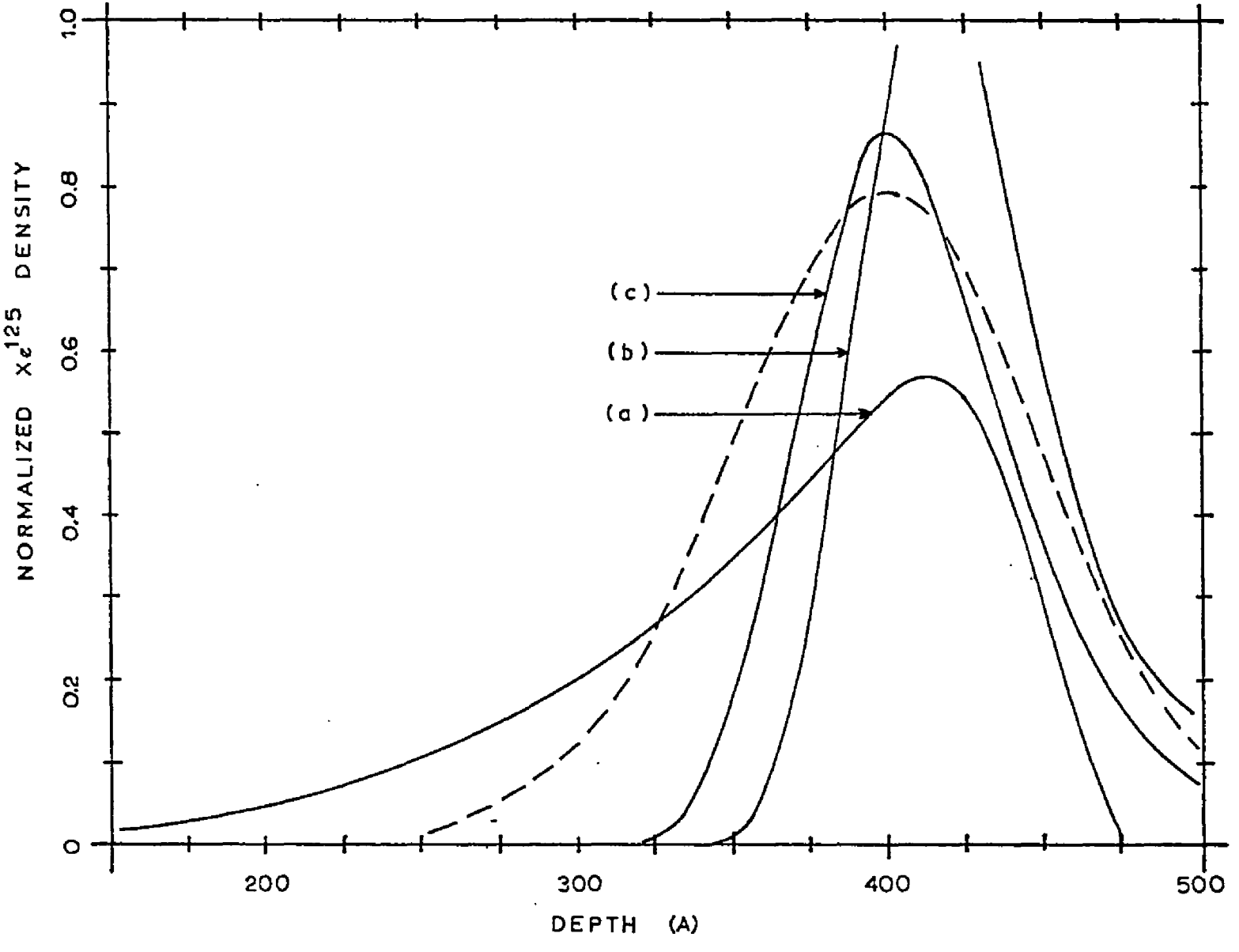

Figure 4-17 Iterative DACES2 Solutions z_o=400A. (a)First Iteration (b)Second Iteration (c) Third Iteration

$$D_j(z) = 0.0 \qquad z = 0.0,\ 1.0,\ 2.0,\ 2.5,\ 6.5$$
$$D_j'(z) = 0.0$$

with only two inequality constraints, given as $D_j(z) \geq 0$ for $z = 3.0,\ 5.0$. A typical result from this trial is shown as (b) in Figure 4-17. As expected the constraints clearly eliminated all non-negative and oscillatory behavior for the (0 A - 300 A) region. However, they also produced a somewhat unnatural peaking behavior and a shift in the peak of the distribution to approximately 420 A. These results persisted for values of SMUL greater than 1.0.

As a final trial the distribution (b) of Figure 4-17 was used to provide prior estimate data, and the various equality and inequality constraints were neglected. The best result is shown as (c) in Figure 4-17 for SMUL = 2.0 and PMUL = 0.4. With elimination of the constraints the peak of the distribution occurred at almost exactly 400 A. In light of the ill-posed nature of this unfolding problem due to the flatness of the kernel, this unfolding solution is an excellent result and indicates the appropriateness of the UNFOLD algorithm for solving ill-posed problems.

4.5 Conclusions Regarding the DACES2 Routine

As a result of the numerical experiments performed with the DACES2 code, several general comments can be made. The flatness of the kernel implies that the problem of unfolding depth distributions from conversion electron spectra is very ill-posed, especially for

low-lying distributions. Consequently, straight-forward solution techniques, such as matrix inversion or simple least-squares methods, are doomed to failure because of experimental errors in the spectral data. To circumvent these problems, the UNFOLD algorithm seeks appropriate solution estimates by incorporating any auxiliary information that may be available. Such auxiliary information can be incorporated in the form of an initial estimate of the unknown, smoothing constraints, and/or equality and inequality constraints. In this chapter a number of methods were studied using such auxiliary information, and good results to very difficult problems have been obtained. Based on the present study, the following general rules are inferred as the most appropriate solution technique for unfolding source distributions:

(1) For beginning calculations the unfold functional with smoothing alone cycled on values of SMUL are most useful.

(2) For accurate conversion electron spectra due to source distributions lying relatively close to the surface, smoothing alone may provide an adequate solution estimate.

(3) For lower-lying source distributions, however, as the parameter SMUL is increased the general behavior of the solution estimate changes rapidly from being undersmoothed and oscillatory to become oversmoothed with negligible spatial resolution. In such cases it is helpful to include auxiliary information in the form of equality and inequality constraints. For example, by comparing the spectrum to be unfolded with spectra due to source distributions of

known depths it is usually possible to determine the general depth range of the unknown.

(4) By constraining the unknown to be zero at depths far removed from the expected range of the unknown and by employing non-negativity in the form of inequality constraints, the DACES2 result will generally indicate the basic features of the unknown, although the result will usually be somewhat distorted.

(5) The distortions can be minimized, however, if another iteration using the distorted result as an initial estimate is performed. For this latter calculation, the equality and inequality constraints may be neglected. The best estimates are usually obtained for small values of PMUL and large values of SMUL.

Qualitatively, the initial estimate serves to limit the class of all feasible solutions to those solutions which are physically appropriate in some sense, i.e., the distributions occur in the correct region. The smoothing constraint further restricts the class of physically appropriate solutions to the solution estimates which are smooth and undistorted.

5.0 APPLICATION OF THE ELTRAS AND DACES2 CODES TO THE CASE OF CO57 IN AN IRON SPECIMEN

5.1 Introduction

Because of the technological importance of iron and iron alloys and compounds, and the favorability for observing the Mossbauer effect in Fe^{57}, the possibility for obtaining spatially resolved Mossbauer spectra in iron-containing materials is considered in this chapter. The Co^{57}-iron system is examined and values of the various parameters employed in ELTRAS are determined. ELTRAS is then used to compute conversion electron spectra due to Co^{57} in iron as a function of depth into the specimen. These spectra are used to construct the transport kernel $W(E,z)$ for the Co^{57}-iron system. Simulated Co^{57} spectra due to arbitrary source distributions are generated using the ELTRAS kernel, and the feasibility of unfolding these source distributions from the conversion electron spectra is investigated using the computer code DACES2. As there are no applicable experimental results available, to the author's knowledge, the results of this chapter are necessarily predictive.

The important feature of the system chosen for this study (a 7.3 KeV conversion electron source distributed in a uniform metallic iron lattice) are its simplicity, and ease of preparation and handling for experimental use. For example, such sources

could be prepared by bombarding a metallic iron sample (Armco iron) with energetic Co^{57} ions. An alternative method of preparation would be to electroplate or vacuum deposit a thin layer of Co^{57} onto a metallic iron substrate, and then cover the Co^{57} layer with various thicknesses of sublimed iron. By using Co^{57} the availability of a Mossbauer spectrometer would not be required for the initial phases of an experimental program. On the other hand, if a Mossbauer spectrometer complete with a source capable of exciting the 14.4 KeV Fe^{57} level is available, it would probably be advantageous to directly employ Fe^{57} rather than Co^{57}, thereby avoiding the handling problems associated with radioactive materials. The major experimental problem associated with this system would be the rapid surface oxidation of the metallic Fe samples. While such oxidation would be of major interest at later stages, it is undesirable in the initial calibration phase of such a study, and methods designed to minimize the surface oxidation using vacuum techniques should be employed whenever possible.

5.2 The Electron Transport Kernel W(E,z) for Metallic Iron

In Chapter 3, the most satisfactory theoretical method of computing $W(E,z)$ for the case of Ta_2O_5 was found to be the Monte Carlo code ELTRAS. Since the author was unable to find any Fe^{57} conversion electron spectra obtained for various depth distributions reported in the literature, ELTRAS was used to provide theoretical conversion electron spectra from which $W(E,z)$ could be constructed.

Iron has on outer electronic configuration of $3d^6 4s^2$ and it is a member of the first transition metal series. If all the 3d and 4s electrons are considered as being "free," the theoretical plasma loss energy is 32.6 eV for metallic iron. Investigations of the characteristic electron energy loss spectra of iron have been performed by Marton and Leder (62), Watanabe (63), and Robins and Swan (64). The more complete results of Robins and Swan indicate small characteristic losses at 5.3, 8.0, 15.8, and 56.6 eV, and an intense loss at 23.0 eV. Because of its prominence, this latter loss was previously considered to be the plasma loss. However, comparison with X-ray absorption data (65) indicates this loss is probably due to a strong interband transition. Based on a general consideration of losses in the first transition series, Robins and Swan identify the 15.8 eV loss as the plasma loss, the 8.0 eV loss as a lowered plasma loss (for a theoretical treatment of the lowered plasma loss consult reference (66)) and the 5.3 and 56.3 eV losses as ionization losses.

Interband electron transitions in conductors and semiconductors from the valence of a more tightly bound band to a free state in the valence or conduction band can be induced by photon absorption or electron bombardment. While transitions to the Fermi level usually dominate in conductors, transitions to other higher lying bands are also possible.

In photoabsorption, the induced interband transitions appear as fluctuations in the relative reflectivity and transmissivity of

the material. From such optical measurements the complex dielectric constant can be determined. In electron energy loss measurements, the occurrence of such transitions appears as peak structure in the scattered electron energy loss spectrum. The loss structure can be directly correlated with the $-\mathrm{Im}(1/\epsilon)$ function which can be calculated from the optical measurements.

Assuming that an interband transition occurs from a state g in the band a to a state f in band b, the energy of such a transition will be $\hbar\omega(a_g,b_f) = E(a_g) - E(b_f)$, where the E's are the energies of the states a_g and b_f as indicated. Such a resonance transition adds in effect a negative term to the expression for the dielectric constant (67), as given by

$$\begin{aligned} \epsilon(\omega) &= 1 - \frac{\omega_p^2}{\omega}(\omega + i/\tau)^{-1} + \delta\epsilon^{(b)}(\omega) \\ &= \epsilon^{f}(\omega) + \delta\epsilon^{(b)}(\omega) \\ &= \epsilon_1(\omega) + i\,\epsilon_2(\omega) \end{aligned} \tag{5-1}$$

where $\epsilon^{(f)}(\omega)$ is the contribution due to excitation of the free electron plasma. The term $\delta\epsilon^{(b)}(\omega)$ is the contribution to the dielectric constant due to induced transitions of bound electrons. The last expression in Equation (5-1) is given in terms of the dielectric constant as obtainable from optical measurements. $\delta\epsilon^{(b)}(\omega)$ consists essentially of the sum over the individual states g and f in the bands themselves and can be represented in general by

$$\delta\epsilon^{(b)}(\omega) = \frac{-e^2}{m\pi^2} \int \sum_{a,b} f_a(g) \times \frac{f^{\mu}_{a,b}}{(\omega + i/\tau_{ab})^2 - \omega^2_{a,b}} dg \qquad (5\text{-}2)$$

where $f_a(g)$ denotes the Fermi distribution function for the state g in the band a . $f^{\mu}_{a,b}$ is the oscillator strength and $\tau_{a,b}$ is the interband relaxation time. The amplitude of the function $\delta\epsilon^{(b)}(\omega)$ is proportional to the oscillator strength $f^{\mu}_{a,b}$, which in turn is roughly equal to the electron density in the valence band. Transitions from filled s- and p- bands are therefore expected to contribute more weakly than those from unfilled bands.

The exact origin of the intense 23.0 eV interband transition in iron has not been precisely determined, but such information is not required to proceed with the ELTRAS computation. The strengths of the ionization and plasma losses are also not precisely known; they are, however, small in comparison with the interband transition loss. Consequently, for the case of metallic iron, the function $-\mathrm{Im}(1/\epsilon)$ was assumed to consist of a single Lorentzian resonance representing the interband transition. The mean energy of the loss peak and the loss width were specified as 23.0 eV and 20 eV respectively, in agreement with the results of Robins and Swan.

Since the probability for inelastic scattering (Equation (A-33) was derived for a generalized energy loss based on a dielectric treatment of the scattering material, the angular dependent scattering cross section and the angular probability distribution function for interband transitions are identical to the expressions

for the plasmon losses, Equations (A-31) and (A-34). However, the parameter $\theta_E = \frac{\Delta E}{2E_o}$ is now defined in terms of the interband transition energy loss ΔE, rather than the plasma loss $\Delta E = \hbar\omega_p$.

The total inelastic and elastic cross sections for iron, as calculated from Equations (B-8) and (B-4) for 7.3 KeV electrons, are 1.32×10^{-6} cm^{-1} and 4.57×10^{5} cm^{-1} respectively. As in the case of Ta_2O_5, the cross section for the primary loss mechanism was computed according to $\gamma\Sigma_i$. For this study the value of the parameter γ was arbitrarily specified as 0.8. While this value gave good agreement with experiment in the case of Ta_2O_5, such agreement cannot reasonably be expected for the case of iron. Nevertheless, $\gamma = 0.8$ guarantees that most of the inelastic losses in the analog simulation will be due to the primary interband mechanism. Consequently, the behavior of the resulting ELTRAS spectra is expected to be representative of the true behavior.

The simulated electron transport was carried out using the prejudiced source and forced first collision routines. A total of 20,000 particles were introduced in each case. Approximately one-half of the source electrons were born with initial direction cosines in the range $-1 \le w \le \bar{w} = -0.8$, with the weight of each particle equal to 0.2. On the other hand, the weight of each particle for which $-0.8 \le w \le 1$ was specified as 1.8. Collisions were forced for particles with direction cosines in the range $-1 \le w \le -0.5$, which had suffered fewer than six collisions, the collision cut-off serving as an effective low weight cut-off. In

addition, the history of a particle was terminated if it suffered energy losses totaling more than 250 KeV, or if it reached a depth of more than 1000 A. The spectrometer acceptance angle was specified as 0.1 radian.

The result of the analog simulation represents an approximation of the function $W(E_o \longrightarrow E,z)$. To obtain the observed conversion electron spectrum, $W(E' \longrightarrow E,z) \simeq W(E_o \longrightarrow E,z)$ must first be integrated over the Lorentzian energy distribution of Fe^{57} conversion electrons to obtain the source-weighted spectrum according to $\int_E^\infty W(E' \longrightarrow E,z)\ J_c(E')\ dE'$. The observed spectrum is then computed by folding the source-weighted spectrum with the spectrometer window function as $\int_{-\infty}^{\infty} X(E,E')dE' \int_{E'}^{\infty} W(E'' \longrightarrow E',z)\ J_c(E'')dE''$. According to Compton and Allison (68) the natural width of the 7.3 KeV conversion line, $J_c(E')$, is approximately 3.5 eV. The spectrometer window function was assumed to be Gaussian with a standard deviation of 0.625 eV, corresponding to a commercially available spherical electrostatic beta spectrometer with 0.02% energy resolution (69).

Using this information ELTRAS was employed to compute the observed conversion electron spectra due to hypothetical source depth distributions $S_i(z) = \delta(z - z_i)$, for depth z_i ranging from 20 A to 380 A, distributed at 40 A intervals. Selected spectra are displayed in Figure 5-1. They have not been normalized in any manner. Each spectrum thus represents the probability that an electron born at the specified depth will emerge from the surface

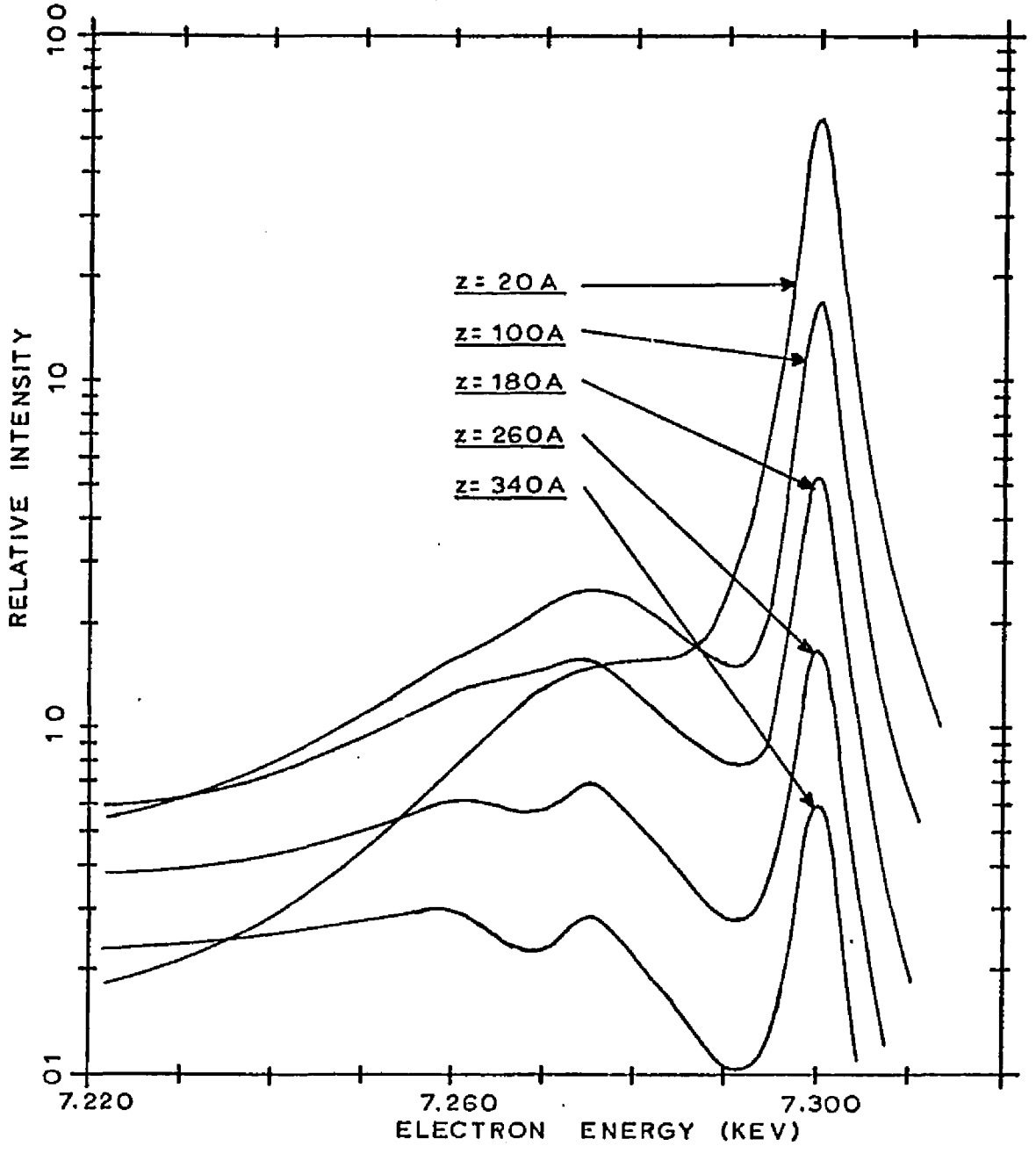

Figure 5-1. ELTRAS Final Spectra for Various Depths in Fe Metal. E_o = 7.3 KeV.

into the acceptance angle of the spectrometer with energy E. The experimental analog would be spectra obtained from samples containing the same initial number of radioactive Co^{57} atoms after counting each sample for the same specified time.

For the case of 21.79 KeV Xe^{125} conversion electrons in Ta_2O_5 the natural width of the conversion line was relatively wide (13 eV) owing to the natural width of the atomic level in which the conversion took place. In addition, the instrumental resolution contributed strongly to the spectral line width. For a momentum resolution of 0.08% the spectrometer contribution to the line width was 36 eV. As the depth of the source distribution was increased, the resulting spectral line became very much broader and shifted to lower energies because of the characteristic energy loss structure on the lower side of the natural peak.

For the case of 7.3 KeV Fe^{57} conversion electrons, however, the initial electron distribution is much sharper (3.5 eV). Also, the spectrometer contribution to the line width at 7.3 KeV for .02% energy resolution is only 1.5 eV. It is consequently possible to distinguish between the nonloss peak and the loss structure. The line peak position does not become altered nor does the peak become broader as the depth of the Fe^{57} source distribution increases. However, a change in the relative intensities of the natural peak and the loss structure is readily apparent.

The kernel $W(E,z)$ for iron was constructed in the same manner as the kernel for tantalum oxide. From each spectrum

corresponding to a depth z_i , data points were evaluated at various energies E_k , thereby forming a set of vectors $\vec{W}_k = \left| W_{ki} \right|$ $= \left| W(E_k,z) \ , \ W(E_k,z_2) \ ,\ldots, \ W(E_k,z_{10}) \right|$.

It was assumed that the kernel could be adequately represented by an expansion in terms of a set of linearly independent four-joint cubic splines as $W(E_k,z) = \sum_{j=1}^{8} C_j(E_k) \ D_j(z)$. The four spline joints were placed at 40 A, 100 A, 180 A, and 300 A, respectively. The C_j were evaluated as the expansion coefficients which minimized the functional Z_k given by

$$Z_k = \sum_{i=1}^{10} \frac{1}{ERP_i}^2 \left\{ \sum_{j=1}^{8} C_j(E_k) \ D_j(z_i) - W_{ki} \right\}^2 \qquad (5\text{-}3)$$

$$+ \ SMUL \int_A^B \frac{dz}{ERS^2} \left\{ \sum_{j=1}^{8} C_j \frac{\partial^2 D_j(z)}{\partial t^2} \right\}^2$$

The first term of this equation represents a least squares functional, and the second term represents a smoothing functional as previously discussed for Equation (3-26). For $ERP_i = 0.05 \ P_i$, ERS = 15.0 , and SMUL = 2.0 , the spline coefficients obtained in this fashion are presented in Table 5-1. Graphs of the kernel computed from these coefficients are displayed in Figure 5-2.

5.3 The Determination of Depth Distributions from Fe^{57} Conversion Electron Spectra

While the transport kernel $W(E,z)$ of Section 5.2 is not expected to be totally correct, its main features are expected to be representative of the correct behavior. In this section, the

TABLE 5-1

Spline Function Coefficients for the Kernel of Co^{57} in Metallic Iron. Conversion Electron Spectra Generated by ELTRAS. Spline Joints Placed at 40 A, 100 A, 180 A, and 300 A.

Energy	C_1	C_2	C_3	C_4
7.310	.12954 E01	.23129 E01	-.11512 E01	.63471 E-1
7.305	.83578 E01	-.76044 E01	-.16425 E01	.42790 E01
7.302	.33099 E02	-.28940 E02	-.48849 E01	.12905 E02
7.300	.57903 E02	-.46978 E02	-.45720 E01	.12471 E02
7.298	.33926 E02	-.30157 E02	-.58516 E01	.15266 E02
7.295	.82432 E01	-.65171 E01	.67566 E01	-.90446 E01
7.290	.22895 E01	.32179 E00	-.60935 E00	-.93723 E00
7.285	.12868 E01	.12409 E01	.28496 E01	-.50236 E01
7.280	.96958 E00	.24546 E01	.42367 E01	-.76543 E01
7.275	.86866 E00	.29792 E01	.17454 E01	-.42863 E01
7.270	.7003 E00	.2928 E01	.20441 E01	-.47295 E01
7.260	.35531 E00	.17195 E01	.32869 E01	-.51390 E01
7.240	.11605 E-1	.12797 E01	.64357 E00	-.16621 E01
7.200	.12460 E00	-.41830 E00	.31201 E01	-.32214 E01

TABLE 5-1
(Cont.)

Energy	C_5	C_6	C_7	C_8
7.310	.88136 E00	-.11276 E01	.13196 E00	.70103 E-1
7.305	-.49476 E01	-.46338 E-2	.49209 E00	.26420 E00
7.302	-.13122 E02	-.30103 E01	.26219 E01	.62028 E00
7.300	-.73344 E01	-.11450 E02	.52149 E01	.11554 E01
7.298	-.16720 E02	-.15873 E01	.24206 E01	.62934 E00
7.295	.14207 E02	-.73435 E01	.22848 E01	-.33718 E00
7.290	.21714 E01	-.13169 E01	.42742 E-1	-.68404 E-2
7.285	.66064 E01	-.12843 E01	-.35779 E00	-.96254 E-2
7.280	.10118 E02	-.20707 E01	-.43597 E00	-.13189 E00
7.275	.54182 E01	-.41511 E00	-.72585 E00	-.81979 E-1
7.270	.60368 E01	-.56121 E00	-.82930 E00	.55388 E-1
7.260	.64472 E01	-.11475 E01	-.20015 E-1	-.36207 E00
7.240	.22918 E01	-.60797 E00	.82621 E-1	-.37801 E00
7.200	.37496 E01	-.81236 E00	.50133 E00	-.44360 E00

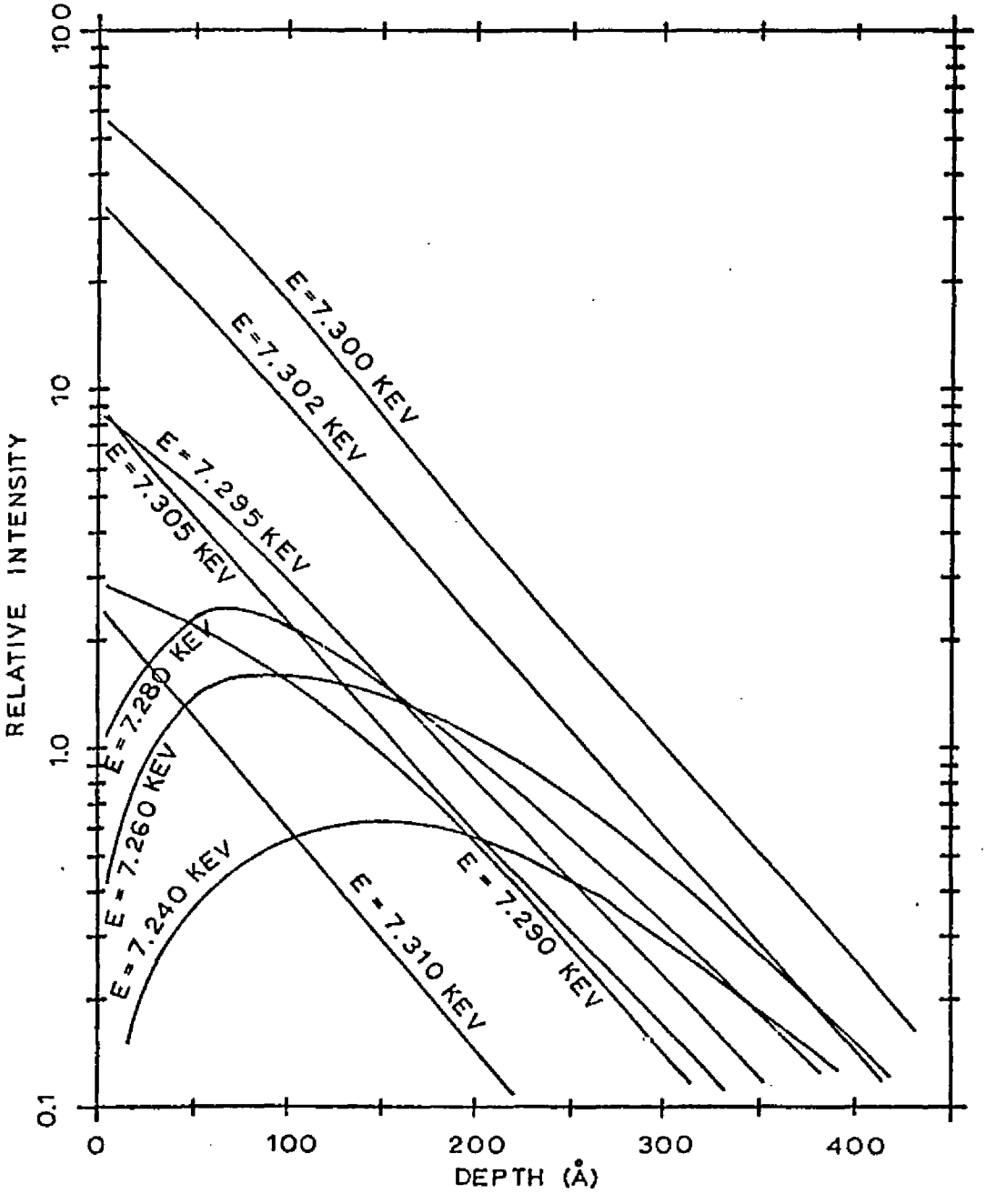

Figure 5-2. ELTRAS Kernel for Co^{57} (E_o = 7.3 KeV) in Metallic Iron.

correctness of $W(E,z)$ is assumed, and the possibility for unfolding the depth distribution of Fe^{57} nuclei (and, hence, for obtaining spatially resolved Mossbauer spectra) from the 7.3 KeV Fe^{57} conversion electron spectrum is examined using the DACES2 code discussed in Chapter 4.

Simulated conversion electron spectra for use in subsequent numerical unfolding experiments were generated according to $N(E_k) = \hat{N}(E_k) \left\{ 1 + \frac{\alpha \, ERR_k}{\sqrt{N}} \right\}$, where $\hat{N}(E_k)$ was computed according to $\hat{N}(E_k) = \sum_{j=1}^{8} C_j(E_k) \int_0^{\infty} D_j(z) \, S(z) \, dz$. The parameter ERR_k is a random number generated in the range (-1,1), and is used to simulate the presence of statistical errors in experimentally obtained conversion electron spectra. The source distributions used to compute the $N(E_k)$ were normalized Gaussian distributions whose mean depths were varied from 20 A to 380 A at 40 A intervals. The standard deviation was specified as 30 A for each distribution. Such Gaussian sources could be approximated experimentally, for example, with source preparation by ion bombardment, or by vacuum deposition and temperature-controlled diffusion. From the magnitude range of $N(E_k)$ computed in the integration, a value of the parameter α equal to 0.035 can produce errors in the simulated spectra ranging from 0.5% to 15%.

Using these spectra as the input information a number of unfolding trials using DACES2 have been carried out following the procedures developed in Chapter 4. For the initial trials, solutions

were obtained by minimizing only the unfold and smoothing functionals for values of the smoothing parameter ranging from 0.1 to 2.0. The parameter ERS, the estimated maximum value of the second derivative of the solution, was specified as 2.4. The results of these trials for various source depths are displayed in Figures 5-3 and 5-4. For the distributions lying relatively close to the surface (mean depths less than 250 A) the imposition of smoothing alone provides very good solutions. In fact, the unfolding results for this case appear to be much better in general than similar results obtained with the Ta_2O_5 kernel. Such a conclusion was expected, however, since the 7.3 KeV electrons interact more strongly with matter than the 21.79 KeV conversion electrons of Xe^{125}. In addition, at the lower energy fine structure in the conversion electron spectrum does not become hidden due to the finite resolution of the spectrometer.

As the mean depth of the source distribution is increased beyond 250 A, however, smoothing alone is not sufficient to produce an accurate solution. For small values of the parameter SMUL the solutions are oscillatory and ambiguous; however, as SMUL is increased, the solution rapidly becomes over-smoothed (refer to curve (d) of Figure 5-3). In an attempt to overcome this difficulty equality constraints were imposed in addition to smoothing. In particular, the DACES2 solution was constrained to be zero for depths less than 100 A, and greater than 450 A. In addition, an inequality constraint required the solution to be non-negative at

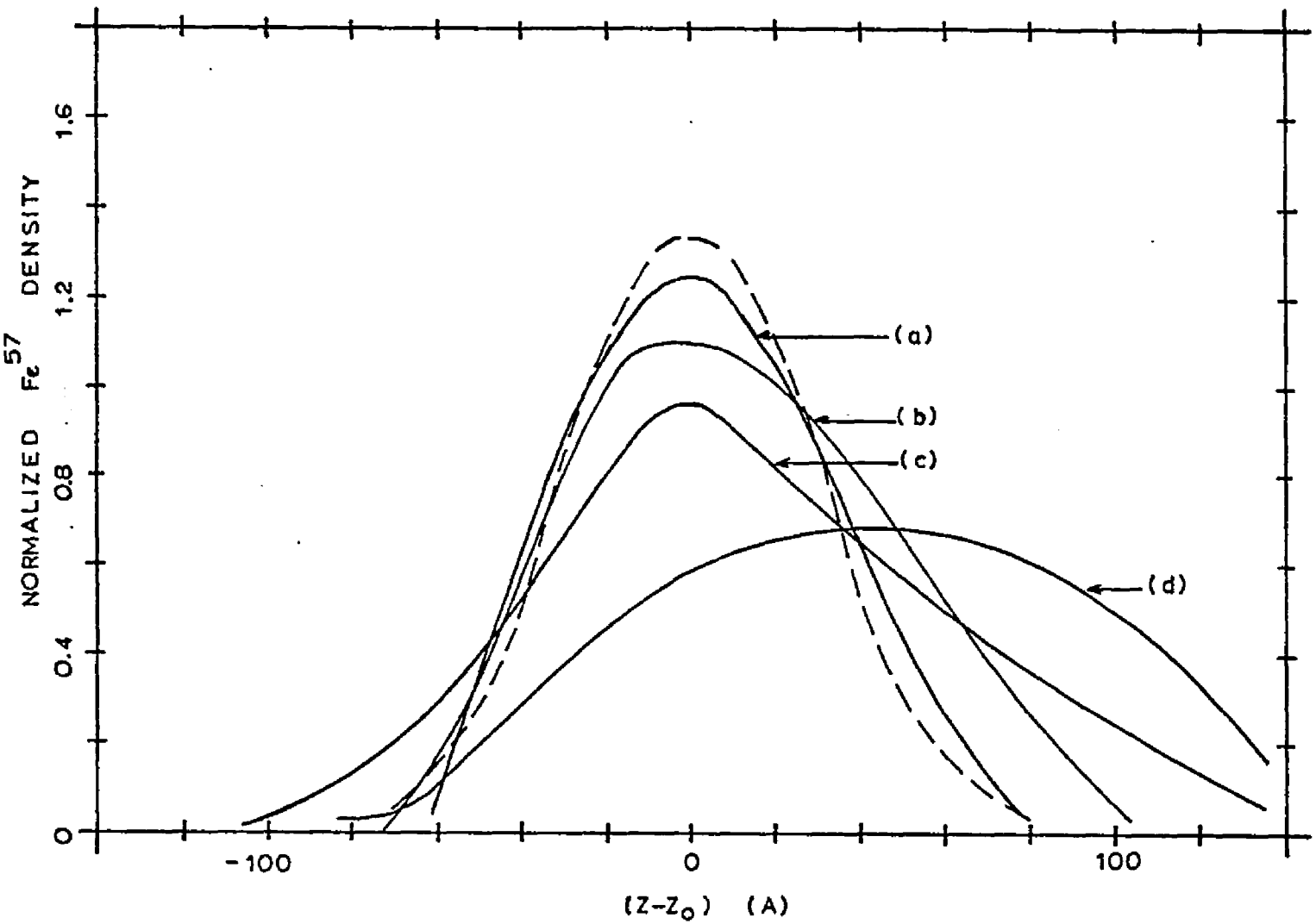

Figure 5-3. DACES2 Solutions for Co^{57} in Metallic Iron at Various Depths. (a) z_o = 60 A, SMUL = 0.6; (b) z_o = 140 A, SMUL = 0.6; (c) z_o = 220 A, SMUL = 0.4; (d) z_o = 300 A, SMUL = 1.0.

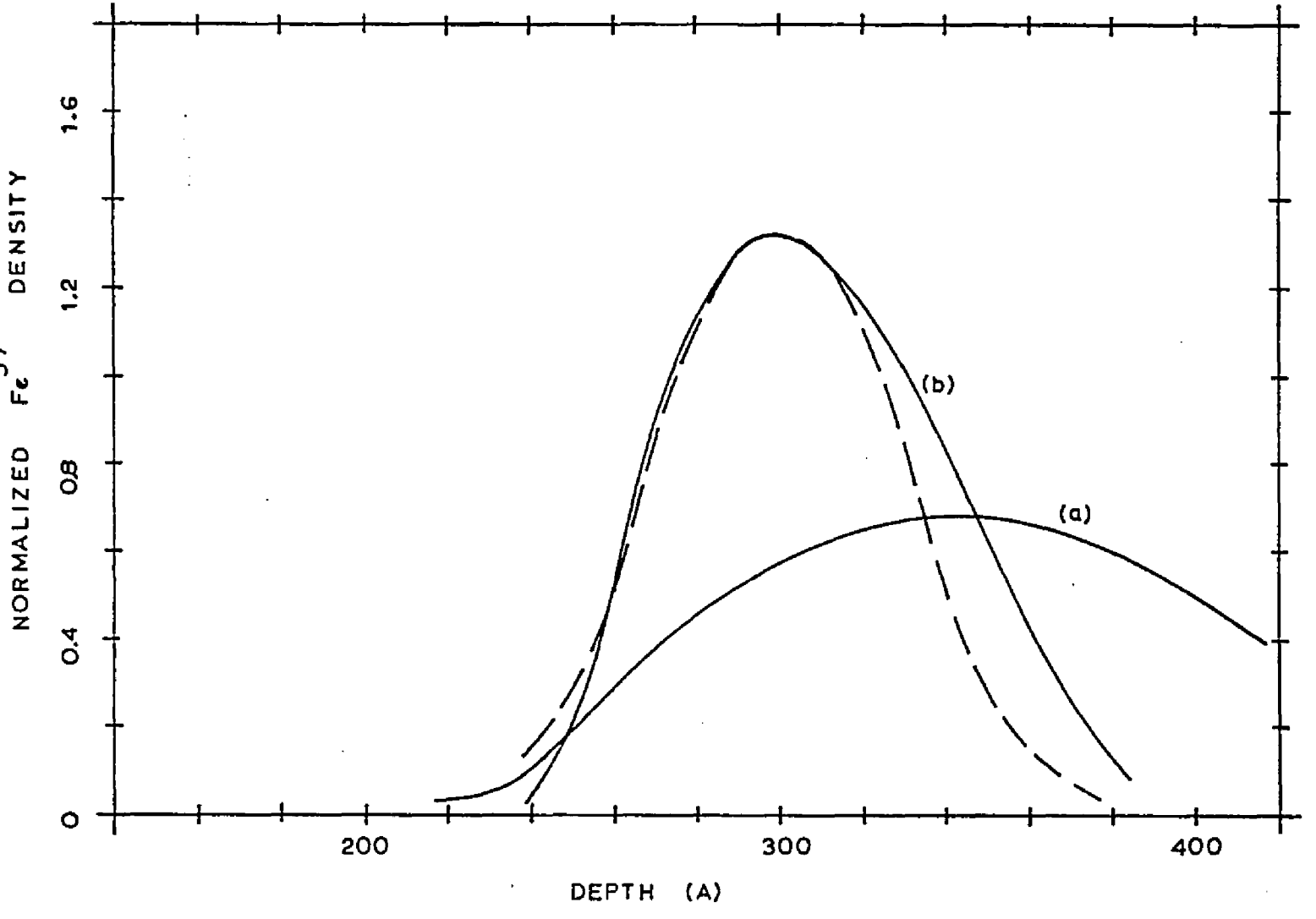

Figure 5-4. DACES2 Solutions for a Mean Depth of 300 A. (a) SMUL = 1.0; (b) SMUL = 1.0 Plus Five Inequality Constraints.

200 A. The result is illustrated as graph (b) of Figure 5-4 and is in excellent agreement with the "known" solution.

The material of this chapter has illustrated how the computer codes ELTRAS and DACES2 can be used to investigate the feasibility of spatially resolved Mossbauer spectroscopy for a practical case of interest. The results of this study seem to indicate that it is possible to do spatially resolved Mossbauer spectroscopy with the 7.3 KeV conversion electron of Co^{57} (Fe^{57}).

6.0 DISCUSSION OF RESULTS AND APPLICATIONS

6.1 Discussion

Although much theoretical and experimental research has been performed concerning the high-temperature oxidation of iron and iron-based alloys, a satisfactory explanation of the growth of transient oxide phases on the base metal or alloy is not yet available. An understanding of the kinetics of oxide nucleation and oxide growth and the processes which ultimately lead to loss of oxide protection would greatly aid in the development of more reliable high-temperature alloys. Of particular importance are pre-parabolic oxidation rate constants, alloy inter-diffusion coefficients, oxygen solubilities and diffusivities in metals and alloys, and transport properties in doped alloy oxides, which largely determine the spatial distribution and size of initial phases in the oxide scale.

In this thesis a new method which utilizes the techniques of both Mossbauer spectroscopy and β-spectroscopy for obtaining spatial information concerning the various chemical phases is proposed and analyzed. The method is descriptively referred to as spatially resolved Mossbauer spectroscopy.

The position, shape, and intensity of Mossbauer resonances are intimately related to the chemical environment in which the

resonant nucleus is embedded. Hence, the identity of a particular chemical phase can be established by reference to its Mossbauer spectrum. While a corroding iron specimen is likely to contain many chemical phases, by Doppler shifting the 14.4 KeV photon source line to lie in resonance with an absorption line characteristic of a particular phase, only Fe^{57} nuclei in that phase will absorb source photons, and thus de-excite by emitting 7.3 KeV conversion electrons. Since conversion electron energy spectra observed at the surface of the specimen are known to vary with conversion electron emission depths because of electron energy loss collisions, it is possible, in principle, to determine the depth of the particular chemical phase by examining the shape of the conversion electron spectrum. In summary, to measure the depth distribution of a particular chemical phase in a corroding iron specimen, for example, the phase is selected by adjusting the Mossbauer source velocity. The energy spectrum of the conversion electron current is then analyzed to determine the depth of the particular phase.

The general framework for spatially resolved Mossbauer spectroscopy was established in Chapter 2. The fundamental equation was shown to be a Fredholm integral equation of the first kind relating the conversion electron spectrum $N(E)$ to the depth distribution of conversion electron sources, $S(z)$ by means of an electron transport kernel, $W(E,z)$, as given by

$$N(E) = \int W(E,z)\ S(z)\ dz \qquad (6\text{-}1)$$

In addition the relationship between the conversion electron source distribution and the distribution of Mossbauer resonant nuclei was established by taking into account the attenuation of Mossbauer source photons due to both conventional interactions (photoelectric and Compton effects) and Mossbauer interactions. Finally, a general equation was written for the response function $W(E,z)$ which explicitly included the three principle factors which determine the conversion electron energy spectrum as measured by an electron spectrometer: the natural line shape, the spectrometer window curve, and electron collision and slowing down processes.

The accuracy with which the integral equation describes the physical problem depends critically upon the kernel $W(E,z)$. In addition the shape of the kernel function largely determines the ease with which source distributions can be unfolded from conversion electron spectra. For these reasons much effort has been expended in characterizing the response function. Chapter 3 presents computations of the response function obtained according to three methods: an age diffusion calculation, unfolding from experimental data, and a Monte Carlo calculation.

The Fermi age diffusion approach of Bethe, et al., was used as a first approximation because it represented the simplest applicable electron transport approach based upon the Boltzmann transport equation. There is little doubt that this simple model gives

better than an order-of-magnitude estimate of the conversion electron spectrum in the broad sense (i.e., spectra calculated over the broad energy range $\frac{1}{2}E_o \leq E \leq E_o$, where E_o is the emission energy). However, the results of the age diffusion approach indicate that the current due to electrons that have suffered many energy loss collisions will be of extremely small intensity and carry very little spatial information. In addition, spectral complexities associated with Auger electrons and photoelectrons ejected by X-rays emitted as the Fe^{57} atomic configuration returns to the ground state further indicate the necessity for restricting the energy range to lie relatively close to the conversion electron emission energy. In this event the applicability of the age diffusion approach must be reexamined because the Bethe theory assumes the validity of continuous slowing down. Consequently the initial transient stage of the penetration in which the conversion electrons move directly away from the source and undergo discrete energy loss collisions is given incorrectly.

To provide a comparison for assessing the validity of the age diffusion theory, experimental Xe^{125} conversion electron spectra and the associated source distributions generously provided by J. P. S. Pringle were used to numerically construct the response function $W(E,z)$ for tantalum oxide. In contrast to the ultimate objective of unfolding unknown conversion electron source distributions from conversion electron spectra given the transport kernel $W(E,z)$, the immediate objective was to unfold the kernel from the

conversion electron spectra due to known source distributions. Since the successful solution of all unfolding problems depends greatly upon the shape of the known function under the integral, the narrow Gaussian source distributions of Pringle distributed over the entire depth range of interest virtually guaranteed the success of obtaining an accurate representation of the kernel.

The unfolding was carried out with a computer code, DACES1, adapted especially for this type of problem from the more general code, UNFOLD, recently developed by Biggs and Amos. As a result of these computations an accurate analytical representation of the kernel in terms of four joint cubic spline functions was developed. When these DACES1 results were compared with the age diffusion theory, the latter exhibited noticeable shortcomings, the most obvious of which was an immediate shift of the spectrum peak to lower energies as the source depth increased. This behavior, in contrast to the more gradual shifting and rapid broadening observed experimentally, is explicitly due to the assumption of continuous energy loss, rather than discrete losses. The DACES1 results further indicate that it is simply not possible to categorize electrons which emerge from the surface with a certain energy as having a well-defined mean depth of origin. This conclusion implies the absolute necessity of developing an unfolding capability in order to infer spatial information from conversion electron spectra.

In view of the inadequacy of the Fermi age diffusion theory for calculating conversion electron spectra, a more sophisticated

theoretical calculation capable of providing better agreement with experiment was sought. Since the common feature of all electron transport calculations based upon the Boltzmann transport equation is the assumption of continuous slowing down for computational convenience, this type of approach was abandoned in favor of a Monte Carlo simulation devised to explicitly account for discrete energy loss collisions.

The computer code ELTRAS which was developed in this thesis to compute the kernel $W(E,z)$ performs three basic calculations, a Monte Carlo simulation, and two folding integrations. The Monte Carlo simulation determines the probability that an electron born at a depth z with emission energy E_o will emerge from the surface with direction cosine w and energy E. According to the values of these parameters the particle is assigned to a two-dimensional direction cosine, energy loss tally box. The second calculation uses a specified spectrometer acceptance angle, establishing the allowed direction cosines, to compute the energy spectrum for a strictly monoenergetic source at a depth z. Using this result, the source-weighted spectrum is then computed for a natural conversion electron line shape. Since the source-weighted spectrum is distorted by the spectrometer, the final calculation of ELTRAS folds the spectrometer window function with the source-weighted spectrum to yield the observed conversion electron line shape due to the hypothetical depth distribution $S(z') = \delta(z' - z)$.

Since the final two calculations are primarily integrations, the essence of the ELTRAS code is the Monte Carlo simulation, which has been divided into a set of well-defined routines. A source routine introduces each particle and assigns appropriate initial parameters. A particle then passes to the mean free path and transmission routine which calculates the point of collision. If there are no collisions, the particle emerges from the surface and is classified according to the final values of its parameters. If there is a collision, new particle parameters are determined in a probabilistic sense in the collision routine. If the new parameters do not exceed any parameter cut-off values the particle is returned to the mean free path and transmission routine. If the particle is cut off or it emerges from the surface, it is classified accordingly in the termination routine. The source routine then introduces another particle.

Before proceeding immediately to the calculation of the kernel $W(E,z)$, several preliminary tests were performed to ensure proper operation of the code and to gain insight as to the most efficient mode of calculation. As a result of this experience several conclusions became apparent. Statistical fluctuations in the loss spectra as computed via the Monte Carlo simulation are much reduced by a forced collision routine for particles directed toward the surface. In addition, such fluctuations are also reduced by directing more source particles of correspondingly smaller weight into the importance cone. The importance cone must be large

enough, however, to prevent particles of relatively large weight from scattering into the importance cone.

Although the plasmon interaction appears to be the most important inelastic energy loss mechanism for Ta_2O_5, electron-electron interactions, such as interband transitions and ionization processes, could not be completely ignored. Since these interactions result in generally higher energy losses, they were treated in an approximate manner as representing capture processes. Multiple plasmon loss peaks were difficult to distinguish even in the source-weighted spectra. When the source-weighted spectra were folded with the relatively broad instrumental window function, practically all multiple loss peak structure was lost.

The calculation of the kernel for Ta_2O_5 by ELTRAS was performed in the following manner. Conversion electron spectra were computed for delta function source distributions placed at 50 A intervals ranging from 50 A to 500 A. These spectra were then compared with the corresponding spectra as computed according to the experimental Pringle kernel. For source depths near the surface the peaks of the theoretical and experimental spectra agreed quite well. For large depths, however, the peaks of the theoretical spectra fell below the peaks of the experimental spectra, implying that the mean emission energy should be increased for better agreement. This shifting behavior, which is complete at approximately 200 A, is believed due to the averaging effect of the spectrometer window function on the zero-and single-loss peaks in

the conversion spectrum. The reason as to the absence of such shifts in the experimental spectra is not understood. A possible explanation is that the binding energy of the K shell electron varies according to depth, i.e., a surface effect may exist.

After shifting the mean emission energies so that the ELTRAS spectra closely coincided with the spectra calculated from the Pringle kernel, the theoretical kernel was constructed from the ELTRAS spectra by minimizing a least squares functional subject to smoothing constraints. The agreement between the experimental Pringle kernel and the kernel constructed from the ELTRAS code is quite good. The only major difficulty is that at lower energies in the spectrum, the theoretical kernel is too small. This discrepancy is believed to be due to an interband transition (s) or ionization processes with a corresponding energy loss in the range of 50-100 eV.

The development of the ELTRAS and the DACES1 codes provides methods for calculating the kernel based upon purely physical considerations in the case of ELTRAS, and for obtaining the kernel from available experimental data in the case of DACES1. This effort satisfies one major requirement for obtaining spatially resolved Mossbauer spectroscopy. The other principle requirement is to develop an efficient technique for unfolding the depth distribution of conversion electron sources from the conversion electron energy spectrum.

Two approaches are generally available for solving unfolding

problems. The first method would parameterize the conversion spectrum and the kernel, and a Laplace transform would be found to express the solution. In the early stages of this research such a method was developed for the age diffusion kernel. In view of the questionable validity of the age diffusion approach, however, this technique was abandoned in favor of the second method which replaces the integral equation with an appropriate set of simultaneous linear equations that can be solved by numerical techniques. The computer code developed for this purpose, also based upon the UNFOLD code, is termed DACES2.

To assess the feasibility of unfolding source distributions from conversion electron spectra, the experimental Pringle kernel for Ta_2O_5 was used to generate conversion electron spectra due to known source distributions. Errors were introduced into the spectra to simulate statistical variations. DACES2 was then used to unfold the source distributions from the conversion electron spectra. The results of these numerical experiments indicate that it is possible to obtain spatial information from conversion spectra even though the flatness of the kernel implies that the problem is extremely ill-posed, especially for deep sources ($\sim$ 500 A) and large statistical errors ($>$ 10%). DACES2 overcomes this ill-posed nature by incorporating any available auxiliary information, such as initial solution estimates, smoothing constraints, and/or equality and inequality constraints, into the solution technique.

In this study a number of methods for incorporating such auxiliary information were examined. Based on this work several conclusions were drawn as to the most appropriate solution techniques. For beginning calculations trials performed with various smoothing constraints usually indicate the magnitude of unfolding difficulties.

For accurate spectra due to distributions lying relatively close to the surface, smoothing alone will probably provide an adequate solution. As the magnitude of statistical errors in the spectra is increased and/or the distributions become deeper, however, the general behavior of the solution estimate changes rapidly from being undersmoothed to become oversmoothed with negligible spatial resolution as smoothing constraints are increased. In these instances it is necessary to include additional auxiliary information in the form of equality and inequality constraints. By constraining the unknown to be zero at depths far removed from the expected range of the unknown and by employing non-negativity in the form of inequality constraints, the DACES2 result will generally indicate the basic features of the source distribution, although there may be some distortion. Such distortions can be reduced, however, by performing another iteration using the distorted solution as an initial estimate. For this iteration, equality and inequality constraints can usually be neglected, although it is helpful to impose smoothing constraints. Qualitatively, the initial estimate serves to limit the class of all feasible solutions to

those solutions which are physically appropriate in some sense, i.e., the distributions occur in the correct region. The smoothing constraint further restricts the class of physically appropriate solutions to those solution estimates which are smooth and undistorted.

The studies reported above were concerned with the conversion electron spectrum of Xe^{125} (21.786 KeV) in Ta_2O_5, primarily because of the availability of data for this system. However, since Xe^{125} is not a Mossbauer-active nuclide, it was necessary to examine a system containing Mossbauer nuclei. While the Mossbauer effect has been observed in over thirty isotopes, only a few possess appropriate nuclear properties for the effect to be seen easily. Of these Fe^{57} and Sn^{119}, are the most significant. Since Sn^{119} emits 19.6 KeV conversion electrons, the Xe^{125} results are expected to be representative of Sn^{119} systems. On the other hand, Fe^{57} emits 7.3 KeV conversion electrons, and in view of the technological importance of iron and iron alloys and compounds, the possibility of spatially resolved Mossbauer spectroscopy in iron-containing materials was subsequently considered. The particular system consisted of Co^{57} (which decays to Fe^{57}) distributed in a uniform metallic iron lattice, the primary feature of this system being its simplicity.

The investigations were carried out in the following manner. First, the computer code ELTRAS was used to compute conversion electron spectra for delta function sources placed at varying

depths into the sample. In contrast to the case of Ta_2O_5, the very strong loss peak in the electron energy loss spectrum of metallic iron is probably due to a strong interband transition, rather than a plasmon excitation. However, since the probability for inelastic scattering was derived for a generalized energy loss based on a dielectric treatment of the scattering material, the angular-dependent scattering cross section and the angular probability density function for an interband transition are identical to the expressions for the plasmon losses. Consequently, it was not necessary to alter the inelastic scattering subroutine of the ELTRAS code.

For the case of 21.79 KeV Xe^{125} conversion electrons the natural width of the conversion line was relatively wide (13 eV) owing to the width of the corresponding atomic level. In addition, the instrumental resolution (.08% momentum) contributed strongly to the spectral line width (36 eV). Consequently, as the depth of the source distribution was increased, the observed spectral line became broader and shifted to lower energies of the increased characteristic energy loss structure on the lower side of the natural peak. For the 7.3 KeV Fe^{57} conversion electrons, however, not only is the initial electron distribution much sharper (3.5 eV), but the spectrometer contribution to the line width at 7.3 KeV is only 1.5 eV for 0.02% energy resolution. It is thus possible to distinguish between the nonloss peak and the loss structure, which is displaced from the nonloss peak by approximately 20 eV. The

line peak position does not change nor does the peak broaden as the depth of the Fe^{57} source distribution increases. What does occur is a change in the relative intensities of the natural peak and the loss structure.

From the results of the ELTRAS calculations, the transport kernel $W(E,z)$ was computed by determining the coefficients of a four-joint cubic spline which minimized a functional consisting of least squares and smoothing terms. While the kernel was not expected to be totally correct, its main features were expected to be representative of the true kernel behavior.

The kernel $W(E,z)$ generated in this fashion was then used to simulate conversion electron spectra produced by normalized Gaussian source distributions whose mean depths varied from 20 A to 380 A. The standard deviation of each distribution was specified as 30 A. Random numbers were generated to simulate statistical errors ranging from 0.5% to 15%.

Using these spectra as input information, a number of unfolding trials using DACES2 were performed following the procedure developed in analyzing the Xe^{125} results. For Co^{57} (Fe^{57}) distributions lying relatively close to the surface (mean depths of less than 250 A) good results were obtained by imposing only smoothness constraints. In general, unfolding results for the case of Fe^{57} in metallic iron were much better than results obtained in a similar fashion for Xe^{125} in Ta_2O_5. Such a conclusion was not wholly unexpected, however, since the 7.3 KeV electrons interact more

strongly with matter. In addition, at the lower energy fine structure in the conversion electron energy spectrum is not smoothed by the finite resolution of the electron spectrometer.

It thus appears that spatially resolved Mossbauer spectroscopy is entirely feasible for iron and iron-containing compounds for source depths in the range of 0-500 A. For tin-bearing compounds, however, it may be necessary to incorporate additional auxiliary information into the DACES2 code to obtain good unfolding results.

6.2 Applications of Spatially Resolved Mossbauer Spectroscopy

The technique of spatially resolved Mossbauer spectroscopy is theoretically capable of providing a unique representation of a particular specimen in the form of a three-dimensional graph with axes corresponding to Mossbauer source velocity, Mossbauer spectrum intensity, and depth into the specimen; i.e., the Mossbauer spectrum is plotted as a function of depth into the specimen.

Consider the simplified example of a specimen consisting of two chemical phases, A and B, with spatial distributions, $S_A(z)$ and $S_B(z)$, and associated Mossbauer spectra, $M_A(v)$ and $M_B(v)$, as described in Figure 6-1. According to spatially resolved Mossbauer spectroscopy, as proposed here, the spatial distributions are determined from conversion electron spectral analysis according to

$$N_A(E) = \int W(E,z)\ S_A(z)\ dz \qquad (6\text{-}2)$$

$$N_B(E) = \int W(E,z)\ S_B(z)\ dz \qquad (6\text{-}3)$$

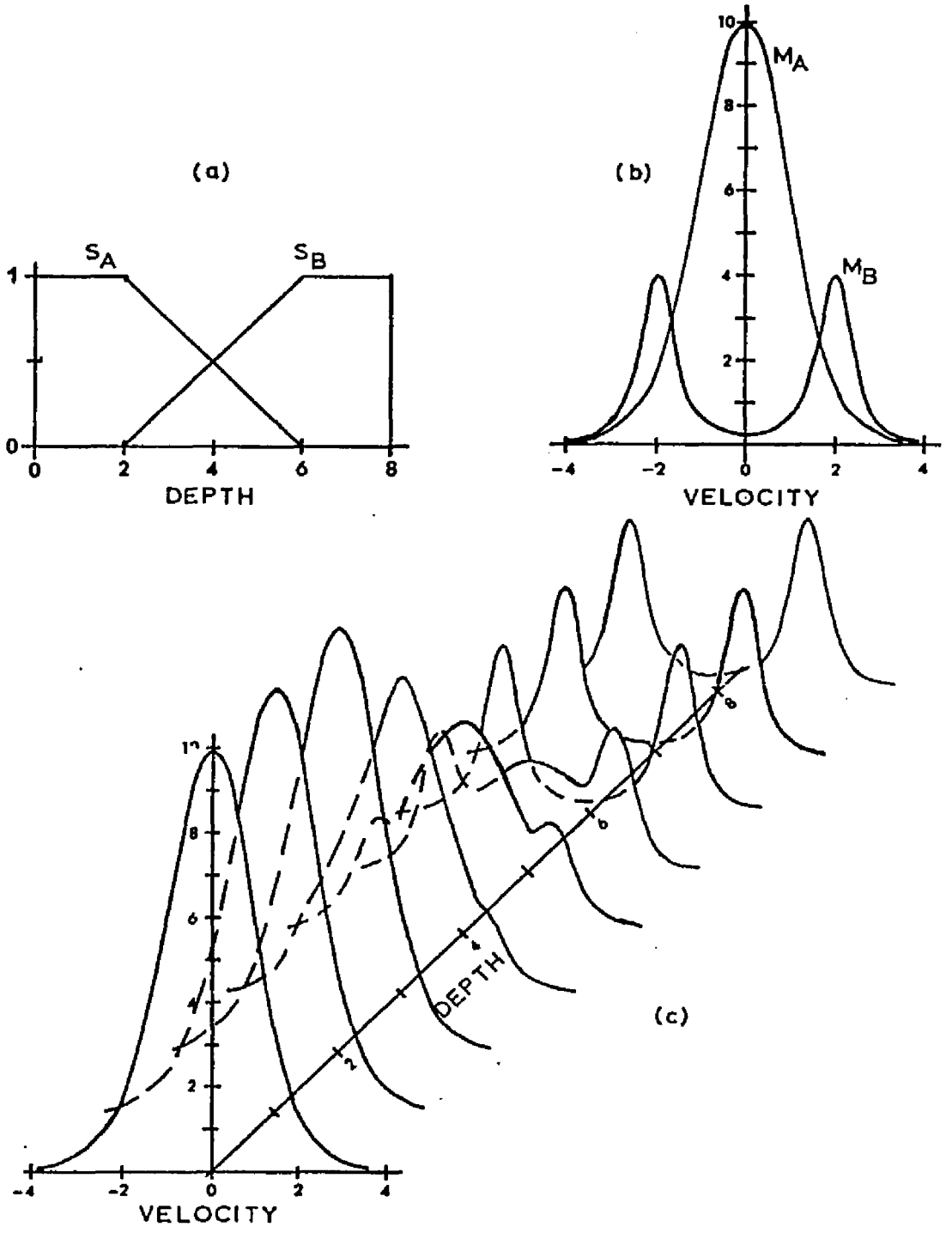

Figure 6-1. Mossbauer Spectrum as a Function of Depth. (a) Source Distributions S_A and S_B; (b) Corresponding Mossbauer Spectra M_A and M_B; (c) Depth Dependent Mossbauer Sqectrum Corresponding to (a) and (b).

Since each phase has a characteristic Mossbauer specturm, the intensity of each spectrum can be modulated by depth into the specimen according to $M_A(v)\ S_A(z) = M_A(v,z)$ and $M_B(v)\ S_B(z) = M_B(v,z)$. Thus, the Mossbauer spectrum as a function of depth into the specimen is given by $M(v,z) = M_A(v,z) + M_B(v,z)$.

The foregoing analysis also provides the connection between spatially resolved Mossbauer spectroscopy as proposed here, and as proposed by Bonchev et al., which attempts to obtain spatial information by recording the entire Mossbauer spectrum as a function of spectrometer energy. When Equations (6-2) and (6-3) are multiplied by $M_A(v)$ and $M_B(v)$ respectively and subsequently summed, the result is given by

$$M_A(v)\ N_A(E) + M_B(v)\ N_B(E) = \int W(E,z) \left[M_A(v)\ S_A(z) + M_B(v)\ S_B(z) \right] dz \qquad (6\text{-}4)$$

$$M(v,E) = \int W(E,z)\ M(v,z)\ dz$$

where the quantity on the left hand side of the equation has been identified as the conversion electron energy dependent Mossbauer spectrum of the specimen. With the Bonchev technique the chemical phases are not immediately separated. In addition, in computer analyses of Equation (6-4), both $M(v,E)$ and $M(v,z)$ must also be considered as two-dimensional arrays, thus requiring increased machine storage and computing capabilities.

There are other possible applications of the procedures described here. For example, it may occasionally be difficult to determine which lines in a composite Mossbauer spectrum correspond to the same chemical phase. In such cases, the beta spectrometer can provide positive identification by permitting comparisons of the conversion electron spectra produced when the Mossbauer source velocity is adjusted to lie in resonance with the various lines.

Also, the results of this research are obviously not restricted to Mossbauer-active nuclei. The ELTRAS and DACES1 and DACES2 codes can also be applied to the problem of following the movement of inert conversion electron emitting tracer atoms during oxidation of metallic specimens. Such tracer studies have been useful in determining the mobile species in the growth of oxide films (70). However, a detailed treatment of the electron transport and unfolding problems has been lacking until now.

These codes may also be of interest in a secondary manner to experimentalists working in fields in which the effects of characteristic energy loss processes are significant. For example, such losses can give rise to structure in isochromatic X-ray spectra (71), X-ray absorption (72), and in electron microscopy studies (73). In addition, such effects are also of importance to photoelectron, Auger, and internal conversion electron investigations. In particular, the influence of characteristic energy losses and the spectrometer window function upon energy determinations of internal conversion lines and measurements of the natural widths of atomic levels from internal conversion measurements have already been noted.

7.0 CONCLUSIONS AND RECOMMENDATIONS

7.1 Conclusions

The major conclusion of this research is that spatially resolved Mossbauer spectroscopy appears to offer a viable method for observing the surface changes that occur when a specimun is exposed to a chemically active environment. The method is applicable, however, only to materials which bear Mossbauer nuclei that decay by emitting conversion electrons, the primary isotopes of interest being Sn^{119} and Fe^{57}. The results of this technique, if sufficiently developed, would provide a complete map, for example, of a stainless steel corrosion specimen.

The relationship between the depth distribution of Mossbauer muclei and the conversion electrum spectrum has been represented by an integral equation. If experimental data are available the DACES1 computer code has been written to compute the kernel function of the integral equation. If data are not available, the Monte Carlo simulation code ELTRAS can provide theoretical conversion spectra from which the kernel may be computed. Finally, the computer code DACES2 has been written to unfold the depth distribution from the conversion electron spectrum.

Experimental Xe^{125} conversion spectra in Ta_2O_5, generously provided by J. P. S. Pringle of the Chalk River Laboratories, have

been used in DACES1 to compute the transport kernel in a spline function representation. A theoretical construction of the kernel using the ELTRAS code is in good agreement with the experimental results. The ELTRAS code has also been used to construct the transport kernel for a Co^{57} (Fe^{57}) - metallic iron system. Unfolding calculations have been performed for both systems using DACES2. The results of these computations indicate that spatially resolved Mossbauer spectroscopy is feasible for iron containing system for source depths $\lesssim 500$ A. However, less satisfactory results would be expected for tin bearing materials because Sn^{119} emits conversion electrons of higher energy (comparable to Xe^{125} conversion electrons).

7.2 Recommendations

In the opinion of the author the research reported here has demonstrated the theoretical feasibility of spatially resolved Mossbauer spectroscopy. The next step is to develop the capability for carrying out such experiments in the laboratory.

Since the Mossbauer source is always in resonance with nuclei in the chemical phase under examination, source strength does not appear to offer any serious limitations. Using completely general considerations Bonchev et al. (5) have evaluated an expression for the number of conversion electrons incident on the detector, as given by

$$N_{\text{conv el}} = n \cdot a \cdot f' \cdot \sigma_o \cdot \alpha \cdot f \cdot A \cdot \Omega \cdot \Omega' \qquad (7\text{-}1)$$

where

n = number of atoms in one cm^2 of the resonator

a = fractional abundance of Mossbauer nuclei

f' = probability of recoilless absorption in the resonator

σ_o = maximum resonance cross section

α = internal conversion coefficient

A = Mossbauer photon source activity

f = probability of recoilless emission in the source

Ω' = solid angle of the source subtended by the resonator

Ω = spectrometer transmission

Assuming a 100 A thickness of naturally occurring metallic iron, and $\Omega' \sim \Omega \sim 10^{-2}$, Equation (7-1) yields approximately 10^2 el/sec for a source strength of 10 mC.

The relative numbers of K-, L-, and M-shell conversion electrons have been indicated in Table 3-1. The numbers of L-and M-shell conversion electrons, which could slow down to the 7.3 KeV energy range, are much smaller, and these should pose no difficulty when a high resolution spectrometer is used.

In addition to the conversion electron, the incident photons will also create Compton electrons and photoelectrons. From Goldstein (74) the total cross section for photoelectric and Compton events for 14.4 KeV photons in metallic iron is 5.6×10^3 barns. The approximate number of electrons resulting from these processes is given by

$$N_{e,p} = n \cdot \sigma \cdot A \cdot \Omega \cdot \Omega' \qquad (7\text{-}2)$$

Evaluation of Equation (7-2) with the values of the parameters used previously yields approximately 20 el/sec. Since these electrons have a much wider energy distribution than the almost monoenergetic conversion electrons, the background noise level of the beta spectrometer should be very small.

The re-emission of Mossbauer photons by Fe^{57} nuclei in the resonator would result in slight increases in both the number of conversion electrons and Compton and photoelectrons. The conversion electrons will still be emitted from the chemical phase under examination, however, since Mossbauer photons emitted by nuclei in a particular phase can only be resonantly absorbed by nuclei in that same chemical phase if there is no relative motion.

The apparatus required for such investigations would consist of a constant velocity Mossbauer spectrometer (source, source drive unit, absorber (resonator), and detector) operating in the conversion electron backscatter mode. A block diagram of the overall system is shown in Figure 7-1. Rather than collecting electrons of all energies a spherical electrostatic electron spectrometer has been inserted between the absorber and detector to provide energy selection of the conversion electrons which emanate from the resonator. The recently developed channel electron multiplier (75) appears to offer much promise as an electron detector in this system.

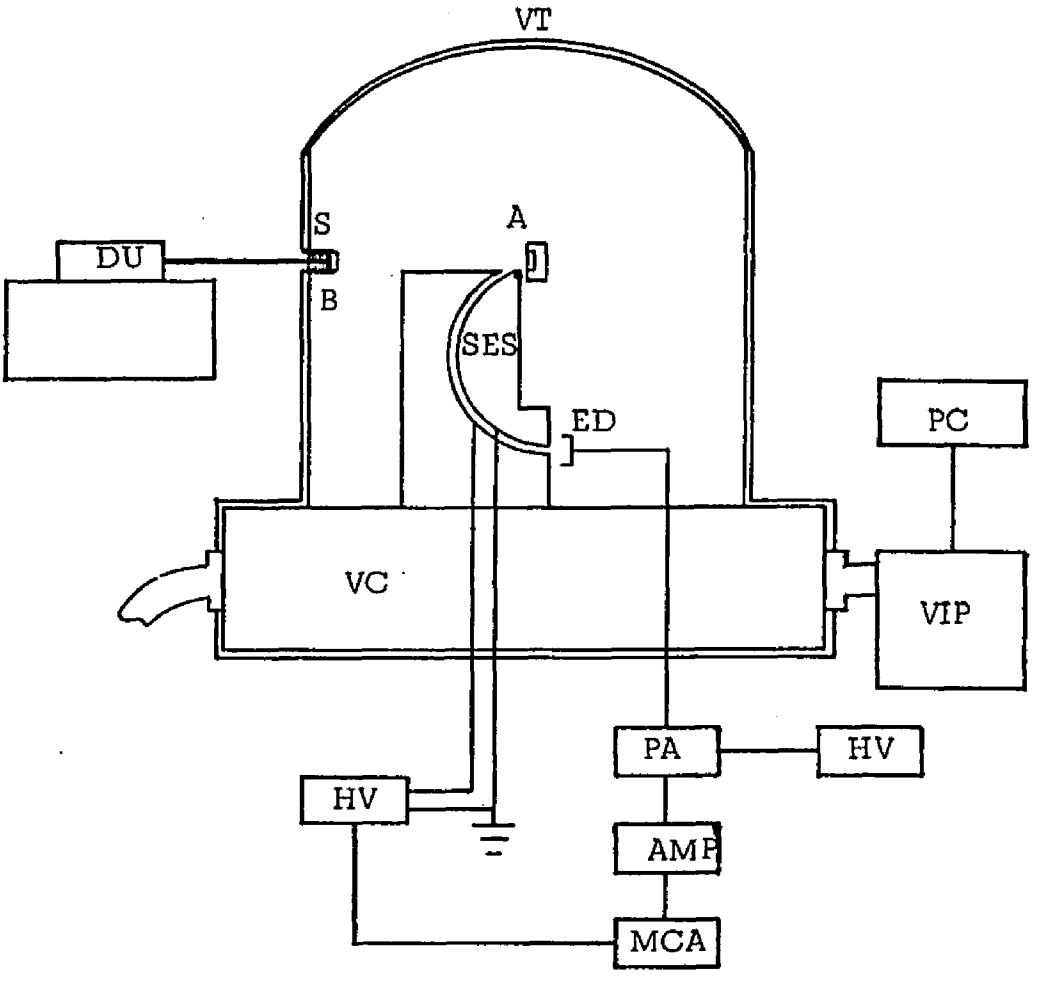

Figure 7-1. Diagram of Experimental Apparatus.

LEGEND:

A	Absorber (Resonator)	PC	Pump Controls
AMP	Amplifier	SES	Spherical Electron Spectrometer
B	Bellows		
DU	Drive Unit	VC	Vacuum Collar
ED	Electron Detector	VIP	Vacuum Ion Pump
HV	High Voltage	VG	Vacuum Gauge
MCA	Multichannel Analyzer	VT	Vacuum Tank
PA	Preamplifier	S	Mossbauer Source

The Mossbauer source and the entire electron spectrometer have been placed inside a vacuum enclosure to eliminate window attenuation of Mossbauer photons, attenuation of the electron beam, and corona discharge between the spherical electrodes of the spectrometer. The Mossbauer source drive unit has been placed outside of the vacuum chamber to reduce stray magnetic fields in the region of the spectrometer, and to prevent magnetization of the iron absorbers.

All of the major components are currently available as separate units. The major construction task would be the integration of the components into a total system.

In addition to the development of an experimental capability and subsequent experimental studies, further efforts are required regarding refinement of the ELTRAS and DACES2 codes. At this stage the weakest link in the procedure is the integral unfolding with DACES2. Since the ill-posed nature of the problem is inherent, future studies with DACES2 should concentrate on the development of more efficient means for incorporating auxiliary information about the solution estimate. On-going attempts to include the technique of "singular value decomposition" in the UNFOLD code for badly conditioned problems also deserve close attention (76). In addition, the recently developed stochastic extension method of Franklin (77, 78) offers an alternative means of incorporating auxiliary information

There are also many possible refinements to the ELTRAS code. At present ELTRAS assumes one principle energy loss mechanism (plasma excitation or interband transitions), and an elastic scattering mechanism. Higher energy loss collisions are treated in only an approximate fashion as representing capture processes. If the complete characteristic loss spectrum for a particular specimen is known it should be fairly easy to incorporate this information into the ELTRAS collision routine. Another relatively simple modification would be a provision for multi-phase specimens. With the addition of this feature important questions could be resolved regarding the effects of variations in loss spectra and emission energy from one phase to another on the shape of the kernel and the subsequent unfolding problem.

If the experimental feasibility studies establish spatially resolved Mossbauer spectroscopy as a reliable, useful technique for surface analysis, the possibilities for developing a completely automated system should be considered. Instead of a constant velocity source drive unit, such a system would employ a constant acceleration unit with a capability for setting several velocity windows bracketing several resonance lines in a composite Mossbauer spectrum. As each window is encountered in the velocity sweep, all electron counts recorded by the spectrometer would be routed to the appropriate scaler bank. Thus, conversion electron spectra associated with all selected resonance lines could be recorded simultaneously on cards or tape for later computer analysis. The actual

analysis would be performed by unfold codes such as DACES2, or perhaps library comparison codes, using data regarding the kernel provided, for example, by ELTRAS to yield not only depth information regarding the various chemical phases, but also the identity of the phases, and finally the Mossbauer spectrum as a function of depth.

APPENDIX A. THEORY OF ELECTRON COLLISIONS AND TRANSPORT

A.1 Introduction

As energetic electrons traverse matter, they undergo many collisions with atomic electrons and nuclei, for each of which there are many possible energy losses and angular changes. For electrons with energies below 10 MeV, the most significant interactions for predicting the resulting spatial, angular, and energy distributions by transport calculations are elastic nuclear (Coulomb) scattering, inelastic electron scattering in both individual collisions and collective (plasmon) interactions, and radiative (bremsstrahlung) interactions with both nuclei and atomic electrons. Early reviews of these interactions (excluding plasma excitations) have been given by Evans (79), Rossi (80), Bethe and Ashkin (81), and Fano (82). The first extensive review of the plasmon interaction was given by Pines (54), while Birkhoff (55) discusses all interactions except bremsstrahlung. The plasma theory was developed relatively recently in an attempt to explain the experimentally observed result that when traversing solid materials electrons lose energy in combinations of certain discrete amounts. It is interesting to follow the progress in this field as the plasma excitation theory has generally gained favor, although

the review as late as 1967 by Zerby and Keller (22) completely ignores this interaction.

In the following sections the details of electron interactions are discussed with the intention of providing results that can be incorporated into an electron transport theory.

A.2 Basic Interactions

A.2.1 Nuclear Coulomb Scattering

The nuclear Coulomb scattering cross section is very large and heavily concentrated in the forward direction. Since the mass of the target nucleus is very much greater than the mass of the electron, the energy loss suffered by the electron is negligible, and these collisions may be considered elastic.

The classical treatment of nuclear scattering of an incident charged particle was first given by Rutherford (83). Assuming the nuclear Coulomb potential, i.e., neglecting the screening effects of the atomic electrons, he obtained the differential cross section per atom for scattering through an angle between θ and $\theta + d\theta$ into a solid angle $d\Omega = 2\pi \sin \theta \, d\theta$ as given by

$$\frac{d\sigma}{d\Omega} = \frac{1}{4} \left(\frac{e^2 Z}{mv^2}\right)^2 \sin^{-4} (\theta/2) \qquad \text{(A-1)}$$

Equation (A-1) actually overestimates the scattering, particularly for small angles of deflection, because the full nuclear charge is shielded by atomic electrons.

Using the Born approximation (84) in the quantum mechanical theory of scattering, Goudsmit and Saunderson (85) have calculated the scattering amplitude for the case of a screened Coulomb potential given by

$$V(r) = \frac{Ze^2}{r} e^{-r/a} \qquad \text{(A-2)}$$

where $a = a_o Z^{-1/3}$, and $a_o = \frac{\hbar^2}{me^2}$ is the Bohr radius. From this calculation the differential cross section is determined as

$$\frac{d\sigma}{d\Omega} = \left(\frac{e^2 Z}{mv^2} \right)^2 (1 - \cos\theta + \tfrac{1}{2}\theta_1)^{-2} \qquad \text{(A-3)}$$

with $\theta_1 = \frac{\lambda\!\!\!^{-}}{a}$ and $\lambda\!\!\!^{-} = \frac{\hbar}{mv}$. This result is seen to be reduced from the Rutherford cross section (Equation (A-1)) only for small angles $\theta \leq \theta_1$.

More accurate treatments employing the Born approximation, but using the Thomas-Fermi statistical atomic model to estimate shielding of the nuclear charge, have been given by Bethe (86) and by Bullard and Massey (87). In addition, Moliere (88) has also performed this calculation with Fermi-Thomas screening by using the WKB method (89), rather than the Born approximation, and he obtained a screening angle θ_s similar to θ_1 of Equation (A-3). The Moliere theory is valid for a scattering angle up to about $\pi/2$ and for nonrelativistic electron energies greater than $Z^{4/3}$ x (100 eV).

A.2.2 Electron-Electron Collisions

The essential features of the interaction between an energetic incident electron and an electron "free" of binding forces have been given in the classical treatment of Thomson (90) and Bohr (91). The calculation assumes that only a relatively small fraction of the incident electron energy is transferred in a single collision and the incident electron direction does not change appreciably. Defining the cross section per free electron in terms of the impact parameter as $d = 2\pi bdb$, the calculation yields

$$\frac{d\sigma}{d(\Delta E)} = \frac{\pi e^4}{E} (\Delta E)^{-2} \qquad \text{(A-4)}$$

The cross section for free electron scattering has been calculated quantum mechanically by Mott (92), and Moller (93) has performed the relativistic quantum mechanical calculation. In terms of an energy distribution, Mott's result becomes

$$\frac{d\sigma}{d(\Delta E)} = \frac{\pi e^4}{E} \left| (\Delta E)^{-2} + (E - \Delta E)^2 - \left[\Delta E(E - \Delta E)\right]^{-1} x \cos\left(\frac{e^2}{\hbar v} \ell n \left(\frac{E - \Delta E}{\Delta E}\right)\right)\right| \qquad \text{(A-5)}$$

Equation (A-5) approaches Equation (A-4) in the limit of small energy transfers. The small difference in the two expressions leads to extensive use of the former in electron transport analyses.

A.2.3 Electron Stopping Power

In first approximation the energy transfer to an electron in a stopping medium is given by Equation (A-4). When an incident electron travels a distance dx, the energy loss to all electrons with impact parameters between b and b + db is given by $\frac{e^4}{Eb^2}(2\pi b db) \cdot (NZ) \cdot dx$ where N is the atomic density and Z is the atomic number. The total energy loss per unit length, termed the stopping power, is calculated from

$$-\frac{dE}{dx} = 2\pi NZ \frac{e^4}{E} \int_{b_{min}}^{b_{max}} \frac{db}{b} \qquad \text{(A-6)}$$

where b_{min} and b_{max} are the lower and upper limits of the impact parameter for which the stopping power formulation is expected to be valid. For distant collisions involving the smallest energy transfers, the collision time is of the order of $\frac{b_{max}}{v}$, where v is the velocity of the incident electron. Assuming the classical picture of an electron bound to a nucleus with binding energy $\hbar\omega$, an energy transfer in which the collision time is longer than the electron period is unlikely, and the maximum impact parameter is evaluated as

$$b_{max} = \frac{v}{\omega} \qquad \text{(A-7)}$$

The minimum impact parameter may be evaluated by considering the maximum possible energy transfer. Because of the indistinguishability

of identical particles, the maximum energy transfer is assumed to be equal to one-half the energy of the incident electron, and b_{min} is given by $\frac{1}{2}E = \frac{e^4}{Eb_{min}^2}$ or

$$b_{min} = \sqrt{2}\,\frac{e^2}{E} = \frac{2\sqrt{2}e^2}{mv^2} \qquad \text{(A-8)}$$

Using Equations (A-7) and (A-8), the classical stopping power formula becomes

$$-\frac{dE}{dx} = 2\pi NZ\,\frac{e^4}{E}\,\log\frac{mv^3}{2\sqrt{2}e^2\omega} \qquad \text{(A-9)}$$

In the quantum mechanical treatment of Bethe (86) the single frequency ω is replaced by an assembly of oscillators with frequencies ω_i and oscillator strengths f_i, such that $\sum_i f_i = Z$. For this case Equation (A-6) becomes

$$-\frac{dE}{dx} = 2\pi N\,\frac{e^4}{E}\,\sum_i \int f_i\,\frac{db}{b} \qquad \text{(A-10)}$$

where $b_{i\,max} = \frac{v}{\omega_i}$.

Collisions in which the impact parameter is smaller than the deBroglie wavelength will be meaningless in a quantum mechanical sense; therefore, $b_{min} = \frac{\hbar}{mv}$. This distance is usually larger than the classical value and must be used in preference to Equation (A-8). In this case Equation (A-10) can be evaluated as

$$-\frac{dE}{dx} = 2\pi NZ\,\frac{e^4}{E}\sum_i f_i \log\frac{mv^2}{\hbar\omega_i} \qquad \text{(A-11)}$$

For most substances, there is insufficient experimental or theoretical information about values of f_i or ω_i. To circumvent this problem, an average ionization potential, I, is defined as

$$I^Z = \prod_i (\hbar\omega_i)^{f_i} \qquad \text{(A-12)}$$

With this definition, Equation (A-11) becomes

$$-\frac{dE}{dx} = 2\pi NZ\,\frac{e^4}{E}\log\frac{mv^2}{I} \qquad \text{(A-13)}$$

On the basis of a statistical model of the atom, Bloch (94) has shown that the value of I should be proportional to the atomic number of the material, with the proportionality being of the order of the Rydberg energy 13.5 eV.

A.2.4 Plasma Excitations

For a gaseous medium, the absorption frequencies ω_i of the previous section are determined by the excitation and ionization energies of the individual atoms which constitute the medium. For condensed matter, however, although the larger values of ω_i corresponding to inner electronic shells will remain unchanged, the smaller frequencies will also be determined by the structure of the absorber. In particular, the electrons in the conduction band of a metal closely approximate a degenerate Fermi gas in a general

homogeneous positive potential. Collective mode excitations of this plasma can give rise to quantized energy losses which depend upon the free electron density and dielectric properties of the metal. An extensive treatment of the interactions in a collection of electrons has been given by Pines and Bohm (40). Since this mode of interaction is not as generally well-known as the previously treated interactions, a more detailed treatment of the plasma excitation will be given here.

When an electric field $\vec{E}$ is introduced in a medium (for example, by an incident electron), the field is diminished by polarization of the medium of an amount $4\pi\vec{P}$, where $\vec{P}$ represents the electric dipole moment per unit volume. If there are n electrons per unit volume and each experiences a displacement $\vec{x}$ due to the polarization force, then $\vec{P} = -ne\vec{x}$, and the equation of motion becomes

$$4\pi e(-ne\vec{x}) = m\ddot{\vec{x}} \qquad \text{(A-14)}$$

The form of Equation (A-14) is recognized as that of a simple harmonic oscillator with an oscillation frequency given by

$$\omega_p = \sqrt{\frac{4\pi ne^2}{m}} \qquad \text{(A-15)}$$

ω_p is termed the plasma frequency.

Since the small frequencies ω_i may be considerably altered for solid materials, the stopping power formula (Equation (A-13)) may have a restricted range of validity. In their extensive

calculations, Pines and Bohm have considered the stopping power due to metallic conduction band electrons. One of the consequences of this work is that the minimum impact parameter should be of the order of the Debge length λ_D . With the maximum impact parameter being given by $\frac{v}{\omega_p}$, the stopping power due to conduction electrons in which only the plasma oscillations are excited is given by

$$\frac{dE}{dx} = 2\pi NZ \frac{e^4}{4} \log \frac{v}{\lambda_D \omega_p} \qquad \text{(A-16)}$$

Since the stopping power formula depends on the logarithm of the ratio of b_{max} to b_{min} , it is possible to compare the importance of plasma and electron-electron interactions. For 100 KeV electrons incident upon aluminum (three conduction elections per atom), Birkhoff (55) has evaluated the various limiting impact parameters and finds $\frac{v}{\omega_p}$ 73 A , $\lambda_D \simeq 0.5$ A , and $\hbar/mv \simeq .0059$ A . Therefore, $\frac{v}{\lambda_D \omega_p} \simeq \frac{\lambda_D mv}{\hbar}$, and the contribution due to plasma oscillations is the same order of magnitude as the contribution due to electron-electron interactions. However, the plasma excitation is a long-range interaction, and the energy loss per interaction for plasma oscillations will be much smaller in general than losses due to electron-electron interactions.

Because of the long-range nature of the electron-plasma interaction (the interaction distance is large compared to the interelectronic spacing), the scattering may be described in terms of a dielectric theory in which the solid is treated as a continuous, homogeneous medium. A classical theory of the dielectric constant

of a free electron gas has been given by Lindhard assuming the existence of a common electric field in which the electrons move and to which they give rise. A result of the theory is a dependence of the dielectric constant $\epsilon(\vec{k}, \omega)$ on the wave vector $\vec{k}$ of the disturbance. The dielectric treatment has been extended by Hubbard (96), and later, Ritchie (66) to the calculation of the energy-angle distribution of fast electrons in passing through and losing energy to solids.

As long as the fractional changes in momentum and energy are small, the incident electron may be considered as a point charge with a well-defined path. The equation for the electric potential $\Phi(\vec{r}, t)$ due to a point charge moving with uniform velocity $\vec{v}$ in a uniform infinite plasma, is given by Poisson's equation

$$\epsilon(\vec{k}, \omega) \quad \nabla^2 \Phi \quad (\vec{r}, t) = 4\pi\delta(\vec{r} - \vec{v}t) \tag{A-17}$$

Taking the Fourier transform of Equation (A-17) in both space and time yields

$$\phi(\vec{k}, \omega) = -\frac{8\pi^2 e}{\epsilon(\vec{k}, \omega)} \cdot \frac{\delta(\vec{k} \cdot \vec{v} + \omega)}{k^2} \tag{A-18}$$

where

$$\phi(\vec{r}, t) = \frac{1}{(2\pi)^4} \int d\vec{k} \int d\omega \quad \phi(\vec{k}, \omega) \; e^{i(\vec{k} \cdot \vec{r} + \omega t)} \tag{A-19}$$

The energy loss per unit path length in the medium (stopping power) is given by

$$-\frac{dE}{dx} = e\,\mathcal{E}_x\Big|_{\vec{r}=\vec{v}t} = \frac{e}{v}\,\vec{v}\cdot\vec{\mathcal{E}}\Big|_{\vec{r}=\vec{v}t} \qquad \text{(A-20)}$$

where $\mathcal{E}_x = \frac{\partial\phi}{\partial x}$ is the x component of the electric field due to the medium. ($e\,\mathcal{E}_x$ is the reaction force.) Expressing $\phi(\vec{r},t)$ in terms of its Fourier representation, Equation (A-20) becomes

(A-21)

$$-\frac{dE}{dx} = \frac{e^2}{\pi 2}\,\frac{1}{v}\,\vec{v}\cdot\nabla\left[\int d\vec{k}\int d\omega\left(\frac{1}{\epsilon}\right)\frac{\delta(\vec{k}\cdot\vec{v}+\omega)}{k^2}\,e^{i(\vec{k}\cdot\vec{v}+\omega t)}\right]$$

Since the gradient is evaluated at the position $\vec{r} = \vec{v}t$, the gradient operator may be transformed as $\nabla = \frac{\hat{v}}{v}\frac{\partial}{\partial t}$, and integration by parts yields

$$-\frac{dE}{dx} = \frac{e^2}{\pi 2}\,\frac{1}{v}\int d\vec{k}\int d\omega\left(\frac{i\omega}{\epsilon}\right)\frac{\delta(\vec{k}\cdot\vec{v}+\omega)}{k^2}\,e^{i(\vec{k}\cdot\vec{r}+\omega t)} \qquad \text{(A-22)}$$

Again, since the interaction occurs at position $\vec{r} = \vec{v}t$, it is noted that $(\vec{k}\cdot\vec{r}+\omega t) = t(\vec{k}\cdot\vec{v}+\omega)$. Since $(\vec{k}\cdot\vec{v}+\omega)$ is the argument of the delta function in the integrand, the exponent may be neglected. In addition, only the real part of the expression contributes to the energy loss, and the result becomes

$$-\frac{dE}{dx} = \frac{e^2}{\pi 2_v}\int d\vec{k}\int d\omega\ \ \mathrm{Im}\left(\frac{1}{\epsilon}\right)\ \frac{\delta(\vec{k}\cdot\vec{v}+\omega)}{k^2} \qquad \text{(A-23)}$$

The integrand of Equation (A-23) represents the energy absorbed per unit volume in $\vec{k}$ space per unit frequency interval and per unit

path length of the electron. Dividing the integrand by $\hbar\omega$ therefore yields the probability for absorption of energy $\hbar\omega$ and momentum $\hbar\vec{k}$ per unit length. This result becomes

$$P(\vec{k}, \omega) = \frac{e^2}{\pi^2 \hbar v} \text{ Im } \left(\frac{1}{\epsilon} \right) \frac{\delta(k \cdot v + \omega)}{k^2} \qquad \text{(A-24)}$$

Dividing the wave vector $\vec{k}$ into components which are perpendicular and parallel to $\vec{v}$, the integration over the parallel component is easily performed because of the delta function properties, and Equation (A-24) becomes

$$P(k_\perp, \omega) = \frac{e^2}{\pi^2 \hbar v^2} \text{ Im } \left(\frac{1}{\epsilon} \right) \frac{1}{k_\perp^2 + \omega^2/v^2} \qquad \text{(A-25)}$$

In principle the problem is solved with evaluation of an expression for the dielectric constant. Ritchie has obtained an approximation of the Lindhard dielectric constant for a free electron gas, and he finds

$$\text{Im } \left(\frac{1}{\epsilon} \right) = \frac{2\gamma\omega_p\omega}{\left| \omega^2 - \omega_p^2 (1 + \delta) \right|^2 + 4\gamma^2\omega^2} \qquad \text{(A-26)}$$

where

$$\delta = \frac{1}{\omega^2} \frac{\hbar^2}{m^2} \left(\frac{k^4}{4} + \frac{3k^2 k_c^2}{5} \right) \qquad \text{(A-27)}$$

k_c represents the maximum (cut-off) wave vector of the undisturbed plasma. The factor γ represents the damping of a plasma oscillation

due to emission of electromagnetic radiation, through creation of excitons (97), through plasma phonon interactions, or through energy transfer to a single plasma electron.

Electron plasma oscillations of wavelengths that are large compared to the mean interelectron distance are collective in nature. As the wavelength decreases (k increases) however, the notion of collective oscillations becomes obscure. In addition, the probability for the transfer of the plasmon energy to an individual electron increases (γ increases), and the plasma oscillation is damped out. When the phase velocity of plasma wave propagation approaches the velocity of plasma electrons, the damping becomes complete yielding the cut-off wave number for plasma oscillations. This picture is somewhat similar to the explanation given for Landau damping of general plasma oscillations.

Substituting Equation (A-26) into Equation (A-25) and employing the approximation $\theta \simeq \frac{\hbar k_\perp}{mv}$, good for small scattering angles θ, the probability per unit solid angle $d\Omega$ of an energy loss $\hbar\omega$ at an angle of deflection θ becomes

$$P(\theta, \omega) = \frac{\omega_p^2 e^2 \omega}{\pi^2 \hbar v^2} 2\gamma \left\{ \left[\omega^2 - \omega_p^2 (1 + \delta) \right]^2 + 4\gamma^2 \omega^2 \right\}^{-1} \cdot \left[\theta^2 + \left(\frac{\hbar\omega}{mv^2} \right)^2 \right]^{-1} \tag{A-28}$$

Assuming a long-range interaction ($k \ll k_c$), the damping constant γ becomes vanishingly small and the factor within the braces assumes

the character of a delta function with the resonance occurring at $\omega^2 \quad \omega_p^2 (1 + \delta)$. By iteration with Equation (A-27), this result becomes

$$\omega^2 \simeq \omega_p^2 + \frac{\hbar^2}{m^2} \left(\frac{k^4}{4} + \frac{3k^2 k_c^2}{5} \right) \tag{A-29}$$

which is the Bohm-Pines plasma dispersion relation. Considering a free Fermi gas, the cut-off wave number k_c may be taken as the maximum wave number k_F according to $E_F = \frac{\hbar^2 k_F^2}{2m}$ where E_F is the energy of the Fermi level. Making this assumption and taking the square root of Equation (A-29), the dispersion relation for a plasmon created through electron scattering becomes

$$\omega(k) = \omega_p \left[1 + \alpha \frac{\hbar}{m\omega_p} k^2 + \frac{1}{\hbar \omega_p} \left(\frac{\hbar}{2m} \right)^2 \left(\frac{1}{2} - \frac{6}{35} \frac{E_F^2}{\hbar^2 \omega_p^2} \right) k^4 + \ldots \right] \tag{A-30}$$

where $\alpha = \frac{3}{5} \frac{E_F}{\hbar \omega_p}$. Recalling that $\theta = \frac{\hbar k}{mv}$, Equation (A-30) may be re-expressed in terms of energy as

$$\Delta E(\theta) = \hbar \omega(\theta) = \Delta E(0) + \alpha \cdot 2E\theta^2 + \left(\frac{1}{2} - \frac{6}{35} \frac{E_F^2}{\hbar^2 \omega_p^2} \right) E^2 \theta^4 + \ldots \tag{A-31}$$

where $\Delta E(0) = \hbar \omega_p$.

Equation (A-31) thus represents the plasma loss energy for a particular scattering angle θ. To find the probability of scattering through an angle θ, Equation (A-28) must be integrated over all energy losses. Thus $P(\theta)$ is given by

$$P(\theta) = \frac{\omega_p^2 e^2}{\pi^2 \hbar v^2} \int_\delta^\infty \frac{\omega \, d\omega}{\left[\theta^2 + \left(\frac{\hbar\omega}{mv^2}\right)^2\right]} \cdot \frac{2\gamma}{\left|\omega^2 - \omega_p^2(1+\delta)\right|^2 + 4\gamma^2\omega^2}$$

Utilizing the approximate delta function behavior of the second term in the integrand, the first term in the integrand can be moved through the integral by assuming that ω takes its resonance value. Hence, the equation becomes

$$P(\theta) = \frac{\omega_p^2 e^2}{\pi^2 \hbar v^2} \cdot \left[\theta^2 + \left(\frac{\hbar}{mv^2}\right)^2 \left(\omega_p^2 + \frac{\hbar^2}{m^2}\left(\frac{k^4}{4} + \frac{3k_c^2 k^2}{5}\right)\right)\right]^{-1} \cdot \int \frac{2\gamma\omega \, d\omega}{\left|\omega^2 - \omega_p^2(1+\delta)\right|^2 + 4\gamma^2\omega^2} \qquad \text{(A-32)}$$

The remaining integration has been evaluated in an approximate manner by Ritchie. Under the assumption of small damping, the half-width of the resonance $(2\gamma\omega)$ is assumed to be approximately constant, and the integration yields $\frac{\pi}{2}\left[\omega_p^2 + \frac{\hbar^2}{m^2}\left(\frac{k^4}{4} + \frac{3k_c^2 k^2}{5}\right)^{-\frac{1}{2}}\right]$.

The resulting angular distribution is then given by

$$P(\theta) = \frac{e^2 \omega_p^2}{2\pi\hbar v^2}\left[\omega_p^2 + \frac{\hbar^2}{m^2}\left(\frac{k^4}{4} + \frac{3k_c^2 k^2}{5}\right)\right]^{-\frac{1}{2}} x \qquad \text{(A-33)}$$

$$\left\{\theta^2 + \frac{\hbar^2}{(2E)^2}\left[\omega_p^2 + \frac{\hbar^2}{m^2}\left(k\frac{4}{4} + \frac{3k_c^2 k^2}{5}\right)\right]\right\}^{-1}$$

Neglecting higher powers of $\hbar\omega_p$, and $\frac{\hbar^2 k_c^2}{2m}$ compared with E, the energy of the incident electron, Equation (A-33) reduces to

$$P(\theta) = \frac{1}{2\pi a_o} \frac{(\hbar\omega_p/2E)}{\theta^2 + (\hbar\omega_p/2E)^2} \qquad \text{(A-34)}$$

where a_o is the Bohr radius. Ritchie has also shown that for small electron densities, Equation (A-33) approaches the Rutherford scattering formula given by

$$P(\theta) \longrightarrow \frac{4ne^4}{m^2v^2} \frac{1}{\theta^4} \qquad \text{(A-35)}$$

Thus, to a certain extent, Equation (A-33) displays both collective and individual interaction characteristics. It shows that when the scattering angles are very small the collective behavior of the ensemble of electrons determines the angular distribution. For larger angles or for very low electron densities, individual interaction between the fast electron and the electrons in the medium becomes the determining effect.

A.2.5 Bremsstrahlung

A complete treatment of electron energy losses due to bremsstrahlung has been given by Bethe and Heitler (98), employing Dirac's equation for the electron and the Born approximation. A principle result of their computations is the cross section for the scattering of an incident electron of total energy E, accompanied by the emission of a photon with frequency ν, the maximum value of ν being determined from the equation

$$h\nu_o = E - mc^2 \tag{A-36}$$

The radiation probability depends on the effective distance from the electron to the nucleus because of the screening effect of atomic electrons. For sufficiently high energies of the incident particle, the screening can be considered complete for all photon frequencies, whereas for low incident electron energies and high photon frequencies the screening may be neglected. For the latter case Bethe and Heitler give the cross section as

$$\sigma(E,\nu)d\nu = \frac{Z^2}{137}\left(\frac{e^2}{mc^2}\right)^2 \frac{d\nu}{\nu}\, 4\left[1 + \left(\frac{E}{E_o}\right)^2 - \frac{2}{3}\left(\frac{E}{E_o}\right)\right] \cdot \left(\log \frac{2E_oE}{mc^2h\nu} - \frac{1}{2}\right) \tag{A-37}$$

Later developments in the theory of bremsstrahlung, including various screening correction results, are contained in the review article of Koch and Motz (99).

In analogy with inelastic electron interactions, it is possible to develop a stopping power formula for the case of bremsstrahlung. Since the number of photons produced with frequency in the range ν to $\nu + d\nu$ when an electron of energy E traverses a thickness dx of stopping material is $N\sigma(E, \nu)d\nu dx$, where N is the atom density. The energy loss by radiation per unit path is given by

$$-\left(\frac{dE}{dx}\right)_{rad} = N\int_0^{\nu_0} h\nu\,\sigma(E, \nu)d\nu \qquad \text{(A-38)}$$

Since σ is roughly proportional to $(1/\nu)$, the quantity $h\nu\sigma(E, \nu)$ is approximately constant. The energy loss per unit path is then approximately proportional to the incident electron energy E. Thus, the energy loss due to bremsstrahlung is proportional to Z^2 and increases nearly linearly with incident electron energy. In contrast, for the case of electron-electron collisions (see Equation (A-9), for example) the energy loss is proportional to Z and increases only logarithmically with energy.

At the higher energies, therefore, the energy loss by radiation dominates. As the energy of the electron decreases, ionization and excitation collisions become more and more important until at a certain critical energy E_c they become comparable. This critical energy has been approximately expressed by Bethe and Heitler as

$$E_c \simeq \frac{1600\ mc^2}{Z} \qquad \text{(A-39)}$$

with the ratio of the radiative loss to the collision loss given by

$$\frac{dE/dx_{rad}}{dE/dx_{coll}} \simeq \frac{EZ}{1600\ mc^2} \qquad \text{(A-40)}$$

Thus, for electrons of energy $E \ll E_c$, the effects of bremsstrahlung are not significant, and the bremsstrahlung interaction may be neglected in transport theories concerned with this energy range.

A.3 Multiple Interaction Studies

A.3.1 Continuous Slowing Down

Since an electron performs a large number of inelastic collisions with atomic electrons while traversing a fraction of its total range, in some instances it is very use ful to describe the electron energy degradation in terms of a continuous statistical multiple collision model. Defining a total stopping power $-\left(\frac{dE}{dx}\right)_{tot}$ as the sum of stopping powers due to electron-electron collisions, electron-plasma oscillations, and bremsstrahlung, a unique relationship can be found between the total pathlength, s, traveled by the electron and its residual energy, E, according to

$$S = -\int_{E_o}^{E} \frac{dE}{(dE/dx)} \qquad \text{(A-41)}$$

A.3.2 Straggling

Actually, the relationship given by Equation (A-41) is not unique because electrons experience discrete and sometimes large energy losses as they travel through matter. As a result, at any particular distance a spectrum of electron energies is possible. The deviation of the energy of the electrons from the average is historically known as straggling and was first studied by Williams (100), with subsequent treatments having been given by Landau (101) and by Blunck and Leisegang (102). Since the straggling distributions allow energies higher as well as lower than those obtained with the continuous slowing down model, there will be a tendency to shift any energy spectrum under consideration to higher energies when straggling is included. In conjunction with this shift will be a depletion and modification of the lower energy portion of the spectrum.

A.3.3 Multiple Scattering Theory

Electrons not only lose energy by multiple interactions but they are also deflected laterally from their original paths as they make multiple discrete changes in direction. Because of the analytical complexity of the problem, a number of approaches have been developed, and these have been reviewed by Birkhoff (55), and Bethe and Ashkin (81). In general, the approaches of Moliere (103), Snyder and Scott (104), Goudsmit and Saunderson (85), and Lewis (105), are directed at finding the angular distributions without regard to the lateral displacement. In addition, since the

continuous slowing down model is assumed to apply, the angular distributions derived by these techniques are all a function of the total pathlength traveled, rather than the depth of penetration.

A.4 Thick Target Studies

The common feature of all the multiple interaction models discussed heretofore is their dependence on total distance traveled (pathlength) rather than position; since the cross sections for nuclear, electron-electron, and electron-plasmon scattering are so large, the path of the electron quickly deviated from a straight line, and these models can only be applied to penetrations that are a small fraction of the electron range. Their applicability is further limited because of the restrictions necessary for an analytical treatment to be possible. For example, the theories of Landau and Blunck and Leisegang deal with fluctuations in energy loss only in the limit where the energy loss is small compared to the initial energy. The angular scattering theories of Williams, Fermi, Snyder and Scott, and Moliere are only valid in the small angle approximation, and consider energy loss either not at all, or only in the continuous slowing down approximation. On the other hand, the theory of Goudsmit and Saunderson places no limit on the magnitude of angular deflections, but disregards spatial deflections resulting from multiple scattering, a limitation shared by all the above theories. When applied to deeper penetrations these theories fail to yield even qualitative results.

As a first departure from the previous calculations Spencer and Fano (106) have calculated the actual flux spectrum in a uniform, infinite medium containing uniformly distributed electron sources, such suppositions removing spatial and angular dependence from the problem. In the Spencer-Fano theory the continuous slowing down approximation is modified by the generation of secondary electrons through occasional violent collisions, and by energy losses due to bremsstrahlung.

A treatment assuming more realistic boundary conditions has been given by Bethe et al. (24), whose work in turn was extended by Weymouth (26), Roesch (27), Meister (25), and Archard (28). These theories attempt to account for energy loss by employing the continuous slowing down model, and for the diffusion of the electrons by using an age diffusion approximation to the Boltzmann transport equation. In general, these descriptions fail in not adequately representing the region near the source, where the electrons are generally directed away from the source, and regions far from the source where asymptotic solutions are required.

More formal treatments such as those of Wentzel (107), Wang and Guth (108), and Breitenberger (109) in principle yield general solutions, but in practice can be evaluated only through drastic assumptions and loss of generality.

Various attempts have been made to solve the complete electron transport problem by employing numerical techniques that combine the results of several theories. For example, Spencer (23) has adapted

the moments equations of Lewis to the electron transport problem of calculating the radiation dose in homogeneous, unbounded media. The electron transport equation derived by Bethe et al. in the small angle approximation has been solved numerically by Brown and Ogilvie (110) using the finite difference approximation in connection with problems in electron microanalyses. This treatment was later refined by Brown, Wittry, and Kyser (111) who used a single scattering equation for short pathlength, a transport equation for intermediate pathlengths, and a diffusion equation for long pathlengths in the treatment of electron scattering. The predictions of this transport equation program appear to agree favorably with experimental data pertaining to electron microanalysis, although the technique has not yet been adapted to other problems in electron transport.

In principle, the Monte Carlo method can provide a complete simulation of the entire collision history of an electron. In practice, individual collisions are not treated, however, because of the staggering number of collisions that occur in thick target studies. Instead, analytic results describing various aspects of electron transport are used to describe large numbers of single collisions as a single segment of the calculation; the computation then proceeds through the electron history segment by segment. Monte Carlo methods for electron transport calculations have been developed by several authors, including Perkins (48),

McGarrigle and Mar (49), Wittig (112), Berger (50), and Jordan (113). Berger's code, ETRAN, has the flexibility of being able to incorporate a variety of simulation techniques. Angular deflections may be computed by the method of Goudsmit and Saunderson, Moliere, or Fermi's Gaussian distribution; the energy spectrum is determined by either the continuous slowing down model, or the modified Laudau energy straggling distribution. Provisions are also made for secondary electron production and bremsstrahlung. Calculations based on ETRAN have generally shown good agreement with experiment; discrepancies that do occur can usually be attributed to a particular aspect of the simulation scheme and are predictable. Tha major restriction of the Monte Carlo method is the statistical variation inherent in the random selection techniques.

The discrete ordinates method of Carlson (114), which is widely used as the ANISN code for neutron and gamma ray transport, offers a viable alternative to the Monte Carlo method. Recently, a first attempt has been made by Bartine et al. (115) to adapt the discrete ordinates method to electron transport. In principle, ANISN could be used for electron transport by simply introducing the differential cross sections for electron collisions. In practice these cross sections are quite different from neutron transport cross sections, however, and the method has shown only partial success for transporting electrons.

APPENDIX B. THE COMPUTER CODE ELTRAS

B.1 Introduction

In this appendix the three principle computations of ELTRAS, an analog simulation and two folding integrations, are discussed in detail, incorporating many of the results of the previous appendix on electron transport.

B.2 The Monte Carlo Simulation Scheme

The present problem involves estimation of the percentage of monoenergetic electrons born at a specified depth that can be expected to emerge from the surface of the sample in certain stipulated categories, e.g., energy loss and emergence angle. For this problem, the Monte Carlo method can be subdivided into a well-defined set of routines: (1) a source routine which introduces an electron at a particular depth and energy and assigns to it an angular parameter (the direction cosine with respect to the surface normal) chosen from a specified angular distribution; (2) a mean free path and transmission routine which determines whether an electron starting with known angular parameters from an arbitrary depth either suffers a collision or reaches the surface without interaction; (3) a collision routine which specifies the nature of the collision and determines the immediate fate of the electron after collision; and (4) a termination routine which tallies the

ultimate fate of a particular electron in the appropriate category. These routines are schematically indicated in Figure B-1 which contains the generalized flow diagram for the electron transport simulations. In the following the various routines used in the Monte Carlo method are discussed in detail.

B.2.1 The Source Routine

For problems of this type, a particle is completely characterized by a set of parameters which are sufficient to determine its probable behavior in all situations it may encounter during its history. These always include its position and angular coordinates; other parameters are dictated by the specific nature of the problem. For example, in this problem it is essential to introduce an energy loss parameter. In problems involving very high or very low transmission it is often desirable to introduce a weight parameter W to improve statistical accuracy of the Monte Carlo results. It is also useful to include a parameter ν which records the number of collisions undergone by a particle.

Electrons emerging from the source routine have not undergone any collisions by definition; therefore, $\nu = 0$ and $\Delta E = 0$, where ΔE is the energy loss parameter. Since the problem geometry is that of an infinite planar slab, the depth coordinate z and the direction cosine w of the angle θ which the electron line-of-flight makes with the positive z-axis are the only relevant coordinates. Since the depth of origin, z_o, is specified for a

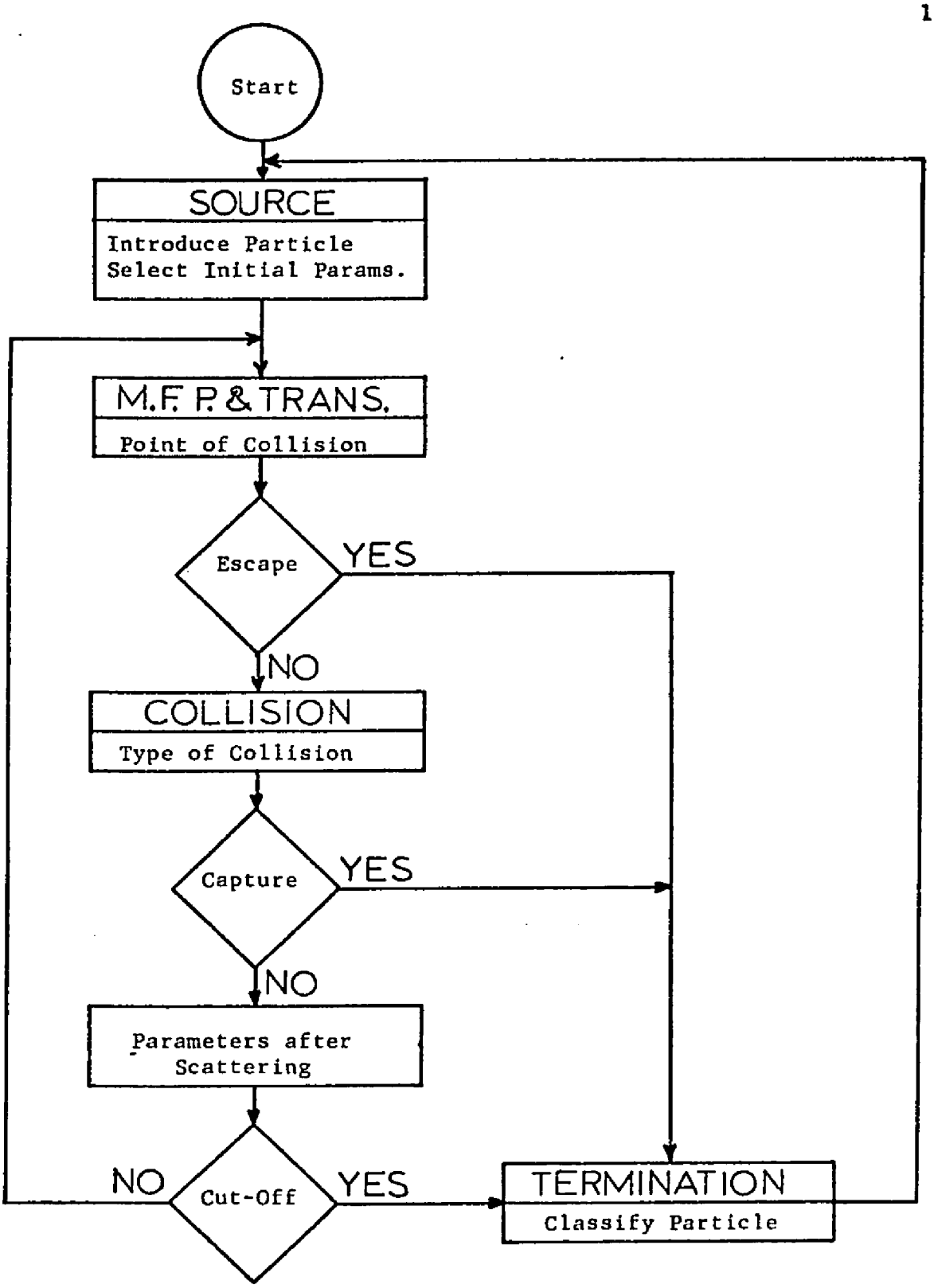

Figure B-1. Generalized Flow Diagram of Electron Transport Simulation.

particular calculation, electrons emerge from the source routine with depth parameter $z = z_o$. Thus, the only particle parameter in the source routine that needs to be chosen from a distribution function is the direction cosine w. Because the conversion electrons are emitted isotropically, the problem of choosing a direction cosine is equivalent to selecting an elemental strip of area $2\pi \sin\theta d\theta = dw$ on the unit sphere. Dividing by 4π, the total area of the unit sphere, the probability density function becomes $\rho(w) = \frac{dw}{2}$. Since the integral of $\rho(w)$ is a monotonically increasing function of w with minimum and maximum values of zero and one, $\rho(w) = \int_{-1}^{w} \frac{dw}{z}$ can be identified as a probability distribution function. According to the fundamental principle of the Monte Carlo method (116), if the direction cosines are chosen according to $\rho(w) = r$, where r denotes a random number on the range $0 \leq r \leq 1$, the direction cosines will be distributed in accordance with the probability density function. Thus, $r = \rho(w) = \frac{1}{2}(w + 1)$, or $w = (2r - 1)$ and w is equally distributed over the range $-1 \leq w \leq 1$ as required by the probability density function.

In this problem electrons which emerge from the surface into the acceptance angle of the spectrometer are considerably more important than other electrons, and it is desirable to sample a certain region of the angular distribution more thoroughly. For example, electrons emitted with direction cosines in the range $-1 \leq w \leq \bar{w}$, where $\bar{w}$ is some maximum direction cosine on the order

of the cosine of the spectrometer acceptance angle, are more likely to be detected. Source electrons can be given equal liklihood of starting on this range or its complement $\bar{w} \leq w \leq 1$, provided that the weights $(1 - \bar{w})$ and $(1 + \bar{w})$ are properly assigned. In this way about half of all source particles, of relatively smaller weight $(1 - \bar{w})$ originate in the importance cone $-1 \leq w \leq \bar{w}$, while the total weight processed for N electrons has the correct expectation value, i.e., $\frac{1}{2}N(1 - \bar{w}) + \frac{1}{2}N(1 + \bar{w}) = N$. The value of the prejudiced source routine is that the statistical accuracy can be much improved although the number of electrons introduced by the source routine remains the same. A flow chart (116) for the prejudiced source routine is presented in Figure B-2.

B.2.2 The Mean Free Path and Transmission Routine

In all problems a routine is required which conducts a particle from an arbitrary point to its next point of collision, or departure, if a boundary is reached without collision. The mean free path for collision, λ, is defined in terms of the total cross section, σ_t, as $\lambda = 1/N\sigma_t$, where N is the number of scattering centers per unit volume. The probability that an electron travels a distance without collision and then collides in the interval $(\ell, \ell + d\ell)$ is given by $\frac{a\ell}{\lambda} e^{-\ell/\lambda}$. Integrating this quantity from the lower limit 0 to the upper limit ℓ yields $\frac{1}{\lambda^2}(1 - e^{-\ell/\lambda})$, which becomes $\frac{1}{\lambda^2}$ as ℓ is extended to infinity. Thus, the normalized probability distribution function becomes $P(\ell) = (1 - e^{-\ell/\lambda})$,

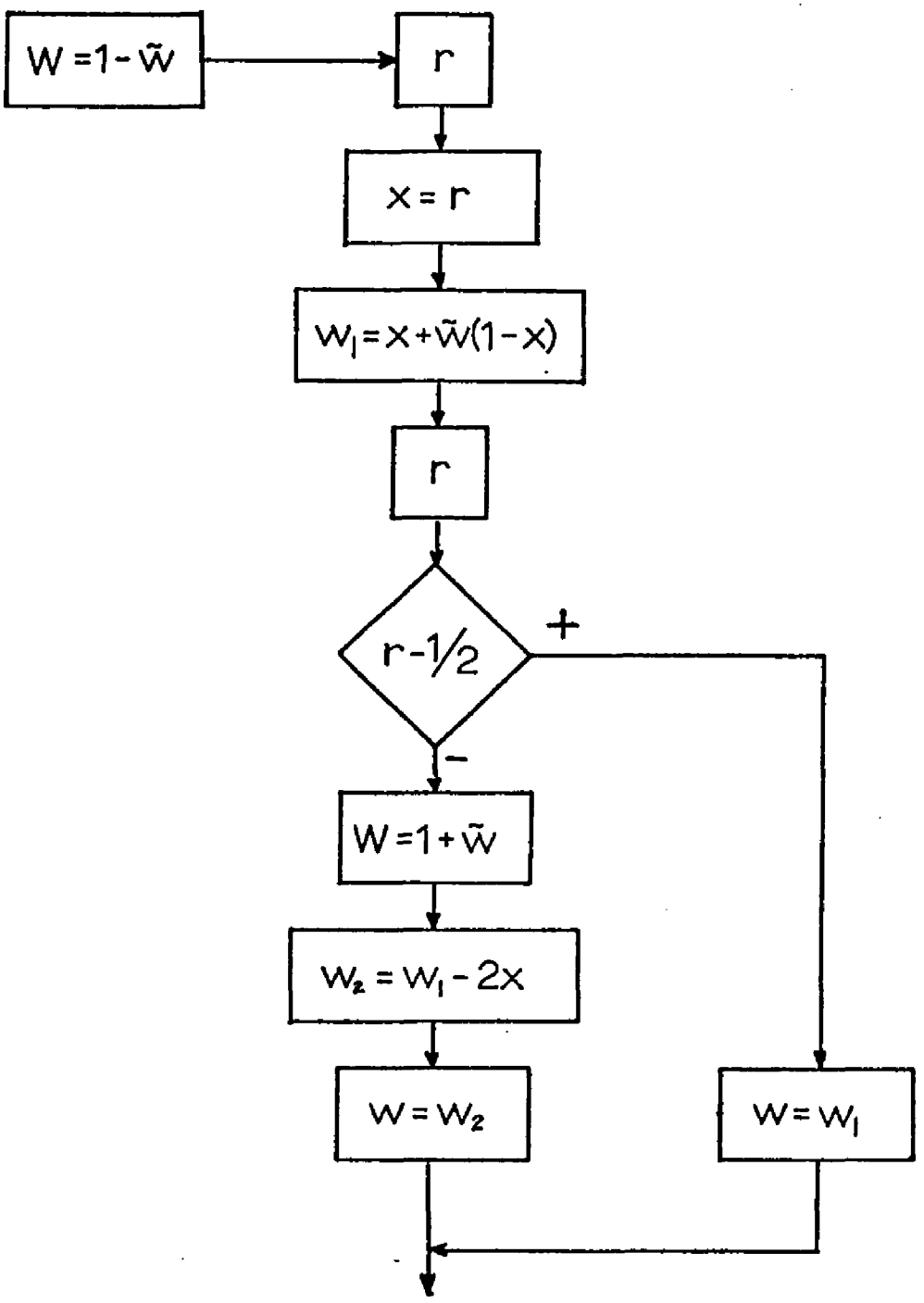

Figure B-2. Flow Diagram of Prejudiced Source Subroutine.

and the distance ℓ to the first collision is computed according to the fundamental principle of Monte Carlo as $r = P(\ell) = 1-e^{-\ell/\lambda}$, or $\ell = -\lambda \ln(1 - r)$. Since r is randomly distributed on $0 \leq r \leq 1$, equivalently, ℓ can be computed according to

$$\ell = -\lambda \ln r \tag{B-1}$$

If the distance from the source to the boundary along a particular direction is L, then for a beam of N particles, $Ne^{-L/\lambda}$ will escape without collision. If $L \ll \lambda$, most of the source particles will escape, thereby requiring needlessly large numbers of particles to produce effective samples. For such a problem a significant improvement results from the device of forcing collisions to occur. For example, if a particle leaves the source with weight W, a partial weight $We^{-L/\lambda}$ is transmitted and tallied in a category reserved for total transmission without collision. A position of first collision is then determined on the interval $0 \leq \ell \leq L$ for the particle of remaining weight $W(1 - e^{-L/\lambda})$ according to the formula $r = P(\ell)/P(L)$, where $P(\ell) = 1-e^{-\ell/\lambda}$. Thus, the position of the forced first collision is determined by

$$\ell = -\lambda \ln \left\{ 1 - r \left[1 - e^{-L/\lambda} \right] \right\} \tag{B-2}$$

The device of forcing collisions of the non-transmitted weight may be applied to collisions after the first, provided the particle is still directed toward a boundary and the particle weight is greater than some minimum weight cut off, W_{min}. The combined mean free path and

transmission flow chart, including the forced collision routine in addition to the standard routine, is shown in Figure B-3.

B.2.3 The Collision Routine for Electrons

In the previous routine, the immediate fate of a particle was determined on the basis of the equation, $\ell = -\lambda \ell n\, r$, as a collision or an escape at the surface. The collision routine is devoted to determining what happens, in a probabilistic sense, when an electron undergoes a collision. After the collision the new values of ΔE, w, and ν, as well as the cosine of the laboratory angle of deflection from the incident line of flight must be calculated; this task is performed by the collision routine. The principle types of collisions suffered by low energy electrons in condensed matter are: (a) elastic nuclear scattering; (b) electron-plasmon interactions; and (c) single electron-electron collisions. These interactions are discussed in detail in Appendix A; results from that discussion will be employed here from the point of view of the Monte Carlo technique.

Collision processes (b) and (c) above are both inelastic events in which an incident electron may lose energy. Letting Σ_e and Σ_i denote the total elastic and inelastic macroscopic cross sections where $\Sigma_i = \Sigma_p + \Sigma_{e-e}$, the total macroscopic cross section for interaction, Σ_t, is computed according to $\Sigma_t = \Sigma_e + \Sigma_i$. The branching decisions for determining the particular type of collision are facilitated by using random numbers.

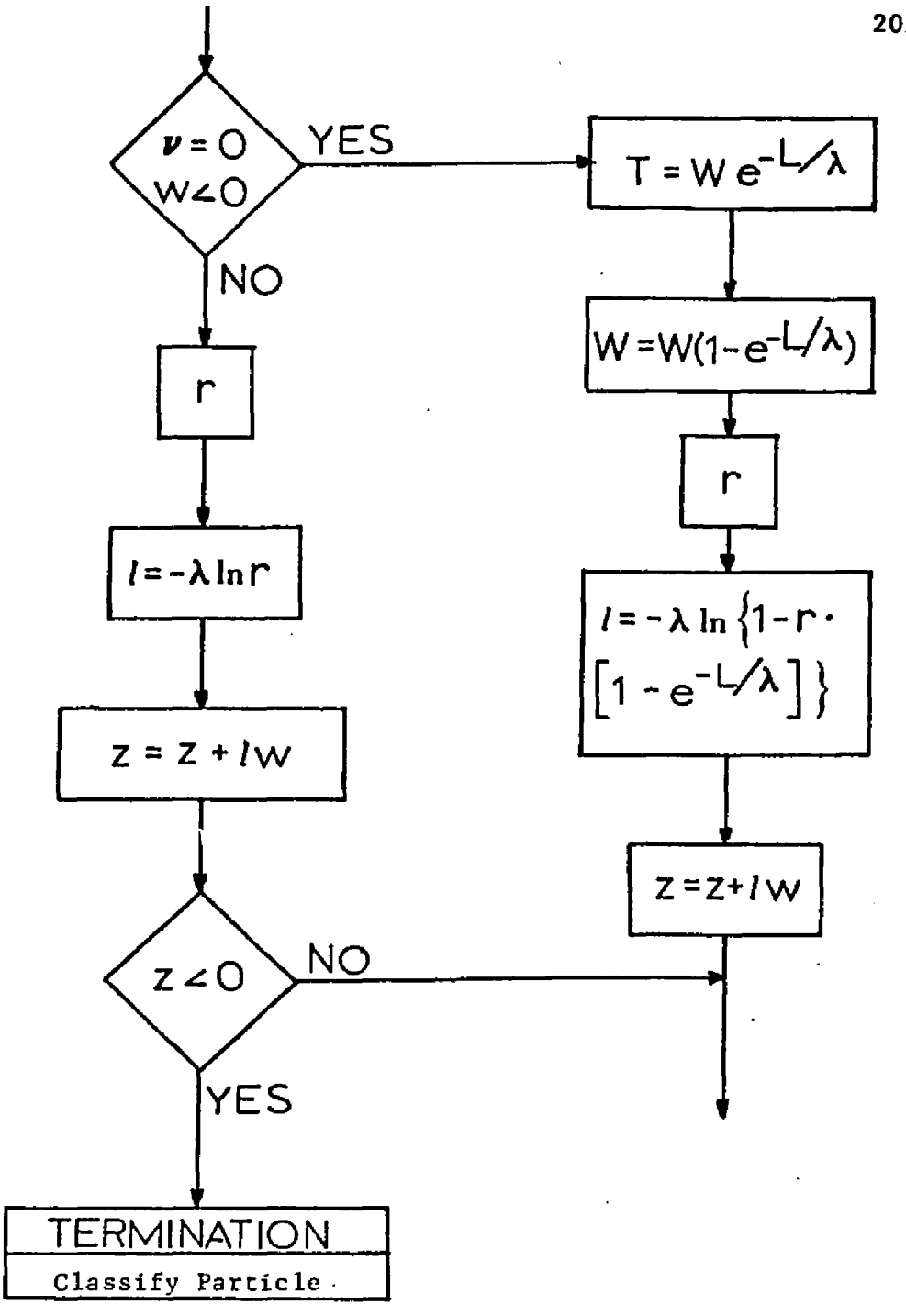

Figure B-3. Flow Diagram of Mean Free Path and Transmission Routine.

For example, if a random number r is less than the ratio $\frac{\Sigma_i}{\Sigma_t}$, the collision is specified as inelastic; while if another random number is less than $\frac{\Sigma_p}{\Sigma_i}$, the collision is specifically a plasmon interaction. Having determined the type of collision, the particle parameters are evaluated based on the details of that collision.

In the case of elastic nuclear collisions the Goudsmit-Saunderson formula for the differential electron cross section per atom for scattering into a solid angle $d\Omega = 2\pi \sin\theta d\theta$ is given by

$$\frac{d\sigma_e}{d\Omega} = \left(\frac{e^2 Z}{mv^2}\right)^2 (1 - \cos\theta + \tfrac{1}{2}\theta_1)^{-2} \qquad \text{(B-3)}$$

θ_1 is a constant equal to $\lambda\!\!\!^{-}/a$, where $\lambda\!\!\!^{-} = \frac{\hbar}{mv}$ and $a = a_o Z^{-1/3}$, and a_o is the Bohr radius. The integration of Equation (B-3) over all scattering angles θ yields the total elastic cross section per atom, σ_e, which can be written as

$$\sigma_e = \frac{8}{\theta_1(\theta_1 + 4)} \cdot \frac{2\pi e^4 Z^2}{p^2 v^2} \qquad \text{(B-4)}$$

The probability density function for elastic scattering is obtained by dividing the differential cross section by the total cross section. This result is $p_e(\theta) = \frac{\theta_1(\theta_1 + 4)}{8} \frac{\sin\theta}{(1 - \cos\theta + \theta_1)^2}$,

and the probability distribution function for elastic scattering at an angle ψ_1, is given according to $P_e(\psi_1) = \int_0^{\psi_1} P_e(\theta)d\theta$ $= \frac{(1 - \cos\psi_1)(\theta_1 + 4)}{2(\theta_1 + 2(1 - \cos\psi_1))}$. In the Monte Carlo technique the scattering angle is selected according to $P_e(\psi_1) = r$, where r is a random variable on the range $0 \leq r \leq 1$. Explicit evaluation of the scattering angle yields

$$\cos\psi_1 = 1 - \frac{2r\theta_1}{\theta_1 + 4(1 - r)} \qquad \text{(B-5)}$$

The inelastic electron loss processes are not so easily characterized as is elastic nuclear scattering primarily because of the difficulty in distinguishing between the two most important loss mechanisms, the plasmon interaction and single electron-electron collisions resulting in interband transitions. Most of the experimental characteristic energy loss work has been done on the pure elements, and of these an emphasis has been placed on those which exhibit plasma oscillations. Such elements (e.g. Al, Mg, and Be) are characterized by having small binding energies for their valence electrons and large binding energies for the core electrons. The valence electrons are then considered to constitute a free electron gas and the plasma theory is directly applicable. On the other hand, for the transition metals (of which Fe and Ta are members) the electronic d band is incompletely filled and there is no sharp distinction between free and bound electrons. It is therefore to be

expected that the observed loss value may differ from $\hbar\omega_p$ due to the strong influence of interband collisions. Nozieres and Pines (117) qualitatively predict that on passing from the first to the last metal in a transition element group, the observed loss values will first be greater than and then become less than $\hbar\omega_p$, if the calculation is made assuming that all 3d and 4s electrons are free. Nozieres and Pines also indicate the correlation between the optical properties of a solid and its characteristic energy losses. They show that the loss peaks due to plasma excitation should not appear in the optical absorption spectra at corresponding absorption energies and that a large increase in the optical transmittivity with increasing frequency should occur at $\hbar\omega_p$.

Early measurements on the characteristic loss spectra performed by Robins and Swan (118) for the first group of transition metals indicated that for elements occurring early in the group the electrons in both the s and d bands must be considered to be free, but that for the elements of higher atomic number at least some electrons in these bands are more tightly bound, as shown by a decrease in plasmon energy below the value given by the simple theory. Later experiments performed by Lynch and Swan (119) for the second and third series transition metals also support this conclusion.

The energy dependence of the differential cross section for single inelastic scattering into a solid angle $d\Omega = 2\pi \sin\theta \, d\theta$

by the volume plasma process is given by Equation (A-34) of Appendix A

$$d^2(N\sigma_p) = \frac{1}{2\pi^2 a_o E} \cdot \frac{1}{\theta^2 + \theta_E^2} \left[-\mathrm{Im}\left(\frac{1}{\epsilon}\right)\right] dE d\Omega \qquad \text{(B-6)}$$

using the Lindhard dielectric constant for a free electron gas where $\theta_E = \frac{\hbar\omega_p}{2E}$, a_o is the Bohr radius, N is the free electron density, and E is the incident electron energy. Because of the plasma dispersion relation (Equation A-30), the value of $\hbar\omega_p$ depends on the scattering angle θ to a small degree. Integrating Equation (B-6) over all allowed scattering angles yields

$$d(N\sigma_p) = \frac{1}{\pi a_o E} \ln\left(\frac{\theta_c}{\theta_e}\right) \left[-\mathrm{Im}\left(\frac{1}{\epsilon}\right)\right] dE \qquad \text{(B-7)}$$

assuming the cut-off scattering angle, θ_c, is much greater than θ_E. Since the behavior of the denominator of the quantity $\left[-\mathrm{Im}\left(\frac{1}{\epsilon}\right)\right]$ is approximately that of a Lorentzian, integration of this quantity over all energy losses yields approximately $\frac{\pi}{2}\omega_p$, and the total cross section for plasmon interaction is evaluated as

$$\sigma_p = \frac{\theta_E}{N a_o} \ln \frac{\theta_c}{\theta_E} \qquad \text{(B-8)}$$

Thus, the probability distribution for electron scattering at an angle ψ_1, is given by

(B-9)

$$P_p(\psi_1) = \frac{1}{2\pi \ell n(\theta_c/\theta_E)} \int_0^{\psi_1} \frac{2\pi\theta\, d\theta}{\theta_E^2 + \theta^2} = \frac{\ell n \dfrac{\left(\theta_c^2 + \theta_E^2\right)^{\frac{1}{2}}}{\theta_E^2}}{\ell n(\theta_c/\theta_E)}$$

The scattering angle can then be evaluated as $P_p(\psi_1) = r$, which gives

$$\psi_1 = \theta_E \left\{ (\theta_c/\theta_E)^{2r} - 1 \right\}^{\frac{1}{2}} \qquad \text{(B-10)}$$

The energy dependence of the plasmon interaction cross section is assumed to be suitably approximated by a normalized Lorentzian. Hence, the probability distribution for an energy loss ΔE is given by

$$P_p(\Delta E) = \frac{1}{\frac{\pi\Gamma}{2}} \int_{-\infty}^{\Delta E} \frac{dE}{1 + \left(\frac{E - \Delta E_o}{\Gamma/2}\right)^2} = \frac{1}{\pi} \operatorname{Tan}^{-1}\left(\frac{\Delta E - \Delta E_o}{\Gamma/2}\right) \qquad \text{(B-11)}$$

where $\Delta E_o = \hbar\omega_p$, and Γ represents the full width at half maximum of the loss peak. The plasmon energy loss can then be computed as $P_p(\Delta E) = r$ which yields

$$\Delta E = \Delta E_o + \frac{\Gamma}{2} \tan(\pi r) \qquad \text{(B-12)}$$

A flow chart of the collision routine including only elastic nuclear scatterings and plasmon interactions is shown in Figure B-4.

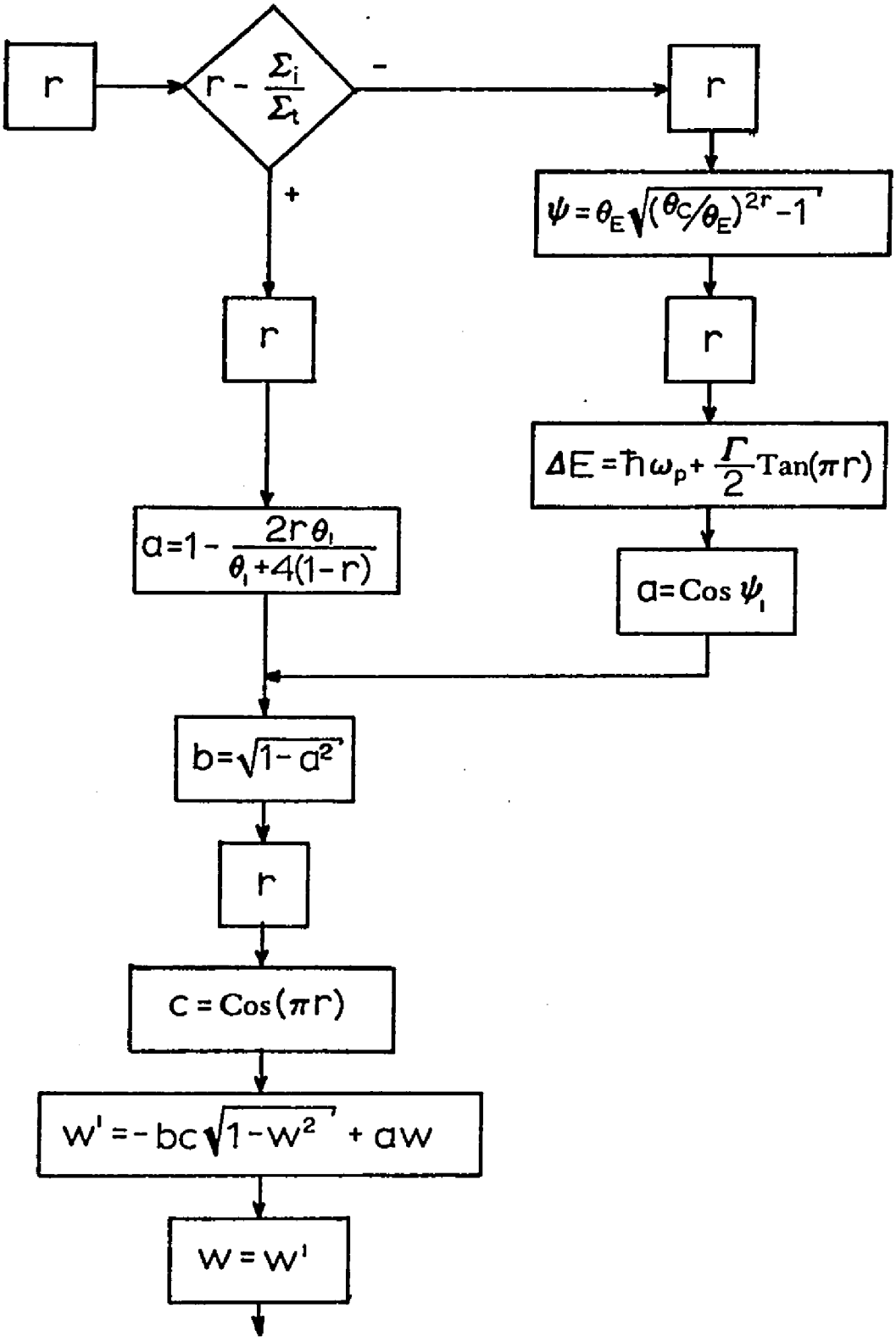

Figure B-4. Flow Diagram of Collision Routine.

Once the scattering angle, ψ_1, has been determined for a particular collision, the new direction cosine must be computed before the flight of the particle can be continued. The calculation of the coordinate transformation equations (116) is straight forward but tedious and will not be considered here. The result of the transformation for the special case of slab geometry is that the new direction cosine w' is related to the direction cosine w of the particle before the collision according to

$$w' = -c\sqrt{1 - a^2}\sqrt{1 - w^2} + aw \qquad \text{(B-13)}$$

where $a = \cos\psi_1$, and $c = \cos\delta$ where δ is the azimuthal angle of the collision uniformly distributed on $-\pi \leq \delta \leq \pi$. Since $\cos(-\delta) = \cos\delta$, δ can be limited to the range $0 \leq \delta \leq \pi$, and, hence, calculated according to $\delta = \pi r$, where r is randomly distributed on $0 \leq r \leq 1$. The simple, purely geometric routine for computing the direction cosine after collision forms the lower half of the flow diagram of Figure B-4.

B.2.4 The Termination Routine

There may be many possible terminal events in the history of a particle. The general function of the termination routine is to correctly classify any particle which escapes the system. Of primary importance in the present problem is the classification of electrons which emerge from the surface according to the values of the energy loss and direction cosine parameters. Thus, for an

electron of weight W which emerges with energy loss and direction cosine parameters such that $\Delta E_{i-1} \leq \Delta E \leq \Delta E_i$ and $w_{j-1} \leq w \leq w_j$, the weight W is accumulated in the $\left|ij\right|$ tally box. Other important terminal events that need to be considered include capture, loss to a maximum energy loss cut off, and loss to a maximum depth cut off.

Having considered the operation of each routine separately, the generalized flow diagram of the Monte Carlo method (Figure B-1) is more easily understood.

(1) The source routine introduces the particles one by one and assigns the appropriate initial particle parameters.

(2) The particles then pass to the mean free path and transmission routine which calculates the point of collision. If there is no collision, the particle emerges from the surface and is classified accordingly in the termination routine. If there is a collision, new particle parameters are determined in the collision routine.

(3) If the new parameters do not exceed any parameter cut off values the particle is returned to the mean free path and transmission routine.

(4) If the particle is cut off or it emerges from the surface, it is classified accordingly in the termination routine.

B.3 The Source-Weighted Spectrum

In order to compute the source-weighted spectrum, i.e., the energy distribution of electrons emerging from the source computed according to $\int_E^\infty W(E' \longrightarrow E,z)\ J_c(E')dE'$, the angular acceptance aperture of the spectrometer, which limits the range of acceptable direction cosines, must first be determined. Assuming that the limiting direction cosine w_ℓ is known, the loss spectrum can be described in terms of the probability, $P_i(z)$, that an electron emitted with energy E_o at depth z emerges from the surface within the acceptance angle of the spectrometer with a final energy E such that $\Delta E_{i-1} \leq \Delta E = E_o - E \leq \Delta E_i$. The probability $P_i(z)$ can be defined in terms of the previously given P_{ij} as

$$P_i(z) = \sum_{j=1}^{J} P_{ij}(z) \qquad \text{(B-14)}$$

where J is defined by $w_J \leq w_\ell$. $P_i(z)$ thus represents the Monte Carlo approximation of the quantity $W(\Delta E_{i-1} \leq \Delta E = E_o - E \leq \Delta E_i, z)$.

With this result only an integration over the natural conversion electron line shape, $J_c(E')$, is required to compute the conversion electron spectrum that emerges from the sample into the acceptance angle of the spectrometer. From Equation (2-16) and the results of this section, the integral $\int_E^\infty dE'\ J_c(E')\ .\ W(E' \longrightarrow E,z)$ can be approximated as

(B-15)

$$\int \simeq \int_{E}^{E+\Delta E_1} P_1(z)\, J_c(E')dE + \int_{\Delta+\Delta E_1}^{E+\Delta E_1+\Delta E_2} P_2(z)\, J_c(E')dE$$

$$+ \ldots + \int_{E+\sum_{i}^{n-1}\Delta E_i}^{E+\sum_{i=1}^{n}\Delta E_i} P_n(z)\, J_c(E')dE + \ldots = P_1(z) \int_{E}^{E+\Delta E_1} J_c(E')dE'$$

$$+ \ldots + P_n(z) \int_{E+\sum_{i=1}^{n-1} E_i}^{E+\sum_{i=1}^{n}\Delta E_i} J_c(E')dE' + \ldots$$

$$= \frac{1}{\pi} \left\{ P_1 \left[\tan^{-1}\left(\frac{E - E_o + \Delta E_1}{\frac{1}{2}\Gamma} \right) - \tan^{-1}\left(\frac{E - E_o}{\frac{1}{2}\Gamma} \right) \right] + \ldots + \right.$$

$$P_n \left[\tan^{-1}\left(\frac{E - E_o + \sum_{i=1}^{n} E_c}{\frac{1}{2}\Gamma} \right) - \tan^{-1} \right.$$

$$\left. \left. \left(\frac{E - E_o + \sum_{i=1}^{n-1} \Delta E_i}{\frac{1}{2}\Gamma} \right) \right] + \ldots \right\}$$

If the energy intervals are assumed to be equal in size, i.e., $\Delta E_i = \Delta E$, Equation (B-15) reduces to

(B-16)

$$\int \simeq \frac{1}{\pi} \left\{ -P_1 \tan^{-1}\left(\frac{E-E_o}{\frac{1}{2}\Gamma} \right) + \sum_{n=1}^{\infty} (P_n - P_{n+1}) \tan^{-1}\left(\frac{E-E_o+ n\Delta E}{\frac{1}{2}} \right) \right\}$$

In practical computations it is necessary to terminate the summation at some $n = n_{max}$, which corresponds to an effective upper limit, E_{max}, for the integration as given by

$$\int_{E}^{E_{max}} dE' \; J_c(E') \; W(E' \longrightarrow E,z).$$ As $W(E' \longrightarrow E,z) = 0$ for $E > E'$, $J_c(E')$ is the most important term in the integrand and E_{max} must be chosen large enough to encompass the range of $J_c(E')$. Since $J_c(E')$ is a normalized Lorentzian function, a suitable upper limit value is $E_{max} = E_o + 3\Gamma_c$. Assuming equal energy intervals, n_{max} corresponds to the smallest integer such that $n\Delta E \geq E_{max} - E$.

B.4 The Observed Line Shape

Because of the finite resolution of the beta spectrometer, the conversion electron spectrum of the previous section will be distorted when observed experimentally. Since the instrumental window curve will probably not be Lorentzian in shape while the natural electron line shape is Lorentzian, the width of the observed peak will be neither the sum (Lorentzian) nor the root of the sum of the squares (Gaussian) of the widths of the two distributions. A general empirical formula for the experimentally observed line width, Γ_L, has been written as (59)

$$\Gamma_L^{\,n} = \Gamma_{sp}^{\,n} + \Gamma_e^{\,n} \qquad \text{(B-17)}$$

where Γ_{sp} is the width of the spectrometer window curve, Γ_e is the natural width of the atomic level involved, and n takes a value between 1 and 2.

To obtain the observed line shape, the source-weighted spectrum of the previous section is folded with the instrumental window function $\chi(E,E')$. The window function is assumed to be a Gaussian whose standard deviation is related to Γ_{sp}. The folding integral is given by Equation (2-17) which can be evaluated by Gaussian quadrature, with the integration limits specified as $E_{max} = E + 3\sigma$ and $E_{min} = E - 3\sigma$.

APPENDIX C. FREDHOLM INTEGRAL EQUATIONS OF THE FIRST KIND

C.1 Introduction

Many problems of mathematical physics can be reduced to the study of the equation

$$A\phi = f \tag{C-1}$$

where f is a known function or vector, A is a linear operator, and ϕ is the unknown function or vector. The notion of correctness given by Hadamard (120) is very importamt in the investigation of such problems; a convenient statement of the notion of correctness has been given by Lavrentiev (121). If ϕ and F are complete metric spaces, and if $A\phi$ is a function with domain of definition Φ and range of values F, the problem of solving Equation (C-1) is said to be properly posed if the following conditions are satisfied:

(i) The solution exists for any $f \in F$

(ii) The solution is unique in Φ

(iii) The solution ϕ depends continuously on f.

These requirements are satisfied if there exists a function Bf, defined and continuous over all F, which is inverse to the function $A\phi$.

In some practical situations, the operator A may blur sharp details of the unknown ϕ; a variation, $\delta\phi$, with large amplitude and large oscillations may yield only an imperceptible change, δf, in the data. Conversly, a small measurement error, δf, may produce large oscillations, $\delta\phi$, in the solution. Such a mathematical problem clearly does not satisfy the correctness notion, and is said to be incorrectly posed. All Fredholm integral equations of the first kind (122)

$$\int_{c_1}^{c_2} a(x,y)\ \phi\ (y)dy = f(x) \qquad \text{(C-2)}$$

in which the kernel $a(x,y)$ is continuous, are incorrectly posed problems in the classical sense of Hadamard. To verify that the integral operator of (C-2) does not have a bounded inverse, assume that $\phi(y)$ is the solution and add to it the function $\phi_m = \sin(my)$. For any integrable kernel it is know that

$$f_m = \int_{c_1}^{c_2} a(x,y)\ \sin(my)dy \rightarrow 0 \quad \text{as} \quad m \rightarrow \infty \qquad \text{(C-3)}$$

Hence, an infinitesimal change f_m in the data could cause a finite change ϕ_m in the solution.

As shown by Twomey (123) the extent of the difficulty of solution depends in large part upon the shape of the kernel function, $a(x,y)$. The smoothness of the kernel $a(x,y)$ with respect to y can be expressed as an explicit property of the spectral kernel function, $a(x,w)$, the Fourier transform of

$a(x,y)$. For any particular value of y, $a(x,w)$ is analogous to a low pass filter; consequently, the physical measurement system represented by the kernel will be inherently insensitive to high frequency fine structure in the solution, and any attempt to find the exact inverse would be unreasonable. In general, the narrower the width of the kernel, the wider the pass band of $a(x,w)$ and the better the fine structure of $\phi(y)$ can be seen in $f(x)$; conversely, the wider the kernel, the narrower the pass band of $a(x,w)$ and the greater the smoothing effect on $\phi(y)$.

Shaw (78) has emphasized the four points to be kept in mind when attempting to solve this type of equation:

(1) The solution, ϕ, must always be determined in the presence of background noise.

(2) The physical process of recording the data, f, is an important source of error.

(3) Certain data functions cannot be produced by the physical system.

(4) Because of the smoothing property, certain sources will not produce a measureable response.

From (1) and (2) above, any measurement whatsoever will have some associated error, and from (4) additionally, any attempts to solve ill-posed problems would appear to be pointless. In fact, as exhibited by numerous authors, direct calculations of the solution using the formula

$$\phi = A^{-1}f, \quad \text{or} \quad \phi = (A^TA)^{-1}A^Tf \tag{C-4}$$

yield large oscillating, meaningless results. In actual practice, however, some additional information can almost always be brought to bear. The physics of the problem often provides such auxiliary information; for example, the unknown, ϕ, may be limited to positive values only. Often rough bounds exist for errors in the data, and it may be known that the solution is reasonably smooth in a certain interval. In some cases, prior experimentation may have produced enough information on which to base an initial estimate of the solution. In all these examples, the auxiliary information is significant, and any method of unfolding the integral equation should take advantage of the a priori information as much as possible. Since the data, $f(x)$, will not be known accurately, the problem should be restated as

$$\int_{c_1}^{c_2} a(x,y)\ \phi(y)dy = f(x) + \epsilon(x) \tag{C-5}$$

where $\epsilon(x)$ is some arbitrary error function. Instead of a unique solution, there will be a family of solutions; the a priori information should be utilized to determine an appropriate solution, $\phi(y)$, from the family Φ.

C.2 Solution Methods

No comprehensive reviews of unfolding methods are presently available, although brief comparisons of selected methods have been

given by Marshall (124), Lavrentiev (121), and Shaw (78). The methods of solution often fall into three general categories:

(1) least square methods,

(2) iterative methods,

(3) smoothing methods.

In all of these methods, Equation (C-5) is approximated by a matrix equation using a suitable quadrature formula to represent the integral as given by

$$f_i + \epsilon_i = \sum_{j=1}^{N} a_{ij}\phi_j \omega_j \qquad i = 1, \ldots, M \tag{C-6}$$

where M is the total number of data points, N is the total number of quardature points, the ω_j are the weights associated with the quadrature, and $f_i = f(x_i)$, $\phi_j = \phi(y_i)$, $a_{ij} = a(x_i, y_i)$. Introducing the matrix notation $A = (a_{ij}\,\omega_j)$, $\phi = (\phi_j)$, $f = (f_i)$, $\epsilon = (\epsilon_i)$, Equation (C-6) becomes

$$\underline{f} + \underline{\epsilon} = A\underline{\phi} \tag{C-7}$$

C.2.1 Least Squares Methods

The success of the least squares technique depends upon finding an appropriate functional form that will adequately describe the solution ϕ. The error vector is ignored and the various parameters in the function are then varied until those values are found which minimize the sum of the squares of the differences

between the data points, f_i, and the points, f_{iapp}, that are obtained from the approximate solution. If enough a priori information exists to provide a suitable functional form, the least squares method will usually provide an adequate approximation to the solution vector. The only restriction is that the number of data points must be greater than the number of parameters to be determined. A suitable function is not often available, however, and another method must be used. Also, as shown by Twomey (123), the nearness of the data, f_i, and f_{iapp} does not reliably gauge the nearness of the true solution ϕ and the least squares solution.

C.2.2 Iterative Methods

Although lacking in mathematical elegance, iterative methods have quite often been used for solving integral equations of the first kind (125) - (128). As in the least squares method the error vector of Equation (C-7) is neglected. Following Gold (129), the matrix A is assumed nonsingular and an attempt is made to find a real diagonal matrix D such that $d_{ii} = \phi_i/f_i$, of $\underline{\phi} = D\underline{f}$. After an initial estimate of the solution vector $\underline{\phi}^{(o)}$, the iteration proceeds according to the algorithm

$$\underline{f}^{(k)} = A\underline{\phi}^{(k)}$$

$$d_{ii}^{(k+1)} = \phi_i^{(k)}/f_i^{(k)} \qquad \text{(C-8)}$$

$$\underline{\phi}^{(k+1)} = D^{(k+1)}\,\underline{f}^{(k)}$$

and continues until a particular convergence criterion is satisfied. The primary difficulty with this iterative method lies in proving the convergence to an appropriate solution under less restrictive assumptions than those used by Gold. Again, the nearness of the data, f_i, and the data, f_{iapp}, obtained from the approximate solution cannot in general be used as a convergence criterion. According to Marshall (124) the iterative techniques should give satisfactory results when the uncertainties in the data are small and when the kernel is quite narrow so that $\underline{f}$ does not differ greatly from $\underline{\phi}$.

C.2.3 Smoothing Methods

Due to measurement errors and the smoothing properties of the integral there may exist an infinite family $\tilde{\Phi}$ of solutions. As direct methods have shown, most of these solutions will be implausible because of rapid oscillations. An empirical method suggested by Phillips (130), and independently, Tihonov (131), seeks an approximate solution that is constrained to be the smoothest in some sense. Specifically, the solution $\bar{\phi}$ was sought that minimized the following additive functional

(C-9)

$$Q = \sum_{j=1}^{M} \left(\sum_{i=1}^{N} a_{ji} \overline{\phi}_i - g_j \right)^2 + \gamma \sum_{i=1}^{N} \left(\overline{\phi}_{i-1} - 2\overline{\phi}_i + \overline{\phi}_{i+1} \right)^2$$

where the weighting parameter, γ, is a Lagrangian multiplier, and the summation it multiplies (the regularizing functional in the terminology of Tihonov) is a measure of the mean-square derivative of $\overline{\phi}$. As shown by Phillips, this method leads to replacement of A^{-1} in Equation (C-4) by $(A + \gamma H)^{-1}$, where H is a matrix representing the smoothing functional. For even small values of the smoothing parameter, γ, the matrix $(A + \gamma H)$ is much better conditioned than A.

The approach of Phillips was immediately applied and extended by Twomey (123), and later, Biggs (132). Twomey suggested estimates of the general type

$$\phi = B^{-1} (A^T \underline{f} + \gamma \phi^{(o)}) \qquad (C\text{-}10)$$

where $B = A^T A + \gamma H$, H is the identity matrix, and $\phi^{(o)}$ is a prior estimate of the solution. In addition, Twomey has evaluated the correct form of the matrix H using several different smoothing criteria, assuming the prior estimate of ϕ is $\phi^{(o)} = \underline{0}$.

The Lagrangian multiplier can be thought of as a weighting factor; decreasing γ results in less weight given to the constraint. If the errors are bounded, i.e., $\sum_j \epsilon_j^2 = e^2$, then γ can be implicitly determined; this bound is seldom known, however. In practice, it is only necessary to determine a solution for several

values of γ , compute $A\phi$ for each, and compare it with f to find $\sum_j \epsilon_j^2$. According to Marshall, the first value for which $\sum_j \epsilon_j^2$ is not less than an estimated safe upper bound of $\sum_j \epsilon_j^2$ is usually the best one.

C.2.4 Recent Developments

The minimization of Equation (C-9) has been viewed by Bellman (133) as a multistage decision process, and the theory of dynamic programming has been applied to derive a computational algorithm. To obtain reasonable results, however, a smoothing method must also be incorporated. At the present time this approach appears to be impractical.

The work of Strand and Westwater (134) has shown that for problems in which there is a thorough knowledge of the background and measurement errors including their full covariance matrices and an expected value of the solution itself, the arbitrariness in the best linear estimate of ϕ no longer remains. Their solution includes Twomey's estimate (with arbitrariness removed) as a special case.

While other statistical methods of solving improperly posed problems have been known since 1957 (135) according to Lavrentiev, the very recent approach of Franklin (77) appears to be the clearest and the most general. According to Franklin, if the improperly posed problem is replaced by its well-posed stocastic extension,

the best linear estimate of the solution based on the sample data can be computed if an estimate of the solution and the background- and instrument-generated noise processes are known. As restated and applied by Shaw (78), the computational method called best accessible estimation is a finite iteration scheme, of which the three essential ingredients are:

(1) A starting estimate of the solution.

(2) Iterative improvement of the estimate.

(3) A rule for terminating iteration.

Being only very recently developed, Franklin's method has not been widely applied to physical problems, although the numerical results of Shaw in connection with the instrument resolution problem would seem to indicate the value of this approach.

APPENDIX D. THE UNFOLD ALGORITHM FOR DACES1 AND DACES2

D.1 Introduction

The computer codes DACES1 and DACES2 both use the UNFOLD algorithm of Biggs and Amos to obtain solutions to a Fredholm integral equation of the first kind. This equation may be generally written as

$$G_i = \int_A^B R(\vec{x}_i, t)\hat{f}(t)dt + \hat{\epsilon}_i, \qquad i = 1, \ldots, NU. \tag{D-1}$$

where the G_i are approximate data values (the actual measurement data) containing errors $\hat{\epsilon}_i$, $R(\vec{x}_i, t)$ are known response functions, and $\vec{x}_i$ is a vector which specifies the response function parameters for the i^{th} data point. The solution estimate $f(t)$ of the unknown function $\hat{f}(t)$ is obtained from UNFOLD in terms of

$$G_i = \int_A^B R(\vec{x}_i, t)f(t)dt + \epsilon_i, \qquad i = 1, \ldots, NU. \tag{D-2}$$

where the residual errors, ϵ_i, are not, in general, equal to the errors, $\hat{\epsilon}_i$.

D.2 The Quadratic Form

UNFOLD obtains a solution estimate by minimizing a quadratic form subject to constraints, the estimate is then checked for consistency with the auxiliary information. The quadratic form is

defined by

$$Z = Z_u + Z_p + Z_s + Z_m \tag{D-3}$$

where

$$Z_u = \sum_{i=1}^{NU} \frac{1}{ERU_i^2} \left| \int_A^B R(\vec{x}_i, t) f(t) dt - G_i \right|^2 \tag{D-4}$$

$$Z_p = PMUL \sum_{i=1}^{NP} \frac{1}{ERP_i^2} \left| f(t_i) - P_i \right|^2 \tag{D-5}$$

$$Z_s = SMUL \int_{SML}^{SMR} \frac{1}{ERS^2(t)} \left| f^{(m)}(t) - S(t) \right|^2 dt \tag{D-6}$$

$$Z_m = QMUL \sum_{i=1}^{NM} \frac{1}{ERM_i^2} \left| \theta_i \left[f(t) \right] - \beta_i \right|^2 \tag{D-7}$$

From Equation (D-4) Z_u, the unfold term, is seen to be a weighted sum of squares of the residual errors ϵ_i, i.e., a measure of how the integral computed using the solution estimate compares with the actual measurement data. Z_p, the prior estimate term, measures the "closeness" of the solution estimate to any prior estimates, P_i, that may be available. The smoothing term, Z_s, measures the mean square deviation of the m^{th} derivation of the solution from an a priori estimate, $S(t)$. When $S(t) = 0$, this term prevents $f^{(m)}(t)$ from becoming too large thereby controlling oscillations. The final term, Z_m, is called the miscellaneous

auxiliary information term. $\theta_i\left[f(t)\right]$ denotes a linear operation on $f(t)$, and the β_i are the known approximate values. ERU, ERP, ERS, and ERM are the estimated errors in the data, the prior estimates, the smoothing function, and the miscellaneous information, respectively. The quadratic form just outlined is minimized subject to two types of constraints.

D.2.1 Equality Constraints

If it is known that linear operators Q_i operating on $\hat{f}(t)$ give the values H_i, these conditions can be imposed on the solution estimate by using the equality constraints

$$Q_i\left[f(t)\right] = H_i, \qquad i = 1, \ldots, NEC \tag{D-8}$$

D.2.2 Inequality Constraints

If linear operators L_i operating on $\hat{f}(t)$ are known to give values less than or equal to V_i, these constraints may be imposed on the solution estimate by requiring

$$L_i\left[f(t)\right] \leq V_i, \qquad i = 1, \ldots, NIC \tag{D-9}$$

D.3 Parameterization of the Solution Estimate

Expanding the solution estimate as

$$f(t) = \sum_{j=1}^{NC} C_j D_j(t) \tag{D-10}$$

where the $D_j(t)$ are a set of NC linearly independent functions

and the C_j are elements of the solution vector to be determined, the unfold term (Equation D-4) of the quadratic form becomes

$$Z_u = \sum_{i=1}^{NU} \frac{1}{ERU_i^2} \left\{ \sum_{j=1}^{NC} C_j \int_A^B R(\vec{x}_i,t)\, D_j(t)\, dt - G_i \right\}^2 . \qquad \text{(D-11)}$$

Defining the matrix element

$$AU_{ij} = \frac{1}{ERU_i} \int_A^B R(\vec{x}_i,t)\, D_j(t)\, dt \qquad \text{(D-12)}$$

and

$$BU_i = G_i/ERU_i \qquad \text{(D-13)}$$

Equation (D-11) becomes

$$Z_u = \sum_{i=1}^{NU} \left\{ \sum_{j=1}^{NC} AU_{ij}\, C_j - BU_i \right\}^2 \qquad \text{(D-14)}$$

Similarly, using Equation (D-10), Equations (D-5) and (D-7) become

$$Z_p = PMUL \sum_{i=1}^{NP} \left\{ \sum_{j=1}^{NC} AP_{ij}\, C_j - BP_i \right\}^2 \qquad \text{(D-15)}$$

$$Z_m = QMUL \sum_{i=1}^{NM} \left\{ \sum_{j=1}^{NC} AM_{ij}\, C_j - BM_i \right\}^2 \qquad \text{(D-16)}$$

where

$$AP_{ij} = D_j(t_i)/ERP_i \qquad \text{(D-17)}$$

$$BP_i = P_i/ERP_i \tag{D-18}$$

$$AM_{ij} = \theta_i\left|D_j(t)\right|/ERM_i \tag{D-19}$$

$$BM_i = \beta_i/ERM_i \tag{D-20}$$

A 20th order Gaussian quadrature is used to reduce the smoothing term (Equation (D-6)) to a convenient matrix form. For $m = 2$,

$$Z_s = SMUL \int_{SML}^{SMR} \frac{1}{ERS^2(t)} \left\{ \sum_{j=1}^{NC} D_j''(t)\ C_j - S(t) \right\}^2$$

$$\simeq SMUL \sum_{R=1}^{20} \frac{QS_R}{ERS^2(\nu_k)} \left\{ \sum_{j=1}^{NC} D_j''(\nu_k)\ C_j - S(\nu_k) \right\}^2 \tag{D-21}$$

where QS_k and ν_k are the quadrature weights and abscissas. Defining

$$AS_{Rj} = \sqrt{QS_k}\ \frac{D_j''(\nu_k)}{ERS(\nu_k)} \tag{D-22}$$

$$BS_k = \frac{\sqrt{QS_k}\ S(\nu_k)}{ERS(\nu_k)} \tag{D-23}$$

the smoothing term then becomes

$$Z_s \quad SMUL \sum_{k=1}^{20} \left\{ \sum_{j=1}^{NC} AS_{kj}\ C_j - BS_k \right\}^2 \tag{D-24}$$

Using Equation (D-10) in Equation (D-8), the equality constraints are now written as

$$\sum_{j=1}^{NC} E_{ij}\, C_j = H_i, \qquad i = 1, \ldots, NEC \tag{D-25}$$

where

$$E_{ij} = Q_i\, D_j(t) \tag{D-26}$$

Similarly the inequality constraint equations become

$$\sum_{j=1}^{NC} U_{ij}\, C_j \leq V_i, \qquad i = 1, \ldots, NIC \tag{D-27}$$

with

$$U_{ij} = L_i\left[D_j(t)\right] \tag{D-28}$$

To facilitate the handling of the least squares minimization problem the matrices previously defined are arranged as partitions of a larger matrix, QA_{ij}, such that

$$\left.\begin{aligned} QA_{ij} &= AU_{ij} \\ RB_i &= BU_i \end{aligned}\right\} \quad \begin{aligned} &i = 1, \ldots, NU \\ &j = 1, \ldots, NC \end{aligned} \tag{D-29}$$

$$\left.\begin{aligned} QA_{ij} &= (PMUL)\ AP_{kj} \\ RB_i &= (PMUL)\ BP_k \end{aligned}\right\} \quad \begin{aligned} &k = 1, \ldots, NP \\ &i = NU + k \\ &j = 1, \ldots, NC \end{aligned} \tag{D-30}$$

$$\left.\begin{aligned} QA_{ij} &= (SMUL)\ AS_{kj} \\ RB_i &= (SMUL)\ BS_k \end{aligned}\right\} \quad \begin{aligned} &k = 1, \ldots, NS = 20 \\ &i = NU + NP + k \\ &j = 1, \ldots, NC \end{aligned} \tag{D-31}$$

$$\left.\begin{aligned} QA_{ij} &= (QMUL)\ AM_{kj} \\ RB_i &= (QMUL)\ BM_k \end{aligned}\right\} \quad \begin{aligned} &k = 1, \ldots, NM \\ &i = NU + NP + NS + k \\ &j = 1, \ldots, NC \end{aligned} \tag{D-32}$$

The quadratic form Z of Equation (D-3) can now be written in terms of the least squares matrix QA and RB as

$$Z = \sum_{i=1}^{NU+NP+NS+NM} \left\{ \sum_{j=1}^{NC} QA_{ij}\ C_j - RB_i \right\}^2 \tag{D-33}$$

The unfolding problem can now be schematically diagrammed as shown below:

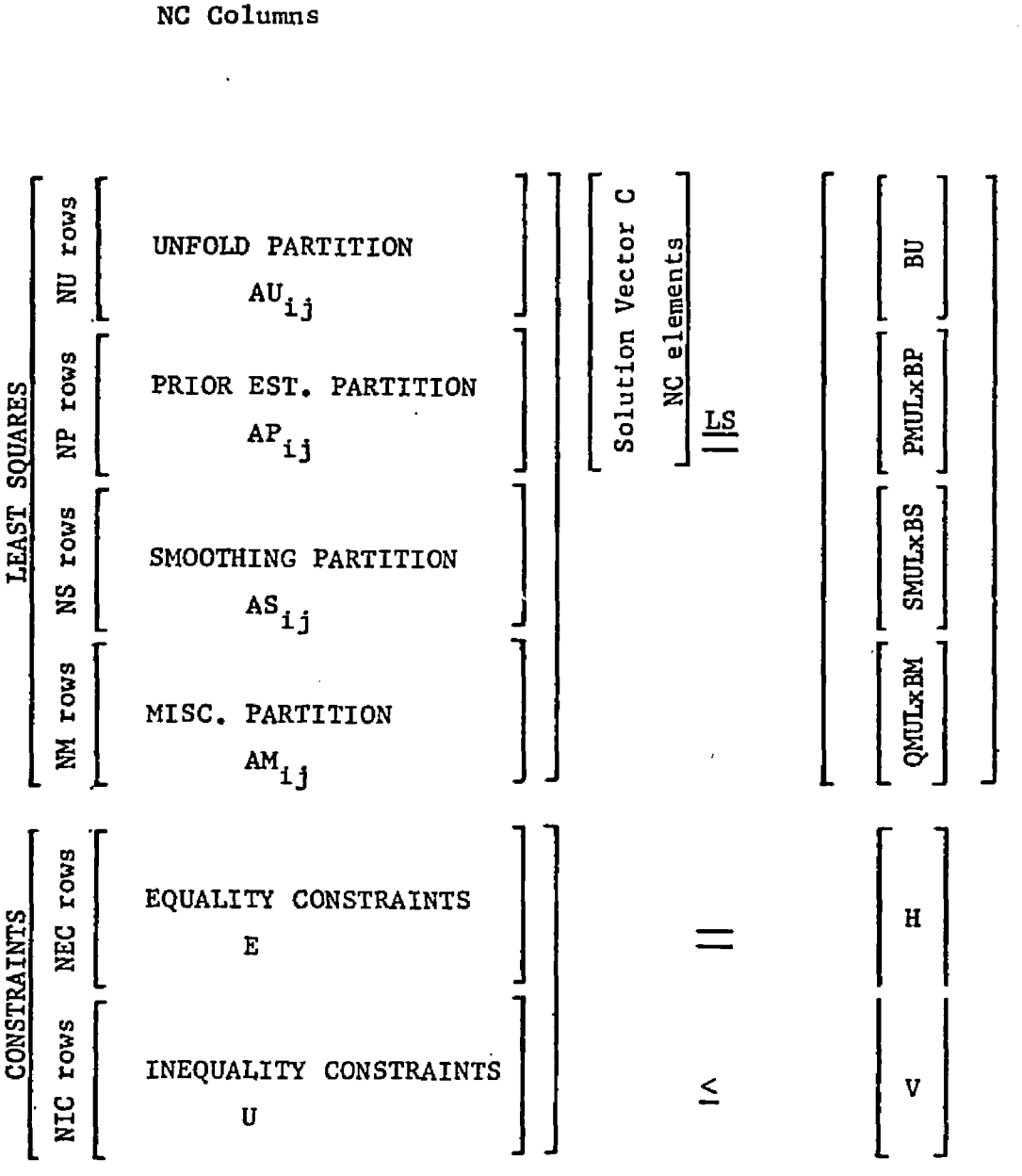

The symbols $\underline{LS}$, $\underline{=}$, are used to imply that the solution vector minimizes the least-squares part of the problem under the conditions imposed by both the equality and inequality constraints.

D.4 Theil-Van de Panne Quadratic Programming Procedure

Because the least squares functional to be minimized is a quadratic form, a quadratic programming approach must be used. Since Bjorck (136) has shown that two successive applications of a stable orthogonalization method (such as the modified Gram-Schmidt orthogonalization) will always solve a quadratic minimization problem subject to equality constraints, the major source of difficulties is the presence of the inequality constraints. These are considered in UNFOLD by the Theil-Van de Panne procedure (46) which treats limiting inequality constraints as equality constraints. The Theil-Van de Panne method employs the following device to generate the solution. First, the solution to the least squares problem with equality constraints is found in the absence of inequality constraints. This solution is then checked for consistency against the inequality constraints. If the result is feasible then it is the true solution; if not, it violates some constraints, at least one of which must be limiting. New solutions are generated by treating each inequality constraint previously violated as an equality constraint. Each of these new solutions is then checked for feasibility against the other inequality constraints. (If again none are feasible, new solutions are found considering all sets of two violated constraints as limiting equality constraints.) This procedure is continued until a solution is found that satisfies all the inequality constraints. This method is easily programmed and will always lead to the

solution, provided a solution exists; however, it has the disadvantage of being time consuming and it also requires large core storage. It is consequently recommended only when the number of inequality constraints is small, or when few are expected to be limiting.

D.5 Modified Gram-Schmidt Orthogonalization

The orthogonalization method used in UNFOLD to solve the least squares minimization problem subject to linear equality constraints is the modified Gram-Schmidt procedure. Referring to Equation (D-33), the least squares functional

$$Z = \sum_{i=1}^{NU+NP+NS+NM} \left\{ \sum_{j=1}^{NC} QA_{ij}\, C_j - BU_i \right\}^2$$

must be minimized subject to the equality constraints

$$\sum_{j=1}^{NC} E_{ij}\, C_j = H_i \qquad i = 1, \ldots, NEC$$

Setting variations of Z with respect to the coefficients C_j equal to zero yields

$$\sum_{i=1}^{NU} \sum_{j=1}^{NC} (QA_{ij}\, C_j - RB_i) = 0 \qquad \text{(D-34)}$$

In matrix notation Equations (D-25) and (D-33) can be combined to form

$$\left[QP\right]\underline{C} = \underline{R} \tag{D-35}$$

where the matrix $\left[QP\right]$ and the vector $\underline{R}$ are defined by

$$QP_{ij} = \begin{cases} A_{ij} & i = 1, \ldots, NU+NP+NS+NM \\ E_{ij} & k = 1, \ldots, NEC;\ i = NU+NP+NS+NM+k \end{cases} \tag{D-36}$$

$$R_i = \begin{cases} RB_i & i = 1, \ldots, NU+NP+NS+NM \\ H_i & k = 1, \ldots, NEC;\ i = NU+NP+NS+NM+k \end{cases}$$

Defining the columns of the matrix QP as vectors, $\underline{W}_1$, ..., $\underline{W}_{NC}$, an equivalent formulation of Equation (D-36) is

$$C_1\underline{W}_1 + C_2\underline{W}_2 + \ldots + C_{NC}\underline{W}_{NC} = \underline{R} \tag{D-37}$$

Gram-Schmidt orthogonalization can now be used to form an orthogonal set of vectors $(\underline{V}_1, \underline{V}_2, \ldots, \underline{V}_{NC}, \underline{V}_{NC+1})$ from the set $(\underline{W}_1, \underline{W}_2, \ldots, \underline{W}_{NC}, \underline{R})$. The C_j can then be written in terms of the orthogonalization parameters. The orthogonal set is formed as shown below:

$$\underline{V}_1 = \underline{W}_1$$

$$\underline{V}_2 = \underline{W}_2 - \alpha_1^2\underline{V}_1 \ ; \quad \alpha_1^2 = \frac{\underline{V}_1 \cdot \underline{W}_2}{\underline{V}_1 \cdot \underline{V}_1}$$

$$\underline{V}_3 = \underline{W}_3 - \alpha_1^3\underline{V}_1 - \alpha_2^3\underline{V}_2 \; ; \quad \alpha_1^3 = \frac{\underline{V}_1 \cdot \underline{W}_3}{\underline{V}_1 \cdot \underline{V}_1} \; , \; \alpha_2^3 = \frac{\underline{V}_2 \cdot \underline{W}_3}{\underline{V}_2 \cdot \underline{V}_2}$$

$$\underline{V}_{NC+1} = \underline{R} - \alpha_1^{NC+1}\,\underline{V}_1 \cdots -\alpha_{10}^{NC+1}\,V_{-10} \; ; \quad \alpha_1^{NC+1}$$

$$= \frac{\underline{V}_1 \cdot \underline{R}}{\underline{V}_1 \cdot \underline{V}_1} \; , \; \ldots, \; \alpha_{NC}^{NC+1} = \frac{\underline{V}_{NC} \cdot \underline{R}}{\underline{V}_{NC} \cdot \underline{V}_{NC}}$$

Upon substitution Equation (D-37) becomes

$$C_1\underline{V}_1 + C_2(\underline{V}_2 + \alpha_1^2\underline{V}_1) + \ldots + C_{NC}(\underline{V}_{NC} + \alpha_1^{NC}\,\underline{V}_1 + \ldots \tag{D-38}$$

$$+ \alpha_{NC-1}^{NC}\underline{V}_{NC-1}) = \underline{V}_{NC+1} + \alpha_1^{NC+1}\,\underline{V}_1 + \ldots + \alpha_{NC}^{NC+1}\,\underline{V}_{NC}$$

The solution coefficients, C_j, are then easily determined and can be written in the convenient form

$$C_j = \frac{\sum_{i=1}^{j} \alpha_i^j \; \alpha_1^{NC+1} \left|\left|\underline{V}_i\right|\right|^2}{\sum_{i=1}^{j} (\alpha_j^j)^2 \left|\left|\underline{V}_i\right|\right|^2} \tag{D-39}$$

with the definition $\alpha_j^j = 1$.

D.6 Fitting Parameter Errors

An approach outlined by Mathews and Walker (137) is used in UNFOLD to investigate errors in the solution parameters and to obtain an estimate of the solution error band.

The quadratic form Z of Equation (D-33) can also be written as

$$Z = CHISQ = \sum_{i=1}^{N=NU+NP+NS+NM} \left\{ \frac{f_i - B_i}{\sigma_i} \right\}^2 \qquad \text{(D-40)}$$

where

$$f_i = f_i(C_1, \ldots, C_{NC}) = \sum_{j=1}^{NC} A_{ij} C_j \qquad \text{(D-41)}$$

The first NU values of σ_i are the ERU_i of Equation (D-4), the B_i are the corresponding G_i, and the first NU rows of the matrix A consist of the $ERU_i * AU_{ij}$ of Equation (D-12). The next NP values of σ_i and B_i are the $ERP_i/\sqrt{PMUL}$ and the P_i, respectively (see Equation (D-5)). The corresponding elements of A are the $D_j(t_i)$ of Equation (D-17). The next NS values of σ_i and B_i are the $ERS(\nu_k)/\sqrt{SMUL}$ and the $\sqrt{QS_k} * S(\nu_k)$, respectively, of Equation (D-6), and the corresponding rows of A consist of the $\sqrt{QS_k} * D_j''(\nu_k)$ of Equation (D-22). The last NM values of σ_i and B_i are the $ERM_i/\sqrt{QMUL}$ and β_i, respectively, of Equation (D-20), and the corresponding rows of A consist of the $\theta_i\left[D_j(t)\right]$ of Equation (D-19).

Assuming for the time being that there are no constraints, some additional insight as to the significance of some of the quantities of the functional Z can be gained. Suppose the B_i were random samples drawn from Gaussian probability distribution centered

at f_i with standard deviations σ_i. Such a hypothesis leads to the likelihood function

$$L(C_1, \ldots, C_{NC}) = \prod_{i=1}^{N} \frac{1}{\sqrt{2\pi\sigma_i^2}} \exp\left[\frac{-(f_i - B_i)^2}{2\sigma_i^2}\right] \tag{D-42}$$

$$= \frac{1}{(2\pi)^{N/2}\sigma_1 \cdots \sigma_N} \exp\left[-\sum_{i=1}^{N} \frac{(f_i - B_i)^2}{2\sigma_i^2}\right]$$

Adjusting the parameters C_j to give maximum likelihood is equivalent to minimizing the exponent of Equation (D-42) which gives the expression for the least squares procedure, Equation (D-40). As a result the ERU_i can be interpreted as estimates of the error in the G_i, with similar interpretations holding for the other weighting factors appearing in Z.

Substituting Equation (D-41) into Equation (D-40) and minimizing CHISQ subject to variations in the coefficients, C_m, lead to the system of equations

$$\sum_{i=1}^{N} \sum_{j=1}^{NC} \frac{A_{im}A_{ij}C_j}{\sigma_i^2} = \sum_{i=1}^{N} \frac{B_i A_{im}}{\sigma_i^2}, \quad m = 1, \ldots, NC \tag{D-43}$$

Defining the matrix $\left[M\right]$ with elements

$$M_{mj} = \sum_{i=1}^{N} \frac{A_{im}A_{ij}}{\sigma_i^2} \tag{D-44}$$

The elements of the solution vector may be written as

$$C_k = \sum_{j=1}^{NC} \sum_{i=1}^{N} \frac{(M^{-1})k_j A_{ij} B_i}{\sigma_i^2} \qquad \text{(D-45)}$$

The errors associated with the parameters C_k may be investigated by either of two methods, both of which yield the same result. First, the likelihood function of Equation (D-42) may be considered to be the probability distribution of the parameters C_k, and the errors are then computed from the mean-square deviations $\left\langle (C_k - C_k^*)^2 \right\rangle$. An alternative point of view is to suppose the entire experiment is repeated a large number of times, M, in the same way (same errors σ_i) to obtain M sets of data $B_i^{(\ell)}$, $\ell = 1, \ldots, M$. From the ℓ-th set of data a solution vector $C^{(\ell)}$ may be calculated using Equation (D-45). From all measurements the average of each parameter C_k is computed from

$$\left\langle C_k \right\rangle = \bar{C}_k = \frac{1}{M} \sum_{\eta=1}^{M} C_k^{(\eta)} = \sum_{j=1}^{NC} \sum_{i=1}^{N} \frac{(M^{-1})_{kj} A_{ij}}{\sigma_i^2} \bar{B}_i \qquad \text{(D-46)}$$

where $\bar{B}_i$ is defined by

$$\bar{B}_i = \frac{1}{M} \sum_{\eta=1}^{M} B_i^{(\eta)} \qquad \text{(D-47)}$$

To find the errors in the parameters, the expected mean-square deviations $\left\langle (C_k - \bar{C}_k)^2 \right\rangle$, or more generally, $\left\langle (C_k - \bar{C}_k)(C_\ell - \bar{C}_\ell) \right\rangle$, must be calculated. Explicitly writing out the implied summation

$$\left\langle (C_k - \bar{C}_k)(C_\ell - \bar{C}_\ell) \right\rangle = \frac{1}{M} \sum_{\beta=1}^{M} \left(C_k^{(\beta)} - \bar{C}_k \right) \left(C_\ell^{(\beta)} - \bar{C}_\ell \right) \qquad \text{(D-48)}$$

In terms of Equations (D-45) and (D-46), Equation (D-48) becomes

$$\left\langle (C_k - \bar{C}_k)(C_\ell - \bar{C}_\ell) \right\rangle = \frac{1}{M} \sum_{\beta=1}^{M} \left\{ \sum_{j=1}^{NC} \sum_{i=1}^{N} \frac{(M^{-1})_{kj} A_{ij}}{\sigma_i^2} \left(B_i^{(\beta)} - \bar{B}_i \right) \right\} \cdot \left\{ \sum_{m=1}^{NC} \sum_{n=1}^{N} \frac{(M^{-1})\ell_m A_{nm}}{\sigma_n^2} \left(B_n^{(\beta)} - \bar{B}_n \right) \right\} \qquad \text{(D-49)}$$

$$= \sum_{j=1}^{NC} \sum_{m=1}^{NC} \sum_{i=1}^{N} \sum_{n=1}^{N} \frac{(M^{-1})_{kj} (M^{-1})\ell_m A_{ij} A_{nm}}{\sigma_i^2 \sigma_n^2} \left(\frac{1}{M} \sum_{\beta=1}^{M} \left(B_i^{(\beta)} - \bar{B}_i \right) \left(B_n^{(\beta)} - \bar{B}_n \right) \right)$$

For $i \neq n$, however, the i-th data and the n-th data are not correlated and

$$\left\langle (B_i - \bar{B}_i)(B_n - \bar{B}_n) \right\rangle = \frac{1}{M} \sum_{\beta=1}^{M} \left(B_i^{(\beta)} - \bar{B}_i \right) \left(B_n^{(\beta)} - \bar{B}_n \right) = \delta_{in} \sigma_i^2 \qquad \text{(D-50)}$$

Equation (D-49) then becomes

$$\left\langle (C_k - \bar{C}_k)(C_\ell - \bar{C}_\ell) \right\rangle = \sum_{j=1}^{NC} \sum_{m=1}^{NC} \sum_{i=1}^{N} \frac{(M^{-1})_{kj}(M^{-1})_{\ell m} A_{ij} A_{im}}{\sigma_i^2}$$

$$= \sum_{j=1}^{NC} (M^{-1})_{kj} \sum_{m=1}^{NC} (M^{-1})_{\ell m} \sum_{i=1}^{N} \frac{A_{ij} A_{im}}{\sigma_i^2} = (M^{-1})_{k\ell} \qquad \text{(D-51)}$$

where Equation (D-50) has just been used.

The root-mean-square error in the fitting parameter C_k is therefore

$$\Delta C_k = \sqrt{\left\langle (C_k - C_k)^2 \right\rangle} = \sqrt{(M^{-1})_{kk}} \qquad \text{(D-52)}$$

D.7 Error Band Calculations

The UNFOLD error band is a root-mean-square error defined as

$$\Delta f(t) = \sqrt{\left\langle (f(t) - \bar{f}(t))^2 \right\rangle} \qquad \text{(D-53)}$$

Using the solution estimate expansion of Equation (D-10), $\bar{f}(t)$ is given by

$$\bar{f}(t) = \frac{1}{M} \sum_{\eta=1}^{M} \sum_{j=1}^{NC} D_j(t)\, C_j^{(\eta)} = \sum_{j=1}^{NC} D_j(t)\, \bar{C}_j \qquad \text{(D-54)}$$

which leads to

$$\left\langle (f(t) - \bar{f}(t))^2 \right\rangle = \frac{1}{M} \sum_{\eta=1}^{M} \sum_{j=1}^{NC} D_j(t) \left(C_j^{(\eta)} - \bar{C}_j \right) \tag{D-55}$$

$$\sum_{k=1}^{NC} D_k(t) \left(C_k^{(\eta)} - \bar{C}_k \right) = \sum_{j=1}^{NC} \sum_{k=1}^{NC} D_j(t) D_k(t) \left\langle (C_j - \bar{C}_j)(C_k - \bar{C}_k) \right\rangle$$

Recalling Equation (D-53) the half width of the error band is obtained.

$$\Delta f(t) = \sqrt{\sum_{j=1}^{NC} \sum_{k=1}^{NC} D_j(t) D_k(t) (M^{-1})_{jk}} \tag{D-56}$$

APPENDIX E. ANALYTICAL INVERSION OF THE FERMI AGE DIFFUSION KERNEL

E.1 Parameterization of the Age Diffusion Kernel

For the "broad" conversion electron spectra for which the Fermi age diffusion theory is expected to be more nearly correct, complications due to the natural conversion electron line width and spectrometer resolution may be neglected. In this case the Fermi age diffusion kernel is given by

$$W(\tau,z) = \frac{1}{4\sqrt{\pi\tau^3}} \left\{ ze^{-z^2/4} + (z + 2d)e^{-(z + 2d)^2/4\tau} \right\}$$

Neglecting the extrapolation distance for simplicity, Equation (3-6) can be explicitly rewritten as

$$N(\tau) = \int_0^\infty S(z) \left\{ \frac{ze^{-z^2/4\tau}}{\sqrt{4\pi\tau^3}} \right\} dz \qquad \text{(E-1)}$$

Equation (E-1) can be viewed as an integral transform of the type

$$F(v) = \int_0^\infty \phi(v,\omega)\ f\ (\omega)d\omega \qquad \text{(E-2)}$$

where

$$\phi(v,\omega) = \frac{e^{-\omega^2/4v}}{(4\pi v)^{\frac{1}{2}}} \qquad \text{(E-3)}$$

This transform has been extensively studied by Widder in connection with the heat conduction equation (138). To use this transform technique Equation (E-1) is rearranged as

$$F(\tau) = 2\tau N(\tau) = \int_0^\infty \phi(\tau,z)\, f(z)dz, \quad \text{where } f(z) = zS(z).$$

Rather than proceed in this manner, however, it is somewhat easier to define two new variable, p and q, according to $p = 1/4\tau$ and $q = z^2$. With these substitutions Equation (E-1) becomes

$$\int_0^\infty S(\sqrt{q})e^{-pq}\, dq = 4\sqrt{\pi}\,(4p)^{-3/2}\, N(\tfrac{1}{4}p) = \tilde{S}(p) \qquad \text{(E-4)}$$

where the tilde (~) denotes the transformed function. The integral in Equation (E-4) is immediately recognized as the Laplace transform of the source distribution, $S(\sqrt{q})$; therefore, $S(\sqrt{q})$ is formally defined by

$$S(\sqrt{q}) = \frac{1}{2\pi i} \int_{C-i\infty}^{C+i\infty} \tilde{S}(p)e^{qp}dp \qquad \text{(E-5)}$$

Hence, by using a suitable approximation for the experimental age distribution, Equation (E-5) may be solved to obtain the depth distribution of conversion electron sources.

E.2 A Sample Calculation

As an example calculation, let $N(\tau)$ be represented by an expansion given as

$$N(\tau) = \frac{S_o}{\sqrt{\pi}} \tau^{-\frac{1}{2}} \sum_{n=0}^{\infty} A_n \tau^{n/2} \qquad \text{(E-6)}$$

where the A_n are the expansion coefficients of the age spectrum determined, for example, by least-squares methods. The transformed source distribution is then given by

$$\tilde{S}(p) = S_o \left| \frac{1}{p} \sum_{n=0}^{\infty} N_n p^{-n/2} \right| \qquad \text{(E-7)}$$

where $N_n = A_n \cdot 2^{-n}$, and $S(\sqrt{q})$ is computed according to Equation (E-5). Dividing the summation into even and odd n terms yields

$$S(\sqrt{q}) = S_o L^{-1} \left\{ \sum_{n=1}^{\infty} N_{2n+1} p^{-n} + \sum_{n=1}^{\infty} N_{2n} p^{-(n+\frac{1}{2})} \right\} \qquad \text{(E-8)}$$

where L^{-1} represents the inverse Laplace transform operator. When the inversion is performed, the source distribution is found to be represented by the power series

$$S(z) = \sum_{n=0}^{\infty} S_n z^n \qquad \text{(E-9)}$$

with the coefficients S_n given by

$$S_n = \begin{cases} N_{n+1}/(n/2)! & n \text{ even} \\ \dfrac{2^{(n+1)/2}\, N_{n+1}}{(1\cdot 3\cdot \ \ldots\ n)\sqrt{\pi}} & n \text{ odd} \end{cases} \qquad \text{(E-10)}$$

While Equations (E-9) and (E-10) constitute a general analytic solution to the unfolding problem with the Fermi age diffusion kernel, in actual practice early numerical experiments indicated that errors generated in the computer computations were sufficient to give rise to oscillations in the solution, $S(z)$. As the applicability of the age diffusion approach is questionable, no further work was done to smooth the oscillations.

BIBLIOGRAPHY

1. Chattopadhyay, B. and Wood, G. C. "The Transient Oxidation of Alloys," Oxidation of Metals, 2, No. 4, 373 (1970).

2. Carlston, R. C. "New Horizons in Characterizing Corrosion Processes," Metals Engineering Quarterly, 10, 30, (1970).

3. Goldanskii, V. I. "The Mossbauer Effect and Its Application in Chemistry," Chemical Applications of Mossbauer Spectroscopy, V. I. Goldanskii and R. H. Herber (eds.), Academic Press, N. Y., (1968).

4. May, L. (ed.). An Introduction to Mossbauer Spectroscopy, Plenum Press, N. Y., (1971).

5. Bonchev, Zw., Jordanov, A., and Minkova, A. "Method of Analysis of Thin Surface Layers by the Mossbauer Effect," Nucl. Inst. and Meth., 70, 36, (1969).

6. Massey, H. S. W. "Electron Scattering in Solids," Adv. in Electronics, L. Martin (ed.), 4, 2, (1952).

7. Davies, J. A., McIntyre, J. D., and Sims, G. A. "The Range of Cs^{137} Ions of KeV energies in Germanium," Can. J. Chem., 40, 1605, (1962).

8. Bergstrom, I., Davies, J. A., Domeij, B., and Uhler, J. "The Range of Rn^{222} Ions of KeV Energies in Aluminum and Tungsten," Ark. Fys., 24, 389, (1963).

9. Powers, D. and Whaling, W. "Range of Heavy Ions in Solids," Phys. Rev., 126, 61, (1962).

10. Domeij, B., Bergstrom, I., Davies, J. A., and Uhler J. "A Method of Determining Heavy Ion Ranges by Analysis of α-Line Shapes," Ark. Fys., 24, 399, (1963).

11. Graham, R. L., Brown, F., Davies, J. A., and Pringle, J. P. S. "A New Method for Measuring the Depths of Embedded Radio-tracer Atoms Using a Precision β-Ray Spectrometer," Can. J. Phys., 41, 1686 (1963).

12. Kundig, W. "A Least Square Fit Program," Nucl. Inst. Meth., 75, 336, (1969).

13. Rhodes, E., Polinger, A., Spijkerman, J. J., and Christ, B. W. "Parabole-Lorentzian Least-Squares Analysis of Mossbauer Data," Trans. Met. Soc. AIME, 242, 1922, (1968).

14. Shirane, G. and Cox, D. E. "Mossbauer Study of Isomer Shift, Quadrupole Interaction, and Hyperfine Field in Several Oxides Containing Fe^{57}," Phys. Rev., 125, No. 4, 1158, (1962).

15. Frauenfelder, H. The Mossbauer Effect, W. A. Benjamin, Inc., New York, (1963).

16. Debrunner, P. G. and Frauenfelder, H. "Introduction to the Mossbauer Effect," An Introduction to Mossbauer Spectroscopy, L. May (ed.), Plenum Press, New York, (1971).

17. Bykov, G. A. and Xien, Pham Zuy. "Calculations of the Parameters of an Experimental Spectrum of the Resonant Absorption of Gamma Quanta in Crystals," Proc. Dubna Conf. on the Mossbauer Effect, Consultant Bureau Enterprises, Inc., N. Y., (1963).

18. Abramowitz, M. and Segun, I. A. (eds.). Handbook of Mathematical Functions, Dover Publications, Inc., N. Y., (1965).

19. Condon, E. U. and Shortly, G. H. Theory of Atomic Spectra, Cambridge University Press, Cambridge, (1951).

20. Sevier, K. D. Low Energy Electron Spectroscopy, Wiley-Interscience, N. Y., (1972).

21. Nordling, C., Sokolowski, E., and Siegbahn, K. "Evidence of Chemical Shifts of the Inner Electronic Levels in a Metal Relative to Its Oxides," Ark. Fys., 13, 483, (1958).

22. Zerby, C. D. and Keller, F. L. "Electron Transport Theory, Calculations, and Experiments," Nucl. Sci. Eng., 27, 190, (1967).

23. Spencer, L. V. "Theory of Electron Penetration," Phys. Rev., 98, 1597, (1955).

24. Bethe, H. A., Rose, M. E., and Smith, L. P. "The Multiple Scattering of Electrons," Proc. Amer. Phil. Soc., 78, 573, (1938).

25. Meister, H. "Zur Theoric der Absorption monoenergetischer Elektronen in metallischen Folien," Z. Naturforsch., 13a, 809, (1958).

26. Weymouth, J. W. "Multiple Scattering in a Semi-Infinite Medium," Phys. Rev., 84, 766, (1951).

27. Roesch, W. C. "Age Diffusion Theory for Beta-Ray Problems," HW-32121, General Electric, Hanford, Atomic Products Operations, (1954).

28. Archard, G. D. "Back Scattering of Electrons," J. Appl. Phys., 32, 1505, (1961).

29. Krakowski, R. A. and Miller, R. B. "An Analysis of Backscatter Mossbauer Spectra Obtained with Internal Conversion Electrons," Nucl. Inst. and Meth., 100, 93, (1972).

30. Lamarsh, J. R. Introduction to Nuclear Reactor Theory, Addison-Wesley Pub. Co., (1966).

31. Bethe, H. A. "Zur Theoric des Durchgangs schneller Korpuskularstrahlen durch Materie," Ann. Physik, 5, 325, (1930).

32. Carslaw , H. C. and Jaeger, J. C. Conduction of Heat in Solids, Oxford Univ. Press, N. Y., (1967).

33. Crank, J. The Mathematics of Diffusion, Oxford Univ. Press, N. Y., (1967).

34. Weinberg, A. M. and Wigner, E. P. The Physical Theory of Neutron Chain Reactors, Univ. of Chicago Press, Chicago, (1958).

35. Bearden, J. A. and Burr, A. F. Atomic Energy Levels, USAEC Division of Technical Information Extension, Oak Ridge, Tennessee, NYO-2543-1, (1965).

36. Bellicard, J. P. and Moussa, A. "Etude des Electrons Auger-K et das Electrons de Conversion du ^{57}Co," J. Phys. Randium, 18, 115, (1957).

37. Arends, E. "Der Ausbeutekoeffizient u der charakteristischen K-strahlung and das Verhaltnis von Luftionisation zu Energie du Rontgenstrahlen," Ann. Physik, 22, 281, (1935).

38. Lingenfelter, J. "An Investigation of the Performance of a Flat, Gas-Flow Proportional Counter for the Detection of Backscattered Low Energy Electrons as Produced by the Mossbauer Effect in Fe^{57}, M.Sc. Thesis, The Ohio State University, (1972).

39. Bergstrom, I., Brown, F., Davies, J. A., Geiger, J. S., Graham, R. L., and Kelly, R. "On the Electromagnetic Separation Method of Preparing Radioactive Sources for Precision β-Spectroscopy," Nucl. Inst. and Meth., 21, 249, (1963).

40. Pines, D. and Bohm, D. "A Collective Description of Electron Interactions," Phys. Rev., 85, 338, (1952).

41. Pines, D. "A Collective Description of Electron Interactions," Phys. Rev., 92, 626, (1953).

42. Pringle, J. P. S. Private Communication, April, 1972.

43. Pringle, J. P. S. "A Very Precise Sectioning Method for Measuring Concentration Profiles in Anodic Tantalum Oxide," J. Electrochem. Soc., 119, 482, (1972).

44. Biggs, F. and Amos, D. "Numerical Solutions of Integral Equations and Curve Fitting," AEC Rept. No. SC-RR-7110212, Sandia Laboratories, Albuquerque, New Mexico, (1971).

45. Miller, R. B. "A User's Manual for UNFOLD: A Numerical Code for Solving Fredholm Integral Equations of the First Kind," The Ohio State University Nuclear Engineering Codes Library, (August, 1972).

46. Theil, H. and Van de Panne, C. "Quadratic Programming as an Extension of Conventional Quadratic Maximization," Management Science, Vol. 7, 1, (1960).

47. Reinsch, C. H. "Smoothing by Spline Functions," Numerische Methematik, 10, 177, (1967).

48. Perkins, J. F. "Monte Carlo Calculation of Transport of Fast Electrons," Phys. Rev., 126, 1781, (1962).

49. McGarrigle, K. S. and Mar, B. W. "Computer Codes for the Evaluation of Space Radiation Hazards," D2-90418, The Boeing Co., (August, 1963).

50. Berger, M. J. "Monte Carlo Calculation of the Penetration and Diffusion of Fast Charged Particles," Methods in Computational Physics, Academic Press, N. Y., 135, (1963).

51. Lilley, J. R. and Yucker, N. R. "CHARGE, A Space Radiation Shielding Code," SM-46335, Douglas Aircraft Co., (April, 1965).

52. Hill, C. W., Ritchie, W. B., and Simpson, Jr., K. M. "Data Compilation and Evaluation of Space Shielding Problems-- Dose Calculations in Space Vehicles," ER7777, Vol. II, Lockheed - Georgia Co., (August, 1965).

53. Best, P. E. "Characteristic Electron Energy Losses in Compounds," Proc. Phys. Soc. (London) 80, 1308, (1962).

54. Pines, D. "Collective Energy Losses in Solids," Rev. Mod. Phys., 28, 184, (1956).

55. Birkhoff, R. D. Handbuch der Physik, 34, Springer-Verlag, Berlin, 71, (1958).

56. Millman, J. and Halkias, C. C. Electronic Devices and Circuits, McGraw-Hill Book Co., N. Y., (1967).

57. Lee-Whiting, G. E. and Tayler, E. A. "On the Design of an Iron-Free $\pi\sqrt{2}$ β-Spectrometer," Chalk River Report CRT-668, (Oct., 1956).

58. Graham, R. L., Ewan, G. T., and Geiger, J. S. "A One-Meter Radius Iron-Free Double-Focusing $\sqrt{2}$ Spectrometer for β-Ray Spectroscopy with a Precision of $1:10^5$," Nucl. Inst. and Meth., 9, 245, (1960).

59. Ewan, G. T. and Graham, R. L. Alpha-, Beta-, and Gamma-Ray Spectroscopy, K. Siegbahn (ed.), North Holland Publishing Co., Amsterdam, 968, (1965).

60. Porter, F. T. and Freedman, M. S. "Outer-Shell Internal Conversion of the 14.4 KeV Transition in Fe^{57}: Chemical Effects and Line Shape Differences," Phys. Rev. C., Nuclear Phys., Vol. 3, No. 6, 2285, (1971).

61. Marion, J. B. "Nuclear Reaction Graphs," in USAEC Nuclear Data Tables, Pt. 3, Nat. Acad. Sciences-Nat. Res. Council, Washington, D. C., (August, 1960).

62. Marton, L. and Leder, L. B. "Energy Loss of Electrons in Passage through Thin Films," Phys. Rev., 94, 203, (1954).

63. Watanabe, H. "On the Velocity Analysis of Electrons Scattered by Thin Foils," J. Phys. Soc. (Japan), 9,920, (1954).

64. Robins, J. L. and Swan, J. B. "Characteristic Electron Energy Loss Spectra of the Transition Metals, Ti to Cu," Proc. Phys. Soc. (London), 76, 857, (1960).

65. Beeman, W. W. and Friedman, H. "The X-Ray K Absorption Edges of the Elements Fe(26 to Ge(32," Phys. Rev., 56, 392, (1939).

66. Ritchie, R. H. "Plasma Losses by Fast Electrons in Thin Films," Phys. Rev., 106, 874, (1957).

67. Ehrenreich, H. and Cohen M. H. "Self-Consistent Approach to the Many-Electron Problems," Phys. Rev., 115, 786, (1959).

68. Compton, A. H. and Allison, S. K. X-Rays in Theory and Experiment, D. Van Nostrand Co., Inc., New York, (1948).

69. Rendian, J. R. "Electron Spectroscopy for Chemical Analysis," American Laboratory, 22, 17, (1972).

70. Davies, J. A., Domeij, B., Pringle, J. P. S., and Brown, F. "The Migration of Metals and Oxygen during Anodic Film Formation," Journal of the Electrochemical Society, 112, 675, (1965).

71. Claus, H. and Ulmer, K. "Untersuchung der Zustandsdichte and der charakteristischen Energieverluste von Ir, Rh, Pt and Pd mit Isochromatenmessungen," Z. Phys., 185, 139, (1965).

72. Rooke, G. A. "Plasmon Satellites of Soft X-Ray Emission Spectra," Phys. Letters, 3, 234, (1963).

73. Burge, R. E. and Smith, G. H. "A New Calculation of Electron Scattering Cross Sections and a Theoretical Discussion of Image Contrast in the Electron Microscope," Proc. Phys. Soc. (London), 79, 673, (1962).

74. Goldstein, H. The Attenuation of Gamma Rays and Neutrons in Reactor Shields, Nuclear Reactor Development Corporation of America, White Plains, New York, (1957).

75. Adams, J. and Manley, B. W. "The Mechanism of Channel Electron Multiplication," Electron Eng., 37, 180, (1965).

76. Biggs, F. and Amos, D. E. Private Communication, (May, 1972).

77. Franklin, J. N. "Well-Posed Stochastic Extensions of Ill-Posed Linear Problems," J. Math. Anal. Appl., 31, 682, (1970).

78. Shaw, Jr., C. B. "Improvement of the Resolution of an Instrument by Numerical Solution of an Integral Equation," J. Math. Anal. Appl., 37, 83, (1972).

79. Evans, R. D. The Atomic Nucleus, McGraw-Hill Book Co., New York, (1955).

80. Rossi, B. High Energy Particles, Prentice-Hall, Englewood Cliffs, New Jersey, (1952).

81. Bethe, H. A. and Ashkin, J. Experimental Nuclear Physics, E. Segre (ed.), Vol. 1, "Passage of Radiation through Matter," John Wiley and Sons, Inc., New York (1953).

82. Fano, U. "Degradation and Range Straggling of High Energy Radiation," Phys. Rev., 92, 328, (1953).

83. Rutherford, E. "The Scattering of α and β Particles by Matter and the Structure of the Atom," Phil. Mag., 21, 672, (1911).

84. Schiff, L. I. Quantum Mechanics, McGraw-Hill Book Co., New York, (1968).

85. Goudsmit, G. A. and Saunderson, J. L. "Multiple Scattering of Electrons," Phys. Rev., 57, 24, (1940).

86. Bethe, H. A. "Zur Theorie des Durchgangs schneller Korpuskularstrahlen durch Materie," Ann. Physik, 5, 325, (1930).

87. Bullard, E. C. and Massey, H. S. W. "Remarks on the Scattering of Electrons by Atomic Fields," Proc. Camb. Phil. Soc., 26, 556, (1930).

88. Moliere, G. "Theorie der Streuung Schneller geladener Teilchen I," Z. Naturforsch., 2a, 133, (1947).

89. Merzbacher, E. Quantum Mechanics, John Wiley and Sons, Inc., New York, (1970).

90. Thomson, J. J. Recollections and Reflections, G. Bell, London, (1936).

91. Bohr, N. "The Penetration of Atomic Particles through Matter," Kgl. Danske Videnskab, Mat.-Fys. Medd., 18, 8, (1948).

92. Mott, N. F. "On the Interpretation of the Relativity Wave Ewuation for Two Electrons," Proc. Roy. Soc. (London), A124, 422, (1929).

93. Moller, C. "Zur Theorie des Durchgangs schneller Elektronen durch Materie," Ann. Physik, 14, 531, (1932).

94. Bloch, F. "Bremsvermogen von Atomen mit Meheren Elektronen," Z. Physik, 81, 363, (1933).

95. Newfeld, J. and Ritchie, R. H. "Passage of Charged Particles through Plasma," Phys. Rev., 98, 1632, (1955).

96. Hubbard, J. "The Dielectric Theory of Electronic Interactions in Solids," Proc. Phys. Soc. (London), A68, 976, (1955).

97. Mahan, G. D. "Excitons in Metals," Phys. Rev. Letters, 18, 448, (1967).

98. Heitler, W. Quantum Theory of Radiation, 3rd ed., Oxford University Press, (1954).

99. Kock, H. W. and Motz, J. W. "Bremsstrahlung Cross-Section Formulas and Related Data," Rev. Mod. Phys., 31, 920, (1959).

100. Williams, E. J. "The Straggling of -Particles," Proc. Royal Soc. (London), 125, 420, (1929).

101. Landau, L. "On the Energy Loss of Fast Particles by Ionization," J. Phys. USSR, 8, 201, (1944).

102. Blunck, J. and Leisegang, S. "Zum Energieverlust schneller Elektronen in Dunnen Schichten," Z. Physik, 128, 500, (1950).

103. Moliere, G. "Theorie der Streuung Schneller geladener Teilchen II," Z. Naturforsch., 3a, 78, (1948).

104. Snyder, H. and Scott, W. T. "Multiple Scattering of Fast Charged Particles," Phys. Rev., 76, 220, (1949).

105. Lewis, H. W. "Multiple Scattering in an Infinite Medium," Phys. Rev., 78, 526, (1950).

106. Spencer, L. V. and Fano, U. "Energy Spectrum Resulting from Electron Slowing Down," Phys. Rev., 93, 1172, (1954).

107. Wentzel, G. "Zur Theorie der Streuung von -Strahlen," Ann. Physik, 69, 335, (1922).

108. Wang, M. C. and Guth, E. "On the Theory of Multiple Scattering, Particularly of Charged Particles," Phys. Rev., 84, 1092, (1951).

109. Breitenberger, E. "Theory of Multiple Scattering," Proc. Royal Soc. (London), 250, 514, (1959).

110. Brown, D. B. and Ogilvie, R. E. "An Electron Transport Model for the Prediction of X-Ray Production and Electron Backscattering in Electron Microanalysis," J. Appl. Phys., 37, 4429, (1966).

111. Brown, D. B., Wittry, D. B., and Kyser, D. F. "Prediction of X-Ray Production and Electron Scattering in Electron-Probe Analysis Using a Transport Equation," J. Appl. Phys., 40, 1627, (1969).

112. Wittig, S. "A Universal Monte Carlo Code for the Solution of Electron Transport Problems," USAEC Document No. ORNL-tr-2126, (1969).

113. Jordan, T. M. "Beta - A Monte Carlo Computer Program for Bremsstrahlung and Electron Transport Analysis," Tech. Rept. No. AFWL-TR-68-111, A.R.T. Research Corp., Los Angeles, Calif., (Oct., 1968).

114. Carlson, B. "Numerical Solution of Neutron Transport Problems," Proc. Symp. Appl. Math., 11, 219, (1955).

115. Bartine, D. E., Alsmiller, Jr., R. G., Mynatt, F. R., Engle, Jr., W. W., and Barrish, J. "Low-Energy Electron Transport by the Method of Discrete Ordinates," ORNL-TM-3438, (18 Aug. 1971).

116. Cashwell, E. D. and Everett, C. J. A Practical Manual on the Monte Carlo Method for Random Walk Problems, Pergamon Press, New York, (1959).

117. Nozieres, P. and Pines, D. "Electron Interaction in Solids. Characteristic Energy Loss Spectrum," Phys. Rev., 113, 1254, (1959).

118. Robins, J. L. and Swan, J. B. "Characteristic Electron Energy Loss Spectra of the Transition Metals, Ti to Cu," Proc. Phys. Soc. (London), 76, 857, (1960).

119. Lynch W. J. and Swan, J. B. "Electron Binding Energies in Transition Metals," Austral. J. Phys., 20, 345, (1967).

120. Hadamard, "Sur les Problems aux Derivees Partielles et leur Significations Physiques," Bul. Univ. Princeton, 13, (1902).

121. Lavrentiev, M. M. Some Improperly Posed Problems of Mathematical Physics, Springer-Verlag, New York/Berlin, (1967).

122. Tricomi, F. Integral Equations, Interscience Publishers, New York, (1957).

123. Twomey, S. "The Application of Numerical Filtering to the Solution of Integral Equations Encountered in Indirect Sensing Measurements," J. Franklin Institute, 279, 95-109, (1965).

124. Marshall, N. H. "Numerical Techniques for Solving Fredholm's Integral Equation of the First Kind," IDO-17175, (May, 1966).

125. Molleneuer, J. F. Univ. Cal. Rad. Lab. Report, UCRL-9748 (1961).

126. Scofield, N. E. "Applications of Computers to Nuclear and Radiochemistry," NAS-NS 3107, OTS, Dept. Commerce, Washington, D. C., (1963).

127. Alberg, M., O'Brien, K., and McLaughlin, J. "An Experimental Determination of the Energy Distribution of Gamma Rays Scattered in Sand," Nucl. Sci. and Eng., 25, 303, (1966).

128. Miller, D., Schlosser, P., Burt, J., Glower, D. D., and McNeilly, J. M. "A Pulsed Radiation Energy Spectrometer Using Ferroelectrics," IEEE TRANS. Nucl. Sci. NS-14, 245, (1967).

129. Gold, R. "An Iterative Unfolding Method for Response Matrices," ANL-6984, (Dec., 1964).

130. Phillips, D. L. "A Technique for the Numerical Solution of Certain Integral Equations of the First Kind," J. Assoc. Comput. Mach., 9, 84-97, (1962).

131. Tihonov, A. N. "Regularization of Incorrectly Posed Problems," Soviet Math. Dokl., 4, 1624-1627, (1963).

132. Biggs, F. "Data Analysis Involving Solutions of the Fredholm Integral Equation of the First Kind," SC-RR-68-711, (Feb. 1969).

133. Bellman, R., Kalaba, R. E., and Lockett, J. A. Numerical Inversion of the Laplace Transform, American Elseview, New York, (1968).

134. Strand, O. N. and Westwater, E. R. "Statistical Estimation of the Numerical Solution of a Fredholm Integral Equation of the First Kind," J. Assoc. Comput. Mach., 15, 100-114, (1968).

135. Sudakov, V. N. and Kalfin, L. A. "A Statistical Approach to Improperly Posed Problems of Mathematical Physics." (in Russian), Dokl. Akad. Nauk. SSSR, 5, (1957).

136. Bjorck, A. "Iterative Refinement of Gaussian Least Squares Solutions II," BIT 8, 8, (1968).

137. Mathews, J. and Walker, R. L. Mathematical Methods of Physics, 2nd ed., W. A. Benjamin, Inc., New York, (1970).

138. Widder, D. V. "The Inversion of a Transform Related to the Laplace Transform and to Heat Conduction," J. Austral. Math. Soc., 4, 1, (1964).